IMPROVING THE MECHANICAL AND PHYSICAL PROPERTIES OF AN ALUMINUM POWDER METALLURGY METAL MATRIX COMPOSITE VIA HOT UPSET FORGING

by

Gregory Alexander Wilson Sweet

Submitted in partial fulfilment of the requirements
for the degree of Doctor of Philosophy

at

Dalhousie University
Halifax, Nova Scotia
March 2019

TABLE OF CONTENTS

LIST OF TABLES ..... **vii**

LIST OF FIGURES ..... **ix**

ABSTRACT ..... **xvii**

LIST OF ABBREVIATIONS AND SYMBOLS USED ..... **xviii**

ACKNOWLEDGEMENTS ..... **xxi**

CHAPTER 1. INTRODUCTION **1**

1.1 ALUMINUM POWDER METALLURGY 1

1.1.1 Powder Characteristics 1

1.1.2 Compaction and Sintering Practices 5

1.1.3 Post-Sinter Processing 14

1.2 HOT FORMING OPERATION: FORGING 15

1.2.1 Forging Techniques and Considerations 16

1.3 FORGEABILITY AND CONSTITUENT EQUATION REPRESENTATION 22

1.4 RECOVERY AND RECRYSTALLIZATION EFFECTS 27

1.4.1 Recovery 30

1.4.2 Recrystallization 37

1.5 HOT WORKING ALUMINUM AND ALUMINUM ALLOYS 44

1.6 POWDER FORGING 50

1.6.1 Hot Pressing and Upsetting 52

1.6.2 Powder Forging Performance 57

CHAPTER 2. RESEARCH OBJECTIVES **63**

CHAPTER 3. CONSOLIDATION OF ALUMINUM-BASED METAL MATRIX COMPOSITES VIA SPARK PLASMA SINTERING **64**

3.1 FORWARD TO CHAPTER 3 64

3.2 ABSTRACT 65
3.3 INTRODUCTION 66
3.4 MATERIALS 68
3.5 EXPERIMENTAL TECHNIQUES 69
3.6 RESULTS AND DISCUSSION 71
3.6.1 Effects of Ceramic Type and Concentration 71
3.6.2 Effects of Ceramic Particle Size 83
3.6.3 Three-Point Bend Properties 87
3.7 CONCLUSIONS 93
3.8 ACKNOWLEDGEMENTS 94
CHAPTER 4. POWDER METALLURGICAL PROCESSING OF A 2XXX SERIES ALUMINUM POWDER METALLURGY METAL ALLOY REINFORCED WITH AlN PARTICULATE ADDITIONS 95
4.1 FORWARD TO CHAPTER 4 95
4.2 ABSTRACT 96
4.3 INTRODUCTION 96
4.4 MATERIALS 98
4.5 EXPERIMENTAL TECHNIQUES 99
4.6 RESULTS AND DISCUSSION 101
4.6.1 Powder Attributes 102
4.6.2 Compaction Response 103
4.6.3 Sintering Response 106
4.6.4 Mechanical Properties 111
4.7 DISCUSSION 120

4.7.1 Ceramic Effects on Processing 120

4.7.2 Ceramic Effect on Sintered Properties 122

4.8 CONCLUSIONS 125

4.9 ACKNOWLEDGEMENTS 126

CHAPTER 5. THERMAL MECHANICAL PROCESSING OF PRESS AND SINTER Al-Cu-Mg-Sn-(AlN) METAL MATRIX COMPOSITE MATERIALS 127

5.1 FORWARD TO CHAPTER 5 127

5.2 ABSTRACT 128

5.3 INTRODUCTION 129

5.4 MATERIALS AND METHODS 133

5.5 RESULTS 137

5.5.1 Densification 137

5.5.2 Microstructural Transitions 138

5.5.3 Flow Curves 146

5.6 DISCUSSION 150

5.6.1 Porosity 150

5.6.2 Hot Ductility 152

5.6.3 Flow Behaviour 153

5.6.4 Constituent Behaviour Analysis 158

5.7 CONCLUSIONS 161

5.8 ACKNOWLEDGMENTS 163

CHAPTER 6. SUPPLEMENTAL ANALYSIS OF THE THERMAL MECHANICAL PROCESSING OF METAL MATRIX COMPOSITES: PROCESS MAPS 164

CHAPTER 7. DEVELOPMENT OF A PROCESS TO INVESTIGATE THE MECHANICAL PROPERTIES OF A POWDER FORGED ALUMINUM ALLOY 177

7.1 FORWARD TO CHAPTER 7 177

7.2 ABSTRACT 178

7.3 INTRODUCTION 179

7.4 MATERIALS 179

7.5 EXPERIMENTAL TECHNIQUES 180

7.6 RESULTS AND DISCUSSION 183

7.6.1 Lab Scale Forging 183

7.6.2 Upscaled Forging Design 192

7.6.3 Properties of Sintered + Forged Cylinders 204

7.7 CONCLUSIONS 209

7.8 ACKNOWLEDGEMENTS 211

CHAPTER 8. MICROSTRUCTURAL EVOLUTION OF A FORGED 2XXX SERIES ALUMINUM POWDER METALLURGY ALLOY 212

8.1 FORWARD TO CHAPTER 8 212

8.2 ABSTRACT 213

8.3 INTRODUCTION 213

8.4 MATERIALS AND METHODOLOGY 215

8.5 RESULTS AND DISCUSSION 218

8.5.1 Physical and Mechanical Property Effects 218

8.5.2 General Microstructure Assessment 223

8.5.3 Prior Particle Boundary Assessment 231

8.6 CONCLUSIONS 238

8.7 ACKNOWLEDGMENTS 239

CHAPTER 9. A MICROSTRUCTURAL AND MECHANICAL PROPERTY INVESTIGATION OF A HOT UPSET FORGED 2XXX SERIES ALUMINUM POWDER METALLURGY ALLOY REINFORCED WITH AlN. 240

9.1 FORWARD TO CHAPTER 9 240

9.2 ABSTRACT 241

9.3 INTRODUCTION 241

9.4 MATERIALS AND METHODOLOGY 244

9.5 RESULTS AND DISCUSSION 249

9.5.1 Physical Attributes 249

9.5.2 Mechanical Performance 258

9.6 CONCLUSIONS 273

9.7 ACKNOWLEDGEMENTS 275

CHAPTER 10. FINAL CONCLUSIONS AND FUTURE WORK 276

10.1 SUGGESTED FUTURE WORK 285

REFERENCES 288

APPENDIX A: COPYRIGHT RELEASE 301

LIST OF TABLES

Table 1-1 Forging temperature ranges for select aluminum forging alloys *[13]* 19

Table 1-2 Die temperature ranges for select forging equipment, listed in order of decreasing nominal strain rates *[13]*..... 21

Table 1-3 Stacking fault energy values for assorted materials [16]..... 33

Table 3-1 Particle size data for the powders employed. 69

Table 3-2 Comparison of the three-point bend properties measured for SPS products. All MMCs reinforced with 10 vol% ceramic..... 90

Table 4-1 Constituent powders utilized in preparing the various blends of interest. 99

Table 4-2 Effects of AlN-C and AlN-F on flow. 102

Table 4-3 Three-point bend fatigue endurance limits of select compositions 116

Table 5-1 Overview of the metallic powders employed. 134

Table 5-2 Fraction of low angle grain boundaries (misorientation ≤ 15 °) in the microstructures presented in Figure 5-4. 145

Table 5-3 Summary of the material chemistries and TMP conditions found to induce circumferential cracking within the forged product. 145

Table 5-4 Effects of TMP conditions and material composition on the peak flow stress..... 149

Table 5-5 Constituent values for the APM materials modeled in accordance with equation (19) 159

Table 6-1 Temperature-corrected instantaneous flow stress values for the material 'Base' 167

Table 6-2 Temperature-corrected instantaneous flow stress values for the material '2C' 168

Table 6-3 Temperature-corrected instantaneous flow stress values for the material '2F' 169

Table 7-1 Chemical nature and particle size of constituent metal powders utilized. 180

Table 7-2 List of preform geometry details and the types of mechanical property specimens that could be extracted under specific levels of applied forging strain. 196

Table 7-3 Go/No Go table for the ability to forge the 30 mm and 50 mm preforms to a critical thickness of 8 mm at various strain rates and temperatures. 197

Table 7-4 Coefficient of friction values measured at the different temperatures and lubrication strategies considered. 199

Table 7-5 Comparison of tensile properties measured for the Al-3Cu-1.5Mg-0.5Sn APM alloy before and after isothermal forging. 208

Table 8-1 Chemical analysis of the starting, sintered specimen, acquired by ICP-OES. 216

Table 8-2 EDS composition of secondary phases noted in Figure 8-7c. 228

Table 9-1 Type, size and composition of the constituent powders employed in raw blend production. 244

Table 9-2 Fatigue strengths of select MMC forgings. 270

Table 10-1 Summary of fatigue performance for T6 specimen in the sintered and various forged conditions. 284

LIST OF FIGURES

Figure 1-1 Schematic of gas atomizing a molten metal into progressivly spherodized metal powders. 2

Figure 1-2 SEM micrograph of an air atomized aluminum powder, showing irregular and ligamental particles. 4

Figure 1-3 Schematic of circular particles rearranging and plastically deforming because of an externally applied force. 7

Figure 1-4 Interaction of a liquid phase in contact with solid and vapour phases, and the resultant wetting angle. 9

Figure 1-5 Solubility map of the behaviour of sintering response in early stages of LPS *[8]* 9

Figure 1-6 Schematic of solution reprecipitation. In the early stages of liquid phase development, particles resemble their original size and geometry. 12

Figure 1-7 Impression die forging with either flash (white) or flashless (shaded area) design. 18

Figure 1-8 Processing map for 2124 P/M extruded alloy at a strain of 0.5 shaded region represents flow instability *[26]* 27

Figure 1-9 Schematic of the evolution of recovery micro mechanisms *[16]*. 31

Figure 1-10 Dipole elimination mechanism in a crystal *[16]* 33

Figure 1-11 Schematic of the progression of annihilation and subsequent rearrangement of dislocations into a low energy configuration [16]. 34

Figure 1-12 True stress-strain curve for the hot deformation of a material undergoing recovery [16]. 36

Figure 1-13 Schematic representation of the recovery of a material with no orientation gradient (a) and (b), or with an orientation gradient (c) and (d) [16]. 40

Figure 1-14 Lattice rotation of subgrains as a function of distance relative to an arbitrary grain resulting from deformation [16]..... 40

Figure 1-15 Time for 50% recrystallization of an Al-Si alloy relative to a single-phase Al system as a function of secondary phase particle size [16]. 42

Figure 1-16 Time for 50% recrystallization of an Al-Si alloy relative to a single-phase Al system as a function of secondary phase interparticle spacing [16]. 43

Figure 1-17 True stress strain behaviour of a 0.68%C steel under various hot deformation conditions exhibiting dynamic recrystallization [16]. 44

Figure 1-18 The yield stress of an aluminum system, varying with subgrain size resulting from unique processing conditions [18]. 45

Figure 1-19 Equivalent stress strain curves for precipitation-hardenable alloys, exhibiting dramatic temperature dependence [28]. 48

Figure 1-20 The loss in mechanical properties as a function of the final part density for PM steel components. 51

Figure 1-21 Schematic representation of upset forging and repressing of porous preforms into fully dense compacts. 55

Figure 1-22 Effect of upset forging and hot pressing on pore collapse. 56

Figure 1-23 The strain at fracture, corresponding hoop strain, for ferrous powder forged compacts. 60

Figure 3-1 Effects of sintering temperature on the density of MMCs prepared with 2, 5 and 10 vol% (a) SiC-F, (b) AlN-F, (c) Si_3N_4-F and (d) BN-F. 73

Figure 3-2 SEM micrographs of sintered MMC mixtures that contained 10 vol% (a) SiC-F, (b) AlN-F, (c) Si_3N_4-F and (d) BN-F. 78

Figure 3-3 SEM micrographs of ceramic clusters observed in sintered MMC mixtures that contained 10 vol% (a) SiC-F sintered at 450°C, (b) SiC-F at 550°C, (c) AlN-F at 450°C, (d) AlN-F at 550°C, (e) Si_3N_4-F at 450°C and (f) Si_3N_4-F at 550°C 79

Figure 3-4 Effects of sintering temperature on the hardness of MMC prepared with 2, 5 and 10 vol% (a) SiC-F, (b) AlN-F, (c) Si_3N_4-F and (d) BN-F. 82

Figure 3-5 Effect of ceramic particle size and SPS temperature on the sintered density of MMCs containing (a) SiC and (b) AlN. 84

Figure 3-6 Optical micrographs of sintered MMC mixtures that contained 10 vol% (a) SiC-C and (b) AlN-C. Both samples sintered at 550°C. 85

Figure 3-7 Comparison of the size distributions measured for the two grades of SiC and AlN powders utilized. 85

Figure 3-8 Effect of ceramic particle size and SPS temperature on the hardness of sintered MMC systems containing (a) SiC and (b) AlN. 86

Figure 3-9 Effects of specimen size on the (a) density and (b) hardness of SiC-C and AlN-C reinforced MMCs. 88

Figure 3-10 Three-point bend stress versus strain curves for MMCs reinforced with 10% (a) SiC-C and (b) AlN-C. 90

Figure 3-11 SEM micrographs of the fracture surfaces from three-point bend specimens containing 10% ceramic additions and sintered at various temperatures..... 91

Figure 4-1 AD data for the powder mixtures considered. 103

Figure 4-2 Green densities of MMC compacts as a function of compaction pressure and ceramic content. 104

Figure 4-3 Green strength of MMC compacts as a function of compaction pressure and ceramic content. 105

Figure 4-4 Relative theoretical density of sintered compacts as a function of ceramic content and type. 107

Figure 4-5 Optical micrographs of (a) the MMC Matrix material 'Base', (b) 2C, and (c) 2F which all sintered to high relative densities. 109

Figure 4-6 Optical micrographs of MMC systems (a) 5C, (b) 5F, and (c) 10F. 110

Figure 4-7 Dynamic elastic moduli of MMC materials as measured through impulse excitation. 112

Figure 4-8 Tensile properties of MMC material as a function of composition. 114

Figure 4-9 Tensile fracture surfaces of the (a) Base, (b) 2C and (c) 2F materials. Arrows highlight residual porosity (blue), fractured AlN particles (red), dense clusters of AlN particulate (yellow) and more dispersed bands of AlN (green). An EDS map of nitrogen (red points) is superimposed showing the location of AlN particulate. 115

Figure 4-10 Crack path morphology for a long fatigue crack growth for the base and MMC materials. 117

Figure 4-11 Scanning electron micrographs of the fracture surfaces of (A) Base, (B) 2C, (C) 2F. 119

Figure 5-1 Gleeble 3500 anvil setup for hot compression testing. 136

Figure 5-2 Densities of APM MMCs as measured before and after TMP. 138

Figure 5-3 Sequence of unetched microstructures of as-sintered alloys (a) Base, (b) 2C, (c) 5C and (d) 10C contrasted by their hot worked counterpart in (e) base, (f) 2C, (g) 5C and (h) 10C. 140

Figure 5-4 EBSD map of (a) Base, (b) 2C and (c) 5C in the as sintered condition as well as variants deformed at 500°C and 0.005 s^{-1} for (d) Base, (e) 2C and (f) 5C. 144

Figure 5-5 Typical appearance of cracks present at the circumference of select products after TMP. Sample 2C processed at 500˚C and 5 s^{-1}. 146

Figure 5-6 Flow stress (true stress – true strain) curves for alloy 2C developed during TMP at temperatures of 350°C to 500°C and strain rates of 5 s^{-1}, 0.5 s^{-1}, 0.05 s^{-1} and 0.005 s^{-1}. 147

Figure 5-7 Data illustrating the effects of isothermal hold time on the flow curves for MMC 5F when deformed at 350°C and 450°C. 150

Figure 5-8 Flow curves for each material composition deformed at 350°C and 0.05 s^{-1} exhibiting the variation in peak flow stress. 157

Figure 5-9 Effect of preform sintered density on the peak flow stress, samples deformed at a strain rate of 0.05 s-1 and temperatures 350°C to 500°C. 158

Figure 5-10 Peak flow stress data for MMC materials plotted versus strain rate. 161

Figure 6-1 Process map of the material 'Base' deformed to a true strain of 0.65 mm/mm. Colored contours represent the efficiency value whereas the shaded portions represent regions of flow instabilities. 170

Figure 6-2 Process map of the material '2C' deformed to a true strain of 0.65 mm/mm. Colored contours represent the efficiency value whereas the shaded portions represent regions of flow instabilities. 171

Figure 6-3 Process map of the material '2F' deformed to a true strain of 0.65 mm/mm. Colored contours represent the efficiency value whereas the shaded portions represent regions of flow instabilities. 172

Figure 6-4 Optical micrographs of MMC composition 2C under the hot forging conditions corresponding to the four corners of its corresponding process map. 174

Figure 6-5 EBSD figures of 2C forged to 0.70 mm/mm at 5 s^{-1} and either 350°C or 450°C, exhibiting a microstructure consistent with dynamic recovery 175

Figure 7-1 Specimen chamber of a Gleeble 3500 thermomechanical tester. 184

Figure 7-2 Flow stress curves generated from samples of the sintered APM alloy when isothermally forged under various temperatures and strain rates. 186

Figure 7-3 DSC thermogram of the APM material in the as sintered (T1) condition. ... 188

Figure 7-4 Pressed, sintered, and machined Gleeble specimens (a) before and (b) after deformation at 450°C ($\varepsilon = 0.5$ s^{-1}; $\varepsilon = 0.70$ mm/mm) 189

Figure 7-5 Comparison of the relative densities measured for sintered and sintered + forged samples. 190

Figure 7-6 (a) Schematic of the three distinctive zones that form during inhomogeneous deformation due to friction during compression tests (adapted from [100]), accompanied by the microstructures of the alloy in the (b) as-sintered and (c) sintered + forged condition. 192

Figure 7-7 (a) Interlaken hydraulic load frame utilized for upscaled isothermal forging trials. (b) Close up of the heated tooling, sample and stopper block arrangement..... 194

Figure 7-8 Comparison of a machined Gleeble sample alongside the sintered 30 mm and 50 mm preforms utilized in upscaled forging trials. 195

Figure 7-9 (a) Nondeformed ring compression test specimen and (b) the corresponding Coefficient of Friction calibration plot. 199

Figure 7-10 Data on the (a) true flow stress and (b) true strain rate as functions of applied true strain for samples deformed using the Gleeble and Interlaken systems. 203

Figure 7-11 Comparison of the peak flow stress values measured in lab scale and upscaled forging tests. 204

Figure 7-12 SEM micrographs recorded from a 30 mm sample deformed at 450°C ($\dot{\varepsilon} = 1.0\ s^{-1}$; $\varepsilon = -1.0$ mm/mm) showing an area representative of the (a) Zone I, and (b) Zone II microstructures. 206

Figure 7-13 Bright field TEM image of a PPB within a forged 50 mm sample and the corresponding EDS map for oxygen. 206

Figure 7-14 Three-point bend fatigue strength of the exemplary APM alloy before and after forging. 209

Figure 8-1 Density of sintered and sintered-forged samples displayed as a function of true compressive forging strain 219

Figure 8-2 Electron micrograph of surface cracks present on the outside circumference of samples hot upset forged at 1.55 mm/mm. 220

Figure 8-3 0.2% offset strength and tensile strength as a function of true compressive upset forging strain 222

Figure 8-4 Tensile ductility as a function of true compressive upset forging strain..... 222

Figure 8-5 Pseudo-binary phase diagram of the alloy system with composition outlined in Table 8-1, the blue line represents the copper concentration used in this study. 225

Figure 8-6 Aluminum-rich corner of the Al-Cu-Mg phase diagram at the artificial aging temperature of 190°C. 225

Figure 8-7 SEM micrographs showing the bulk T6 microstructure of the APM alloy (a) as-sintered and (b) after hot forging to 1.40 mm/mm true strain. 227

Figure 8-8 TEM micrographs showing the bulk T6 microstructure of the APM alloy (a) as-sintered and (b) after hot forging to 1.40 mm/mm true strain. 229

Figure 8-9 TEM micrographs of the sintered-forged (1.40mm/mm)-T6 specimen showing; (a) a bright field image of sprial heterogeneous precipitates on helical dislocations, (b) a second bright field image of another morphology of the heterogeneous precipitates along with accompanying EDS elemental maps of (c) Cu, (d) Mg and (e) Si. 231

Figure 8-10 Optical micrographs contrasting the prior particle boundary nature of the APM alloy (a) as-sintered and (b) after hot forging to 1.40 mm/mm true strain. 233

Figure 8-11 TEM micrographs highlighting the nature of the prior particle boundary of a sintered T6 specimen: including the bright field image and the EDS-acquired elemental maps of oxygen, copper, magnesium, nitrogen and tin. 235

Figure 8-12 TEM micrograph of the phases along a prior particle boundary and the corresponding, annotated, diffraction pattern. 236

Figure 8-13 TEM micrographs highlighting the nature of the prior particle boundary of a sintered – forged (1.40mm/mm) - T6 specimen. 237

Figure 9-1 Photograph of the sample and die assembly in the Interlaken 110 load frame prior to deformation. 246

Figure 9-2 Schematic of TRS specimen orientations sectioned from cylindrical, forged pucks. 248

Figure 9-3 Densification trend of MMC 2C as a function of hot upset forging strain. .. 251

Figure 9-4 Electron micrographs of the hot upset material 2C at strains of (a) 0.15 mm/mm, (b) 0.30 mm/mm, (c) 0.6 mm/mm and (d) 1.4mm/mm. 252

Figure 9-5 Coarse AlN-C particle within an aluminum matrix, showing porosity in black contrast within the ceramic phase. 253

Figure 9-6 Comparison of sintered and forged densities for MMC systems that utilized different types and concentrations of AlN particulate. 254

Figure 9-7 Microstructures of materials (a) Base, (b) 5C, (c)2F and (d) 5F hot upset forged to a true strain of 1.40 mm/mm. 255

Figure 9-8 TEM analysis of an exemplary Al-AlN interface including a BF image and EDX maps for the key elements of interest. 258

Figure 9-9 (a) Summarized tensile properties and (b) stress-strain curves of MMC 2C when forged to different levels of true strain. 260

Figure 9-10 Dynamic elastic modulus of MMC materials hot upset forged to 1.40 mm/mm at a rate of 0.1 s^{-1} as measured by the impulse excitation method. 261

Figure 9-11 Effect of AlN type and concentration on yield strength. 263

Figure 9-12 Effect of AlN type and concentration on UTS. 264

Figure 9-13 Tensile ductility values as a function of ceramic type and concentration at a fixed strain of 1.40 mm/mm and rate of 0.1 s^{-1}. 265

Figure 9-14 Strain hardening exponent of materials hot upset forged to 1.40 mm/mm at a rate of 0.1 s^{-1}. 267

Figure 9-15 Examples of fractured AlN particles observed within the microstructures of (a) 5C and (b) 5F after tensile testing. 268

Figure 9-16 Optical micrographs revealing the fatigue crack paths within fractured fatigue bars of (a) 2F (data set 1) and (b) 2C (Data set 2) at a strain of 1.40 mm/mm in the C-L orientation, followed by 2C at a forging strain of 0,35 mm/mm in the (c) C-L (data set 4) and (d) L-C (data set 6) oritentations. 271

Figure 10-1 Effect of forging strain on the T6 tensile ductility of 50 mm cylinders deformed at 450°C and 0.1 s^{-1} with and without ceramic additions. 282

ABSTRACT

Aluminum powder metallurgy (APM) represents an advanced metal forming technology premised on a three-stage production sequence of die compaction, liquid phase sintering, and post-sinter sizing. It is principally utilized within the automotive sector to produce lightweight structural components including camshaft bearing caps, heat sinks, planetary gear carriers, and transmission retainer plates. While the list of commercialized products continues to grow steadily, certain opportunities remain inaccessible as the physical and mechanical properties of APM products often fall below their wrought counterparts. This restraint is underpinned by two key microstructural traits - residual porosity and a thermodynamically stable 3D-interconnected network of oxide phases. These limit the load bearing capacity of a component while providing an intergranular failure path. Ferrous powder metallurgy has seen notable metallurgical benefits and ensuing commercial proliferation when carefully designed, sintered preforms are forged to full density. The aim of this study was to employ a comparable sinter-forge methodology to APM alloys and then ascertain its effectiveness through detailed characterization of the microstructure and physical/mechanical properties of the forged product. The alloy system used was a commercial 2XXX series APM alloy coupled with one of two aluminum nitride (AlN) ceramic powders to create a metal-matrix composite (MMC). Constitutive analysis of the deformation behaviour was completed using a Zener-Holloman analysis and 2D process mapping. For several compositions, a domain of stable flow characterized by dynamic recovery was observed from 400°C to 500°C and strain rates 0.05 s^{-1} to 5 s^{-1}. Near-theoretical densities (99.5%) were obtained for a variety of MMC compositions, although up to 100.0% densities were also achieved in select instances. Shear strain elongated and flattened residual pores, markedly reduced the level of porosity at Al-AlN interfaces and disrupted the continuous network of fine MgO crystallites into a semi-continuous network without invoking fracture or decohesion of AlN particulate. Such transitions led to demonstrable gains in mechanical properties with the extent dependant on the type and concentration of AlN incorporated. In the case of tensile properties, UTS increased by 48 to 91 MPa, elastic modulus improved by up to 9GPa while tensile ductility saw up to a five-fold rise. Gains in fatigue performance were particularly astute with a 98 MPa (57%) increase in bending fatigue strength observed.

LIST OF ABBREVIATIONS AND SYMBOLS USED

APM	Aluminum Powder Metallurgy
PM	Powder Metallurgy
LPS	Liquid Phase Sintering
θ	Wetting Angle
γ_{SV}	Solid-Vapour Surface Energy
γ_{SL}	Solid-Liquid Surface Energy
γ_{LV}	Liquid-Vapour Surface Energy
T_M	Melting Temperature
T	Temperature
ε	Strain
$\dot{\varepsilon}$	Strain Rate
$\bar{\varepsilon}$	True Strain
$\bar{\sigma}$	True Stress
Z	Zener Hollomon Parameter
Q_{HW}	Activation Energy of Hot Working
σ_s	Steady State Flow Stress
n	Efficiency of Power Dissipation
ζ	Instability Parameter
λ_{SFE}	Stacking Fault Energy
SRV	Static Recovery
DRV	Dynamic Recovery
PSN	Particle Stimulated Nucleation

SRX	Static Recrystallization
DRX	Dynamic Recrystallization
MMC	Metal Matrix Composite
DPN	Dynamic Precipitation
CTE	Coefficient of Thermal Expansion
AlN	Aluminum Nitride
SPS	Spark Plasma Sintering
SiC	Silicon Carbide
Si_3N_4	Silicon Nitride
BN	Boron Nitride
Al_2O_3	Aluminum Oxide
MPIF	Metal Powders Industries Federation
SEM	Scanning Electron Microscope
HRH	Rockwell Hardness H Scale
UBS	Ultimate Bending Stress
NSERC	Natural Science and Engineering Research Council of Canada
TRS	Transverse Rupture Specimen
UTS	Ultimate Tensile Strength
EDS	Energy Dispersive Spectroscopy
AD	Apparent Density
GS	Green Strength
IPF	Interparticle Friction
PPB	Prior Particle Boundary

TMP	Thermal Mechanical Processing
EBSD	Electron Backscatter Diffraction
LAGB	Low Angle Grain Boundary
HAGB	High Angle Grain Boundary
DSC	Differential Scanning Calorimetry
PF	Powder Forging
GPZ	Guinier-Preston Zone
COF	Coefficient of Friction
SB	Stopper Block
TEM	Transmission Electron Microscopy
EDX	Energy Dispersive X-Ray Spectroscopy

ACKNOWLEDGEMENTS

Above all, I would like to thank Dr. Paul Bishop for his guidance and motivation throughout this project. Thanks are also extended to the rest of the Powder Metallurgy Research Group at Dalhousie University, especially Randy Cooke for enduring my relentless questions. Financial support from the Natural Sciences and Engineering Council of Canada through their Canada Graduate Scholarship program was especially appreciated.

Numerous individuals are thanked for their technical assistance throughout this project. Specifically, David Walker and Jason Milligan at McGill University, Mark Whitney at the University of Waterloo as well as Jonathan McKinley, Lucian Blaga and Babak Shalchi Amirkhiz at CanmetMATERIALS. Technical staff at Dalhousie, including Dean Grijm, Peter Jones, Angus MacPherson, Albert Murphy and Mark Macdonald, are commended for their technical guidance and assistance with my never-ending stream of machining demands.

Finally, those at GKN Sinter Metals that provided their technical guidance and facilities were essential in achieving the industrial-focus this project entailed. Thanks specifically to Ian Donaldson, Alan Taylor and Rich Hexemer.

CHAPTER 1. INTRODUCTION

1.1 Aluminum Powder Metallurgy

Aluminum powder metallurgy (APM) is a metal forming technology used to create metallic components through the consolidation of powder constituents into a single component. Specifically, the material consumed is primarily aluminum with controlled additions of a variety of secondary elements. Together, these constituents tailor the processing of materials as dictated by their physical and mechanical properties. All APM alloy systems are subject to several distinct processes to obtain usable engineered parts. Categorically, these are powder compaction, compact sintering and post-sinter processing; the essentials of each aspect of APM processing are described in detail in the following sections.

1.1.1 Powder Characteristics

The defining trait of APM components is the powdered metallic feedstock of which they are comprised. Primarily made of aluminum, these powders can be of an essentially limitless variety of morphologies, which is entirely reliant on the powder production technique used. Despite the breadth of techniques available to produce these powders, the dominant route is through atomizing a molten heat of aluminum. This technique, aptly named atomization, is a technique readily employed in powder production for any metal or alloy which can be melted. Melting of the metal phase allows for disintegration and subsequent solidification into a powder. Numerous atomizing techniques exist, but for the

scope of APM, gas atomization remains the most relevant. The key events of gas atomization are represented in Figure 1-1. A molten stream of the metal or metal alloy is fed to a nozzle, which is simultaneously and separately supplied a high-pressure gaseous feed. Upon exiting the nozzle, molten metal intimately contacts this pressurized gas; gaseous products are no longer volume constrained at this point, causing them to rapidly expand to equilibrate with atmospheric pressure. Disintegration of the feed stream occurs.

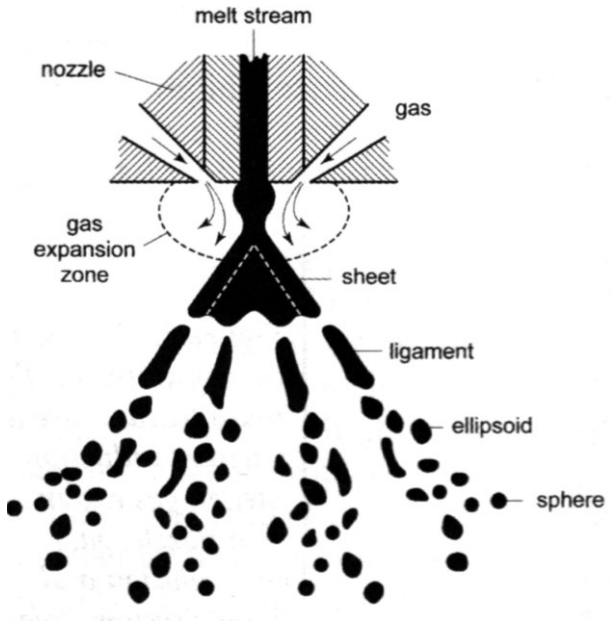

Figure 1-1 Schematic of gas atomizing a molten metal into progressivly spherodized metal powders. Figure adapted from German *[1]*.

Gas atomization techniques are flexible in the chemistry of the gaseous product. Air, nitrogen, argon and helium are all possible, and are used to deliberately tailor the characteristic of the powder. Similarly, the residual gas atmosphere is controlled to influence these properties. Using air for atomizing aluminum has proven to be dominant for industrially consumed powders. In addition to gas type, numerous other process

variables are available, including alloy type, melt temperature, melt feed rate, gas temperature and nozzle geometry.

Residual secondary phases, particle shape and size are all key characteristics controlled during atomization. Again referencing Figure 1-1, the morphology of a powder is dictated by the solidification behaviour early-on in the disintegration phase. Increasing melt superheat inherently increases system energy, delaying solidification and allowing for additional disintegration. Ultimately, the morphology of these metal droplets will approach that of a sphere. Premature solidification will give rise to an increasingly irregular morphology. This is the case for typical air atomized aluminum powders. Oxygen in the air atmosphere reacts with reactive aluminum on the surface of droplets, rapidly forming a strong and solid oxide shell. The final particle shape is a direct result of this early surface solidification event, producing powders that are irregular or ligamental. This morphology can be seen in Figure 1-2 for an air atomized aluminum powder. Many smaller ligamental particles are present amongst several larger, more irregular (more rounded) particles.

To this point, discussion has focused on a single powder or alloy being represented by one powder type. In fact, aluminum is used almost exclusively in an alloyed condition, requiring the deliberate additions of other elements. When introduced as a prealloyed addition, which is an elemental addition made to the melt prior to atomization, the mechanical properties of the powder are typically increased. These mechanical gains are initially undesirable, as they resist subsequent powder consolidation mechanisms. As an

alternative, alloy additions are made by solid state blending of appropriate amounts of alloy additions with the aluminum powder. These can be either elemental in nature (only a single element aside from tramp species) or comprised of multiple species, and can be produced by atomization, among other techniques. The blended addition of alloying elements in any form to an unalloyed aluminum powder allows the compressibility of a powder to be retained while retaining ideal chemical makeup.

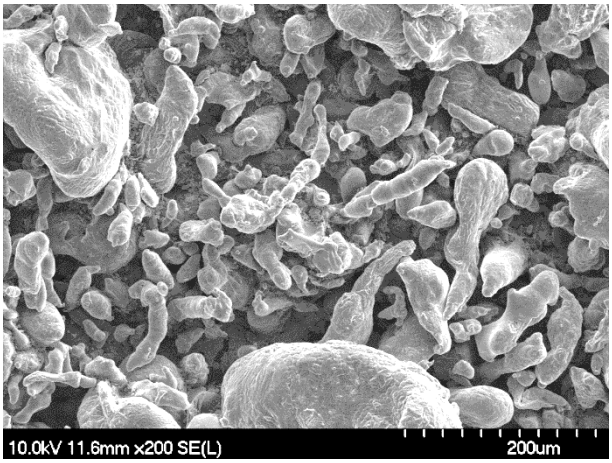

Figure 1-2 SEM micrograph of an air atomized aluminum powder, showing irregular and ligamental particles.

As mentioned, a primary motivating factor to segregate the alloy constituents is to ensure enough compaction response. However, many additional concerns arise with this blending technique. First, chemical homogeneity becomes a concern. Due to the limited thermal exposure during sintering (discussed later), these alloy additions must have an ability to rapidly homogenize with the bulk material. Elements like Cu and Mg have relatively high diffusivity in aluminum, allowing them to more easily approach equilibrium conditions. Elements like Zr or Cr are many orders of magnitude slower for a

given temperature [2] and are less likely to adequately diffuse through the matrix material within the limited time in the furnace. It is for this reason that additions like Cu and Mg can be added as blended additions, while sluggish additions like Zr need to be prealloyed in the base material [3]. A second concern relates to the refractive behaviour of the addition. Elemental additions to an aluminum blend will ultimately be processed at a temperature lower than the melting point of aluminum. Any metal addition more refractive than this will thus be entirely reliant on solid state diffusion of itself into aluminum at the alloy-aluminum boundary. These solid-state conditions are often slow, requiring faster, liquid phase mechanisms [4]. To achieve this, refractive materials can be alloyed to obtain a binary (or ternary, etc.) compound with a more suitable melting point. For example, unalloyed copper remains solid at temperatures exceeding 1000°C, while sintering operations in APM are inherently conducted below aluminum's melting point of 660°C. A copper *master alloy* powder with equal mass fractions aluminum and copper will begin to liquefy at temperatures as low as 548°C [5]. Accordingly, copper master alloy use is widespread in APM [6,7].

1.1.2 Compaction and Sintering Practices

Powder metallurgy is unique in metal-part fabrication operations in that no melting (fully molten) of the material feed is required. Rather, the powder is compacted as a solid into a geometry that resembles the final part. After compaction, the part is exposed to an elevated temperature process, sintering. Sintering instills many of the mechanical properties that would otherwise be inferior in the compacted, so-called green, state. After

sintering, the geometry of the part will remain largely unchanged from the green compact. This unique characteristic allows APM to be a near-net shape technology, whereby parts are processed with minimal secondary operations required to meet specifications following a part-forming operation.

Compaction uses mechanically applied external forces applied to a powder within a container. In APM, uniaxial pressing of a powder in a rigid die represents an area of large commercial interest. External forces cause a loose powder to progressively rearrange and plastically deform, while constrained by the die. A schematic of this behaviour for perfect circular powder particles is represented in Figure 1-3. Porosity, the void space between particles, is consumed at the expense of this compaction; the coordination number of particles increases along with increasing compaction pressure. With suitable compaction, intimate contact between particles can be achieved to stimulate later sintering mechanisms. Simultaneously, the mechanical interlocking and bonding of adjacent particles give the green compact strength – strength that is vital to the handling of parts without causing damage. Large friction forces between adjacent particles as well as particle-die wall interaction inhibit compaction. To counteract this, a sprayed-on die wall lubricant or an admixed lubricant powder are added to minimize friction forces.

Sintering is carried out as a discrete process after compaction. The green compact is fed into a furnace, either batch or continuously, and subject to a specific heating regimen. Gradual heating from room temperature to an intermediate temperature allows for lubricant burnout to occur. With the lubricant removed, compacts are heated to an

isothermal ‘sintering’ temperature and are held at this temperature until optimal properties are obtained. Afterwards, the parts are cooled, ready for post-sinter processing. This elevated temperature process activates diffusion, allowing adjacent particles to develop strong metallurgical bonds. Furthermore, density improvements over the green compact and homogenization of the microstructure are obtained during sintering. As was alluded to in the powder characteristic section, an alloy can be designed to be processed in the fully solid-state condition, or a partially-molten ‘liquid-phase’ condition. For brevity, the more commonplace and effective method of liquid phase sintering (LPS) will be discussed. The scope of this report will solely focus on LPS systems where a mixed powder is considered, rather than LPS for a fully prealloyed powder.

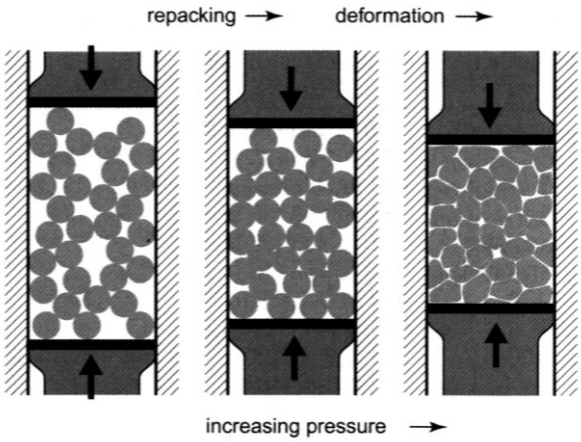

Figure 1-3 Schematic of circular particles rearranging and plastically deforming because of an externally applied force. Figure adapted from German *[1]*.

LPS is the heating and deliberate development of a controlled amount of liquid phase in an otherwise solid compact. This method maintains a large fraction of interconnected solid particles to maintain dimensional stability of the compact while a liquid phase

essentially brazes adjacent solid particles. With this liquid phase comes much greater diffusion rates, allowing for a general increase in sintering kinetics. The most important aspect of this liquid phase is that it maintains good wettability over the solid phase throughout sintering. This wettability is quantified by the wetting angle, equation (1) and is directly related to the surface energies in the system. The wetting angle, θ, is an equilibrium value determined by γ_{SV}, the solid-vapour surface energy; γ_{SL}, the solid-liquid surface energy; and γ_{LV}, the liquid-vapour surface energy. A schematic of this equilibrium is shown in Figure 1-4. A set of surface energies dictated largely by the composition of the materials used will determine whether wetting is favorable. This wetting favourability, termed spreading, can be derived from (1), and is shown in (2)[8]. A combination of surface energies with a positive spreading parameter *S* will result in complete wetting, and liquid spreading to fill pores. A negative spreading parameter will result in unfavorable partial wetting.

$$\gamma_{SV} = \gamma_{SL} + \gamma_{LV} cos\theta \quad (1)$$

$$S = \gamma_{SV} - (\gamma_{SL} + \gamma_{LV}) \quad (2)$$

In addition to wetting characteristics, the solubility of the incipient liquid and the solid base material play a key role in the sintering behaviour. For multicomponent systems made of elemental (or master alloy) powders, it is imperative to review the relevant binary phase diagrams. These mixed powder green compacts represent a non-equilibrium condition and will inherently approach equilibrium as their diffusion rates become thermally activated. Depending on the solubility of the liquid phase in the solid, and the

solid phase into the liquid, sintering dynamics can differ dramatically. There are four extremes of solubility to consider, as represented in Figure 1-5 and outlined by German et al. [8].

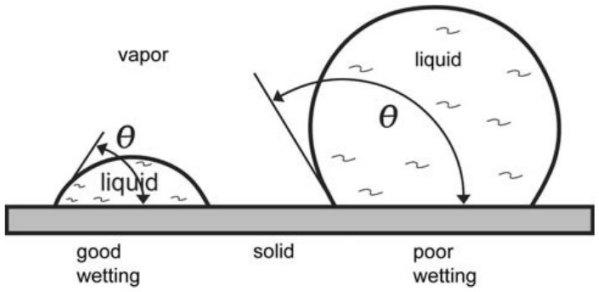

Figure 1-4 Interaction of a liquid phase in contact with solid and vapour phases, and the resultant wetting angle. Figure adapted from German et al. *[8]*.

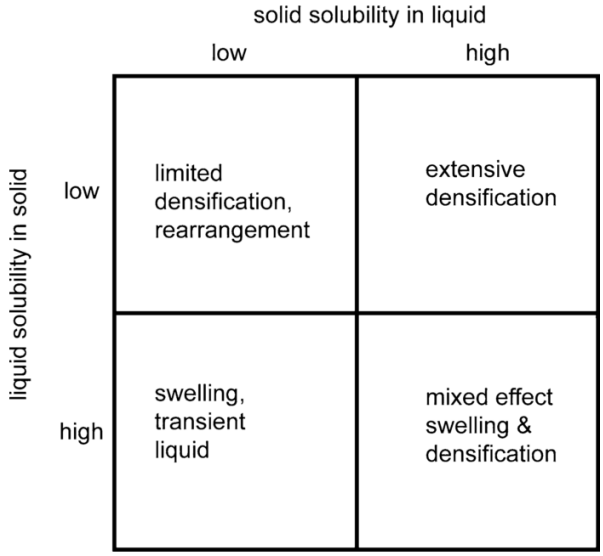

Figure 1-5 Solubility map of the behaviour of sintering response in early stages of LPS *[8]*.

First considered is the condition where neither the liquid nor solid have any extensive mutual solubility (quantitatively less than 10^{-3} at%). Dynamically, both the liquid and solid remain in a fixed composition throughout sintering. When compared to a conventional solid-state sintering mechanism, this form of LPS will benefit from lower interparticle friction, allowing for particle rearrangement mechanisms to occur. Simultaneously, the wetting nature of a liquid with a positive spreading parameter will cause the liquid to spread over the surface of all solid grains. Resultant capillary forces in the interparticle regions induce particle contact and coalescence, leading to additional density gains. Otherwise, the extent of sintering is limited.

The next considered condition is where the solid still has limited solubility in the liquid, but now the liquid has significant solubility in the solid. The incipient liquid components will begin to diffuse into the base material prior to any melt formation. Upon the first liquid formation, kinetics accelerates at the interface of the base material and the liquid. Depending on the number of liquid-forming components added to the system, either all or a significant portion of the liquid will diffuse into the solid. This phenomenon is known as a transient liquid phase, and results in suboptimal efficacy due to the limited duration of liquid phase sintering mechanisms. Often the loss of this liquid phase into the solid phase will leave behind porosity in the location of liquid phase components, and a macro-scale swelling of the part may occur. This condition is generally undesirable.

The third and fourth LPS conditions to consider are similar where both have a high solubility of the solid in the liquid phase. They differentiate in the amount of liquid which

dissolves into the solid phase. Again, high solubility of the liquid phase in the solid is problematic, often giving rise to mixed results. The ideal LPS condition in fact has minimal solubility of the liquid phase into the solid, or where the amount of liquid phase exceeds its solubility in the solid phase [8]. Here, a new sintering mechanism is activated, solution-reprecipitation. This mechanism augments the solid-state sintering and rearrangement mechanisms already described and is commonly the dominant densification mechanism. In solution-reprecipitation, the persistent liquid phase acts as a vehicle for rapid diffusion amongst solid grains. Mass is transported from one solid surface to another via the liquid. Solid dissolution occurs at areas of high energy, while reprecipitation simultaneously occurs onto lower energy areas. So-called high energy areas consist of convex points, small grains and areas under compressive strains, while lower energy areas consist of concave features and large grains in areas not under compression [8]. This redistribution of the solid phase is often accompanied by grain shape accommodation as it allows for more efficient packing of adjacent grains. A schematic of the extreme stages of solution reprecipitation are shown in Figure 1-6. Note the increase in particle size from the annihilation of finer particles and the more efficient packing of adjacent particles.

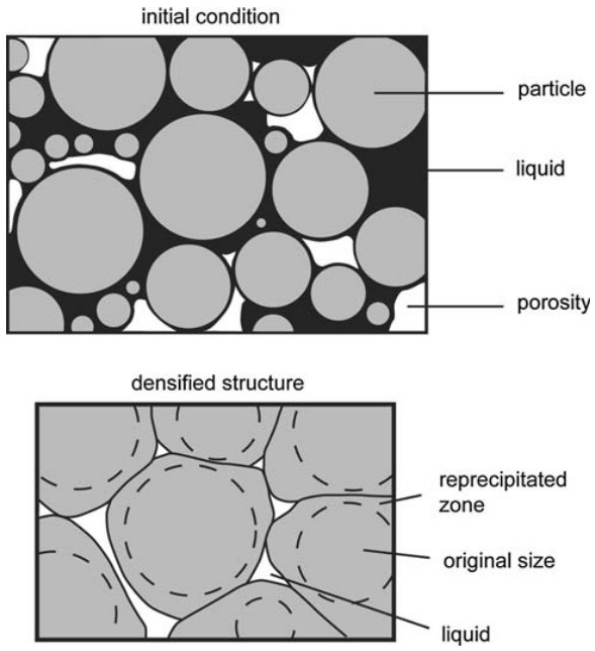

Figure 1-6 Schematic of solution reprecipitation. In the early stages of liquid phase development, particles resemble their original size and geometry. Following solution-reprecipitation, a densified structure is obtained [8].

Following solution-reprecipitation in an ideal LPS system, a solid skeletal network develops. The dominant liquid-phase kinetics are diminished, and slower solid-state sintering mechanisms now dictate ongoing sintering performance. The remaining liquid becomes largely ineffective for mass transport. As grains continually coarsen during prolonged thermal exposure, liquid filling of larger pores progresses, albeit at a slow rate. If no gas pressure exists within closed pores, elimination of porosity can be approached with extended sinter times. Conversely, residual gas within pores retards and ultimately limits pore filling, leaving persistent porosity in the finished part.

An important consideration in sintering operations is the atmosphere composition. Atmospheres can be oxidizing or reducing in nature, with gasses ranging from air, to inert gasses, to hydrogen or even a vacuum. Atmosphere selection relies largely on its chemical interaction with the compact, and whether it aids or disrupts sintering. Aluminum is difficult to sinter because particles all inherently possess a thin but resilient oxide layer that inhibits interparticle bonding. Without disrupting this oxide layer, mechanical properties will inevitably be poor. Unlike more favorable powder metallurgy systems (ferrous powder metallurgy), this Al_2O_3 oxide layer is practically impossible to reduce by modifying the atmosphere. At 600°C, an oxygen partial pressure, P_{O_2}, better than 10^{-50} atm or a dew point better than -140°C are required to reduce it [1]. Neither condition is achievable in modern furnace design. Furthermore, any atmospheric oxygen or moisture will lead to the formation of additional detrimental oxide phases. In a conventional sense, the atmosphere has little ability to aid sintering response, although dew point and oxygen content must be maintained at a minimum to diminish harmful side effects. However, a sintering atmosphere of nitrogen has routinely been shown to produce desirable aluminum sintered compacts [9,10]. Here, it has been suggested that nitrogen reacts with aluminum to form in-situ AlN. This is especially attractive, as trapped nitrogen within closed porosity can be consumed, allowing for the pressure within pores to decrease [11]. This reduced opposing force allows for pore filling and densification to progress further than possible under other atmospheres.

Another important consideration in APM is the addition of elemental magnesium to promote interparticle bonding. It has been shown that the addition of magnesium to a

commercially pure aluminum powder dramatically enhances mechanical and physical properties by way of disrupting surface oxides on the aluminum [12]. The resilient Al_2O_3 layer covering aluminum particles naturally limits the interdiffusivity; reactive elemental magnesium reduces this uniform oxide shell, according to equation (3) or (4) to produce fine spinel ($MgAl_2O_4$) or MgO crystallites [4]. Diffusion between adjacent particles is now possible, while these oxide crystallites remain as dispersoid strengtheners. This break-up of the oxide layer simultaneously promotes wetting of the metallic substrate, promoting sintering and ultimately improving properties.

$$3Mg + 4Al_2O_3 \leftrightarrow 3MgAl_2O_4 + 2Al \quad (3)$$

$$3Mg + Al_2O_3 \leftrightarrow 3MgO + 2Al \quad (4)$$

1.1.3 Post-Sinter Processing

Following sintering, PM components possess many qualities of the end-use part, namely their geometry and the bulk of their physical and mechanical properties. However, machining operations are often inevitable to accommodate as certain geometries are impossible to introduce through compaction. Heat treating is commonplace in conventional aluminum metallurgy as a final processing operation. Solutionizing followed by precipitation hardening at elevated temperatures establishes a fine network of strengthening precipitates throughout the microstructure.

Sizing is a common technique used in APM used following sinter operations to adjust or restore final dimensions. Particularly in LPS, dimensional instability or ‘slumping’ is

common. This variable deviation from a desired geometry can be corrected by repressing, or 'sizing' the part in a closed die. This is generally a low strain uniaxial pressing operation carried out in a die containing dimensions of the end-use part. Additional benefits of this process include greater dimensional uniformity, strain hardening, improved surface finish and even closing of surface porosity. Forging is an additional post-processing technique used in PM and will be investigated further in the following section.

1.2 Hot Forming Operation: Forging

Forging is a metal forming operation in which a billet is subject to an outside force, normally uniaxially, to deform the material into a new geometry. Billets start as simple geometries that are progressively formed into a geometry approaching that of a final part. Forging can be carried out in cold ($T<0.3T_M$), warm ($T<0.5T_M$) or hot ($T>0.5T_M$) regimes. For the sake of this report, hot forging will be exclusively considered. During high temperature forming operations, the microstructure of a material is forced to change as the part undergoes macroscopic geometry changes. Due to the wide variety of microstructures, materials and process parameters, forging response can vary dramatically. The scope of this report will include broad forging processes, aluminum forging and constituent analysis of forgeability.

1.2.1 Forging Techniques and Considerations

Forging itself is a broad category of material processing techniques in which a material can be manipulated. Some more common forging processes include:

- Impression die forging
- Extrusion
- Upsetting
- Radial forging (swaging)
- Open die forging
- Isothermal Forging
- Powder forging

Each forging technique involves stressing a material to undergo plastic deformation. Simultaneously, each process invokes geometric constraints to manipulate the part shape. For example, in extrusion a simple cylindrical billet is forced against a blanking plug with a small opening in it. With the application of pressure, the metal yields and plastically flows through the small opening, causing a continuous extrusion to form. On the contrary, open die forging involves a uniaxial stress applied to a section of a heated billet. Without lateral constraints, the material can flow laterally to accommodate stresses. These two techniques produce drastically different products, but the microstructural evolution concepts discussed in this report remain relevant.

In forming aluminum components for automotive applications, techniques of particular interest include upset forging, impression die forging, open die forging and isothermal forging. For powder metallurgy parts, powder forging is especially interesting, but will be considered in section 1.6, Powder Forging. In impression die forging, the dies, usually in two halves, contain cavities which have a geometry consistent with the final geometry the part is to obtain, as schematically shown in Figure 1-7. Under uniaxial compressive stresses, a heated billet (shown in black) is compressed and forced to flow to the void areas within the die. The billet therefore is forced to obtain the inverse geometry of the dies. This can be accomplished with either a flashless design (no lateral material flow outside the die, Figure 1-7 hashed areas) or a flash design (excess metal is able to flow from the die, Figure 1-7 non-hashed areas). This is an especially useful technique for repeatedly producing parts with relatively net shape products from a variety of materials, including aluminum.

Open die forging is like impression die forging in that it uses compressive uniaxial forces to deform a material. However, in open die forging, material is pressed between simple geometry dies that do not locally constrain material. This type of forging is normally industrially reserved for large simple geometry parts. However, it is notable for the similarity to lab-scale compression tests.

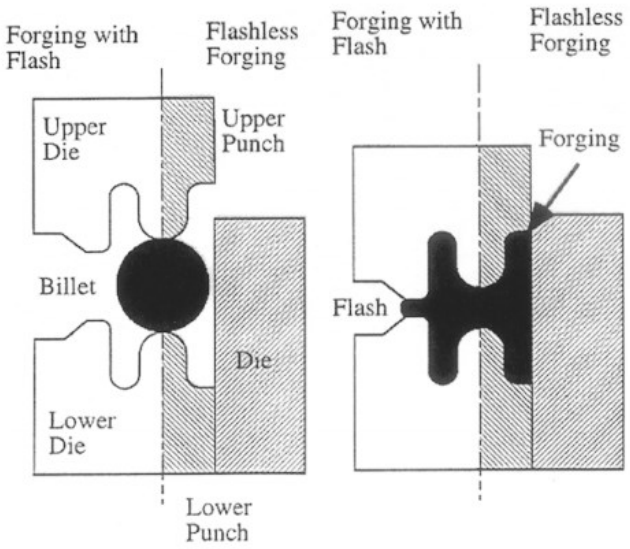

Figure 1-7 Impression die forging with either flash (white) or flashless (shaded area) design.

Hot forging aluminum inevitably requires billets to be preheated. Heating the material provides several benefits over forming operations at room temperature. First, the hot strength of the material is reduced, allowing for small forming equipment. Additionally, the amount of strain the material can tolerate before fracturing generally elevates substantially. Furthermore, the thermal energy from this hot working activates microstructural restorations mechanisms. These include recovery, recrystallization and precipitation, to name a few. Further discussion on the microstructural evolution mechanisms is covered in section 1.4, Recovery and Recrystallization Effects. Due to varying chemical makeup, different aluminum alloys require unique forging temperature regimes. High temperatures coupled with adiabatic heating effects may induce liquid phase formation, whereas certain other unique temperature regimes for an alloy may produce a condition of unstable plastic flow mechanism. Ideally, forging would be

carried out at the lowest appropriate temperature to minimize heating energy (and cost) input. Some general forging temperatures of select common forging alloys is presented in Table 1-1. Note that the forging temperature of 1100 aluminum, an inherently unalloyed and soft alloy, requires relatively low temperatures. Opposing that, some 2000 series alloys possess significant hot strength, requiring more elevated temperatures to ensure suitable forgeability.

Table 1-1 Forging temperature ranges for select aluminum forging alloys *[13]* .

Aluminum Alloy	**Forging Temperature Range (°C)**
1100	315-405
2014	420-460
2025	420-450
2219	425-470
2618	410-455
6061	430-480
7075	380-440

While aluminum billets may be preheated to temperatures ranging from 315-480˚C, the dies generally may be operated at temperatures significantly lower. The lower the operating temperature, the general resistance towards die-degradation increases. Accordingly, heat transfer between the billet and die is a concern in forging. First, for the temperature loss of the part and according increase in strength. Second, for the heating of

the die and associated damage it may endure. Heat transfer can be represented in this case by convective heat transfer [14].

$$Q = hA\Delta T \tag{5}$$

Where Q is the heat flux; h is a heat transfer coefficient; A is the surface area or cross-sectional area at the contact point between die and billet; ΔT is the temperature difference between the billet and die. The heat transfer between the billet and the atmosphere is relatively small in this scenario and will be neglected. Prior to pressing, h for the heat transfer between billet and die is relatively low. Essentially, there is high thermal contact-resistivity between the two adjacent surfaces. Upon pressing of the billet, the h term rapidly increases (experimentally shown to be on the order of 20 kW/m^{2}K for 316 stainless steel [14]). Heat transfer during pressing becomes significant. Cooling of the billet (and heating of the dies) will occur. Accordingly, the billet strength will develop along with temperature loss. A unique counterpoint to this cooling is the phenomenon of adiabatic heating during forging. It's estimated that only approximately 5% of the energy input into forging is stored in the microstructure [14]. The remaining energy is converted to heat, which manifests as a temperature increase in the billet. This adiabatic heating must be considered during forging experiments as it has a natural softening effect on the material that may bias the actual material flow stress depending on the strain rate.

To circumvent the cooling of a billet, it's common practice to preheat the dies. This decreases the ΔT term in (5), reducing heat transfer and billet temperature loss. Akin to

the billet preheat temperatures previously discussed, every type of aluminum forging requires the die material to be heated. Preheating reduces the heat flux, minimizing heat loss to the die and subsequent loss in forgeability. The temperature of the preheated die varies considerably with the type of forming operation. Machinery with faster strain rates and inherently shorter contact times allow lower temperatures. Conversely, low strain rate machinery, as in hydraulic presses, maintain contract with the billet for extended periods of time. In these instances, more elevated die temperatures are necessary [13]. Example die temperatures for select forging equipment are listed in Table 1-2.

Table 1-2 Die temperature ranges for select forging equipment, listed in order of decreasing nominal strain rates *[13]*.

Forging Equipment	**Die Temperature Range (°C)**
Hammers	95-150
Mechanical press	150-260
Screw Press	150-260
Hydraulic Press	315-430

Isothermal forging is an iteration on conventional forging procedures. It is unique in that both the billet and dies are maintained at the same processing temperature. No significant heat transfer between the billet and die occurs. Due to the requirements of the die, this technique is often reserved for higher cost or lower temperature applications where a near-net shape product can be obtained. For aluminum or titanium alloys, it's commonly applied in an impression die forging, or closed die forging application.

1.3 Forgeability and Constituent Equation Representation

The determination of forgeability of a material is determined by simple laboratory tests. Hot tensile tests can be used for processes involving low plastic strains. However, plastic instability during testing (necking) prevents ductility values representative of hot forging form being obtained. Materials inherently extend their strain limits in forging conditions. Therefore, tensile testing is of limited usefulness in metal forming determination experiments. Compression tests and torsion tests alleviate this issue with plastic instability, allowing much higher strains to be obtained. This is especially true for torsion tests, where very large true strains are achievable. However, for the scope of testing herein, only compression tests will be considered.

In compression tests, cylindrical samples are compressed between flat platens at various temperatures, T; at a constant strain, ε; and at a variety of strain rates, $\dot{\varepsilon}$. To eliminate the effects of heat flow into the die, the platens are maintained at a temperature enough to ensure approximate isothermal conditions. Because of the applied stress, the cylindrical sample yields and flows laterally. Ideally, this occurs without any barreling to get values that can be represented by simple relationships. These relationships are as follows [14]:

$$\bar{\sigma} = f(T, \bar{\varepsilon}, \dot{\varepsilon}, S) \tag{6}$$

$$\bar{\varepsilon} = \ln \frac{A}{A_0} \tag{7}$$

$$\bar{\sigma} = \frac{L}{A} \tag{8}$$

$$\dot{\varepsilon} = \frac{d\bar{\varepsilon}}{dt} = \frac{V}{t} \tag{9}$$

Where $\bar{\varepsilon}$ is the true strain; S represents a given microstructure; A is the instantaneous cross-sectional area; A_0 is the initial cross-sectional area; $\bar{\sigma}$ is the true stress; L is the instantaneous load; $\dot{\varepsilon}$ is the strain rate; V is the instantaneous ram velocity and *t* is time. In conventional compression testing (room temperature), only stress and strain are critical parameters. Limited dynamic restoration occurs during testing at these low temperatures However, warm and hot testing activates these dynamic restoration mechanisms. As a result, the rate at which strain is applied plays a key role in the stress-strain behaviour. Despite these quantifiable measures, the hot forming behaviour is further influenced by qualities less easily represented numerically. For example, alloy composition, prior strain history, microstructure and heat treatment all have significant influence. These are qualitatively represented as S but are assigned no numeric value.

Several constituent equations have been proposed for representing the flow stress of materials as a function of the above discussed parameters. The simplest forms are represented in equations (10) and (11). In these 'power-law' equations, a material must be tested for a given strain, temperature and microstructure to be quantified. For each unique condition, a set of constants, K (or C) and *n* (or *m*) are produced. Because of this,

relatively large amounts of cumbersome data are formed [14]. Furthermore, there is discontinuity in the two, as the flow stress dependence transitions from strain at low temperatures to strain rate at elevated temperatures.

$$\bar{\sigma} = K(\bar{\varepsilon})^n \tag{10}$$

$$\bar{\sigma} = C(\dot{\varepsilon})^m \tag{11}$$

A more appropriate representation of flow stress was proposed by Zener and Hollomon [15]. An iteration of this relationship used to correlate flow stress, temperature and strain rate is still used in modern plastic deformations studies and is represented in (12) and (13). Continuity between high and low temperatures can be established.

$$Z = \dot{\varepsilon}\, exp\frac{Q_{HW}}{RT} = \beta(\sinh(\alpha\sigma_s))^n \tag{12}$$

Rearranged to:

$$\bar{\sigma}_s = \left(\frac{1}{\alpha}\right) \ln\left\{\left(\frac{Z}{\beta}\right)^{1/n}\left[\left(\frac{Z}{\beta}\right)^{2/n} + 1\right]^{1/2}\right\} \tag{13}$$

Where Z is the Zener-Hollomon parameter; Q_{HW} is the activation energy associated with hot working a given material; R is the gas constant; T is temperature; β and α are material constants; σ_s is the steady-state flow stress. Z can be thought of as a

temperature-compensating strain rate, where high values represent more strenuous deformation (approaching cold work conditions) while low Z are less strenuous (creep conditions). The versatility of this relationship has been shown accurate at Z values ranging by a factor of 10^{12}, extensively covering all wrought aluminum alloys [16,17]. Other constituent models have been presented to better correlate with creep and cold working [18], but the Zener-Hollomon approach remains relevant, being studied widely in conventional and PM aluminum applications[19,20].

Another form in which hot working is frequently quantified is in processing maps [21,22]. These 2D or 3D maps are especially useful in commercial alloying systems, where they're used to solve problems associated with workability and microstructure as a result of hot work [23,24]. Here, the efficiency of power dissipation, the strain rate sensitivity and instability are quantified and simultaneously graphically represented. These parameters are defined and calculated as described below [25]:

$$\log \sigma = \mathrm{a} + \mathrm{b} \log \dot{\varepsilon} + \mathrm{c}(\log \dot{\varepsilon})^2 + \mathrm{d}(\log \dot{\varepsilon})^3 \tag{14}$$

$$m = \left[\frac{\partial(\ln \sigma)}{\partial(\ln \dot{\varepsilon})}\right]_{\varepsilon,T} \cong b + 2c\,(\log \dot{\varepsilon}) + 3d\,(\log \dot{\varepsilon})^2 \tag{15}$$

$$n = \frac{2m}{m+1} \tag{16}$$

$$\zeta(\dot{\varepsilon}) = \left(\frac{1}{2}\right)\frac{\partial \log n}{\partial \log \dot{\varepsilon}} \cong \frac{2c + 6d \log \dot{\varepsilon}}{m(m+1)\ln 10} + m \tag{17}$$

Where (14) is a third order polynomial regression of the log plot of peak flow stress versus strain rate. The parameters of this polynomial fit are used in approximate equations shown in (15), (16) and (17); *m* represents the strain rate sensitivity; *n* represents the efficiency of power dissipation and ζ represents the instability parameter; values of $\zeta \leq 0$ indicate a condition of flow instability. A 2D contour plot of the power dissipation efficiency as a function of temperature and strain rate can be seen in Figure 1-8; P/M extruded Al2124 shows high power dissipation efficiency at high temperatures and low strain rates, while the opposing conditions may lead to unstable conditions. The shaded region in the upper left corner represents flow instability, where unstable microstructural events (dynamic strain ageing, flow localization or otherwise [26]) occur to the detriment of the materials. Additionally, one can determine 'domains' on this plot where a given microstructural condition is dominant. For example, in Figure 1-8, the author indicated that dynamic recrystallization occurred at temperatures above 400°C while dynamic recovery occurred below 400°C and between true strain rates of 0.01 and 0.2 s^{-1}. Microstructural events are determined by subsequent microscopy or similar techniques.

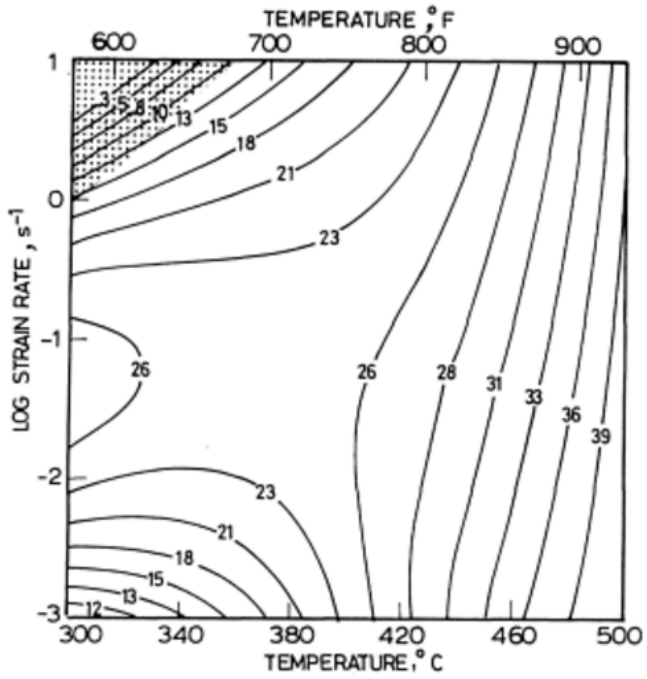

Figure 1-8 Processing map for 2124 P/M extruded alloy at a strain of 0.5 shaded region represents flow instability *[26]*.

1.4 Recovery and Recrystallization Effects

During plastic deformation of any metal, energy from metal forming operations is transferred into a material. This energy input is converted into strain energy by way of microstructure manipulation. This energy is responsible for the mechanical property changes observed from deformation, such as strain hardening in a cold-worked material. In general, this energy can be accounted for in the accumulation of dislocations. However, only a portion of the energy input into a material system is converted in this manner, the remaining energy input is converted into heat, contributing to an increase in workpiece temperature. It has been estimated that the amount of energy lost to heat is

95% [14]. In quantifying the amount of energy associated with dislocations, we must consider their density, distribution and arrangement [16]. These are discussed below.

Dislocation density is the length of dislocations per unit volume of material. Dislocation density increases when newly generated dislocations are incorporated into various microstructural features. Three examples relevant to aluminum and aluminum-MMC (metal matrix composite) systems are discussed.

First, a material that is plastically strained in a plain strain condition will see grains flattening, according to macroscopic changes in sample geometry. This grain shape change requires an overall increase in grain boundary area. Induced-dislocations constitute to the formation of these enlarged boundaries [16].

Second, dislocations contribute to microstructural evolution through the generation of a subgrain structure. This is accomplished through recovery mechanisms and will be discussed in detail in the following section. Here, it's enough to summarize this subgrain generation as the formation of many low angle boundaries through continuous dislocation generation and self-restoration mechanisms. These subgrain boundaries are a direct result of newly generated dislocations.

Third, a more rapid generation of dislocations associated with secondary phase particles within a microstructure can be a considerable source. Secondary phases by way of precipitates or dispersoids can prohibit the movement of dislocations, causing pileups.

Furthermore, relatively strong particles can induce local dislocations from strain or temperature affects [21].

Ultimately, the dislocation density can be related to several key parameters, shown in equation (18). Dislocation density, ρ, can is directly related to the strain a material undergoes, ε, burgers vector, b, and the average distance the dislocation moves, L. Where L is a source of uncertainty [16].

$$\varepsilon = \rho b L \tag{18}$$

To this point, the discussion has been associated with the generation of dislocations associated with the plastic deformation of materials. However, the aim of this report is centralized on forging, and the benefits of processing materials at elevated temperatures. Here, we introduce the mechanisms of static and dynamic restoration of a strained microstructure when subject to a combination of elevated temperatures and plastic deformation. When heated, metallic materials generally exhibit softening, typically acceleration by exposure to higher temperatures. Although a certain amount of the materials inherent strength relies on the processing temperature, the mechanical properties also are reliant on the temper of the material. That is, upon heating and subsequent cooling of a material, a microstructural change occurs such that the material will now behave differently. These microstructural changes are key to hot forming operations. They allow engineers to tailor a process to induce a favorable microstructure to more easily form a material, while simultaneously producing a final microstructure

that promotes desirable final mechanical properties. The mechanisms of interest in these microstructural changes are recovery and recrystallization.

Recovery and recrystallization are competing mechanisms that are driven by the amount of stored energy in a material as a primary result of plastic deformation. The term annealing is often used as a coverall for the resultant property changes that manifest because of recovery and recrystallization. Since the driving force for both these mechanisms is the same, they cannot both simultaneously occur to their mutual full extent. Conceptually, these are two distinct processes activated by similar methods. However, in practice the transient behaviour of many processes may result in the overlap of both recovery and recrystallization in a single thermomechanical treatment. Furthermore, it will be shown that recrystallization itself relies heavily on the mechanisms of recovery.

1.4.1 Recovery

Recovery is the process in which a plastically deformed material undergoes a microstructural change to progress towards its pre-strained, low-energy state. These microstructural changes are focused on the dislocation structure obtained through strain and how they are manipulated with further thermal or thermomechanical processing.

In the earliest stages of plastic deformation, arrays of dislocations are formed according to the prevailing slip systems and dislocation motion of a specific material. As strain is increased, dislocation interactions progress. When the rate of dislocation multiplication is

balanced by their accommodation through dynamic recovery, saturation occurs and leads to tangling od dislocations (Figure 1-9a). Recovery is the mechanism, or rather sum of many micro mechanisms, that progressively accommodate these dislocations, gradually annihilating them or rearranging them in a manner that progresses towards a lower energy state. These micro mechanisms are shown schematically in Figure 1-9b-d. Microscopically, EBSD and TEM methods are well suited to determine the occurrence of recovery. Furthermore, the temperature ranges in which these micro mechanisms may occur varies widely; strain levels, annealing temperature, the nature of the material and amount of solute content all play a key role in these temperatures.

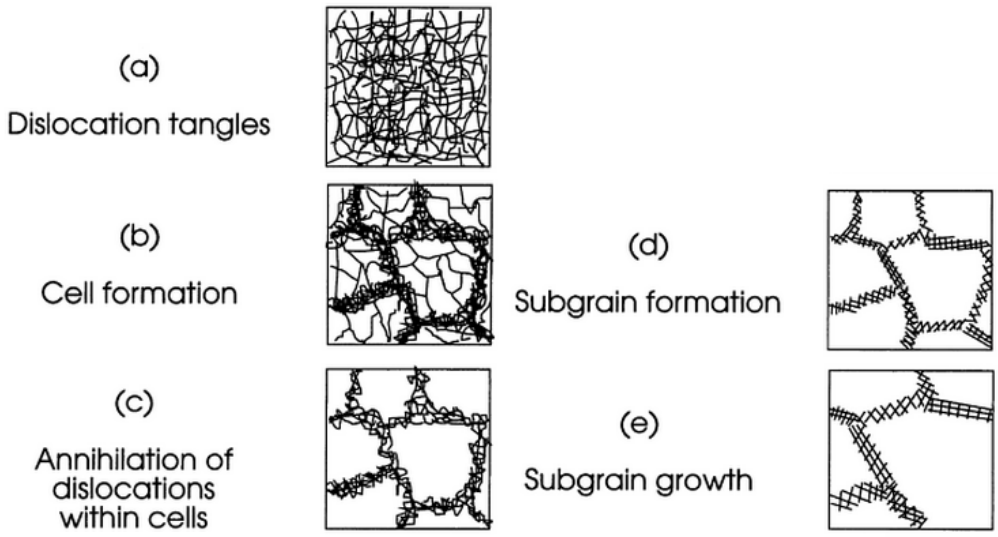

Figure 1-9 Schematic of the evolution of recovery micro mechanisms *[16]*.

The first key mechanism in recovery is the annihilation of dislocations. The simplest representation of this can be seen schematically in Figure 1-10 where arrays of dislocations with opposite Burgers vectors are represented. Upon interaction, two

dislocations with different Burgers vectors will annihilate. Dislocation glide is of little concern in recovery, as this mechanism is activated at low temperatures, essentially happening during the processing of material. The interaction of dislocations A and B in Figure 1-10 represent this. However, for dislocations in different glide planes to interact, C and D, dislocation climb must occur. Dislocation climb, along with cross slip (not schematically shown in Figure 1-10) require thermal activation to occur. The nature of the material plays a large role in the dislocation motion, especially when considering the parameter, λ_{SFE}, stacking fault energy. This parameter is tied with certain material systems, dictated by crystal structure and slip systems, among other properties. Essentially, it is an energy value associated with the interruption to a normal stacking sequence of a crystal structure. Higher λ_{SFE} are associated with a resistance to single dislocations dissociating into two partial dislocation. In these systems, dislocation motion readily occurs through cross-slip, induced at low stress values. On the other hand, materials with low λ_{SFE} cannot deform through cross slip. Aluminum inherently possesses a relatively high λ_{SFE} , as shown in Table 1-3 [16].

Table 1-3 Stacking fault energy values for assorted materials [16].

Metal	λ_{SFE} (mJ m^{-2})
Aluminum	166
Copper	78
Silver	22
Cobalt	15
70:30 Brass	20
304 Stainless Steel	21
Zirconium	240

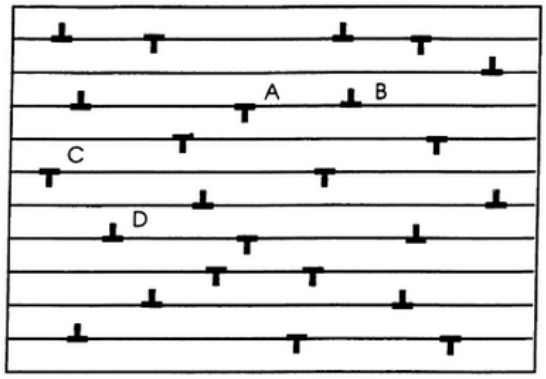

Figure 1-10 Dipole elimination mechanism in a crystal *[16]*

The second key mechanism of recovery is the rearrangement of dislocations into stable arrays. Following the annihilation of all dislocation dipoles, an excess of dislocation of a common Burgers vector may persist, shown schematically in Figure 1-11b. These like-dislocations then arrange into favorable low energy configurations, translating many planes. The result is a polygonised structure made of many low angle boundaries of the order of 1-2 degrees. Further rearrangement occurs when adjacent low angle boundaries

combine to form a boundary of greater misorientation, but fewer overall dislocations. Again, this structure reduces overall system energy.

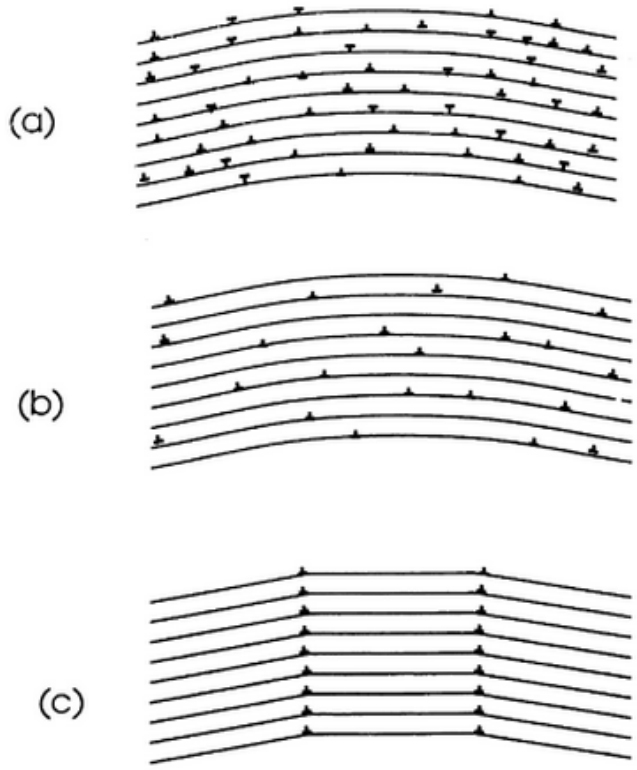

Figure 1-11 Schematic of the progression of annihilation and subsequent rearrangement of dislocations into a low energy configuration [16].

It has been noted that for aluminum, dislocation motion is much more favorable than in many other systems and evidence of recovery is common. One such phenomenon is the development of a microstructure finer than that of the grain size. Complex dislocation tangles form an observable microstructural phenomenal labelled cell formation (Figure 1-9b). Within these cells are more dislocation tangles that are subsequently annihilated (Figure 1-9c). The progression from Figure 1-9a-c should be considered to occur

continuously. With the development of a cell structure, the tangled cell walls further change to adopt a lower energy state, forming a more regular dislocation structure. This is a key step of recovery, as the transient cells develop into more stable subgrains, as shown in Figure 1-11d. It's important to differentiate these subgrains from conventional grains, as they are inherently divided by low angle boundaries whereas conventional grain boundaries are of much higher misorientation. As expected, this subgrain network can undergo growth mechanisms analogous to conventional grain grown, albeit by different mechanisms. Subgrain boundary migration and coalescence of adjacent grains by rotation have been proposed mechanisms here.

To this point, recovery has been discussed as a process that occurs predominantly during elevated temperature exposure as a unique step following deformation. However, this only explains static recovery (SRV). Recovery also occurs during the high temperature deformation of metals, especially those with thermally activated climb and glide dislocation mechanisms, such as Al with its high λ_{SFE}. This recovery during plastic deformation is aptly termed dynamic recovery (DRV). The micro mechanisms described above remain relevant, albeit now with the added complication of an ongoing source of dislocation generation.

As a material is plastically deformed, it undergoes work hardening from the generation and interaction of dislocations. Ongoing strain increases the dislocation density and gives rise to recovery. The rate of recovery increases until it matches that of the work hardening rate; an equilibrium state of dislocation generation and recovery occurs. Higher

strain rates promote higher dislocation generation rates, accelerating recovery. Mechanically, properties diverge from room temperature behaviour. This can be seen in the true stress- true strain behaviour shown in Figure 1-12. Work hardening occurs up to a critical strain, ε_m; the stress reaches a steady state flow stress, where the rate of recovery has matched the work hardening rate. For a given strain rate, this steady-state will endure until damage mechanisms and ultimately fracture occur.

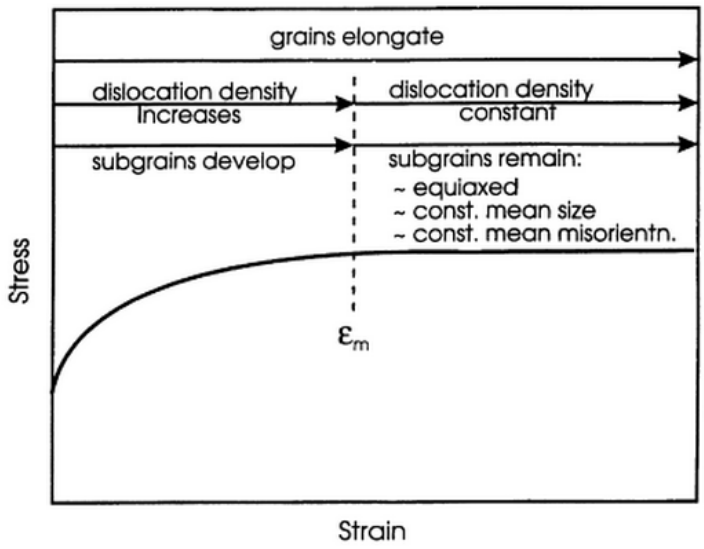

Figure 1-12 True stress-strain curve for the hot deformation of a material undergoing recovery [16].

In SRV, the formation of subgrains and their growth was characteristic. However, in the case of DRV, now the subgrain structure behaves differently. Subgrains are formed and grow as work hardening occurs. However, accelerated and ongoing dislocation generation promotes continuous subgrain formation. When the rate of work hardening and recovery reach equilibrium at ε_m, subgrain growth ceases. Subgrain migration, disintegration and reformation occur to ensure their size and equiaxed nature remain,

despite the progressive shape change conventional grains observe during forging [18]. Higher strain rates introduce higher dislocation densities and give less time for recovery. Macroscopically, these higher strain rates exhibit greater flow stresses.

Although a steady-state flow stress is to be expected in materials solely undergoing recovery, it is often observed that a marginal decrease in stress occurs with greater strain. In this case, if we ignore precipitation behaviour of the material, this phenomenon can be attributed to adiabatic heating. Heating of the material further softens the material, reducing the flow stress required to strain at a given rate. This is especially true at higher strain rates, where the thermal behaviour of the specimen and forging dies is insufficient to remove heat at the rate it self-generates [14].

1.4.2 Recrystallization

Like recovery, recrystallization is a mechanism that occurs to reduce overall system energy, driven by the elimination of dislocations formed during plastic deformation. Unlike recovery, recrystallization can be represented in distinct phases: nucleation and growth. Nucleation is the generation of new strain-free grains that subsequently grow at the expense of strained grains (grains containing a relatively high dislocation density) [16]. While in recovery, the subgrains that generate are separated by low angle boundaries, recrystallization produces conventional grains, separated by high angle grain boundaries.

Nucleation remains the controlling step in the occurrence of recrystallization in a given system. For this report, we simply focus on whether recovery or recrystallization is dominant, and therefor the mechanics of growth will not be discussed further. The inherent material properties play a key role in whether these nuclei form. The occurrence of recrystallization can be conceptually viewed as a critical set of conditions that transition the restoration mechanisms away from recovery. That is, upon straining, a material reaches a dislocation density sufficiently high that it is unable to alleviate through recovery, thus promoting recrystallization. In some materials (i.e. commercially pure aluminum and most aluminum alloys), recovery mechanisms are sufficiently effective that they practically prohibit recrystallization (nucleation) from occurring.

Nuclei are defined as small pre-existing volumes in the deformed microstructure [16]. These are understood to occur in boundary regions with high misorientation. Several different mechanism for nucleation have been shown [16]. Included in this is that nucleation occurred exclusively at grain boundaries. However, it is crucial to understand that, with reasonable certainty, it has been shown that nucleation in fact originates from dislocation cells or subgrains that are formed during deformation. It is here that the recovery behaviour of a material dictates the possibility of recrystallization occurring.

As discussed previously, recovered subgrains are inherently separated by low angle boundaries. In a system with a large number of these low angle boundaries, it's energetically favorable for them to converge and produce a fewer number of relatively higher angle boundaries [16]. This mechanism transforms the microstructure into a

unique form that aid recrystallization. Schematically, this is represented in Figure 1-13. In this schematic example, there are 12 adjacent subgrains within a single grain, 11 low angle boundaries separate them. The angle difference of these subgrains relative to an arbitrary grain can is represented as an integer. The difference in number between adjacent grains represents the local misorientation. Initially, subgrains will always be misoriented by a value of 1-2, indicating low angle grain boundaries. However, two distinct outcomes may arise depending on how the long range orientation relative to an arbitrary grain occurs. First, this orientation difference is small with respect to the arbitrary grain, and there is no long-range orientation gradient of these subgrains (Figure 1-13a). As recovery and subgrain growth occur, subgrains will coarsen at the expense of adjacent grains. In this example, the misorientation averages out, again producing low angle boundaries (Figure 1-13b). In the second condition, the orientation gradient is small with respect to neighboring grains, but independent of the arbitrary reference grain. Here, a long-range orientation gradient, Ω, persists, as evidently shown in Figure 1-14. Low angle boundaries exist between neighboring subgrains in the deformed state (Figure 1-13c), but the orientation difference between subgrains becomes progressively greater as their separation distance increases. When this subgrain structure recovers, coarser subgrains separated by high angle boundaries will result. Additionally, recovery at these areas of high misorientation will be the most rapid. These subgrains will grow faster and become progressively more misoriented from their neighboring grains. In a system where these behaviours persist, it has been determined that the nucleation step of recrystallization is in fact this subgrain growth at sites of high strain energy and high orientation gradient.

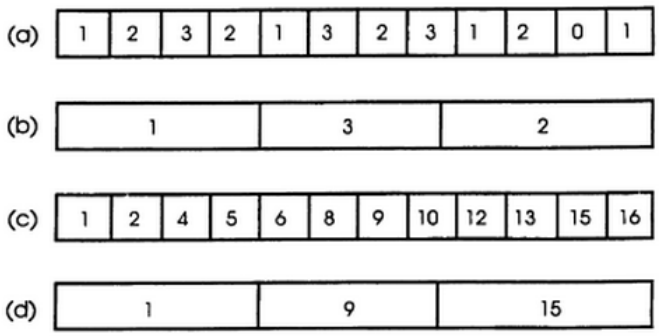

Figure 1-13 Schematic representation of the recovery of a material with no orientation gradient (a) and (b), or with an orientation gradient (c) and (d) [16].

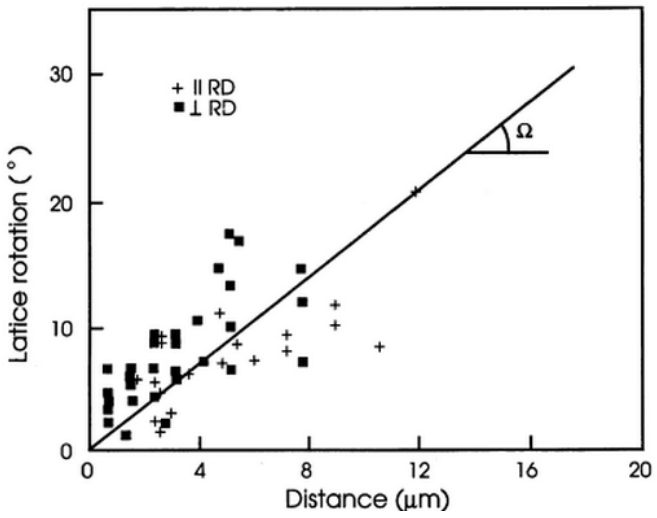

Figure 1-14 Lattice rotation of subgrains as a function of distance relative to an arbitrary grain resulting from deformation [16].

Like recovery, recrystallization behaviour is dictated by the composition of a material. In commercially relevant aluminum alloys, submicron precipitates are introduced into the microstructure. These precipitates are used to introduce higher mechanical properties. Similarly, metal matrix composites can be formed by introducing a ceramic phase into a

metallic matrix to manipulate physical and mechanical properties. Furthermore, aluminum powder metallurgy products inherently contain a 3D skeletal network of aluminum oxide dispersoid because of the active nature of aluminum on particle surfaces. The microstructure of a deformed material thus deviated considerably from what has been considered thus far. The interaction of the matrix with precipitates, dispersoid particles and ceramic and the effects on recrystallization must be considered.

Recrystallization kinetics are heavily influenced by the nature of particles. Particle size is important, but more critically important is interparticle spacing. Interestingly, these parameters can be modified to either accelerate or retard recrystallization. In comparison to a single-phase system, particles provide a nucleation site for recrystallization. Stress gradients around particles stimulate subgrain misorientation, promoting nucleation. Coarser particles are more favorable, accelerating recrystallization further. Fine particles (approaching zero) provide a response that approaches that of a single-phase system. This behaviour is shown in Figure 1-15. Interparticle spacing of second phase shows the contradicting effects is represented in Figure 1-16. Particles with sufficiently close particle spacing show considerable retardation of recrystallization, by several orders of magnitude over a single-phase system. Closely spaced particles pin dislocations, inhibiting slip. As a result, recrystallization is retarded.

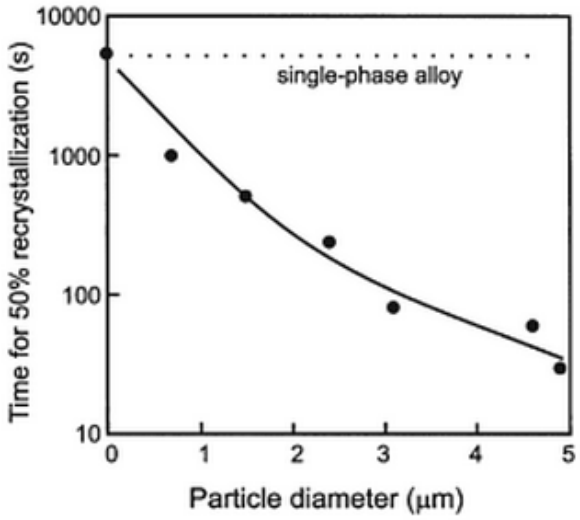

Figure 1-15 Time for 50% recrystallization of an Al-Si alloy relative to a single-phase Al system as a function of secondary phase particle size [16].

For two-phase systems where interparticle spacing is sufficiently large, it has been shown that recrystallization can be accelerated. Furthermore, as the spacing increases, addition acceleration of recrystallization occurs. This acceleration is attributed to two key mechanisms. First, dislocations are generated by strong particles within a matrix, contributing to the overall dislocation density of a system. This accelerates the early stages of recovery and thus recrystallization. Secondly, the inherently larger particles stimulate nucleation through a mechanism known as particle stimulated nucleation (PSN), whereby nucleation rates are stimulated by the high angle boundaries that develop around particles during strain (Deformation bands). This accelerated nucleation greatly increases recrystallization, and depending on the size and spacing of particulates, can be used as an engineering tool to manipulate grain size.

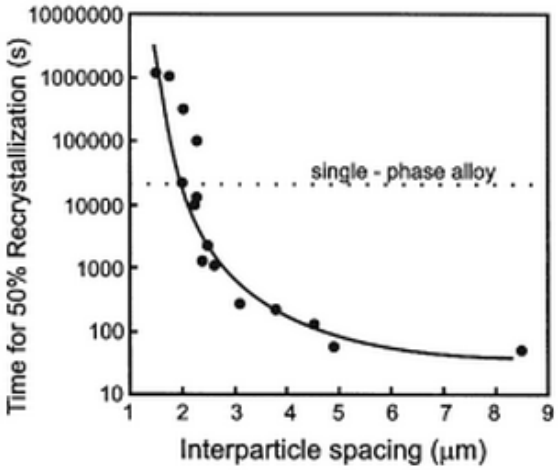

Figure 1-16 Time for 50% recrystallization of an Al-Si alloy relative to a single-phase Al system as a function of secondary phase interparticle spacing [16].

Discussion to this point has fundamentally covered static recrystallization (SRX). However, recrystallization mechanisms are promoted during hot working, allowing for dynamic recrystallization (DRX) to occur. Macroscopically, this results in a softening of the bulk material in a manner like DRV. Microstructurally, strain-free grains are formed and grow as they would in SRX. However, dislocations are generated within these new grains from the ongoing strain. Dislocation generation in new grains stimulates grain growth until grains eventually stop growing. With diminished grain growth and continuous dislocation generation, recrystallization will again begin to consume these strained grains. This segmented type of recrystallization is specifically termed discontinuous dynamic recrystallization due to its intermittent behaviour. The stress strain behaviours of DRX is different than DRV. In DRX, a broad peak flow stress followed by softening is characteristic shown in Figure 1-17. In conditions with a low Z

(Zener-Hollomon parameter, high temperature and low strain rate), many local maxima may be exhibited due to the discontinuity of grain nucleation and growth.

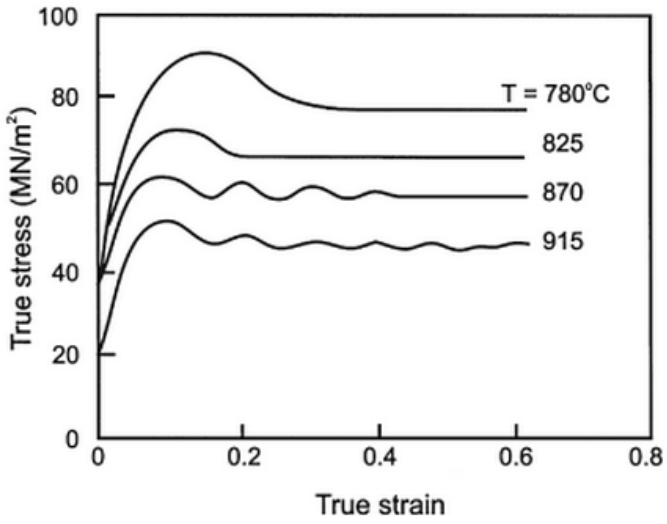

Figure 1-17 True stress strain behaviour of a 0.68%C steel under various hot deformation conditions exhibiting dynamic recrystallization [16].

1.5 Hot Working Aluminum and Aluminum Alloys

The hot working response of aluminum has been extensively studied and has been shown to differ from pure, to alloyed, to MMC systems. In alloyed form, precipitation events complicate flow behaviour. Similarly, in MMC systems, rigid second phase particles resist the plastic flow of material. The response of each of these will be discussed in more depth below.

For pure aluminum, recovery mechanisms are dominant. Stable subgrains form during deformation operations as discussed in the above paragraphs and as shown in Figure 1-9.

During hot work, these subgrains grow until they reach the saturation strain shown in Figure 1-12. Following this, they remain essentially equiaxed with a stable size throughout plastic deformation. For aluminum, the high λ_{SFE} produces subgrains on the order of 1-5um. A direct relationship between the flow stress and the accommodating subgrain size has been established by McQueen and has been noted to also apply to Al Alloys as well, shown in Figure 1-18 [18]. Similarly, the restoration behaviour of many aluminum alloys, including MMC systems, favors towards DRV [21]. DRX is particularly unfavorable, as the critical dislocation density required to initiate recrystallization is readily unattainable with such efficient recovery mechanisms taking place.

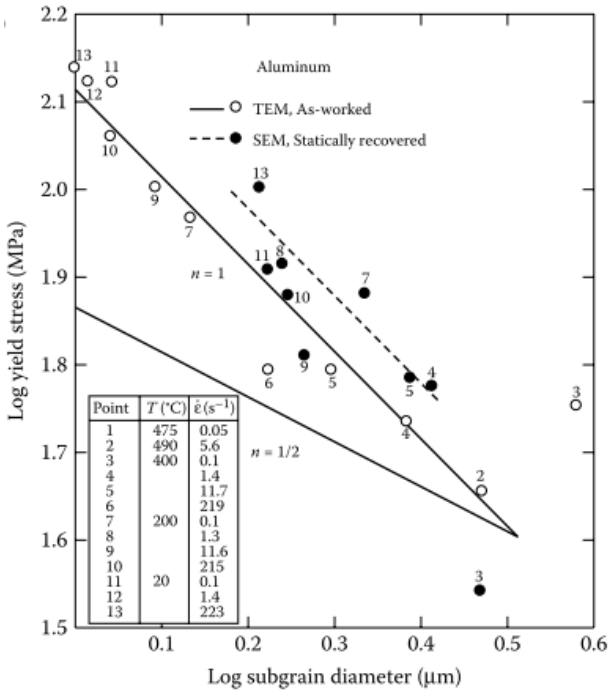

Figure 1-18 The yield stress of an aluminum system, varying with subgrain size resulting from unique processing conditions [18].

Constitutive analysis through various equations have been successfully performed over a wide range of temperature and strain rate conditions. Of these, the Zener-Hollomon approach, equation (12), shows to best represent a wide range of processing conditions. For pure aluminum (commercial purity up to 99.999%), Q_{HW} ranges from 150-170 kJ/mol.

Increased solute or impurity content affects the hot working response. The fine impurities impede dislocation motion and lead to a denser subgrain structure. This finer substructure essentially reduces DRV, causing flow stresses for a given Z to increase. In extreme cases, solute drag may sufficiently impede recovery, such that a dislocation density reaches a critical value, initiating dynamic recrystallization[27].

Aluminum alloys exhibit hot working behaviour different from that of pure aluminum. Of interest is precipitation-strengthened alloys. These alloys promote the formation of coherent submicron precipitates that inhibit dislocation motion, increasing the yield stress of a material. Fundamentally, a precipitation-hardenable alloy is solutionized at a temperature that correlates to a single-phase region of its phase diagram. This is followed by a rapid cooling (quenching) to produce a supersaturated solid solution. The metastable supersaturated condition is kinetically driven to form a secondary phase, albeit at a very slow rate at room temperature. The formation of these precipitates from a supersaturated solid solution is thermally activated by an elevated temperature heat treatment to stimulate the intentional formation of a fine precipitate network. Hot working of a

precipitation-hardenable alloy similarly stimulate the development of these precipitates during deformation. This phenomenon is known as dynamic precipitation (DPN).

DPN is a complex mechanism and covers both for formation of fine precipitates from a highly concentrated solute atmosphere (strengthening of the bulk material), as well as the latter stage of precipitate coalescence. First, we'll consider the case of a metastable, supersaturated solid solution. Here, upon heating to the deformation temperature and during the elevated temperature processing of a material, precipitates will form in the microstructure. These precipitates pin dislocations and reduce substructure cellularity and greatly strengthen the material. When compared to an unalloyed aluminum phase, flow stresses will be considerably higher, while ductility is lower. This response changes with the deformation temperature; higher temperatures promote rapid precipitation, growth and coalescence of secondary phases while flow stresses rapidly decline, and ductility similarly increases. Overall, a material will show considerably higher temperature dependence if it is precipitation hardenable and in the solutionized state. Like pure aluminum, the sole dynamic restoration mechanism that takes place during this process is DRV. However, the stress-strain behaviour now diverges from the stable flow stress observed in Figure 1-12. Now, a broad peak at low strain is observed, like DRX, followed by softening (Figure 1-19). Unlike the adiabatic heating-induced softening shown earlier, this softening behaviour is attributed to the coalescence of precipitates and enhanced DRV. With increased strain and assuming enough ductility is available, the instantaneous flow stress will approach that of an equilibrium (fully precipitated) structure.

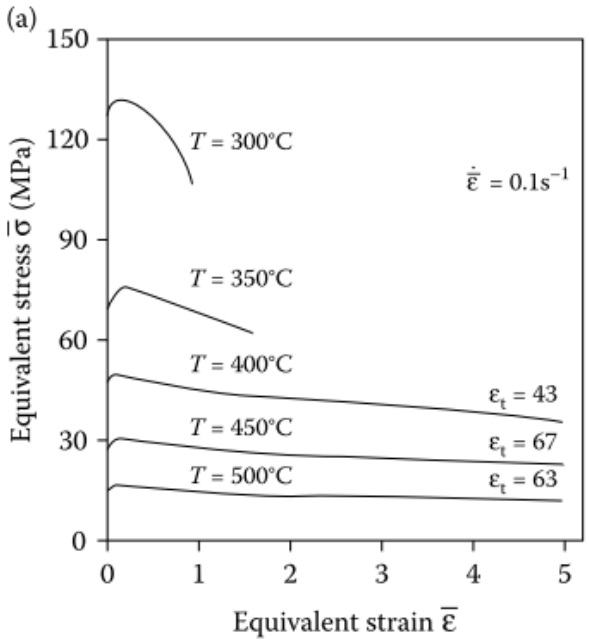

Figure 1-19 Equivalent stress strain curves for precipitation-hardenable alloys, exhibiting dramatic temperature dependence [28].

To contrast the previous example, one can consider a condition where the microstructure approaches equilibrium, where dynamic precipitation does not occur. If the material is cooled slowly from the solutionizing temperature, or artificially aged to an equilibrium state, no solute is available, and precipitates are excessively sized to effectively oppose dislocation motion. When compared to the previously-discussed non-equilibrium condition, flow stresses are significantly decreased, especially at lower temperatures. Deformation in this annealed condition lends itself to hot working operations, but means the material needs to undergo subsequent solutionizing and heat treatment to restore the mechanical properties through a homogenous dispersion of fine precipitates. Constitutive analysis shows that a particular heat treatable alloy in its equilibrium-condition, values of

Q_{HW} ranged from 144 kJ/mol to 177 kJ/mol whereas 230 kJ/mol to 270 kJ/mol were reported in the solutionized condition [28].

Hot working behaviour is similarly influenced by the introduction of hard ceramic particles, as in MMC's. Akin to the precipitation-hardened alloys, these secondary particles create localized stress fields and change the behaviour of dislocation generation and motion. However, these differ from precipitates in the size and way they're introduced. While precipitates are very fine and precipitated from a solid solution, ceramic particles are relatively coarse and often share very little mutual solubility with the matrix. They may suffer from inadequate bond strength with the matrix phase, causing decohesion during hot deformation. Furthermore, they often possess different coefficients of thermal expansion (CTE). This thermal expansion mismatch may induce residual stresses to the detriment of mechanical properties. An aluminum alloy, 2024 for example, possesses a CTE of 22.9 x 10^{-6} C^{-1} while AlN ceramic is 4.5 x 10^{-6} C^{-1}. Therefore, during cooling from an elevated temperature, the aluminum matrix contracts at a faster rate than the reinforcing phase causing localized stress fields around the particles.

The induced-strain of ceramic reinforcing particles is of concern. During heating and cooling operations, so-called ΔCTE dislocations are generated local to reinforcing particles. Large temperature changes result in greater ΔCTE dislocation density. At high temperature, DRV ensures that these dislocations are annihilated. In fact, despite the reinforcing phase the flow stress of a material at high temperature will rival that of the

matrix phase on its own [21]. At lower temperatures, DRV becomes less efficient in accommodating dislocations; not because the mechanisms of DRV have changed but rather because their rate has decreased relative to the augmented dislocation generation rate. Flow stresses are rapidly increased with lower processing temperatures. As expected, the activation energy in these instances rapidly increases, reaching 260 kJ/mol in some instances [21]. With sufficiently low temperature, a steady state flow stress regime may not be obtained, the rate of DRV simply cannot match that of the work hardening produced by dislocations around ceramic particles. Premature fracture is stimulated here, from damage caused by these stress fields.

1.6 Powder Forging

In producing commercial components through powder metallurgy, it is often inevitable that residual porosity remains in the final part. This is especially true for the conventional press and sinter style approach of forming PM components [1]. Residual pores vary in size, shape, spacing and volume fraction, each influencing the bulk material properties. The effect of bulk density of a ferrous PM component is shown in Figure 1-20. Within the scope of mechanical properties of a given PM system, increasing density (reducing total pore volume fraction) proves to be the predominant factor in attaining higher mechanical properties [29]. Therefore, for more demanding applications, it is desirable to achieve the lowest amount of residual porosity in a part.

When compared to an equivalent wrought system, as the severity of porosity increases, mechanical properties see a rapid decline. Larger, closely spaced pores with an irregular morphology prove to be the most damaging, while few, small spherical pores are considerably less-so. Pores within a material do not contribute to strength, but act as stress-raisers, sites for damage to preferentially occur [1]. Static properties (strength, hardness, etc.) see significant losses, while dynamic properties (impact toughness, fracture toughness, fatigue performance) are much more sensitive to porosity and see greater losses. Eliminating residual porosity through post-sinter processing will improve properties, but microstructural defects originating at these prior pore sites may continue to hinder optimal dynamic property performance [1].

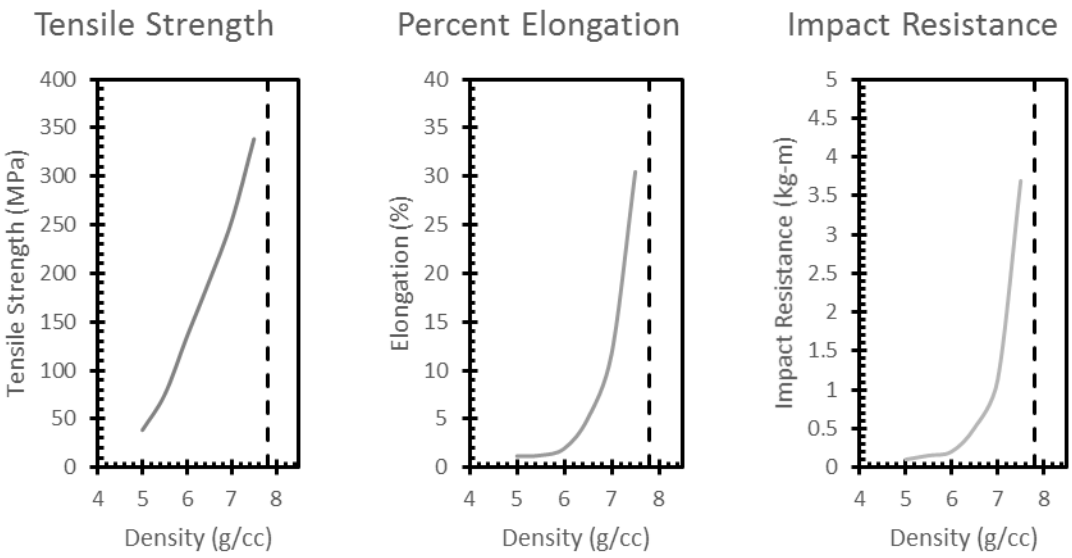

Figure 1-20 The loss in mechanical properties as a function of the final part density for PM steel components. Adapted from [30].

Full density processing of PM components commonly occurs through a process of powder forging. This process involves forging an engineered preform that has undergone sintering and has achieved suitable mechanical properties. This should be distinguished from sinter forging, whereby sintering of a green compact and forging occur simultaneously. Powder forging of various materials has enjoyed commercial success in a variety of parts. Most common are powder forged steel components for the automotive industry, including automatic transmission components, manual transmission synchronizer rings and piston connecting rods [29]. To a lesser extent, aluminum and titanium components have been powder forged for automotive and aerospace applications [30].

1.6.1 Hot Pressing and Upsetting

As anticipated, powder forging is a process largely aimed at achieving full theoretical density of components through the simultaneous application of heat and pressure within a confined die [31]. Powder forging of PM compacts can be divided into two broad categories, dictated by the relationship between the preform and the die geometries.

In a conventional, wrought forging process, simple geometry billets are struck multiple times to gradually manipulate the part into its final shape. This is largely dictated by the means in which the billet is fabricated, and the deformation it can endure in a single striking [14]. It's not uncommon for these conventional forging to create a significant amount of flash (excess material trimmed from the final part). Accordingly, the amount

of waste material generation is directly related to how efficiently the simple billet is transformed into the final part.

In powder forging, the preform geometry can be tailored such that minimal plastic deformation is needed to achieve the final part shape while eliminating residual porosity. The benefits of modifying this preform geometry led to the popularity of powder forging. First, obtaining a fully dense final part with the correct geometry can be typically completed in a single striking operation [30]. This limited post-sinter processing balances with the increased cost associated with creating the unique preform geometry (tooling, pressing, sintering), allowing for an economically competitive process [1]. Furthermore, the carefully designed preform allows for minimal material waste associated with flash [29]. Another unique aspect of powder forging is the use of zero draft angles in the final part. Again benefitting from the preform shape, material waste associated with draft angles can be eliminated, and a near-net shape part requiring minimal secondary machining can be produced [29].

Outside of these process design benefits, metallurgical differences exist between the conventional and powder forging. A key difference is the reduced amount of plastic deformation the material observes throughout its thermal history. In a wrought system, impurities are often distributed in a preferred orientation associated with the working direction. This can be during the initial processing of the wrought billet or during forging. This preferred orientation introduces an anisotropic behaviour into the final part. However, powder forged parts see considerably less plastic flow throughout their

processing history. Internal defects are more equiaxed and randomly distributed, allowing for bulk materials to retain a more isotropic behaviour [29].

Powder forging can be divided into two broad categories, based on the difference between the preform geometry and final part geometry. These are hot pressing and upsetting. In the former, the preform is of a geometry that nearly matches that of the final part. Minimal material flow is required to obtain the final part geometry. In the latter, the preform is sufficiently different in geometry from the die such that significant material flow is required. In addition to densifying a preform, there is considerable lateral material flow necessary to achieve final part geometry [29,30]. Figure 1-21 shows a schematic of the two powder forging methods in their pre-forged state and their dense post-forge state. The forging operation in either case can occur as a distinct process of reheating following sintering. Alternatively, forging can occur immediately after sintering and temperature adjustments [29]. Although both hot pressing and upsetting can achieve parts with the same final density, there are several differences regarding processing and how the material properties respond that are noteworthy.

The key difference between the two categories of powder forging is the stress state of the material when subject to strain. In hot pressing, a preform will yield when struck between forging dies. This preform rapidly fills the die cavity with minimal material flow. With addition applied pressure the stress state rapidly approaches a hydrostatic condition [29]. The pressures required to cause pore collapse in this case are relatively high, as a considerable amount of energy is consumed due to friction effects and straining of the

die. Pores will axially deform, while their dimensions orthogonal to the pressing direction remain less affected [31]. This can be seen schematically in Figure 1-22. In this figure, a pore within a spherical part is collapsed, while the lateral constraint causes a stress, *p*', preventing material flow in these directions.

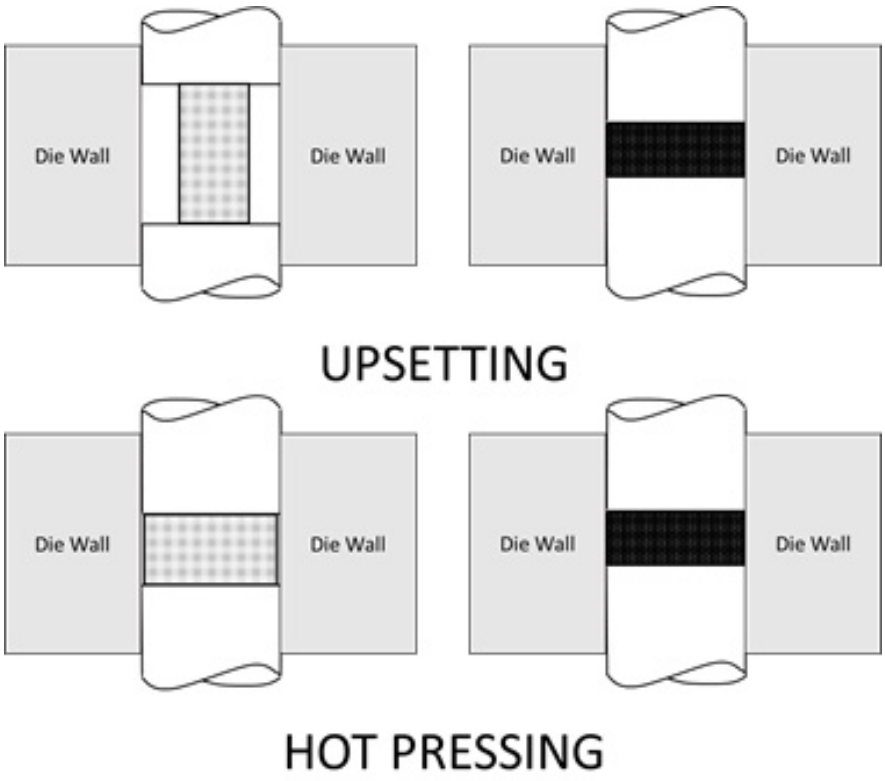

Figure 1-21 Schematic representation of upset forging and repressing of porous preforms into fully dense compacts. Adapted from [31].

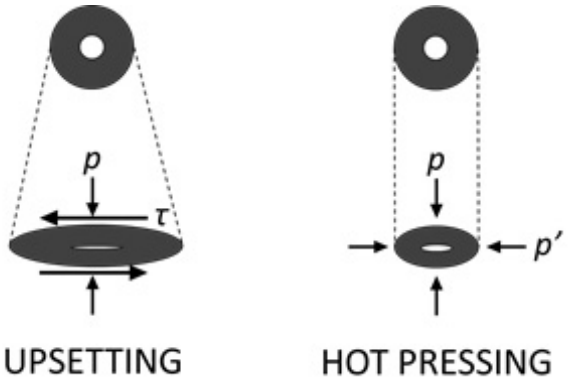

Figure 1-22 Effect of upset forging and hot pressing on pore collapse. Adapted from [31].

In upsetting, the preform is unconstrained laterally, allowing for relatively more lateral flow than in hot pressing. Again referencing Figure 1-22, the unit volume of material containing a pore is subject to a considerable amount of shear. As the pore is flattened with ongoing strain, it becomes elongated in the lateral directions. For an equivalent level of pore collapse, it is typical for pressures in upsetting to be considerably lower. As straining continues, eventually the material will fill the die cavity, reaching a state where mass flow is stopped. In a sense, the preform is subject to upsetting, followed by a phase of hot pressing [29,31].

Pore collapse occurs in both cases when opposite pores surfaces contact through plastic deformation. In upsetting, the high degree of shear locally elongates pore surfaces and causes the brittle oxide surface layer on the metal surface adjacent to the pore is forced to break up. This allows the exposure of the underlying metallic phase, priming the pore walls for metallic bonding should they contact [31]. In hot pressing the pore collapse mechanism differs slightly; without extensive shear strain, less metallic substrate is

exposed, and accordingly metallic bonding is reduced. Mechanical properties in hot upsetting typically trump those in hot pressing, especially sensitive dynamic properties [29].

Previously, it was mentioned that density was the predominant factor in mechanical properties. However, as the density in the forged condition approaches a theoretical maximum, other defects become more important to account for. No longer overshadowed by the effects of density, defects from oxides can deteriorate mechanical properties [29]. Therefore, for instances where the tolerance for dynamic properties is sufficiently large, greater control on residual phases must be emphasized.

1.6.2 Powder Forging Performance

When compared to wrought forging methods, powder forging remains commercially competitive for certain components. Cost savings over conventional forging stem from several unique characteristics of powder forging. First, powder forging is a near net-shape technology, meaning that minimal secondary machining operations are required following processing. This may include grinding of precise bearing surfaces or threading operations. However, bulk material removal machining operations can be negated. Closed die (flashless designs) can be adopted, and thus material utilization in powder forging can be considerably better than in conventional forging [30]. Further benefits and characteristics of powder forging on physical and mechanical properties are discussed below.

1.6.2.1 Density Considerations

As previously indicated, the primary goal of powder forging is the elimination of harmful porosity. In isostatic conditions (such as those approached in hot pressing), pores shrink isotropically. In upset forging, the pore collapse is considerably different, and exhibits several unique benefits. In upsetting, the lateral flow of material shears pores, reducing their height in the pressing direction and stretching them laterally. The pore becomes progressively more lenticular, flattening with increasing strain. The ultimate objective is for the upper and lower pore faces to contact (pore collapse). Achieving full density for a forged component requires careful consideration of many parameters. Forging type (hot pressing or upsetting), preform geometry, die geometry and strain are key components. Relatively high strains may be needed (>0.8) for certain materials to achieve full-density [32].

Obtaining 100% pore collapse can prove to be difficult, even in forging. Sample density can only reach unity if the pore gas pressure is sufficiently low so that that stress field around the pore causes continual deformation. In the case of a trapped insoluble gas within a pore, pressure will build as pore volume decreases, eventually reaching an equilibrium pressure with the resultant stress field in the metal surrounding it, where no further pore collapse can occur. This is circumvented in several ways. First, gas can be evacuated prior to pore closure, as possible in vacuum sintering. Another method would be to sinter in a gaseous atmosphere which has an appropriate solubility in the part (assuming it doesn't negatively affect properties to any serious extent). Finally, as is the

case with aluminum, the selected gaseous atmosphere reacts with the metal to form a solid compound, reducing the gas pressure. The reduction in pore pressure allows for lower stresses required for pore collapse. Sintering aluminum in a nitrogen atmosphere causes the formation of AlN and consumption of nitrogen within pores. This mechanism remains a crucial aspect to the successful sintering of aluminum [11]. This invariably benefits forging processes as pore pressure in the preforms is mitigated.

A further concern in powder forging that may arise in upsetting is localized de-densification of porous compacts. For a given porous preform under compressive stress, the stress state will be such that a hoop strain develops at the outer diameter (for a cylindrical part). Although bulk compressive strain is experienced by the preform, a local tensile strain at this outside surface may lead to pore opening [33]. Rather than densification, de-densification or even fracture may occur in these areas. Powder forging of a component must be designed such that the stress state at these areas does not produce these undesirable effects.

As discussed in Section 1.3, the forgeability of a material can be characterized by the 'temperature compensated strain rate' parameter, Z. For a given alloy, a set of coefficients can be extracted (Q_{HW}, etc...) that characterize that forging response as a function of temperature and strain rate. However, powder forging adds another parameter not captured in the Zener-Hollomon approach. The preform density in the Z-H approach inevitably assumes unity. However, porosity in PM compact is well known to deteriorate mechanical properties. A material with a relatively large amount of porosity will yield at

a lower stress than a denser preform. Therefore, it is imperative to observe the forgeability of the porous compact and how it's influenced by varying porosity.

It's been shown that in addition to the parameter, Z, forgeability can be manipulated by preform density. Flow stresses in a porous preform may show to be lower than in a dense equivalent, while the work hardening rate may be increased [29]. The initial porous structure is relatively weak from the pores, but their rapid collapse with increasing strain cause an increase in strength greater than in a dense part. Furthermore, powder forging is advantageous in processing systems where they would otherwise have insufficient density to be used in the as-sintered state. Powder forging of steels is often done on preforms made of prealloyed powders [29].

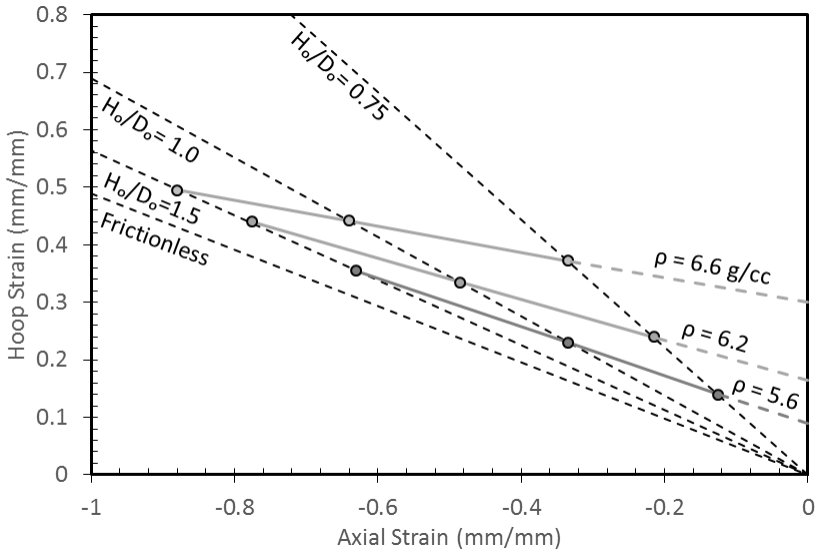

Figure 1-23 The strain at fracture, corresponding hoop strain, for ferrous powder forged compacts. Adapted from [34].

Porous preforms also exhibit decreased deformation tolerance in comparison to their wrought counterparts. Pores, especially those that exist in close proximity to inclusions, can motivate void coalescence, promoting premature fracture [35]. This is the case in the outer diameter of a porous preform undergoing compressive strain. The tensile hoop strain will tend to open pores. Figure 1-23 shows, for a ferrous PM material of varying density, how the axial and hoop strain vary as a function of initial preform density [34]. Greater density preforms can tolerate greater strain before hoop strain-induced cracking occurs. For preforms with large pre-existing pores, the possibly of crack formation is a strong possibility [35].

1.6.2.2 The Effect of Powder Forging on Mechanical Properties

While the primary objective of powder forging is to eliminate porosity, improving mechanical properties remains the root benefit. Outside of pore collapse, mechanical benefits can come from microstructural evolution events. Grain refining by recrystallization may increase strength [31], while the disruption of surface oxide layers at prior-particle boundaries may promote metal-metal bonding and improve ductility [36]. Furthermore for powder forgings compared to wrought forgings, there's promise of less anisotropy and improved dynamic properties [29].

Specifically in aluminum powder forgings, improving metal-metal and metal-ceramic bond strength shows considerable promise [37]. Here, powder forging competes with extrusion-type processes to disrupt the resilient aluminum oxide layer. Successfully incorporating a ceramic phase into an aluminum matrix produces a material with

desirable specific strength, stiffness and fatigue properties. By adding a hard, high-modulus ceramic phase to aluminum, mechanical property gains have been shown by transferring load to these strong particles. However, if the bond strength between these two distinct phases is not sufficient, separation may occur and promote crack formation [21]. Although forging may improve the bond strength between ceramic and matrix phases, the action of forging may introduce small defects as cracks or micro voids [21]. Upon loading at ambient temperatures, these forged-in defects may compromise the strength of the part. Again, forging parameters must be studied to eliminate these features which greatly affected dynamic properties.

CHAPTER 2. RESEARCH OBJECTIVES

The principal objective of this study was to develop an aluminum metal matrix composite (MMC) material with physical and mechanical properties surpassing those of commercially available APM alloys. Moreover, the author set out to investigate the feasibility of hot forging APM components in the context of mass production of high-quality automotive parts. Milestone objectives included:

- Determination of suitable ceramic phases, particle sizes and processing conditions capable of enhancing the mechanical properties of APM components.
- Investigate the effects of a series of lean, discontinuous ceramic additions to a commercial APM press-and-sinter alloy. Specifically, how these additions effect the stages of commercial processing and the mechanical properties of the sintered product.
- Study the response of commercially relevant APM materials to thermal mechanical processing. Particularly the densification and flow stress behaviour as a function of deformation temperature and strain rate, and how this behaviour was influenced by the presence of ceramic particulate.
- Perform industrial-scale hot forging experiments on suitable candidate MMC systems. Compare the physical and mechanical properties of deformed samples to their conventionally processed counterparts.
- Elucidate the physical and mechanical property evolution by identifying the key microstructural features occurring during hot deformation of APM components.

CHAPTER 3. CONSOLIDATION OF ALUMINUM-BASED METAL MATRIX COMPOSITES VIA SPARK PLASMA SINTERING

G.A. Sweet[1], M. Brochu[3], R.L. Hexemer Jr[4], I.W. Donaldson[5], and D.P. Bishop[2]

1 – Graduate Student, Dalhousie University, Halifax, Nova Scotia, Canada
2 – Professor, Materials Engineering, Dalhousie University, Halifax, Nova Scotia, Canada
3 – Professor, Materials Engineering, McGill University, Montreal, Quebec, Canada
4 – Research Engineer, GKN Sinter Metals LLC, Conover, North Carolina, USA
5 – Director of R&D North America, GKN Sinter Metals LLC, Auburn Hills, Michigan, USA

Status: Published Journal Paper. Materials Science and Engineering A. (2015) Volume 648. Pages 123 - 133

Author Contributions: The following experimental procedures, results and discussions were completed by G.A. Sweet, with reviewer and editorial roles played by the subsequent authors.

3.1 FORWARD TO CHAPTER 3

This manuscript precedes hot deformation studies and specifically entails research performed to investigate the suitability of various ceramic powders in an aluminum matrix. The authors selected a variety of potential ceramic powders of roughly equivalent particle sizes. Spark Plasma Sintering was used to consolidate materials to emulate the high densities anticipated in a forged specimen. Three-point bend tests were performed to observe the relative performance benefits of the ceramic additions.

3.2 ABSTRACT

Aluminum-based metal matrix composite (MMC) materials containing SiC, AlN, Si_3N_4 or BN were processed by Spark Plasma Sintering (SPS). Ceramic powder type, size and content were investigated to determine their effect on sinter quality. SiC, AlN and Si_3N_4 proved to be amenable to this style of processing whereas all systems containing BN were not. Full densification of MMCs that incorporated finer ceramic particles was problematic due to the presence of ceramic clusters and the extent to which aluminum could be forced into these regions. MMCs that incorporated coarser ceramic particles were more easily densified, but their hardness benefits were inferior. Three-point bend tests proved to be an effective tool in determining the relative sinter quality of MMC systems. SiC outperformed AlN MMC samples in bend tests. Excellent ductility and bend strength were developed at low temperatures, while equivalent AlN-bearing materials required significantly higher temperatures to achieve comparable properties.

3.3 INTRODUCTION

Metal matrix composites (MMCs) constitute a useful class of materials that often demonstrate properties outside the range of those attainable within conventional alloy systems. Typically, MMCs are implemented when gains in mechanical attributes such as yield and tensile strength are sought, while physical properties like thermal conductivity, hardness and elastic modulus are also of interest in certain scenarios [38,39]. In general, an MMC is comprised of a ductile matrix phase, or majority constituent, that is strengthened by the presence of a hard, inert, secondary phase incorporated within it.

Although MMC technology extends to a variety of matrix materials and secondary phases alike, aluminum systems strengthened with hard particulates are of specific interest. Such systems can either have an unalloyed [40] or alloyed [41,42] matrix and can be strengthened with a variety of hard secondary phases. In particular, finely divided ceramic particulates such as SiC [38–51], Al_2O_3 [47], AlN [52–55], Si_3N_4 [52,56], BN [57,58] and even quasi-crystals [59–61] have all been investigated. However, the commercial applications of MMCs are presently dominated by those reinforced with SiC (brake rotors and drums) or Al_2O_3 (automotive engine cylinders [62], truck driveshafts, tire studs [63]).

A variety of processing approaches have been successfully utilized to fabricate MMC-type materials including casting [62,64], melt infiltration [65,66], and powder metallurgy (PM) technologies [42,63,67,68]. PM-based techniques are particularly advantageous as they avoid the need to handle molten alloys and can facilitate a more homogenous

incorporation of a ceramic additive through solid state blending practices. Various processing techniques within the field of PM have been explored. The most prevalent options include hot pressing [51,57,67], hot extrusion [48,53,68–70] and compaction followed by pressureless sintering [37,52,54]. Less common is the consolidation of MMC systems through spark plasma sintering (SPS) [39,40,43]. Here, the powder mixture is pressed uniaxially at low pressure within a conductive graphite die, while a high intensity pulsed electrical current is passed through the powder/die setup. Joule-heating causes rapid, localized heating of the powder, while uniaxial forces assist with the elimination of porosity while breaking up the otherwise intrusive oxide layer on aluminum matrix particles [12,71]. SPS is intriguing for MMC processing because of its capacity to fabricate products with full densification and excellent mechanical properties in an abbreviated period [46], while simultaneously exhibiting an ability to reduce the levels of residual impurities such as hydrogen and oxygen [72]. Furthermore, the inherently lower processing temperatures coupled with shorter processing times allow microstructural coarsening to be minimized [73]. Given these beneficial traits, this work aims to conduct a fundamental, systematic study on the consolidation of aluminum MMC systems using SPS. A series of ceramic additives were considered (SiC, AlN, Si_3N_4, BN) as the reinforcing species in varying volume fractions (2-10%). The inter-relationships between MMC formulations, SPS processing parameters, and the characteristics of the consolidated products (density, hardness, microstructure, mechanical properties) were investigated.

3.4 MATERIALS

The powders employed in this study and their nominal particle size attributes are shown in Table 3-1. An air atomized aluminum powder was used as the matrix material in all formulations considered. This powder was prealloyed with 0.4 wt% magnesium and was screened to remove particles ≤ 45 μm prior to use. In a previous study by the authors, it was shown that doping a pure aluminum powder with a prealloyed addition of magnesium in this amount was sufficient to aid in disrupting the tenacious oxide layer existing on all aluminum particles, promoting metallic bonding[72]. Four chemically different ceramics were considered as reinforcing agents - SiC, AlN, Si_3N_4 and BN. The SiC and AlN were sourced in two different sizes whereas a single powder source was utilized for Si_3N_4 and BN. To identify these powders throughout the text, the suffix "F" denotes ceramic additions of a fine particle size and the suffix "C" delineates a coarser variant of the powder. Samples of each ceramic were blended with the base aluminum powder in controlled concentrations of 2%, 5% and 10% by volume.

Table 3-1 Particle size data for the powders employed.

Name	Manufacture – Product Name	D_{10} (μm)	D_{50} (μm)	D_{90} (μm)
Al Matrix Powder	Ecka Granules GmbH	49.0	97.3	229.2
SiC-F	Washington Mills - *Carborex C*-5	1.5	3.7	7.4
AlN-F	H.C. Starck – *AlN Grade B*	0.4	3.0	6.2
Si_3N_4-F	UBE America - *SN-E03*	0.9	2.0	3.9
BN-F	Saint Gobain - *Combat BN PHPP325B*	1.1	7.2	23.6
SiC-C	Electro Abrasives – *SiC 400 W*	12.8	21.3	35.4
AlN-C	H.C. Starck – *AlN Grade AT*	1.6	11.8	29.5

3.5 Experimental Techniques

Blending of all binary Al/ceramic formulations was completed in Nalgene bottles using a Turbula Model T2-F powder mixer and a 30-minute residence time. The homogenized mixtures were then consolidated by means of spark plasma sintering using a model 10-3 system manufactured by GT-Advanced Technologies in graphite dies. The resultant specimens were disc-shaped with a nominal diameter and thickness of either 20 mm x 3 mm or 40 mm x 15 mm. Processing was carried out under vacuum ($P \leq 9$ Pa) in dies made from E-970 high strength graphite produced by the Micron Research Corporation. Graphite foil (127 μm thick) was used to line the die wall and punches. Powders were heated at a rate of 100 K min^{-1} when processing 20 mm discs while a more conservative rate of 50 K min^{-1} was used for those with a diameter of 40 mm. Current was pulsed DC, with a 36/8 ms on/off time. Peak sintering temperatures were 450°C, 500°C and 550°C

where each specimen was held isothermally for 120 s prior to furnace cooling that was aided with the introduction of flowing argon gas. A uniaxial pressure of 50 MPa was maintained throughout the complete SPS cycle.

Characterization of finished products included the assessment of sintered density, hardness, bend strength, and the general appearance of the microstructure. The density of sintered specimens was measured using the Archimedes-based approach described in Metal Powder Industries Federation (MPIF) standard 42 [74]. The percent of theoretical density was then determined by comparing the measured value to the full theoretical density of the mixture as calculated through a rule of mixtures approach. Hardness was measured using a Wilson Instruments Rockwell 2000 hardness tester operated in the H scale. Average values were calculated from 6 measurements on each specimen. Thermodynamic calculations were performed using FactSage 6.4. Three point bend tests were performed according to MPIF standard 41 [75], supplemented by ASTM D790-10 [76] for flexural stress and strain calculations. To complete bend tests, 40 mm diameter pucks were milled into rectangular bars (31.7 mm x 12.7 mm x 8.0 mm), with one sample made per chemistry investigated. The machined products were then placed in a three-point bend fixture and loaded to fracture at a rate of 0.2 mm min-1 using an Instron model 5594-200HVL equipped with a 50 kN load cell. Applied load and crosshead displacement were simultaneously recorded, allowing curves for bending stress versus bending strain to be plotted. A strain ‘toe correction’ was performed for all stress-strain plots to compensate for slack take-up during testing, according to ASTM D790-10. This allowed for the calculation of yield strength, ultimate bending strength and bending

ductility for each bar tested. For metallographic examination, samples were cold mounted in epoxy and polished through a standard series of SiC abrasive papers and diamond compounds. Optical imaging was then completed using an Olympus BX51 microscope whereas electron microscopy studies employed a Hitachi S-4700 field emission Scanning Electron Microscope (SEM) operated with an accelerating voltage of 10 kV and a beam current of 15 μA.

3.6 Results and Discussion

Preliminary work in this study focused on the effects of different ceramic types, their respective concentrations, and nominal particle size on the density and hardness of sintered compacts. Using these findings, larger samples of a size sufficient for mechanical property measurements were then processed and tested.

3.6.1 Effects of Ceramic Type and Concentration

To accumulate data that encompassed the complete scope of ceramic types considered, preliminary blends emphasized those that contained varying fractions of the fine particle size only. Results on sintered density as a function of SPS temperature are shown in Figure 3-1. Here, the extent of densification diminished in a manner that was influenced by both the type and concentration of ceramic added. In the case of SiC-F additions (Figure 3-1a) full density (i.e. $\rho \geq 99.8\%$) was achieved for samples containing 2% ceramic when sintered at temperatures $\geq 500°C$. When the concentration of SiC-F was

increased to 5%, full densification was still possible but only with an SPS temperature of 550°C. Below this threshold, densification was markedly impeded by the increased ceramic content. The reduced densities of samples bearing 10% SiC-F added further emphasis to this trend. Here, the highest density recorded for this material was only 98.8% when sintered at 550°C and fell to 94.1% with a SPS temperature of 450°C. As such, full densification was not realized for this blend within the range of conditions investigated. Calculations performed using FactSAGE thermodynamic software indicated a decomposition reaction of SiC into Al_4C and free silicon, among other minor by-products. However, it has been reported in very similar circumstances that short processing conditions of SPS are insufficient to detect any extensive decomposition of the SiC phase [43].

Densification data on MMCs with AlN-F are shown in Figure 3-1b. For samples containing 2% AlN-F, full density was achieved at a temperature of 550°C. At 450°C a near-full density of 99.5% was observed in contrast to the lower value realized for the equivalent 2% SiC-F-bearing material (98.8%). The 5% AlN-F material was not able to achieve full density at the highest sintering temperature, but values that impinged on this target (99.4% and 99.6% at 500°C and 550°C respectively) were still achieved. The highest concentration of AlN-F further inhibited densification as the sample sintered at 450°C achieved a density of only 96.2%. However, this value significantly exceeded the densities obtain for all other 'fine' ceramics tested in this study at 450°C. Furthermore, at 550°C the 10% AlN-F sample was able to achieve a near-theoretical density of 99.4%. Overall, the densification behaviour of MMC materials containing AlN-F additions was

marginally improved over that noted for the SiC-F systems. However, the temperature/ceramic concentration dependencies were less pronounced as evident by a reduced spread between the curves for 2, 5, and 10% AlN-F. Thermodynamic calculations on the AlN-bearing systems indicated that no reaction between any of the phases would occur.

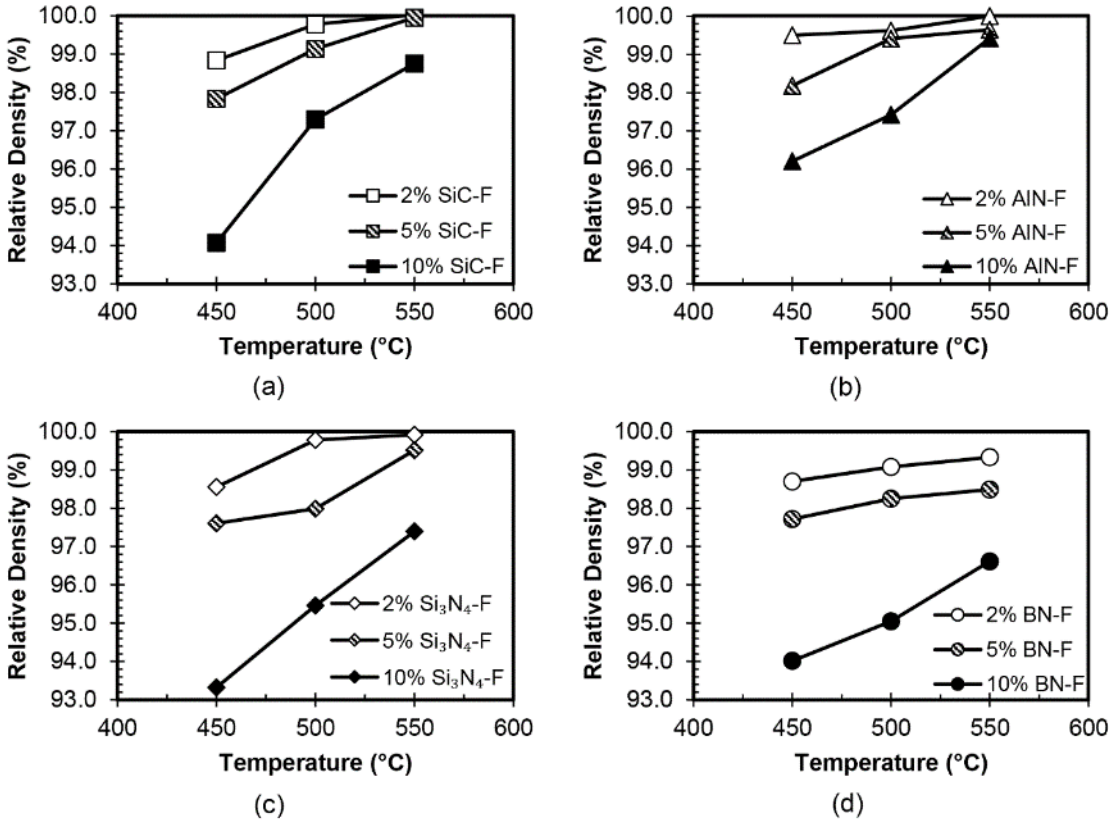

Figure 3-1 Effects of sintering temperature on the density of MMCs prepared with 2, 5 and 10 vol% (a) SiC-F, (b) AlN-F, (c) Si_3N_4-F and (d) BN-F.

The performance of Si_3N_4-F MMC samples proved to be inferior to both AlN-F and SiC-F systems. Near theoretical density was only obtained in samples containing 2% of the ceramic processed at 500°C and 550°C. With increased ceramic content, MMC samples

were unable to achieve near-theoretical densities. The highest processing temperature for the 5% MMC was only able to obtain 99.5%, which decreased to 97.6% when the sintering temperature was lowered by 100°C. Increasing the ceramic content of this powder to 10% exhibited further losses in densification. In this regard, even when sintered at the highest temperature considered, a relatively poor density of only 97.4% was maintained; a value appreciably removed from those reached with SiC-F (98.5%) and AlN-F (99.4%) systems under identical processing conditions. Thermodynamic calculations on this system indicated a reaction between Si_3N_4 and aluminum. Si_3N_4 is expected to decompose into a stable AlN phase as well as free silicon. Again, a previous study on this MMC system indicated a Al-Si_3N_4 interface free of any by-product [56]. It is therefore not anticipated that the SPS conditions in this present study are such that any reaction will occur to a measurable extent.

BN-F reinforced materials were unique among those considered in this study in that their densification behaviour was exceptionally weak and exhibited a reduced dependency on temperature. As such, full density was not observed for any BN-F MMC blend at any SPS temperature. Indeed, additions as small as 2% of the ceramic were enough to compromise densification response. MMC materials containing 5% BN-F behaved even worse while the addition of 10% BN-F resulted in a material that was in no way able to densify effectively.

The reasoning behind the poor performance of the BN-bearing systems was likely a result of the chemical and electrical properties of BN. Regarding the former, thermodynamic calculations completed indicated that a reduction reaction between boron and the

prealloyed magnesium should take place, producing either MgB_2 or MgB_4. Excess boron, as well as liberated nitrogen, would then be expected to react with free aluminum to form AlB_2 and AlN. The preferential reaction of magnesium with boron is specifically problematic, as Sweet et al have shown the importance of this dopant in the SPS processing of aluminum powders [72]. Whereas thermodynamic equilibrium is certainly not expected to occur during the short processing times involved in SPS, a reaction of this type is expected to have an adverse effect at critical locations nonetheless (i.e. those wherein aluminum particles are separated by BN-F). For the latter, the hindered densification may also be related to the high dielectric strength of BN. With a reported value of 374 kV mm^{-1}, that for Si_3N_4 and AlN are over an order of magnitude lower at 17.7 kV mm^{-1} and 15 kV mm^{-1} [77], respectively, while SiC is even lower again at ~5 kV mm^{-1}[78]. During SPS processing, the applied electrical potential causes a flow of electrons through conductive materials. In the case of non-conductive ceramics and conductive aluminum, a potential difference across aluminum particles separated by the ceramic may develop. For BN, the resistance towards the breakdown of this insulating layer would have been greatest and would therefore be less likely to occur than in the other MMC systems. As a result, current would be diverted around Al-BN-Al junctions, thereby reducing the occurrence of localized Joule-heating and in turn, the net level of densification observed.

Low magnification images comparing the general microstructures observed in MMC materials containing 10% ceramic and sintered at 550°C are shown in Figure 3-2. In the case of SiC-F (Figure 3-2a), the angular ceramic particles were distributed throughout the

microstructure along prior matrix particle boundaries. In some instances, these resided as discrete particles while in others, the ceramic had agglomerated into clusters that varied in size from ~5 to 75μm in diameter. Since the clusters were also the principal source of residual porosity, a more detailed inspection of this feature and any transitions that may have occurred with SPS temperature was warranted. In Figure 3-3a and b, SiC-F clusters are considered within specimens sintered at 450°C and 550°C. At the lower temperature, the aluminum matrix demonstrated minimal capacity to penetrate these features. Hence, cluster-associated porosity prevailed throughout and even the smallest clusters remained porous (Figure 3-3a). However, at the higher temperature of 550°C (Figure 3-3b) the flow stress of the matrix was evidently reduced to a level whereby the applied external pressure was sufficient to force aluminum into these features and thereby encapsulate SiC-F particles. This phenomenon was fully effective on small clusters with a complete elimination of porosity noted. However, larger clusters presented a more formidable challenge as aluminum was only forced into the outer layer thereby retaining a porous inner core. Mechanistically, it is postulated that the incomplete densification of large clusters was a result of entrapped gases and/or a localized increase in electrical resistivity that may have caused a more acute diversion of current and subsequently, a localized reduction in the Joule heating needed for densification and aluminum softening.

In general, the same microstructural observations and trends noted in SiC-F systems prevailed in MMCs prepared with AlN-F as well. The one notable difference pertained to the nature of the larger clusters. When using SiC-F, cluster centres were devoid of ceramic particles. It was therefore postulated that the central SiC particles had minimal

adhesion with the adjacent material and had been removed during the grinding and polishing stages of sample preparation. However, for AlN-F, ceramic particles were retained in comparably sized clusters even at the lowest SPS temperature of 450°C (Figure 3-3c). This implied that the ingression of aluminum into AlN-F clusters was potentially more pronounced thereby instilling a greater resilience to particle pull out. This concept agreed with the improved densification observed in MMCs with 10% AlN-F versus those with 10% SiC-F (Figure 3-1b and a respectively).

Microstructural examination of the MMC containing 10% Si_3N_4-F (Figure 3-2c) again showed that the ceramic particulate was distributed along aluminum particle boundaries and in the form of clusters. A closer inspection of the ceramic-matrix interfacial area of 10% Si_3N_4-F sintered at 450°C (Figure 3-3e) revealed that aluminum had not migrated into even the smallest clusters. An increased sintering temperature of 550°C (Figure 3-3 f) showed an improved response as the flow of aluminum was then enough to fill small clusters and partially penetrate those of a larger size. In accordance with Table 3-1, Si_3N_4-F exhibited the smallest average particle size and narrowest size distribution of all the ceramic particulates considered. Accordingly, the voids between ceramic particles were exceptionally small and numerous relative to those in SiC-F and AlN-F systems. It is postulated that this presented a greater impediment to the flow of aluminum into the clusters and thereby deteriorated the extent of densification when compared to counterpart systems employing SiC-F and AlN-F as noted in Figure 3-1.

The exceptionally limited densification of BN-F MMC materials was clear as a comprised microstructure wherein a poor sinter quality prevailed (Figure 3-2d). Here, bonding of the matrix with BN-F was scarcely evident as much of the ceramic had fallen out during polishing procedures. It was also apparent that even adjacent aluminum particles were unable to achieve a satisfactory level of bonding as they too were susceptible to pull out during sample preparation. As discussed earlier, electrical and chemical influences unique to the BN-F ceramic would have locally diminished the extent of Joule heating within the MMC and thereby inhibited densification and the development of strong inter-particle bonds.

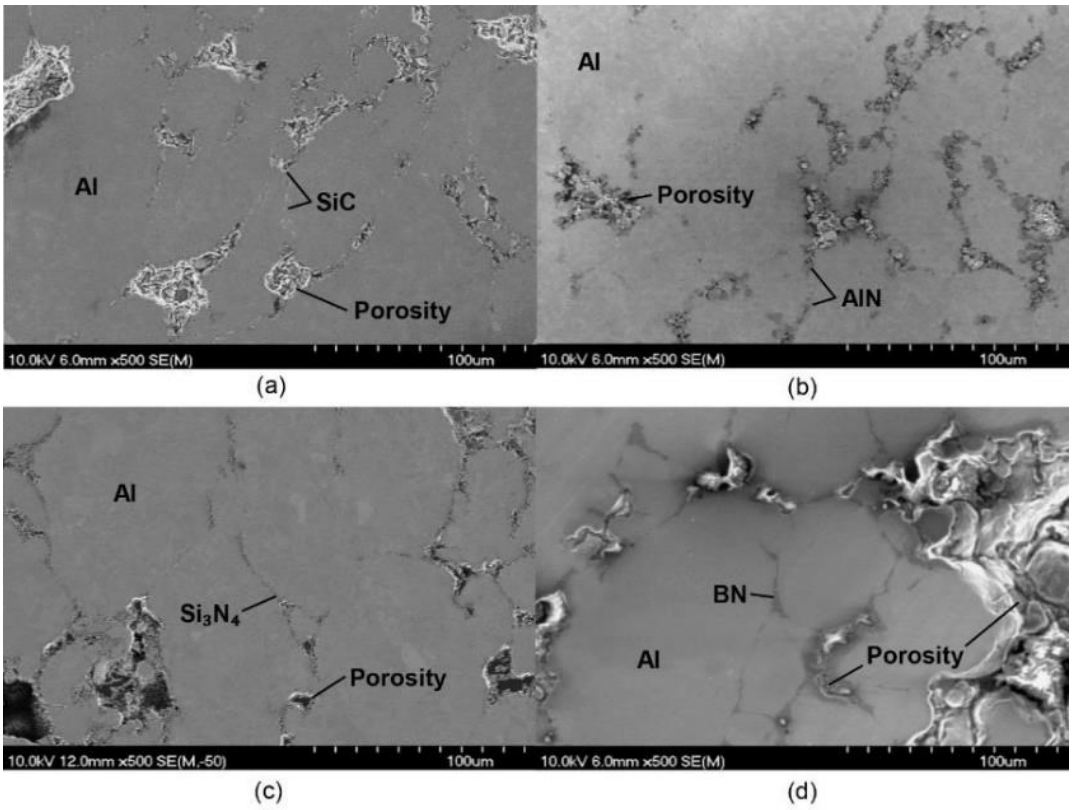

Figure 3-2 SEM micrographs of sintered MMC mixtures that contained 10 vol% (a) SiC-F, (b) AlN-F, (c) Si_3N_4-F and (d) BN-F. All samples sintered at 550°C.

.

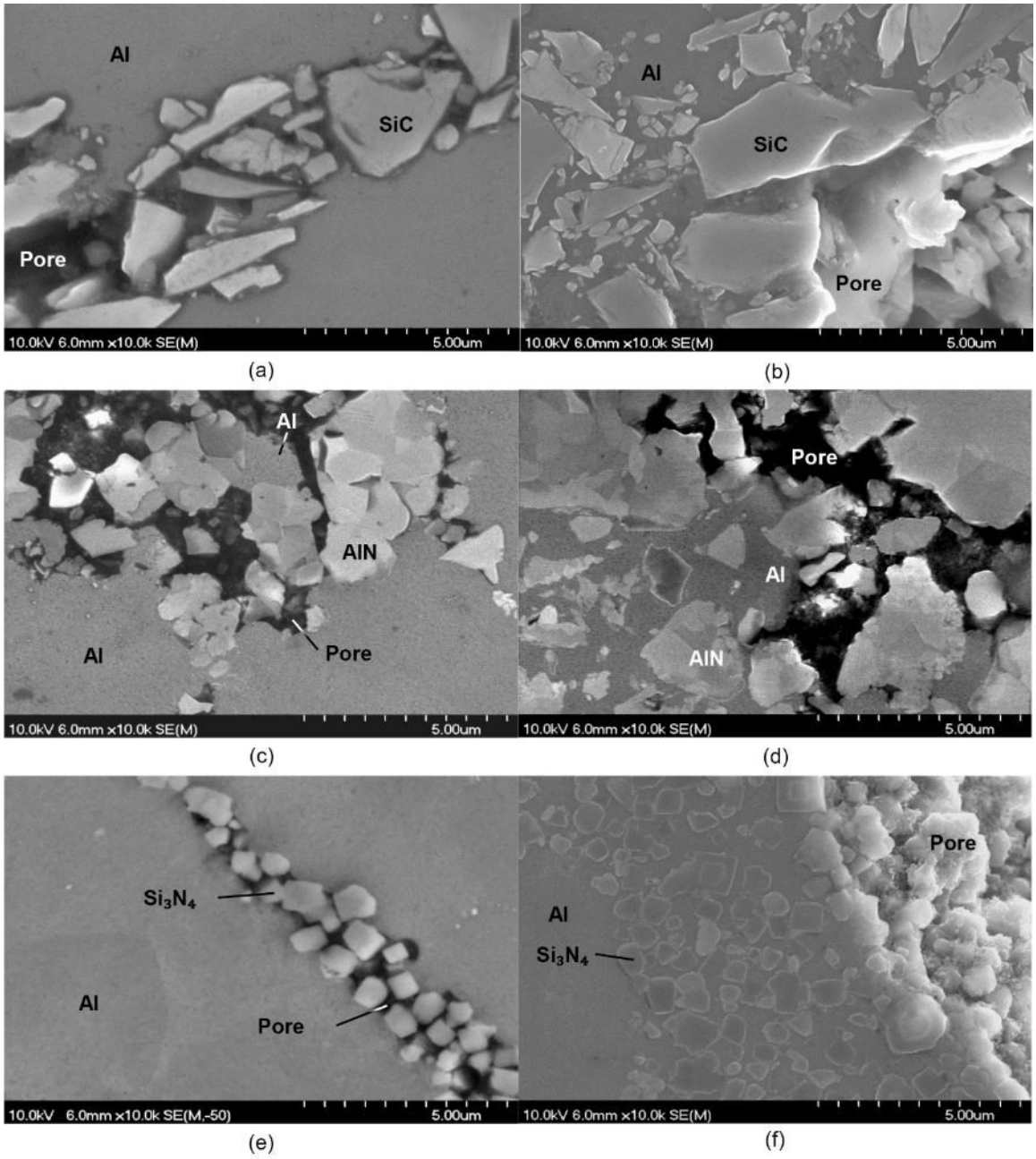

Figure 3-3 SEM micrographs of ceramic clusters observed in sintered MMC mixtures that contained 10 vol% (a) SiC-F sintered at 450°C, (b) SiC-F at 550°C, (c) AlN-F at 450°C, (d) AlN-F at 550°C, (e) Si_3N_4-F at 450°C and (f) Si_3N_4-F at 550°C

Data on the bulk hardness of sintered compacts (Figure 3-4) revealed a clear dependence on processing temperature as well as ceramic composition and concentration. The influence of BN-F samples was contrary to what was observed for the other MMC blends (Figure 3-4d). Here, increased concentrations of the ceramic additive promoted a progressively larger reduction in hardness; so much so that all measured values were actually lower than that of the matrix system devoid of any ceramic additions (56-65 HRH from a previous study) [72]. As BN-F was also found to degrade densification (Figure 3-1) and overall sinter quality (Figure 3-2d), the inferior hardness of these materials came as no surprise. Work on systems containing BN-F was discontinued at this point.

In general, comparable hardness transitions were noted for the systems that contained SiC-F, AlN-F, and Si_3N_4-F (Figure 3-4a-c). Work in a previous study dedicated to the same aluminum matrix powder without any ceramic phase, revealed that hardness values trended downward with increased SPS temperatures [72]. Here, the net softening effect was driven by the fact that hardness losses ascribed to grain growth surpassed the gains that stemmed from porosity elimination. Hardness data on SiC-F materials (Figure 3-4a) indicated that a trend of this same general nature only occurred in the most dilute blend (2%). Increasing the ceramic concentration brought about a progressively more intense inversion in this behaviour. Here, hardness increased with SPS temperature rising by 2 HRH when 5% SiC-F was added and by 10 HRH when the concentration was doubled to 10%. Comparable transitions were observed with the addition of AlN-F and Si_3N_4-F.

That is, an increased hardness with increased ceramic content and a gradual inversion in the slope of the hardness/SPS temperature plots.

The inversion of hardness trends can be explained as follows. At low ceramic concentrations the MMC materials exhibited densification behaviour like their unalloyed counterparts in that near-theoretical densities were more easily obtained at low temperatures. Minor gains in density with further heating accordingly produced marginal hardness benefits. Simultaneously, matrix grain size would have grown from increased levels of thermal exposure, causing a disproportionate loss in hardness. In this case, small density-derived gains were thereby overshadowed by the larger losses from microstructural coarsening resulting in a negative slope on the hardness versus density plot. When 5% or 10% SiC-F was added, density rose more sharply with SPS temperature. Accordingly, the associated gains in hardness would have increased proportionately and thereby more than offset the simultaneous losses ascribable to microstructure coarsening. As a net result, an upward trend in hardness versus SPS temperature was recorded.

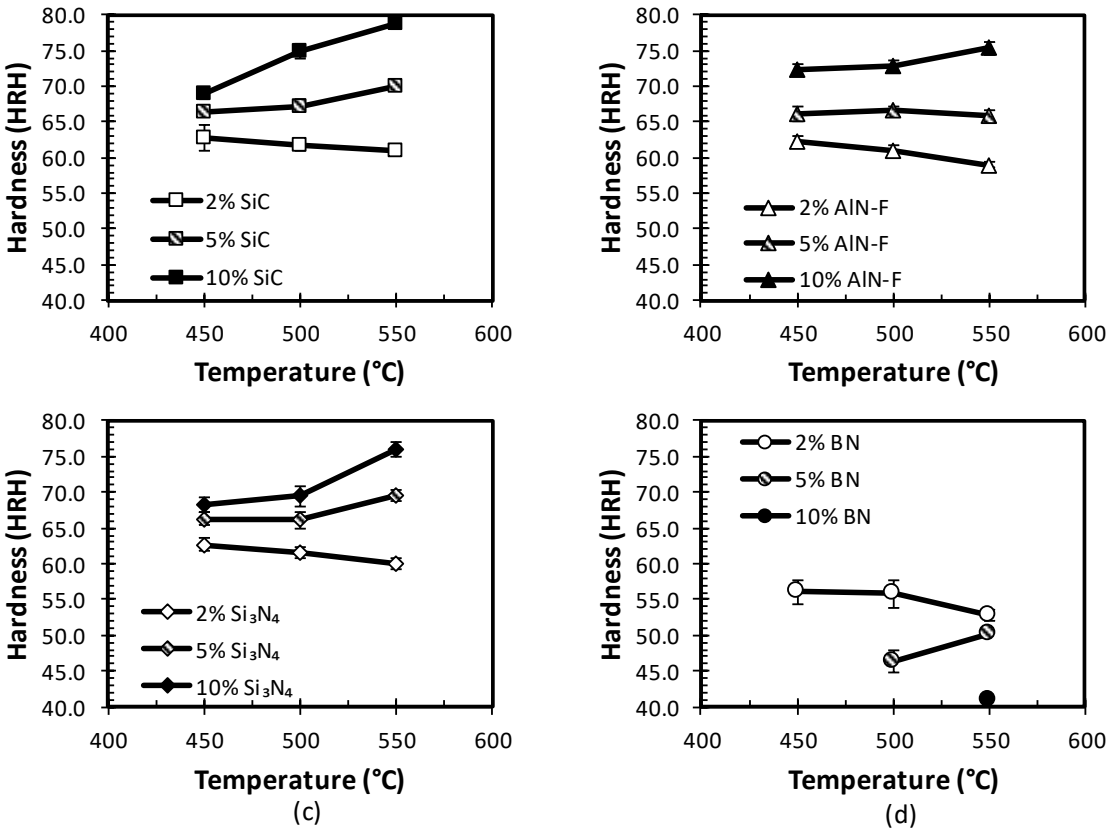

Figure 3-4 Effects of sintering temperature on the hardness of MMC prepared with 2, 5 and 10 vol% (a) SiC-F, (b) AlN-F, (c) Si_3N_4-F and (d) BN-F.

It can be summarized from the above results that the resistance towards the plastic flow of the aluminum matrix within ceramic particle clusters, and in turn, the net extent of MMC densification was largely dictated by the morphology and chemical/electrical characteristics of the ceramic powder selected for strengthening purposes. In this sense, densification was hindered when the ceramic phase was one of a high dielectric strength and/or processed into a condition of very fine particles with a narrow size distribution. Conversely, MMCs with near full theoretical density could be produced when ceramic

particles were of a low dielectric strength, somewhat coarser, and more rounded in morphology.

3.6.2 Effects of Ceramic Particle Size

Of the four ceramics evaluated, SiC and AlN exhibited the more desirable response to SPS processing in terms of density, hardness, and microstructural quality. As such, these reinforcements were the subject of secondary stage of work related to the influence of particle size on these same attributes. Blends containing 10% of the coarse variant of these ceramics, namely, SiC-C and AlN-C, were produced and processed for this purpose. Data illustrating effects on sintered density are shown in Figure 3-5. In the case of SiC additions, the use of a coarser powder source instilled an appreciable improvement in density over the full range of SPS temperatures considered. Such gains were particularly obvious at lower temperatures (+4% at 450°C) but remained significant even after SPS processing at the highest temperature applied (+1% at 550°C). Considering this improved response, a blend with the relatively high concentration of SiC-C could now be processed into a density that closely impinged on the full theoretical value (i.e. 99.8% at 550°C). This was well supported by microstructural observations. Here, the microstructural assessments of the MMC with SiC-C (Figure 3-6a) revealed how clustering of the ceramic was largely eliminated. Accordingly, large residual pores no longer existed and intimate contact between the ceramic and matrix phases was a prominent feature throughout the microstructure.

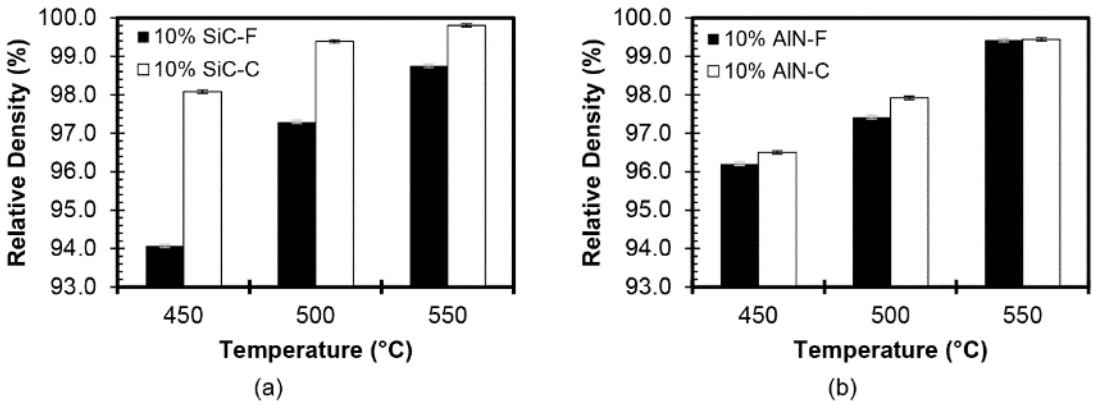

Figure 3-5 Effect of ceramic particle size and SPS temperature on the sintered density of MMCs containing (a) SiC and (b) AlN.

The densification behaviour of blends with AlN-C and AlN-F were quite like each other, as shown in Figure 3-5b. Only a 0.3% increase in density was observed at 450°C whereas the difference at 550°C was well within measurement error with both systems attaining 99.6% of full theoretical. Microstructural investigation (Figure 3-6b), showed that the specimen with AlN-C still contained both relatively large and small reinforcing particulate, whereas the counterpart SiC-C system was free of fines. This is supported by data on the volumetric size distributions of the ceramics (Figure 3-7). Figure 3-7a indicates that both the "F" and "C" grades of SiC had a normal Gaussian distribution about their mean values; that for the latter was particularly narrow with no appreciable presence of particles ≤ 6um in size. Conversely, Figure 3-7b shows that both grades of AlN exhibited more of a bi-modal distribution of particles. In fact, the two AlN powders (from the same manufacturer) differed only in the presence/absence of particulate greater than 10 μm. As such, while AlN-C had an appreciably larger D_{50} than AlN-F, it still contained a significant fraction of fine powder particles far removed from the mean size.

Since fine particulates remained in AlN-C samples, clusters and the associated residual porosity therein remained in the sintered products as well. Given that such clusters were chiefly responsible for the presence of residual porosity, the inability to eliminate this feature when using AlN-C thereby negated the possibility of achieving any remarkable gains in sintered density.

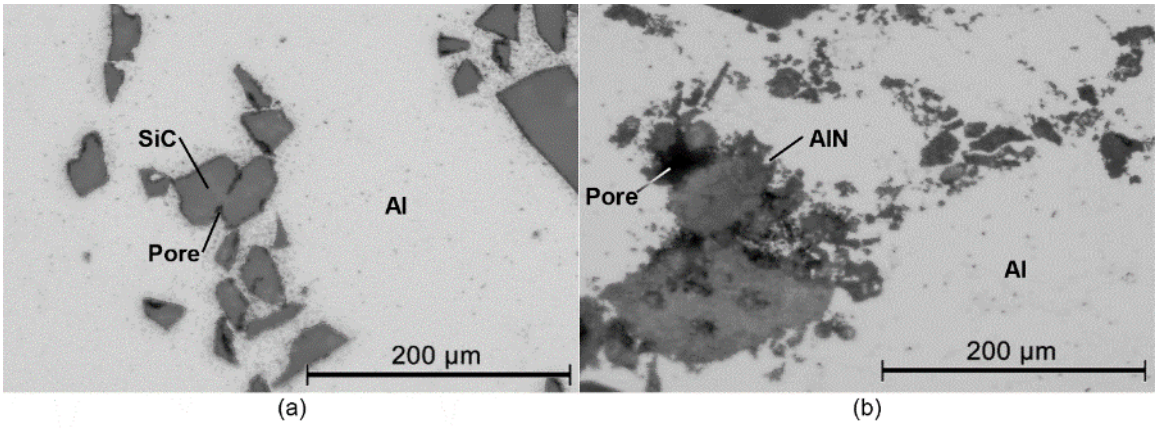

Figure 3-6 Optical micrographs of sintered MMC mixtures that contained 10 vol% (a) SiC-C and (b) AlN-C. Both samples sintered at 550°C.

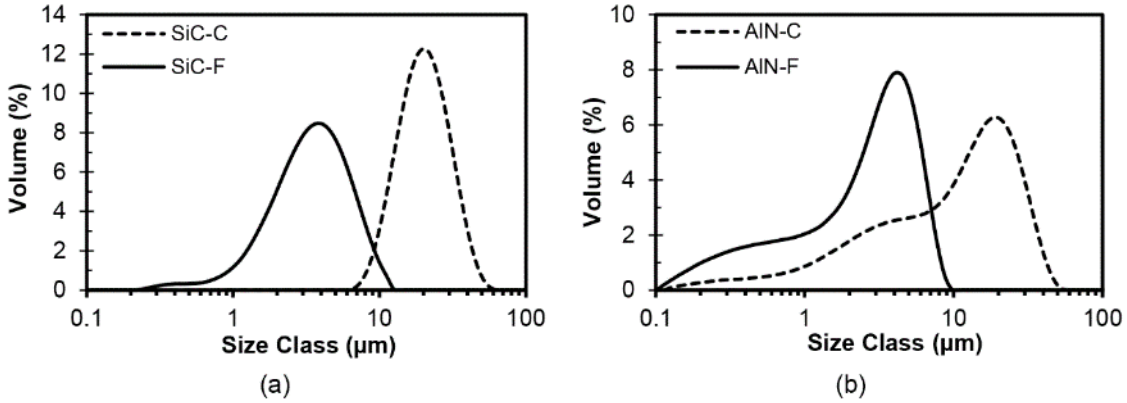

Figure 3-7 Comparison of the size distributions measured for the two grades of SiC and AlN powders utilized.

The data shown in Figure 3-8 represent the changes observed in hardness with increased particle size of the ceramic phase. The coarser SiC-C powder, Figure 3-8a, showed a hardness gain of only 2.1 HRH over the temperature range from 450°C to 550°C. The equivalent SiC-F powders exhibited a higher dependence on temperature, increasing by 9.8 HRH. Interestingly, the hardness of SiC-C at 450°C was superior to the finer powder, while the opposite was observed at 550°C. At low temperatures, the coarser particulate exhibited less impedance to densification, thereby fostering the attenuation of a higher sintered density (Figure 3-5a) and accordingly, greater hardness as well. Sintering temperatures above 450°C provided marginal densification improvements for SiC-C thereby resulting in minimal hardness gains. Ultimately, in a full density condition, SiC-C particulate was a less effective hardening addition than the fine counterpart. Statistically, there was no meaningful difference between the hardness values (Figure 3-8b) of MMCs with AlN-C or AlN-F consistent with density observations (Figure 3-5b).

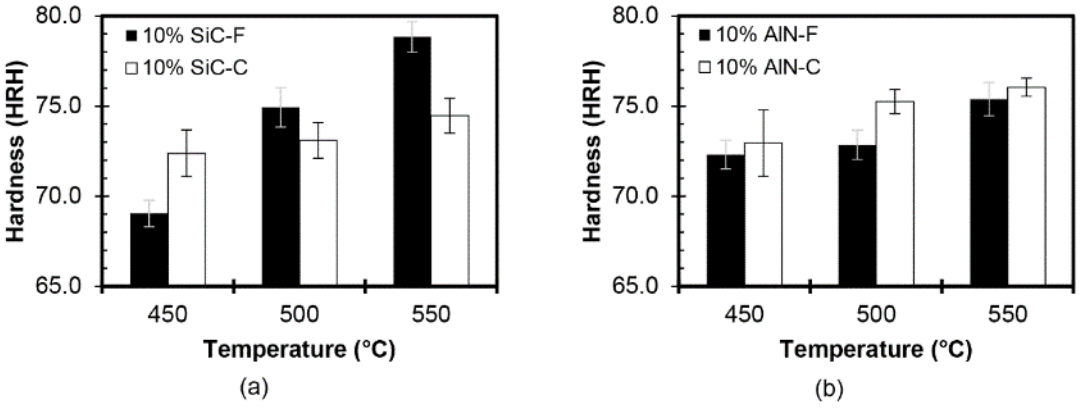

Figure 3-8 Effect of ceramic particle size and SPS temperature on the hardness of sintered MMC systems containing (a) SiC and (b) AlN.

3.6.3 Three-Point Bend Properties

Of the MMC formulations considered, the most promising systems were those that contained 10 vol% of SiC-C or AlN-C as these blends could be sintered to near full density and exhibited a reduced propensity for ceramic agglomeration. As such, these systems were studied in greater detail to gather data on their mechanical properties. Capacity limitations of the SPS system ensured that the resultant sintered billets were of a size insufficient for machining into standard tensile test specimens. As an alternative, three-point bend tests were executed to obtain a general sense of how mechanical properties evolved with SPS temperature. This manner of testing mandated the production of 40 mm diameter pucks from which the required rectangular test bars could be machined. However, all SPS studies to this point had been restricted to the production of 20 mm diameter discs. Since it is known that property variations should be expected when changing SPS die geometries [79], preliminary work was needed to determine if significant differences existed between the two product forms.

Density and hardness results for the two sample sizes are presented in Figure 3-9. Densities for 40 mm samples were on average 0.7% lower than their 20 mm counterparts. As such, full theoretical density was not realized in the larger slugs for either MMC system (Figure 3-9a). This was accompanied by reductions in hardness as well in that the larger pucks were typically lower by 3-7 points on the HRH scale (Figure 3-9b). For a given sintering set point, the actual temperature within the larger samples was likely lower [79]. Since temperature has a decisive impact on both attributes, a marginally

inferior sintering response within the 40 mm pucks was a reasonable observation. Based on these findings, subsequent testing via 3-point bending was expected to yield representative, yet conservative results for the MMCs of interest.

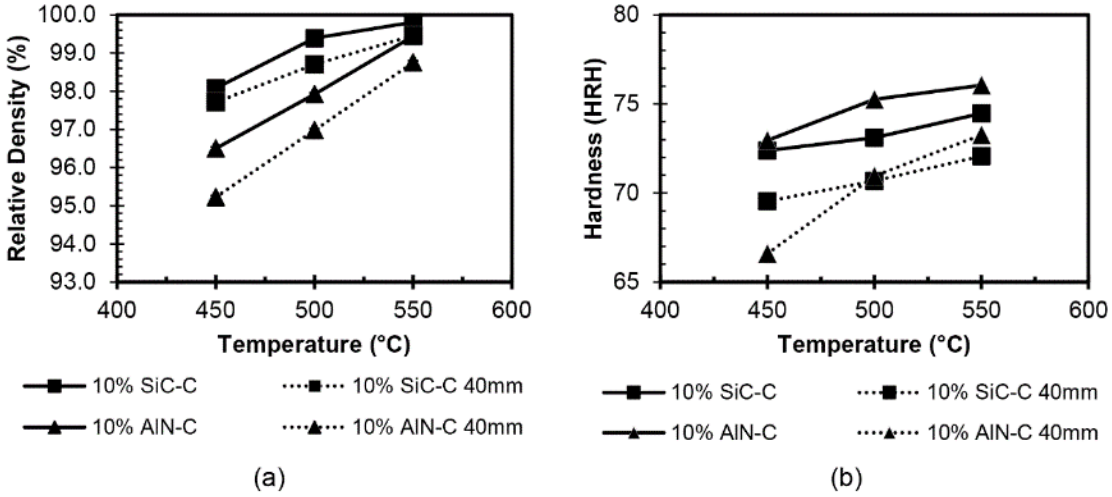

Figure 3-9 Effects of specimen size on the (a) density and (b) hardness of SiC-C and AlN-C reinforced MMCs.

Bend test results for both SiC-C and AlN-C MMC samples sintered at 450°C, 500°C and 550°C are given in Table 3-2. Furthermore, complete curves depicting bending stress and strain behaviour are shown in Figure 3-10. The mechanical behaviour exhibited by SiC-C in these tests was largely representative of the hardness, density and microstructural trends noted earlier. In this sense, the 0.2% offset strength, ultimate bending stress (UBS) and bending ductility were all positively affected by increasing SPS temperatures. The yield strength saw a modest (10 MPa) increase over the temperature ranges observed, coinciding with the mild hardness gain observed in Figure 3-8. These gains were relatively small, as this coarse powder was easily densified at low temperatures, and density gains with increased temperature were minor. However, the

UBS and elongation both showed more dramatic differences with sintering temperature. All SiC-C bend tests showed a continuing work-hardening behaviour until the point of fracture (Figure 3-10a). Thus, the UBS values obtained were all dependant on the level of plastic deformation that the sample could endure. The easily-densified SiC-C powder offered reasonable ceramic-metal bonding to occur at even the lowest temperature of 450°C, prompting a reasonable ductility of 11.8%. Increased sintering temperature promoted a progressive rise in ductility up to a maximum value of 27.3% at the highest temperature considered. This increased temperature allowed metallic aluminum to fill most voids present in the starting compact and thereby improve the net amount of direct physical contact between it and the SiC-C phase. Interestingly, past work on the unmodified matrix material showed that sintering at 450°C was insufficient the break the oxide layer on aluminum particles, and that 500°C was the minimum temperature required in SPS to achieve any appreciable ductility [72]. The ductility improvement with the addition of SiC-C can be attributed to the morphology of these particles. Chawla *et al.* reported the combination of temperature and applied stress during conventional PM processing of aluminum MMC's containing sharp, angular SiC particle results in conditions sufficient to puncture the oxide skin on aluminum [37], allowing for better bonding at lower temperatures. It is postulated that a similar situation existed with the SiC-C MMCs processed via SPS in this study.

Table 3-2 Comparison of the three-point bend properties measured for SPS products. All MMCs reinforced with 10 vol% ceramic.

Ceramic Additive	SPS Temperature (°C)	$\sigma_{0.2}$ (MPa)	σ_{UBS} (MPa)	ε (%)
SiC-C	450	147	266	11.8
	500	149	320	20.9
	550	157	348	27.3
AlN-C	450	141	149	2.9
	500	149	231	7.8
	550	158	321	17.7

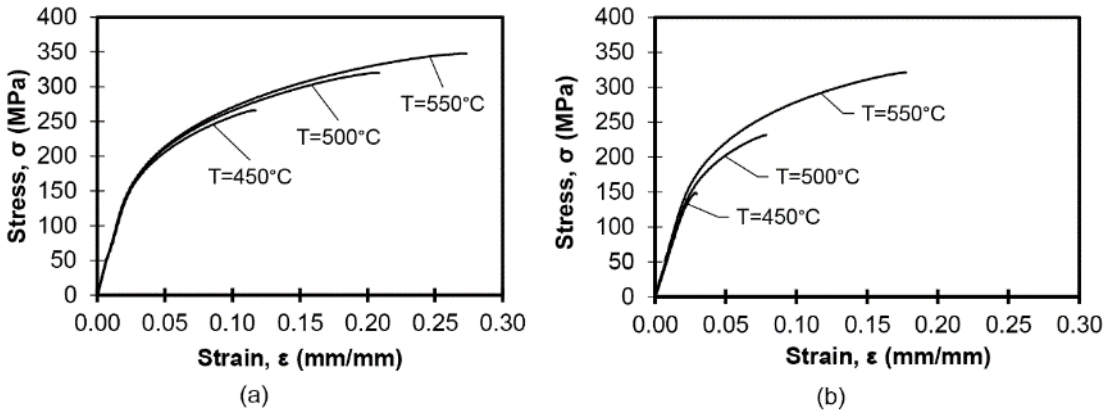

Figure 3-10 Three-point bend stress versus strain curves for MMCs reinforced with 10% (a) SiC-C and (b) AlN-C.

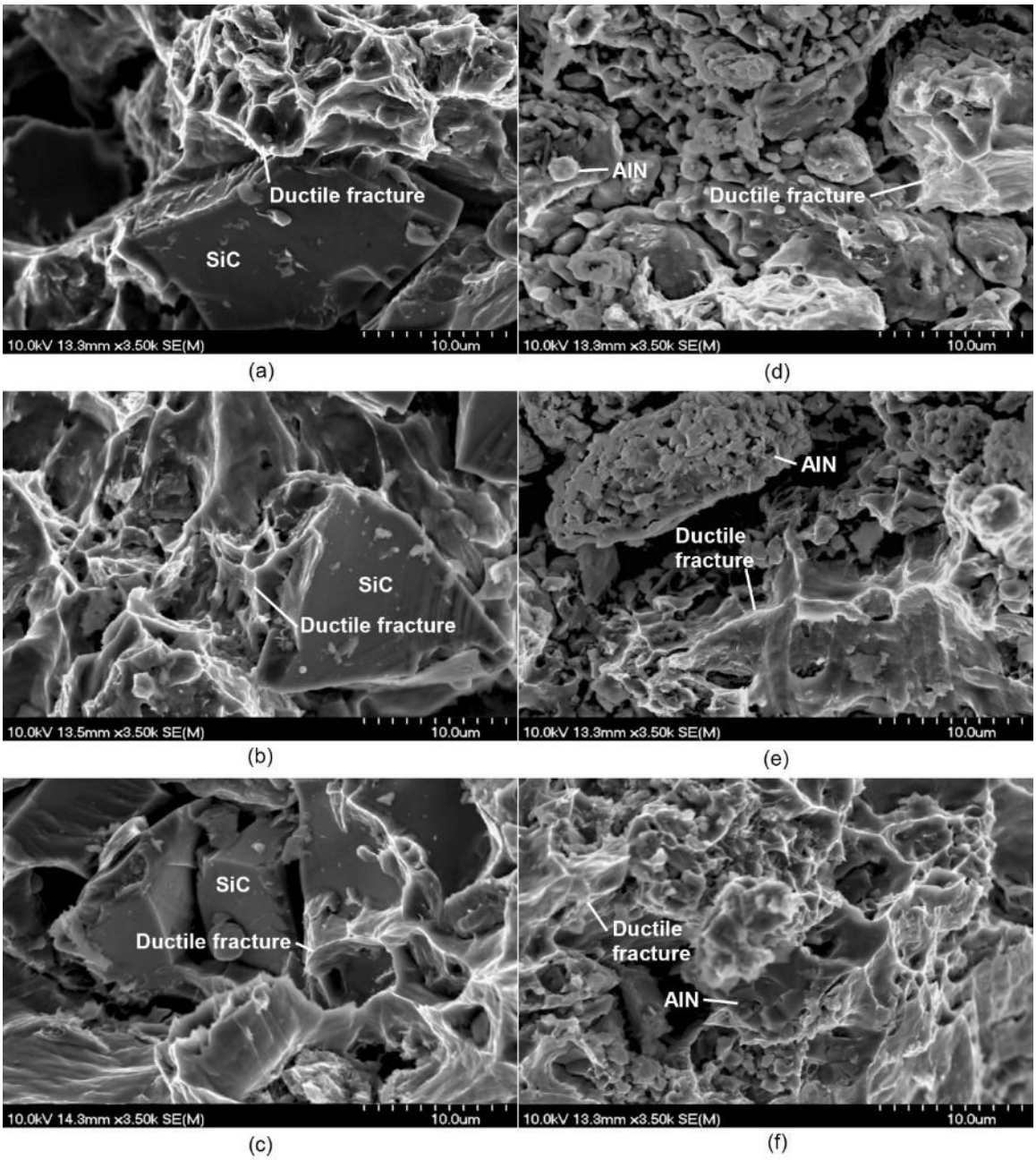

Figure 3-11 SEM micrographs of the fracture surfaces from three-point bend specimens containing 10% ceramic additions and sintered at various temperatures. (a) SiC-C 450°C, (b) SiC-C 500°C, (c) SiC-C 550°C, (d) AlN-C 450°C, (e) AlN-C 500°C, (f) AlN-C 550°C.

The bending behaviour of AlN-C (Table 3-2) highlights the similarities and difference in sinterability between the two different MMC systems. The yield strength was essentially the same as what was recorded in the SiC-C tests. Minor gains in strength were observed with increasing temperature because of the elimination of porosity. Furthermore, large improvements in both UBS and ductility were consistent with the mechanism discussed for SiC-C. However, AlN-C samples exhibit UBS and elongation values significantly below those observed in the rivalling MMC system. Sintering at 450°C was insufficient for this material to establish an acceptable amount of ductility. Even sintering at 500°C was unable to promote ductility to that observed for SiC-C at 450°C. Accordingly, the UBS at these temperatures was inferior to those observed for 450°C SiC-C. Only at 550°C was an appreciable amount of ductility achieved. It is postulated that the more rounded morphology of AlN-C particles did not effectively fracture the oxide skin on aluminum particles as was observed for the highly angular SiC-C. Additionally, the higher concentration of residual porosity (2.2% at 550°C) would have provided a preferred path for crack propagation, thereby providing a secondary mechanism for embrittlement.

Fracture surfaces of AlN-C samples (Figure 3-11d-f) supplement the poor mechanical behaviour reasoning. The fracture surfaces at both 450°C (Figure 3-11d) and 500°C (Figure 3-11e) reveal limited dimpling of the matrix material while metallic bonding of adjacent aluminum particles was inferior to that of the SiC-C systems. The fracture surface of the sample sintered at 550°C (Figure 3-11f) shows a different behaviour altogether. Here, AlN-C particulate were well incorporated in the matrix, which itself

shows considerable dimpling. In contrast to SiC-C fracture surfaces, there was no evidence throughout the microstructure of de-bonding between ceramic and matrix. Accordingly, the role of temperature on the bond strength with AlN-C appeared to be more crucial than what was observed for SiC-C.

3.7 CONCLUSIONS

Aluminum MMCs containing SiC, AlN, Si_3N_4 or BN reinforcing phases were consolidated through SPS. Subsequent observations of density, hardness, microstructure and mechanical properties led to the following conclusions:

- The average particle size and particle size distribution of the ceramic particulate influenced densification. Sources that invoked the formation of clusters of small ceramic particles were the most difficult to densify, while coarser particles with a narrow size distribution favoured full densification.
- The dielectric strength of the ceramic phase also appeared to influence densification. Ceramics with a low value offered an improved response.
- MMC systems strengthened with the addition of SiC-C particulate offered the best response to SPS processing and highest mechanical properties among the array of formulations considered. The average size, narrow particle size distribution, high hardness, and angular morphology of this particulate are all believed to have contributed to this finding.

3.8 Acknowledgements

The authors would like to acknowledge the Auto21 Networks of Centres of Excellence and the Natural Sciences and Engineering Research Council of Canada, (NSERC) for financial support via grant C502-CPM. Dr. Bernhard Mais (Ecka Granules) is acknowledged for the provision of the aluminum powder employed, as are Dr. Jason Milligan and Mr. David Walker of McGill University for their assistance with SPS trials.

CHAPTER 4. POWDER METALLURGICAL PROCESSING OF A 2XXX SERIES ALUMINUM POWDER METALLURGY METAL ALLOY REINFORCED WITH AlN PARTICULATE ADDITIONS

Gregory A. W. Sweet [1], Richard L. Hexemer, Jr. [3], Ian W. Donaldson [4], Alan Taylor [5], and Donald Paul Bishop [2]

1 – Graduate Student, Dalhousie University, Halifax, Nova Scotia, Canada
2 – Professor, Materials Engineering, Dalhousie University, Halifax, Nova Scotia, Canada
3 – Research Engineer, GKN Sinter Metals LLC, Conover, North Carolina, USA
4 – Director of R&D North America, GKN Sinter Metals LLC, Auburn Hills, Michigan, USA
5 – Vice President – Lightweight Technology, GKN Sinter Metals LLC, Auburn Hills, Michigan, USA

Status: Submitted to Materials Science and Engineering: A on January 17, 2019.

Author Contributions: The following experimental procedures, results and discussions were completed by G.A. Sweet. Select material preparation procedures were carried out by R.L. Hexemer. Reviewer and editorial roles were played by all coauthors.

4.1 Forward to Chapter 4

AlN was selected as a suitable ceramic phase to pursue for the entirety of the PhD project. Likewise, the matrix material was selected to be a powder metallurgy 2XXX series aluminum alloy due to its commercial deployment at GKN Sinter Metals. This manuscript investigates the fundamental effects of AlN additions to the matrix and establishes baseline mechanical properties for later comparison to forged properties. All sintering operations were carried out at GKN sinter metals to simulate industrial conditions as closely as possible.

4.2 ABSTRACT

Two AlN powders were admixed with a commercially-relevant press-and-sinter aluminum alloy, differentiated by their mean particle sizes of 3.0 and 12 μm. The effects on powder characteristics and mechanical properties were of primary interest and were compared to nonreinforced compacts. Ceramic additions affected the behaviour of the alloy in the powdered, green and sintered state. AlN additions promoted gains in green strength but negatively affected sinterability in some instances although effects were marginal when coarse or fine AlN powder additions were limited to 5 vol% and 2 vol%, respectively. Decreased densities manifested as marginal decreases in yield strength, UTS and fatigue properties. For a fixed AlN concentration, alloys containing D_{50} =12 um or D_{50} = 3 um AlN exhibited comparable mechanical properties. Above 5%, the coarser particulate maintained a higher sinterability and superior mechanical properties. Dynamic elastic modulus measurements of 73.0 and 74.3 GPa were measured for compacts with 2 and 5 vol% of coarse AlN particulate. AlN additions did not significantly influence the fatigue survival stress.

4.3 INTRODUCTION

Aluminum powder metallurgy (APM) is a component manufacturing technology where low cost, high-quality parts are fabricated from metallic constituent powders. This technology is particularly pertinent to the automotive industry considering the demands for high production rates, near net shape processing, and low part mass. Current societal

trends demand new automobiles that are more fuel efficient. Consequently, decreases in component masses are desirable. Frequently, these are achieved through the substitution of existing materials with low density aluminum-based systems [80]. Despite the adoption of APM to automotive component manufacturing, mechanical and physical limitations of current APM systems have stifled widespread proliferation. Accordingly, the improvement of these properties through a metal matrix composites (MMC) approach has been [81] and continues to be an area of considerable research interest [82,83].

Discontinuously reinforced MMCs involve the incorporation of discrete ceramic particles into a metallic matrix, often via solid-state processing such as APM [63]. Objectively, the material can be selectively tailored to take advantage of the superior physical and mechanical properties of the ceramic phase while maintaining the fabrication characteristics of the metallic component. Examples of mechanical and physical properties that are often manipulated include, but are not limited to: lowering the coefficient of thermal expansion and increasing numerous mechanical properties including elastic modulus, room/elevated temperature tensile properties, hardness, wear resistance, and fatigue performance [82]. MMC's bearing SiC and Al_2O_3 presently dominate commercial automotive applications wherein such materials are exploited [82]. Examples of lesser investigated ceramic phases include AlN, B_4C, TiC, TiB_2, ZrO_2, SiO_2 [83,84]. Mechanically, reported increases in tensile and fatigue properties have been attributed to load transfer to the rigid ceramic phase, thereby minimizing local strain in the matrix phase [85].

Aluminum/AlN MMC's are an area of current research due to the unique physical properties of the ceramic phase. AlN is nonreactive with aluminum, exhibits high hardness, high thermal conductivity and low coefficient of thermal expansion [86]. Strong interfacial bonding with an aluminum matrix allows for promising gains in tensile properties [38]. Additions as low as 5 wt% significantly improve the wear resistance over the monolithic matrix phase [54]. Despite the benefits of this ceramic addition, its effect on the processing and properties of an industrial press-and-sinter APM alloy have yet to be published in detail. Hence, the objective of this work was to investigate the effects of lean, discontinuous AlN additions to a commercial 2xxx series press-and-sinter alloy. Specifically, how these additions effect the stages of commercial processing and the mechanical properties of the sintered product.

4.4 Materials

An aluminum alloy matrix was prepared by blending elemental and master alloy constituent powders. Select attributes of these powders are shown in Table 4-1. These raw materials were blended to a nominal matrix composition (referred to as 'Base' and devoid of admixed ceramic particulate) of 3.0 wt% Cu, 1.5 wt% Mg and 0.5 wt% Sn. Two different grades of AlN powder were considered differing only in particle size distribution. Denoted as coarse (AlN-C) and fine (AlN-F) variants, each source of ceramic reinforcement was admixed with the matrix pre-mix to attain MMC systems with 2, 5 and 10 vol% AlN. Henceforth, blends are addressed by their volume percent and type of ceramic phase (i.e. 5F for 5 vol% AlN-F or 10C for 10 vol% AlN-C). It is also noted

that 1.5 wt% of Licowax C powdered lubricant was admixed to every blend to facilitate die compaction.

Table 4-1 Constituent powders utilized in preparing the various blends of interest.

Powder	Powder Type	Size	Composition (wt%)							
		(D_{50}, µm)	Al	Mg	Si	Cu	Fe	Sn	O	N
Al	Elemental	99	Bal.	*T*	0.02	*T*	0.10	0.03	-	-
Cu	50:50 Al: Cu	16	Bal.	0.01	0.02	46.5	0.05	0.05	-	-
Mg	Elemental	32	0.01	Bal.	0.01	*T*	0.01	*T*	-	-
Sn	Elemental	*12*	*T*	*T*	*T*	*T*	0.01	Bal.	-	-
AlN-C	Ceramic	12	Bal.	-	-	-	0.05	-	1.3	32.0
AlN-F	Ceramic	3	Bal.	-	-	-	0.05	-	1.5	32.0

T = a non-zero trace concentration measured at less than 0.01 wt%.

4.5 Experimental Techniques

Constituent powders were blended for 40 minutes in Nalgene bottles using a Turbula model T2-F mixer. Apparent density was measured using an Arnold Meter according to MPIF standard 48. Flow properties were the calculated rate in grams per second for 25 g of powder to pass through a Carney Apparatus. Blends were compacted into rectangular green compacts (31.7 x 12.7 x 10 mm 'TRS bars' or 76.1 x 12.7 x 12.7 mm 'Charpy bars') at pressures ranging from 100 to 500 MPa. All components used in sintering trials were compacted to approximately 2.50 g/cc. An Instron model 5594-200HVL 1 MN load

frame coupled with floating die tool sets were used for this. Sintering was carried out in an industrial mesh belt furnace for commercial production of APM components. The thermal profile included a 10-minute hold at 400°C for delubrication followed by sintering at 600°C for 15 minutes. Throughout, the atmosphere was flowing nitrogen with a dew point between -55°C and -60°C and an oxygen concentration no greater than 5 ppm. All samples were subject to a T6 heat treatment process (solutionized at 510°C for 2 hours, water quenched, artificially aged at 190°C for 10 hours) prior to any necessary machining operations. Green and sintered densities were performed in accordance with MPIF Standard 42 using the dry approach. All density values are reported as a percentage of the theoretical maximum, which was calculated for each distinct alloy.

Green strength was quantified with TRS specimens using a three-point bend approach outlined in MPIF Standard 15. Modulus values were obtained through an impulse excitation technique using machined specimens (70.0 x 12.0 x 3.00 mm) according to the NPL Measurement Good Practice Guide No. 98 [87]. Tensile tests were carried out according to MPIF standard 10 using machined round specimens. Tests were carried out on the same frame used in compaction, but when equipped with a 50 kN load cell and an Epsilon 3542 extensometer that remained attached to fracture. Fatigue tests were carried out on an Instron model 1332 servo-hydraulic load frame set up for three-point bending. The staircase statistical fatigue approach described in MPIF standard 56 was adapted to three-point bend tests. Room temperature tests were carried out in a non-humidity-controlled environment using a runout criterion of 10^6 cycles and an R-ratio of 0.1. Error bars in fatigue measurements represent the 10 and 90% survival stresses (i.e. 50%

confidence that 10% or 90% of samples will pass at 10^6 cycles) based on at least 11 unique tested specimen and calculated according to the standard practices, whereas error bars elsewhere represent a single standard deviation about the mean. To test the statistical significance a threshold value of $\alpha = 5\%$ was employed throughout, except for $\alpha = 10\%$ in tabulating the 10% and 90% survival stresses of fatigue data per MPIF Standard 56.

Metallographic examination of samples was performed using either an Olympus model BX51 light optical microscope or a Hitachi model S-4700 cold field scanning electron microscope. Cross sections were prepared by hot mounting in conductive thermosetting plastic and polishing with conventional SiC or diamond grinding media and concluding with colloidal silica polishing compound. Tensile and fatigue fracture surface stubs were prepared for SEM imaging. Electron micrographs were imaged using an accelerating voltage range of 5-15 kV and an emission current range of 10 – 20 μa. EDS maps were acquired using an Oxford Instruments X-Max 80 mm^2 EDS detector; map data were superimposed on corresponding electron micrographs.

4.6 Results and Discussion

Characterization of an APM system encompasses powder attributes, compaction response, sintering response as well as final mechanical properties. Research was completed in all these areas using the material formulations of interest.

4.6.1 Powder Attributes

The fundamental powder attributes of Apparent Density (AD) and flow are crucial to the design of a PM die compaction process. Flow behaviour is intimately related to the powder morphology and friction conditions. The effects of admixed AlN particles on this attribute are presented in Table 4-2. Ceramic additions appeared to negatively affect the flow behaviour, aside from 2C, which was essentially unaffected by its respective ceramic constituent. Otherwise, the flow behaviour was observed to be significantly lower than that of the base blend. Above threshold concentrations, flow behaviour degraded to a non-free flowing state. The coarser AlN-C ceramic at concentrations up to 5% remained free flowing, while up to only 2% AlN-F additions flowed spontaneously.

Table 4-2 Effects of AlN-C and AlN-F on flow.

Ceramic	**Flow (g/s ± stdev)**		
(%, vol)	**Base**	**AlN-C**	**AlN-F**
0	2.4 ± 0.3	-	-
2	-	2.7 ± 0.2	1.6 ± 0.4
5	-	1.7 ± 0.3	NF
10	-	NF	NF

NF = No Flow; powder failed to flow freely through the Carney apparatus.

Variation in AD (Figure 4-1) showed that the magnitude of change in this attribute through additions of ceramic particles was minimal. The breadth of values was limited to within 1.0% of that measured for the base powder devoid of AlN. Additions up to 5% ceramic phase exhibited marginal changes. Despite this, the two ceramic particulate types

were opposite in their effect. Type AlN-C ceramic additions exhibited an increase in AD while AlN-F trended negatively.

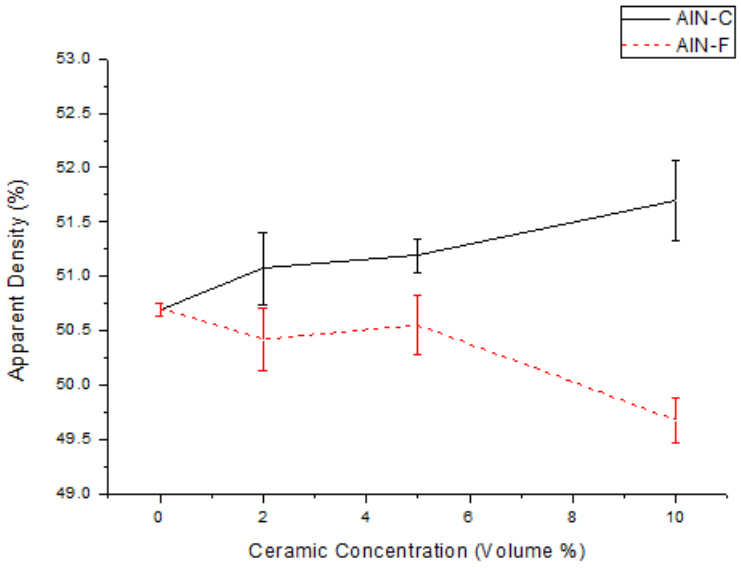

Figure 4-1 AD data for the powder mixtures considered.

4.6.2 Compaction Response

The compressibility and green strength of a blend are also critical to the successful die compaction of a powder system into a complex geometry. Reduced compressibility increases the required press capacity and internal density gradients. The compressibility of the base powder and its modifications through AlN particulate additions is illustrated through the data shown in Figure 4-2.

At any given compaction pressure, a loss in compressibility was observed through admixed AlN additions. At compaction pressures of 200 MPa and lower, the difference in

the trends between AlN-C and AlN-F was determined to be insignificant. At 300 MPa on the other hand, the difference of slope in the regression between AlN-C and AlN-F was significant (p-value = 0.005). AlN-C was less detrimental to green density. Practically, the divergent behaviour of the two ceramic additions is only substantial at 10%.

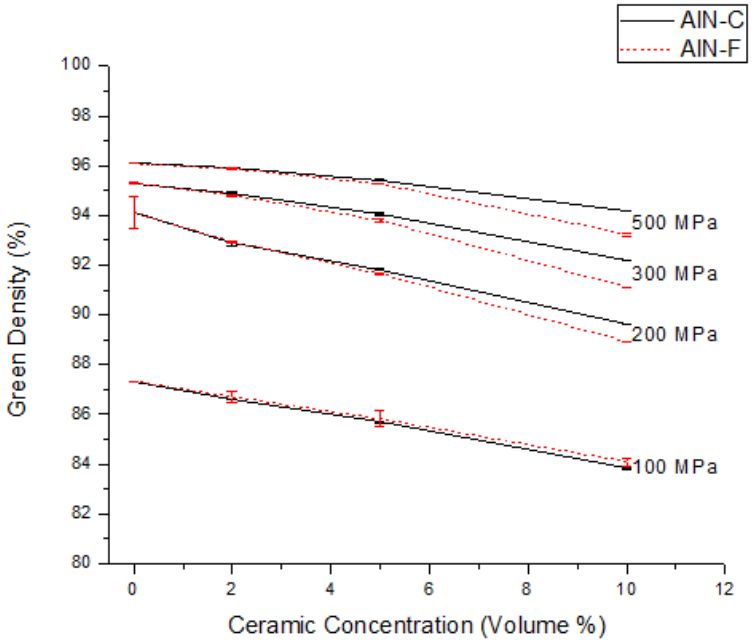

Figure 4-2 Green densities of MMC compacts as a function of compaction pressure and ceramic content.

Increases in the transverse rupture strength of green compacts, known as green strength (GS), were observed to be an effect of compaction pressure, ceramic content and, to a lesser extent, ceramic type. Figure 4-3 shows this. A significant and positive linear regression of GS as a function of ceramic content up to a concentration ≤ 5% was observed. Pressed at 100 MPa, the GS of the base alloy was 2.8 MPa. The utilization of 2% AlN-C increased this to 4.0, and at 5% ceramic up to 4.7 MPa. Higher compaction

pressures wholly increased GS, and the positive effect of ceramic was retained at all pressures. At 500 MPa, the Base alloy was not significantly stronger than at 300 MPa. With as little as 2% AlN-C or AlN-F, increasing the compaction pressure to 500 MPa was found to impart significant gains in GS.

Consideration of the AlN grade shows a weak affect on green strength. At all compaction pressures, and ceramic concentration of 5% or less, the difference in the mean green strength was minimal. Furthermore, despite the apparent difference in green strength at 10% ceramic at either 200 MPa or 300 MPa, this behaviour was not statistically significant; more samples would be required to prove the significance.

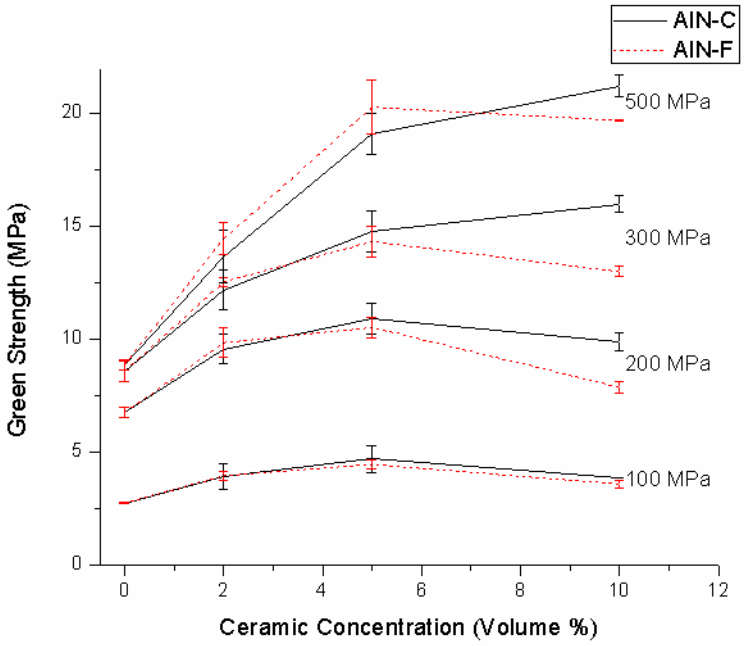

Figure 4-3 Green strength of MMC compacts as a function of compaction pressure and ceramic content.

4.6.3 Sintering Response

Densification through sintering relates to the development of mechanical properties. The density of the sintered compact, measured as a percentage of the maximum theoretical value, remains one of the key means of determining the sinter quality. Figure 4-4 plots the sintered density trends of alloys as a function of ceramic content, as well as how sintering is influenced by the type of AlN. A singular green density of 2.5 g/cc was targeted prior to sintering, consistent with industrial processing.

Without any ceramic phase, the sintered density was determined to be near-full theoretical (99.53%). However, minor additions of AlN proved to significantly and detrimentally influence densification. 2C sintered to a mean final density of 99.24% while 2F was sintered to 99.10%. At this concentration, the difference between these two ceramics was not statistically significant. However, at 5%, the difference in ceramic became significant. 5C sintered to an acceptable density of 98.48%, while the sinter quality of 5F was significantly compromised at 95.29%. At 10%, both types of ceramic showed losses that were more pronounced.

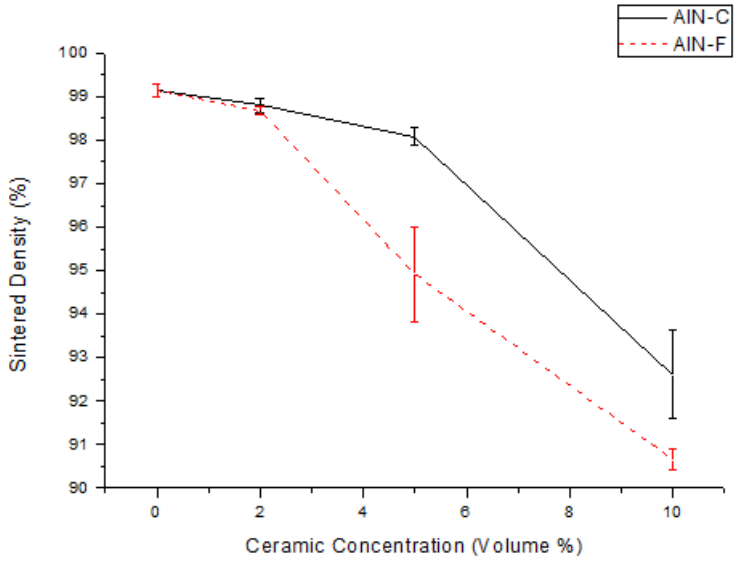

Figure 4-4 Relative theoretical density of sintered compacts as a function of ceramic content and type.

To understand the dampened sinterability of the alloy through increasing ceramic contents, optical micrographs of uncompromised materials, Figure 4-5, were compared to those with significantly diminished sintering response, Figure 4-6. Without any ceramic addition, the Base system (Figure 4-5a) exhibits a microstructure consistent with an aluminum PM alloy with a high sinter quality. There are relatively few pores, and remaining porosity is generally rounded. Prior particle boundaries are largely unnoticeable. With the addition of 2% AlN-C (Figure 4-5b) the microstructure is largely similar. Pores are similar in number and morphology. AlN particles resided along prior particle boundaries and were generally well incorporated within the matrix. There was limited porosity directly associated with ceramic particles. Given the relatively coarse and limited number of ceramic particles in this alloy, prior particle boundaries were largely free of any ceramic particles that would impede densification. The microstructure

of 2F (Figure 4-5c) was consistent with the high sintered density. Fine, rounded pores persisted along prior particle boundaries. For the most part, ceramic particles were well-incorporated with the matrix. However, some ceramic particles lay on the surface of internal pores.

Exemplary micrographs of MMCs containing ≥ 5% AlN (Figure 4-6) illustrate the result of heightened ceramic concentration. In the case of the 5C composite (Figure 4-6a), more prior particle boundaries were now lined with ceramic particles, although adjacent particles were largely uninhibited from direct contact. Specifically, coarse AlN particulate were well-incorporated with the matrix and were not associated with porosity. The finer particles in this ceramic type however exhibited an association with pores. Such phenomenon was exasperated in the microstructure of 5F (Figure 4-6b). As the relative number of fine particles was now significantly higher, prior particle boundaries in this alloy were now lined to a greater extent; approaching that of a continuous structure. Pores associated with fine AlN clusters were also more prevalent. In the most extreme case, the microstructure of 10F (Figure 4-6c) exhibited a continuous network of fine AlN particulate that essentially encapsulates all prior particles. Intuitively, decreasing the matrix powder particle size would improve the homogeneity of the ceramic phase during blending. However, this route is undesirable as the coarser nature of the matrix powder facilitates enhanced compressibility/sintering/safety characteristics and was more economical.

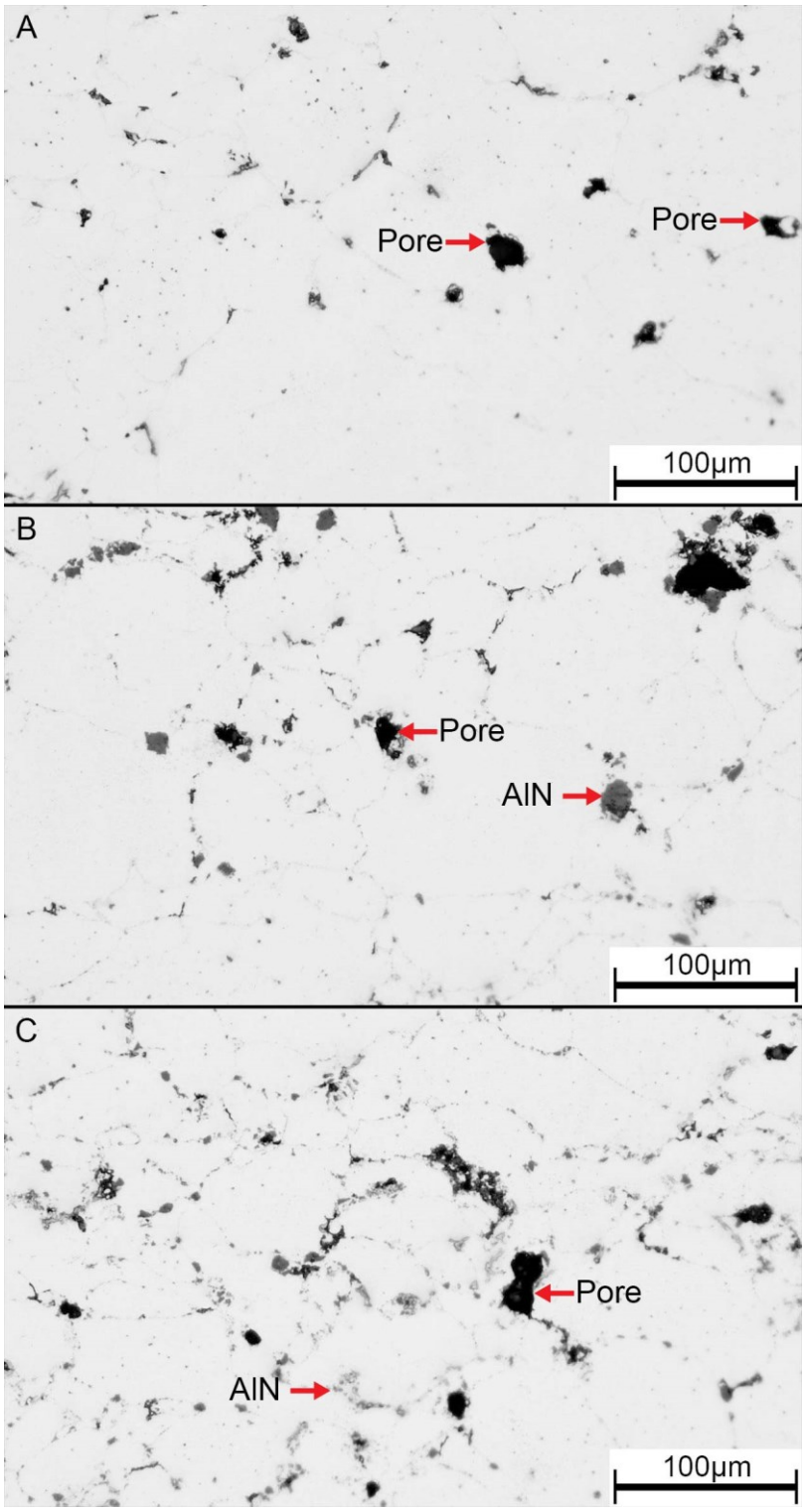

Figure 4-5 Optical micrographs of (a) the MMC Matrix material 'Base', (b) 2C, and (c) 2F which all sintered to high relative densities.

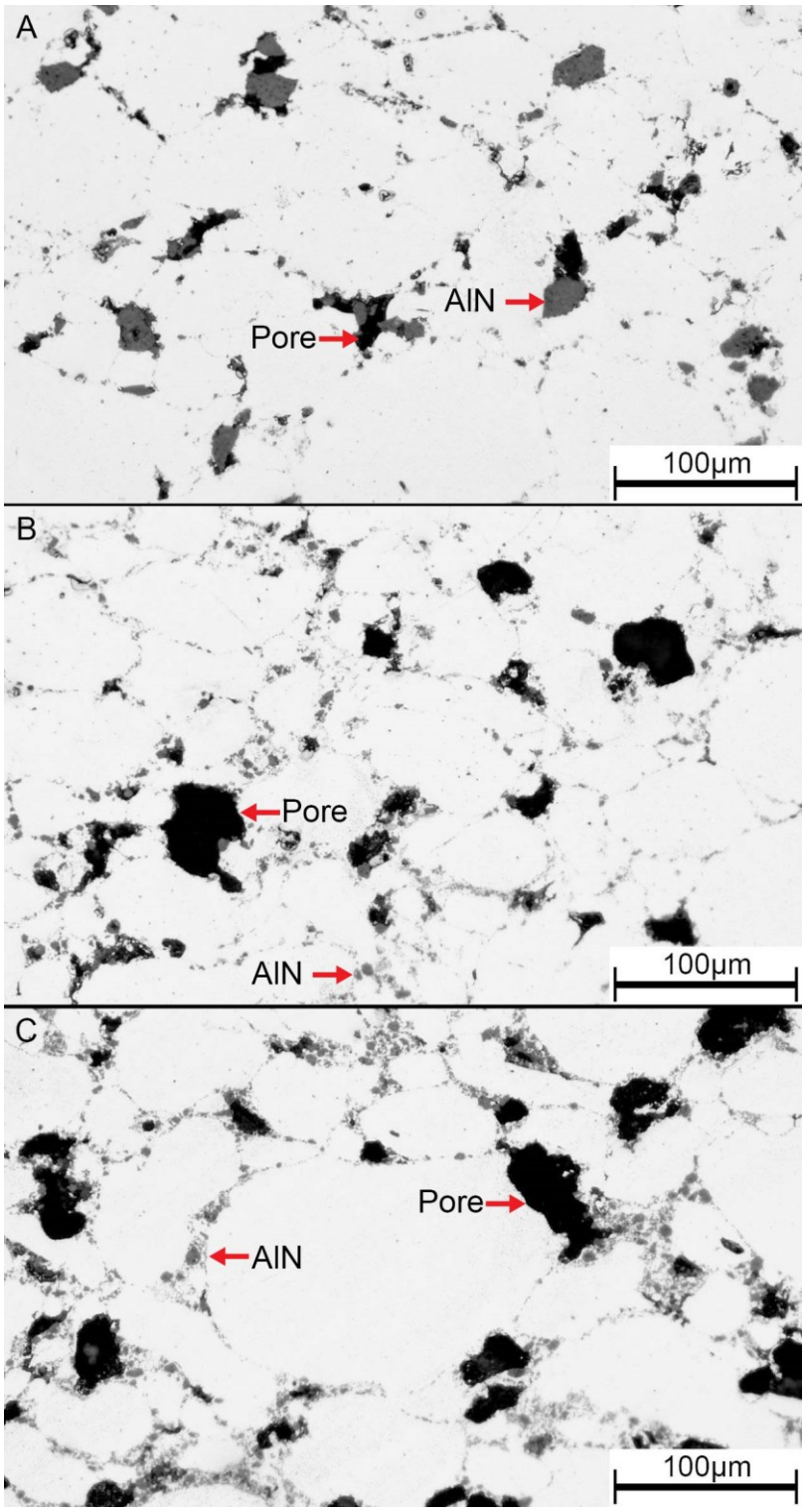

Figure 4-6 Optical micrographs of MMC systems (a) 5C, (b) 5F, and (c) 10F.

4.6.4 Mechanical Properties

Mechanical properties were captured through impulse excitation tests, uniaxial tension, and three-point bending fatigue. Such tests were limited to MMCs containing ≤ 5% AlN as the weak sintering behaviour exhibited by mixtures with higher concentrations ensured inadequate mechanical integrity. Statistically relevant changes in these attributes were observed through modification of the ceramic concentration. Dynamic elastic modulus measurement of ceramic-bearing materials, Figure 4-7, proved to surpass those of the matrix alloy (71.9 GPa). With increasing AlN-C additions, a significant positive linear relationship was observed with both 2 and 5% additions. Conversely, the modulus of AlN-F alloys showed a mixed response. Here, 2F was higher than the matrix alloy, at 72.7 GPa, while 5F exhibited a unique deviation from the trend declining to 67.8 GPa to invoke a significant loss in modulus relative to the base system.

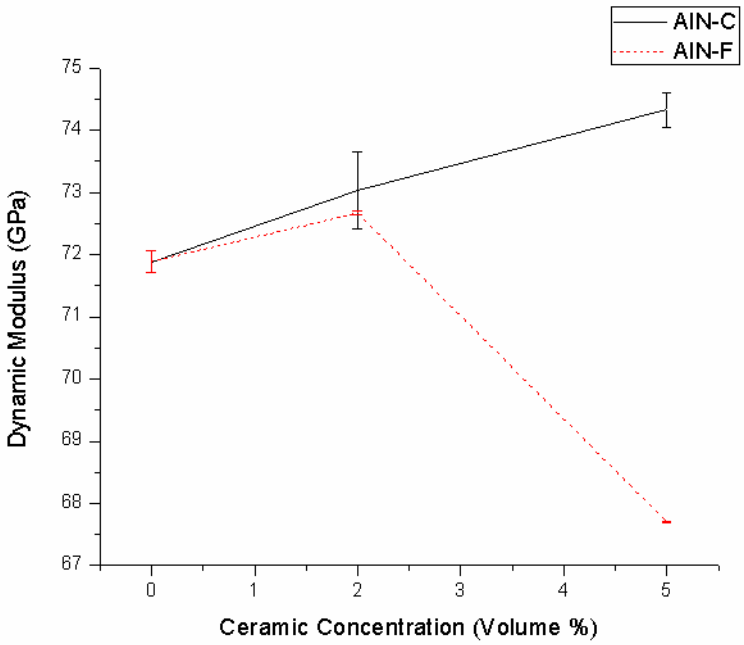

Figure 4-7 Dynamic elastic moduli of MMC materials as measured through impulse excitation.

Tensile data are shown in Figure 4-8. Ductility measurements, Figure 4-8a, trended significantly negative with additions of AlN. The mean ductility of the base alloy, 5.0%, was nearly double that of 2C (2.7%) or 2F (2.6%). Further losses in ductility were observed with additions of either ceramic at 5% although the decline was marginal. Differences between the two ceramic types were insignificant here. Exemplary electron micrographs of the fracture surfaces of Base, 2C and 2F are shown in Figure 4-9a, b and c, respectively. The largely cleaved surface of these particles suggests that a predominately brittle fracture transpired. However, the moderate ductility of this material was backed up with the observation of select surfaces exhibiting microvoid coalescence. Interestingly, the standard deviation in ductility of the base material (1.7%) significantly exceeded all other materials tested (2F exhibits the next highest at 1.0%). The base

material exhibited evidence of residual porosity on the fracture surface, as noted by the blue arrow in Figure 4-9. The fracture surface of a 2C specimen exhibited coarse, fractured AlN particles (red arrow(s)). No occurrences of ceramic-matrix decohesion were observed. 2F similarly exhibits AlN particles on its fracture surface, although fracturing of individual particles was not noted. An EDS map of nitrogen (red) superimposed on the fracture surface of 2F. AlN was present as somewhat dense clusters (yellow arrow) or more dispersed bands (green arrows). Furthermore, regions largely devoid of AlN concentrations were observed.

Yield strength was not statistically different for 2C or 2F alloys versus the base alloy. However, the trend observed with additions of either ceramic again indicated a negative influence of the reinforcing particulate. Unlike the trends observed in ductility measurements, the yield strength of AlN-C reinforced alloys was significantly better than the equivalent AlN-F alloys. The UTS followed similar trends as the yield properties. AlN-C bearing alloys exhibited lower strengths than the equivalent AlN-F alloys, while an overall downwards trend was observed through the addition of either.

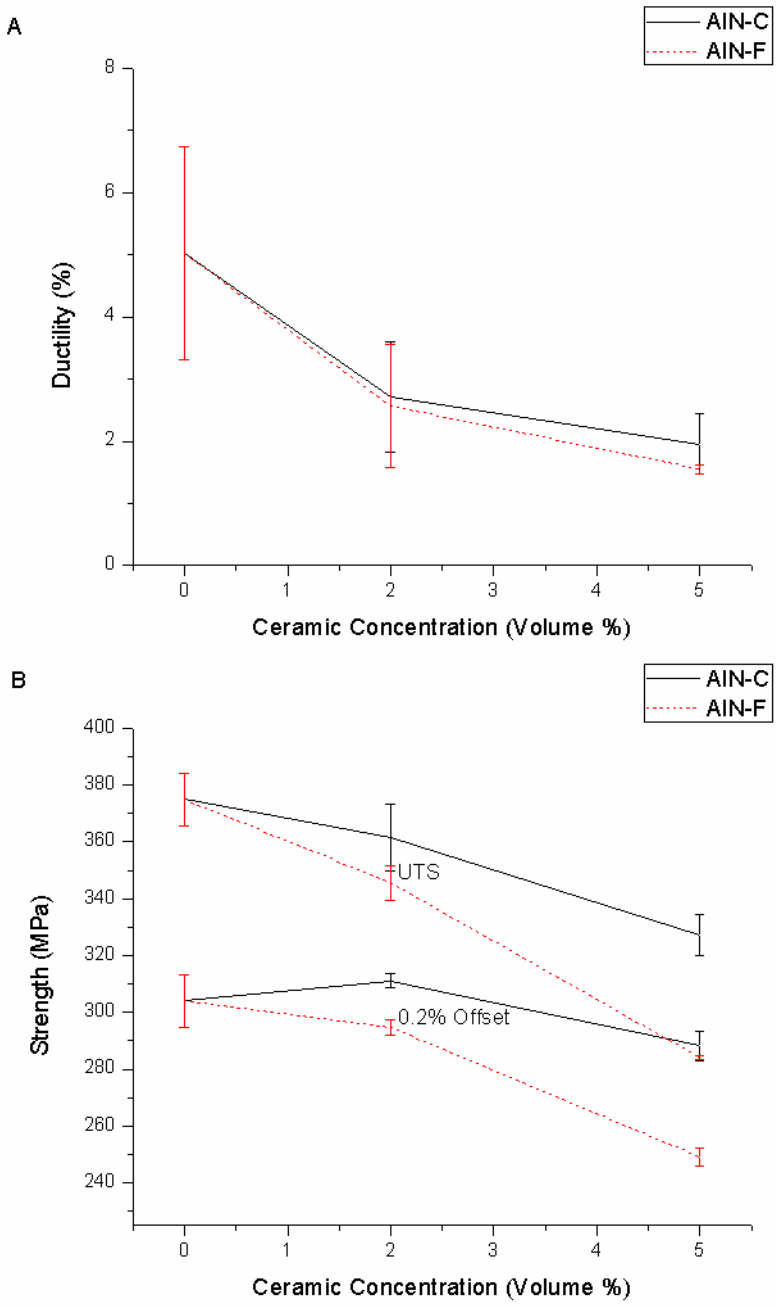

Figure 4-8 Tensile properties of MMC material as a function of composition. All samples heat treated to the T6 state.

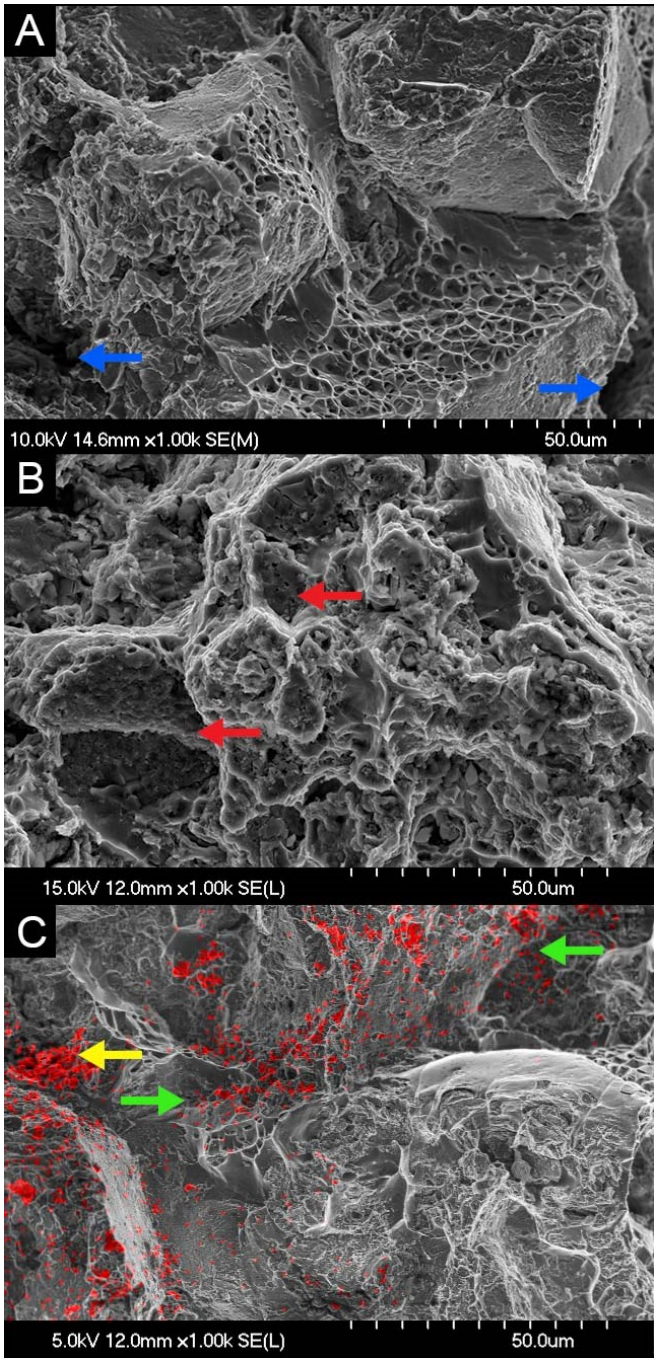

Figure 4-9 Tensile fracture surfaces of the (a) Base, (b) 2C and (c) 2F materials. Arrows highlight residual porosity (blue), fractured AlN particles (red), dense clusters of AlN particulate (yellow) and more dispersed bands of AlN (green). An EDS map of nitrogen (red points) is superimposed showing the location of AlN particulate.

The fatigue performance of select MMC materials is shown in Table 4-3. The difference in the mean endurance limit (50% survival) was subtle. Incorporation of 2 vol% additions of either ceramic caused losses. AlN-F proved to be marginally better than its coarser counterpart.

Table 4-3 Three-point bend fatigue endurance limits of select compositions

Composition	Fatigue Strength (MPa)		
	$\sigma_{a,10}$	$\sigma_{a,50}$	$\sigma_{a,90}$
Base	247.6	204.5	161.4
2C	178.8	171.5	164.2
2F	188.8	181.5	174.2

Optical metallography was used to observe the fatigue crack propagation behaviour of the tested material systems. Exemplary cracks are shown in Figure 4-10. Crack paths for all material systems were transgranular and relatively planar. Small local slip band cracks were observed for all materials consistent with their prior particle size. Occasional observations of residual porosity were noted along the crack paths of all materials, approximately proportionate to the amount of residual porosity in the bulk specimen. 2C exhibited fractured coarse AlN particulate along the crack path and no evidence of AlN-matrix debonding. The micrograph for 2C uniquely exhibited two simultaneous but converging crack paths. Such behaviour is not uncommon for all compositions when testing via this method. The finer ceramic content in 2F was not readily resolvable and differentiating between particle fracture and debonding was inconclusive.

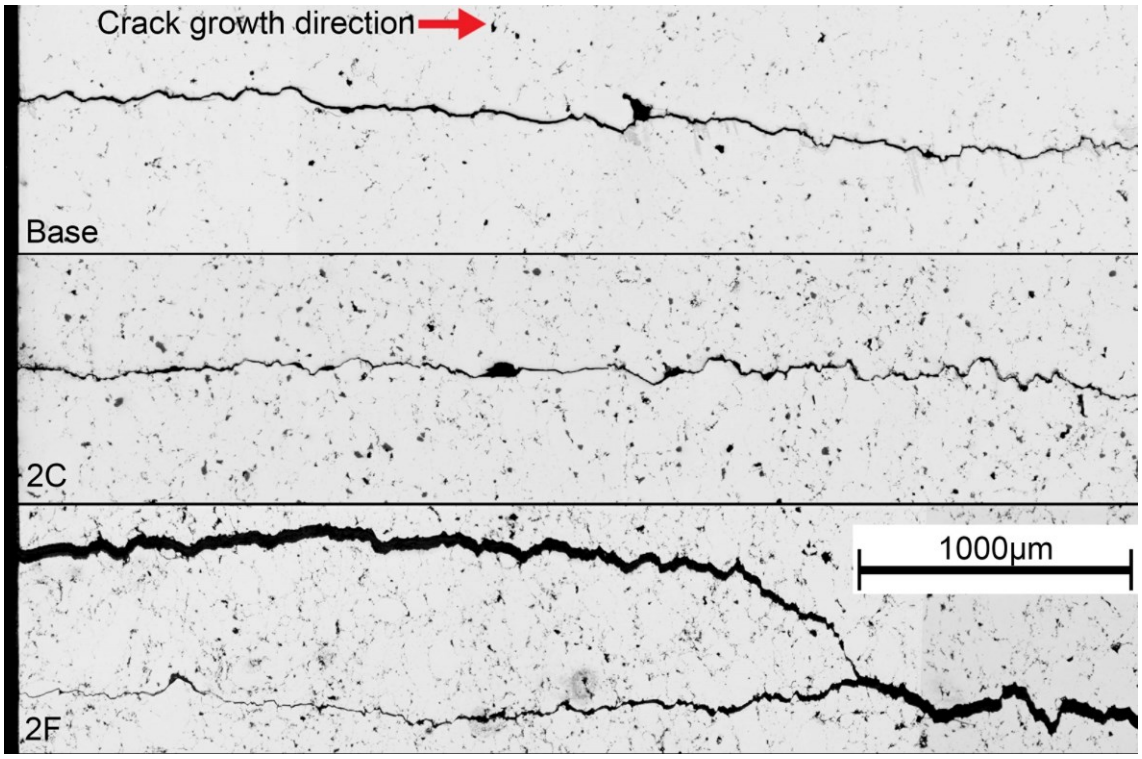

Figure 4-10 Crack path morphology for a long fatigue crack growth for the base and MMC materials. Sections were taken perpendicular to the crack surface near the initiation site. Crack growth direction from left to right.

Scanning electron micrographs of the fatigue fracture surface for 3 materials systems are shown in Figure 4-11. The crack initiation sites were oriented to be at the top-center of each micrograph, with crack growth downwards. Several varieties of crack growth appear, with bands apparently oriented orthogonally to the crack growth direction. These predominantly include irregularly spaced step-like and 'cross-hatched' morphologies. Minor changes in band orientation were observed across adjacent grains. Evidence of crack growth through fine residual porosity was evident in all micrographs. Pore size ranged from several microns to tens of microns, consistent with the fine porosity present in well-sintered specimens observed in Figure 4-5. Furthermore, complex unidentified

secondary phases (relatively dark phases, approximately 10um diameter) were cleaved along the crack path. Crack initiation sites were variable from sample to sample, but primarily were observed to be surface connected and near-surface porosity. Other initiation sites included intermetallic phases and clusters of fine ceramic particles.

The fatigue fractograph of 2C showed fractured coarse AlN particles proportionate to the volume perfect of ceramic added to the system. Observed AlN particles mostly fell in the 10-50 um particle size range. Finer particles were less apparent, although this may be an artifact of the resolvable detail in the micrograph. Porosity in 2C was mostly small and rounded. In general, the fractography of 2C was largely comparable to that of the Base, albeit with a slight increase in fine rounded porosity. AlN particulate on the crack surface was not readily identifiable, though AlN on the surface of fractures pores was observed. Fractography of 2F was comparable, although the fine AlN particulate that was incorporated into the matrix was not observed on the fracture surface. Unique directions of fatigue crack striations between pores suggested crack propagation from one pore to the next.

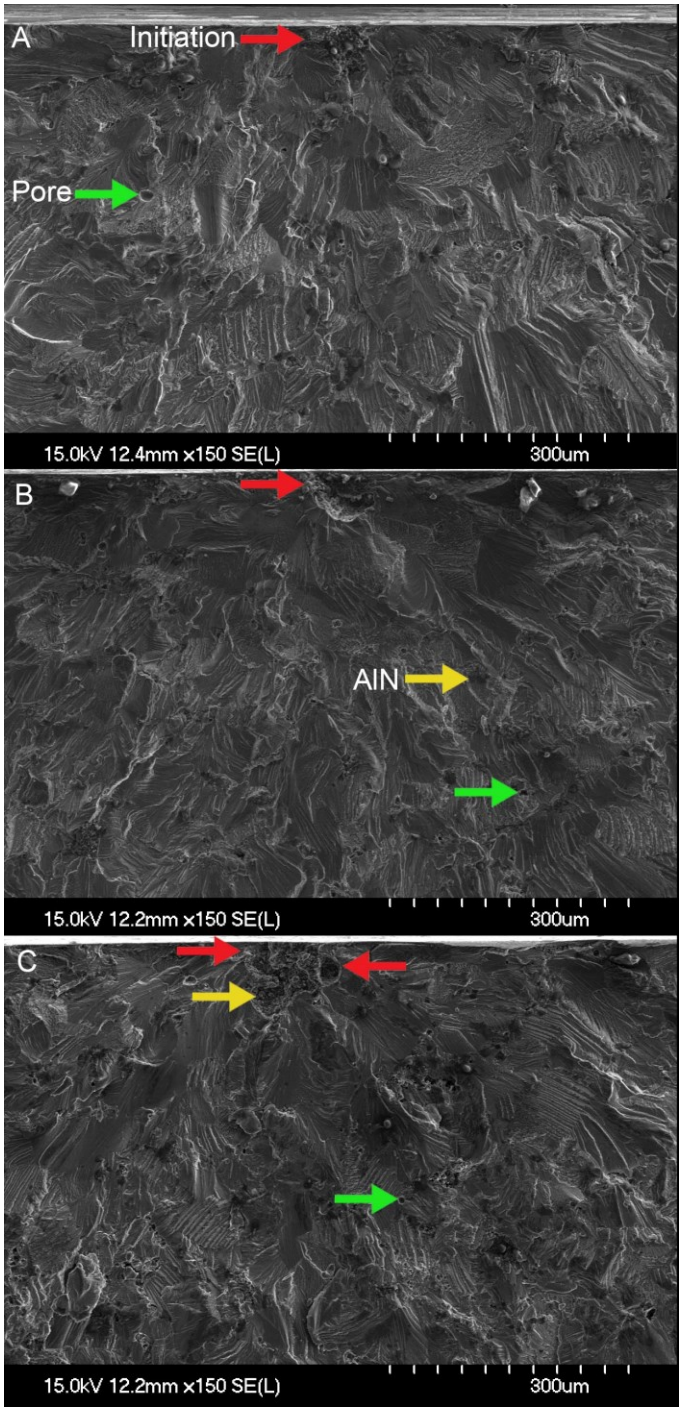

Figure 4-11 Scanning electron micrographs of the fracture surfaces of (A) Base, (B) 2C, (C) 2F. Fatigue crack growth is from the top of the image downwards, with the crack initiation site centered in the fractograph (red arrows). Examples of pores (green arrows) and AlN particulate (yellow arrows) are denoted.

4.7 Discussion

4.7.1 Ceramic Effects on Processing

Powder flow rates indicate the interparticle friction (IPF) conditions of a powder blend. The insignificant difference between Base and 2C materials suggested that the Base blend does not undergo an increase in IPF. However, further additions of AlN-C were enough to increase IPF, decreasing flow significantly. This effect is attributed to a negative change of surface area and surface roughness from the AlN phase. Accordingly, the inferior flow performance (and consequently higher IPF) of AlN-F systems was attributed to the higher surface area to volume ratio of this finer powder. The powder packing efficiency similarly suffered from increased IPF due to limited powder sliding under gravity. AlN-F blends showed this detrimental effect in the AD data. AD values in Figure 4-1 are plotted as a percent of their theoretical potential, excluding the effect of the difference of AlN and metallic phases. The trended increase in AD for AlN-C blends opposed the increased IPF conditions concluded above. This trend is evidence of the phenomenon of increased particle packing through a bimodal mixture of coarse and fine powders. The ratio of the mean particle size of Al to AlN-C approaches the 7:1 particle size ratio needed to optimize this effect [1]. Effectively, fine AlN particulate situated itself in the triangular vacancies between Al particles. The Al: AlN-F size ratio deviated more from this ideal ratio while IPF effects simultaneously overshadowed any benefits.

Decreased compressibility with increasing AlN content followed the IPF effects. Rising IPF restricted particle sliding, inhibiting the rearrangement phase of compaction. Again, AlN-C was the superior ceramic particulate due to the better IPF conditions that prevailed. Additionally, hard AlN particles were inherently more resistant towards deformation than the metallic base material. Decreased compressibility with increased volume fraction of ceramic was consistent with a rule of mixtures approach. The bulk of green density was achieved at pressures up to 200 MPa, typical of APM. Further marginal gains in green density were observed of all systems up to 500 MPa. However, such gains did not necessarily translate into a stronger compact.

Without AlN, the green strength (GS) developed rapidly at low pressures, from 2.8 to 8.6 MPa (100 to 300 MPa, respectively). GS was effectively limited though, as a compaction pressure of 500 MPa only provided 8.9 MPa. AlN particulate additions invariably promoted the green strength of the material system. Additionally, AlN extended the effectiveness of compaction pressures over 300 MPa to strengthen green parts. Mechanical interlocking and smearing of adjacent particles during compaction provided strength to the compact. Relatively fine and hard AlN particulate likely stimulated localized plastic deformation of metallic constituents, enhancing mechanical interlocking. This new mechanism benefitted from increased compaction pressures by allowing additional plastic deformation around ceramic particles. Increasing the ceramic content up to 5% consistently increased GS. Further changes in green strength with 10% ceramic content were mixed, likely due to frictional effects, as well as saturation of interparticle boundaries with the ceramic phase. The sintered compact of 10F, shown in Figure 4-6c,

showed considerable clustering of fine AlN particulate at prior particle boundaries (PPB), particularly those of three or more prior particles. Such clustering in the green state were expected to negatively contribute to the green strength.

4.7.2 Ceramic Effect on Sintered Properties

From a sinter density perspective, both types of ceramic phase had an acceptable range in which they were introduced without substantial losses in sinter quality. Given that all materials were pressed to the same green density, the sintered density was representative of the effect of the ceramic phase on sintering mechanisms. 2% AlN-F and 5% AlN-C appeared to be reasonable maximums of both ceramic types amongst the actual values evaluated. The physical manifestation of the decreased density in the 5C system were pores associated with fine AlN particles, observed as a black phase in Figure 4-5 and Figure 4-6. Given that this matrix system relied on liquid phase sintering mechanisms for densification, it was apparent that liquid infiltration into these fine AlN clusters was impeded. The authors had observed this encapsulated porosity phenomenon previously in solid state sintering of various aluminum MMC's [84]. In that study, finer ceramic particulate worsened the effect.

Mechanical property changes with ceramic addition were explained by the sintered density trends. Dynamic elastic modulus measurements generally showed a positive trend with ceramic content, as expected from a rule of mixtures approach. Sintering of alloys containing up to 5% AlN-C and 2% AlN-F proved to be enough to incorporate the

ceramic phase as a beneficial addition in this context. Incidentally, these samples sintered to a relatively high density of 98.3% or greater. Modulus benefits of this stiff secondary phase addition overshadowed any detrimental effect of decreased density. 5F did not follow the anticipated rule of mixtures approach as this ceramic addition affected the modulus in a manner inconsistent to all other measurements. It was postulated that the relatively inferior sintered density (95.2 ± 1.1%) was sufficiently low to offset any positive effect from the ceramic addition in this instance.

0.2% offset yield stress was acutely sensitive to the sintered density. No significant gain in yield stress were recorded for any MMC material relative to the Base system. Hence, the potential gains anticipated through load transfer to stiffer ceramic particles were not seen, as it was overshadowed by the losses instilled through higher levels of residual porosity. The coarser ceramic particulate was more homogenously incorporated within the matrix, minimizing the occurrence of ceramic clusters and associated porosity. Without adequate incorporation into the matrix, a ceramic particle was unable to bear a significant portion of the applied stress. The losses of UTS were observed to be more aggressive than those of the yield strength; likely a result of the compromised ductility coupled with the weakened microstructure.

Ductility measurements indicated there was no significant differences between the two ceramic types, despite the physical and mechanical differences to this point. Both AlN types were found to diminish ductility at concentrations as low as 2%. This is consistent with comparable 2000 series aluminum MMC's in literature [47]. Tensile fractography

(Figure 4-9b) indicated that the AlN-C phase was incorporated well within the matrix; fractured coarse AlN particles (red arrows) were observed and no debonding was noted. This suggests these particles were load bearing, as it is not uncommon in Al-MMC's for localized deformation of the soft matrix around hard ceramic particles to cause particle decohesion and damage initiation sites [21]. AlN-F particles (Figure 4-9c) showed several different distributions. Dispersed bands of AlN on the right of the fractograph as well as the bottom left (red arrows) suggested AlN incorporated with the matrix along prior particle boundaries. The region on the left-middle of the fractograph (yellow arrow) was densely populated with AlN particulate and porosity. This complex clustered AlN and pore region was consistent with the largest pores shown in Figure 4-5(c). Clusters of loosely bonded AlN particles would have contributed minimally to the load bearing capacity of the bulk part, and would likely have promoted brittle behaviour in adjacent areas due to increases in local stresses [88].

Fatigue properties of Al-MMC's did not deteriorate to any significant degree through the addition of either ceramic particulate. Literature suggests ceramic additions are effective for enhancing the fatigue strength of aluminum, particularly with smaller particle size, narrower PSD and smaller interparticle spacing [85]. AlN additions did not follow this trend. The propensity for this phase to cluster and inhibit matrix penetration abated any load carrying benefits. Entrained porosity appears along fatigue crack paths (Figure 4-10) and fracture surfaces (Figure 4-11), suggesting these pores negatively affect crack growth. Fatigue initiation sites observed in Figure 4-11 routinely display surface-connected or near-surface porosity, typical of 2000 series press and sinter aluminum alloy

[89]. Improvements in fatigue properties are only observed when ceramic particles are sufficiently well incorporated with the matrix, to eliminate residual porosity and ceramic clustering. Otherwise, any load bearing capacity of AlN is overshadowed by these negative microstructural defects.

4.8 Conclusions

This study investigated the effects of additions of AlN particles to a 2000 series APM alloy. The powder characteristics, green properties as well as mechanical properties of the aluminum alloy in question were influenced by admixed AlN additions. The effects can be summarized as follows:

- AlN additions increase the interparticle friction of a powder blend. This interparticle friction manifests itself as a reduction in flow, apparent density and green density. However, AlN additions of both particle size enhanced mechanical interlocking of compressed powders, significantly increasing green strength. Frictional effects were generally more severe for the finer, AlN-F, ceramic type, while AlN-C additions positively affected AD through a more ideal mixture of fine and coarse particulate.
- The sintering response of this alloy exhibited sensitivity to AlN additions, particularly regarding grade AlN-F. This finer grade had a relatively higher number of discrete particles than the AlN-C grade on a unit mass basis. These finer particles were more susceptible to agglomerations that could not be readily infiltrated through the pressureless sintering approach employed.

- Significant gains in modulus were observed with up to 5% AlN-C or 2% AlN-F. This implied that the sinter quality of these specimens was adequate to allow load sharing to the ceramic phase.
- At 2% AlN, marginal differences in 0.2% yield strength were observed. The difference between either alloy and the matrix material were insignificant, although the coarser ceramic-bearing alloys were superior. The coarser ceramic was generally more homogenously distributed, and compacts were sintered to higher densities than the finer-AlN counterpart.
- The fatigue strength (50% survival stress) of the matrix material as well as with 2 vol% of coarse or fine AlN was not significantly different, ranging from 171.5 MPa to 204.5 MPa. Fatigue crack paths favored residual porosity and AlN clusters.

4.9 Acknowledgements

The authors would like to acknowledge the Natural Sciences and Engineering Research Council of Canada (NSERC) for financial support via the Collaborative Research & Development grant CRDPJ 486528 - 15. Dr. Bernhard Mais (Kymera International) and Mr. Jessu Joys (Ampal Inc.) are acknowledged for the provision of the powdered metals employed. Laboratory assistance provided by colleagues at Dalhousie University (Randy Cooke, Dean Grijm) is gratefully appreciated as well.

CHAPTER 5. THERMAL MECHANICAL PROCESSING OF PRESS AND SINTER Al-Cu-Mg-Sn-(AlN) METAL MATRIX COMPOSITE MATERIALS

Gregory A. W. Sweet [1], Mary A. Wells [3], Alan Taylor [4], Richard L. Hexemer, Jr. [5], Ian W. Donaldson [6] and Donald Paul Bishop [2]

1 – Graduate Student, Dalhousie University, Halifax, Nova Scotia, Canada
2 – Professor, Materials Engineering, Dalhousie University, Halifax, Nova Scotia, Canada
3 – Professor, Materials Engineering, Waterloo University, Waterloo, Ontario, Canada
4 - Vice President – Lightweight Technology, GKN Sinter Metals LLC, Auburn Hills, Michigan, USA
5 – Research Engineer, GKN Sinter Metals LLC, Conover, North Carolina, USA
6 – Director of R&D North America, GKN Sinter Metals LLC, Auburn Hills, Michigan, USA

Status: Published Journal Paper. Metals. (2018) Volume 8, Issue 7. Pages 1 - 18

Author Contributions: The following experimental procedures, results and discussions were completed by G.A. Sweet, with reviewer and editorial roles played by the subsequent authors.

5.1 FORWARD TO CHAPTER 5

Following the discovery of the mechanical and physical properties of the MMC materials system in the sintered condition, the authors performed a preliminary investigation on the response to thermal-mechanical processing. Small scale forging tests were performed at the University of Waterloo using a Gleeble 3500. Appropriate temperature and strain rates were determined from literature and past projects within the research group. The objective was to model the flow behaviour of the materials keeping in mind the high throughput a commercial forging operation might require.

5.2 ABSTRACT

The forging of sintered aluminum powder metallurgy alloys is currently viewed as a promising industrial technology for the manufacture of complex engineered products. Further, the powder metallurgy process facilitates the use of admixed ceramic particles to produce aluminum metal matrix composites. However, fundamental data on the thermal-mechanical response of commercially relevant powder metallurgy alloy systems under varying conditions of temperature and strain rate are lacking. To address this constraint, the current study investigates the thermal-mechanical processing response of a family of metal matrix composite materials that employ a commercially exploited base alloy system coupled with admixed additions of aluminum nitride. Industrially-sintered compacts were tested under hot compression using a Gleeble 3500 thermal-mechanical test system to quantify their flow behaviour. The nominal workability was assessed as function of material formulation, sintered preform condition, and processing parameters (temperature and strain rate). Optical metallography and electron backscatter diffraction were used to observe the grain evolution through deformation. Full densification was achieved for materials with ceramic concentrations of 2 vol% or less. Zener-Hollomon constituent analyses were also completed to elucidate a more comprehensive understanding the flow behaviour inherent to each material. Flow behaviour varied directly with the sintered density, which was influenced by the concentration and nature of ceramic particulate.

5.3 INTRODUCTION

Aluminum powder metallurgy (APM) is a well-established component manufacturing technique routinely adopted within the automotive sector. Conventional APM involves the compaction and subsequent sintering of blended aluminum alloy powders into coherent, near-net shape components. Successful commercial applications include the high-volume production of camshaft bearing caps, transmission components, and heat sinks to name but a few. To capitalize on this momentum, sustained proliferation of APM-derived components requires the development of new materials and/or processing technologies that yield products with improved mechanical properties. In many instances, the ability to meet this goal is underpinned by the capacity to address key metallurgical features common within APM materials. For instance, the starting aluminum powders employed are inevitably encased in an oxide layer [90] that exhibits high thermodynamic stability. Although this feature is partially disrupted through conventional powder metallurgy (PM) operations [4] it still persists as a semi-continuous feature within the sintered product [36]. Residual porosity is a secondary feature encountered in sintered APM materials. Both attributes provide crack initiation sites [91] to the detriment of several properties including fatigue behaviour and tensile ductility.

One approach that can be applied to mitigate the defects is elevated temperature plastic deformation; hot forging (a.k.a. thermal mechanical processing (TMP)). Conventionally, hot forging begins with fully dense, simple-shaped (i.e. bar, cylinder, etc.) wrought or cast billets that are progressively formed into the desired geometry through multiple hits

in a series of forging dies. A competing technology rooted in the PM sector is known as powder forging (PF). Here, powder is compacted into the requisite preform shape which is then sintered and hot forged. Although predominantly utilized in ferrous applications for the production of PF connecting rods [29], the forging of APM preforms has been studied as well [6–10] albeit to a lesser degree. PF is particularly advantageous in that practitioners have a tremendous capacity to engineer the preform shape [31]. Hence, preform and final part geometry are designed concurrently such that material utilization is maximized while plastic flow in critical areas is sufficient to promote increased mechanical properties; non-critical areas can be designed such that they undergo minimal material flow thereby limiting die wear [30]. Ultimately, this allows forging to be efficiently completed in a single uniaxial stroke [30] while plastic strain coupled with frictional forces invoke pore collapse [35], grain refinement [31], and the disruption of persistent oxide networks [36]

Successful PF requires intimate knowledge on the flow behaviour of a sintered material for a breadth of forging and microstructural conditions. A Zener-Hollomon type of constitutive analysis is one of the modelling tools commonly implemented in such endeavors. Here, it is understood that for a deforming metal, the instantaneous flow stress, $\bar{\sigma}$, varies as:

$$\bar{\sigma} = f(\theta, \bar{\varepsilon}, \dot{\varepsilon}, S) \tag{19}$$

Where θ is the isothermal forging temperature, $\bar{\varepsilon}$ is the strain, $\dot{\varepsilon}$ is the strain rate and S is a parameter representing material and microstructure [14]. The material and microstructural contributions to flow stress are principally dictated by composition, although many secondary effects such as porosity, age-hardened state, equilibrium/non-equilibrium conditions, and the presence of secondary phases, etc. can also bear significant influence [18]. The peak flow stress, $\dot{\bar{\sigma}}$, is the maximum flow stress observed during deformation. For fixed material composition and fixed strain, a set of constituent values can be extracted that represent the systems forging behaviour.

The Zener-Hollomon (Z-H) constituent analysis approach is especially well documented in aluminum hot deformation [18]. More specifically, the Sinh version, as shown in (20), was selected for its flexibility in correlating data with extreme variations in Z values [18]. The relationship is as follows:

$$\mathrm{A}(\sinh(\alpha\dot{\bar{\sigma}})^{\mathrm{n}} = \dot{\varepsilon}\exp\left(\frac{\mathrm{Q_{HW}}}{\mathrm{R}T}\right) = \mathrm{Z} \tag{20}$$

Where Q_{HW} is the activation energy of hot working (kJ mol^{-1}), R is the ideal gas constant (8.314 kJ mol^{-1} K^{-1}), T is the absolute temperature (K) and Z is the Zener-Hollomon parameter. Material-dependent constituent parameters include the stress multiplier α (MPa^{-1}), n and A. These constituents were derived in accordance with the technique outlined by Mosher et al. [20]. For a characterized material system, the peak flow stress value may be predicted by [18]:

$$\sigma = \left(\frac{1}{\alpha}\right)\ln\left\{\left(\frac{Z}{A}\right)^{1/n} + \left[\left(\frac{Z}{A}\right)^{2/n} + 1\right]^{1/2}\right\} \quad (21)$$

The activation energy of hot working correlates to the deformation behaviour of a material and gives a good comparison as to how different alloys respond to deformation under a variety of forging conditions. Higher activation energies are attributed to materials that show greater change in peak flow stress behaviour with temperature. For example, the activation energy of pure aluminum is ~140-156 kJ/mol [18], which is remarkably similar to non-heat treatable 3003, 152 kJ/mol. However, higher Q_{HW} values are observed in systems that undergo precipitation hardening to achieve their strength (i.e. fully annealed 2004 aluminum exhibits a value of 154 kJ/mol whereas, the same material in the solutionized state has an increased activation energy of 270 kJ/mol as a result of significant strengthening of the material due to dynamic precipitation (DPN) favored at low temperatures [94]). Indeed, gains in Q_{HW} are attributed to increased solute, precipitates, dispersoids, inclusions and their effects on the retardation of dynamic recovery (DRV) [94]. Ceramic or dispersoid-bearing alloys also tend to exhibit relatively high activation energies. This was exemplified in the work of McQueen et al when they determined that an extruded PM 2618 alloy strengthened with 10 and 20 vol% Al_2O_3 had activation energies of 315 kJ/mol and 400 kJ/mol, respectively [95]. Here, the secondary phases imparted heterogeneous dislocation generation that substantially increase flow stresses at low temperatures. However, at elevated temperatures DRV is sufficiently effective to cope with the added dislocations such that the observed flow stresses for a

composite material can often approach those measured for an unreinforced counterpart [21].

The purpose of this study was to investigate the response of commercially relevant APM materials to TMP. Specifically, a family of 2xxx series metal-matrix composites (MMCs) was considered. The alloy used in this study was selected because of its current commercial relevance and potential proliferation through improved mechanical properties. Comparable 2xxx series APM components see current use in camshaft bearing caps as well as automotive automatic transmission retaining plates and planetary gear carriers. Of interest was the densification and flow stress behaviour as a function of deformation temperature and strain rate. A variety of ceramic contents were investigated alongside the unreinforced base alloy to observe how they influenced hot deformation behaviour.

5.4 Materials and Methods

The materials of interest in this study were blended from a single base alloy composition coupled with concentrations of AlN as the ceramic additive. Nominally, the base alloy chemistry was 95 Al (U.S. Metal Powders, Inc., Palmerton, PA, USA), 3 Cu (U.S. Metal Powders, Inc., Palmerton, PA, USA), 1.5 Mg (Tangshan Weihao Magnesium Powder Co., Ltd., Qian'an, China) and 0.5 Sn (Ecka Granules GMBH., Furth, Germany) (in wt%); pertinent metal powder information is provided in Table 5-1. An admixed lubricant powder, Licowax C (Clariant, Muttenz, Switzerland), was blended in at 1.5

wt%. Admixed with the base alloy was one of two AlN ceramic powders (H.C. Starck, Munich, Germany), AlN-C (Coarse) and AlN-F (Fine). Included in the scope of this study were ceramic volume fractions of 0, 2, 5 and 10, for both AlN-C and AlN-F. These blends will be referred to in this report by a numerical prefix representing the volume percent ceramic, and a lettered suffix representing the ceramic type (i.e. 2C for 2 vol% AlN-C). These will be contrasted to the 'Base' system that indicates samples of the matrix alloy devoid of admixed AlN.

Table 5-1 Overview of the metallic powders employed.

Element	**Type**	**Particle size (µm) (D_{10}, D_{50}, D_{90})**		
Aluminum	Elemental	37	99	250
Copper	50:50 Al: Cu Master	5	16	45
Magnesium	Elemental	28	32	48
Tin	Elemental	5	12	34

Blending of all powders was completed in Nalgene bottles using a Turbula T2-F powder mixer (Glen Mills, Clifton, NJ, USA) with a 40-minute residence time. Homogenized blends were then pressed once into cylindrical (15 diameter x 26 mm height) green compacts with a targeted density of 2.48 g/cc. An Instron model 5594-200HVL 1 MN load frame (Instron, Norwood, MA, USA) coupled with a floating die tool set was utilized for this purpose. Green compacts were then sintered once in an industrial belt furnace used in commercial APM manufacturing. The thermal cycle included a hold at 400°C for 10 minutes for delubrication immediately prior to sintering at 600°C for 15

minutes. The sintering atmosphere was high purity nitrogen with a dew point between -55°C to -60°C and an oxygen concentration no higher than 5 ppm. Sintered specimens were subsequently machined into cylindrical samples that were 10 mm in diameter and 15 mm in height. Forging simulations were carried out on the machined cylinders in a Gleeble 3500 thermal-mechanical system (Dynamic Systems Inc., Poestenkill, NY, USA), seen in Figure 5-1, to a total strain of 0.70 mm/mm. Samples were individually loaded between two WC anvils (black arrows) and retained with a 50 N preload force. These uniaxial compression tests were completed using varied strain rates (5 s^{-1}, 0.5 s^{-1}, 0.05 s^{-1} or 0.005 s^{-1}) and isothermal temperatures (350°C, 400°C, 450°C or 500°C). All specimens were held at temperature for 15 s prior to loading to minimize temperature gradients. Additional tests were performed using an extended isothermal hold time of 150 s to investigate the effects of microstructural evolution prior to deformation. Strain values were measured using a diametrical "C" gauge, while temperature was controlled/monitored through a type-K thermocouple welded to the circumference of each test specimen equidistant from both compression anvils. Upon achieving a strain of 0.70 mm/mm samples were immediately and automatically water quenched to room temperature to preserve the microstructural features.

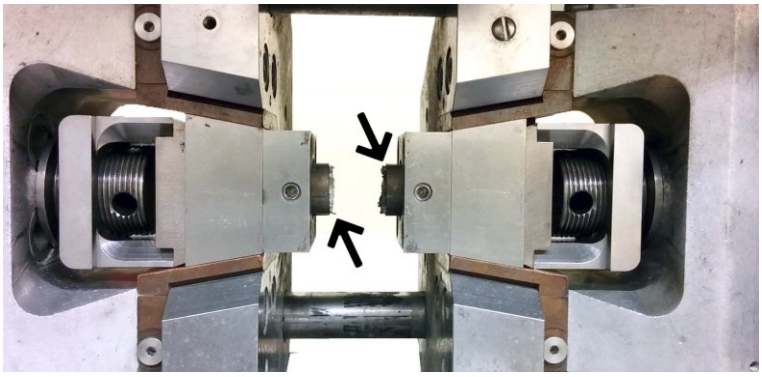

Figure 5-1 Gleeble 3500 anvil setup for hot compression testing.

Densities were measured before and after thermal mechanical processing using the Archimedes approach outlined in MPIF standard 42. These measurements were reported as a percentage of the full theoretical density for each respective material. Metallurgical examinations were performed on cold-mounted samples that were ground and polished through progressively finer SiC pads, diamond pastes, and finally, with colloidal silica media. Electron Backscatter Diffraction (EBSD) was performed on select samples in the as-polished state to investigate the nature of grains, subgrains and their boundaries. A Hitachi model S-4700 cold field SEM (Hitachi High-Technologies Co. Ltd., Tokyo, Japan) coupled with an HKL EBSD equipped with a Nordlys Oxford Instruments detector (Oxford Instruments, Abingdon, United Kingdom) was employed for this purpose. Backscatter electron micrographs of the aluminum phase for the relevant samples were also captured. Optical microscopy was performed with an Olympus BX51 light optical microscope (Olympus Corporation, Tokyo, Japan) on samples etched using Keller's reagent unless otherwise noted. Error bars for relevant plotted data represent one standard deviation from the mean value obtained through measurements on no less than five unique samples.

5.5 Results

5.5.1 Densification

Data on the density of samples before and after TMP are shown in Figure 5-2. The Base, 2C and 2F compositions were sintered to near-theoretical (99.0 % or better) densities. Hence, these relatively minor additions of AlN did not interfere with the sintering-induced densification behaviour of the material to any meaningful extent. However, greater AlN contents, as exhibited by 5C, 10C, 5F and 10F, proved that the as-sintered densities were measurably reduced through higher ceramic additions. Furthermore, the matrix alloy appeared to be more sensitive to the finer particle size AlN-F ceramic. In this sense, whereas 5C sintered to 98.4 % of its theoretical potential, 5F only reached 96.1 %. At higher concentration, density values are further compromised in a comparable fashion; 92.8 % and 90.8 % for 10C and 10F, respectively.

After hot deformation, the average density of a given material statistically exceeded that of the as-sintered counterpart in all instances. It was found that regardless of the temperature and strain rate conditions applied, the magnitude of density change was effectively identical. Accordingly, the ‘Forged’ values in Figure 5-2 represent the mean value of samples thermal mechanically worked under the complete range of parameters considered. Through TMP, the alloys Base, 2C and 2F densified by approximately 0.8 % to 1.0 %, achieving their theoretical maximum value. 5C exhibited densification of a similar magnitude but failed to reach the theoretical maximum. The magnitude of density

changes for the alloys that exhibited a reduced sintered density was more significant. Here, 5C increased by 2.5 % while 10C and 10F increased by 4.2 % and 5.9 %, respectively. Despite the density of as-sintered parts indicating AlN-C was the preferable ceramic for concentrations above 2 %, there was no significant difference between the two after TMP.

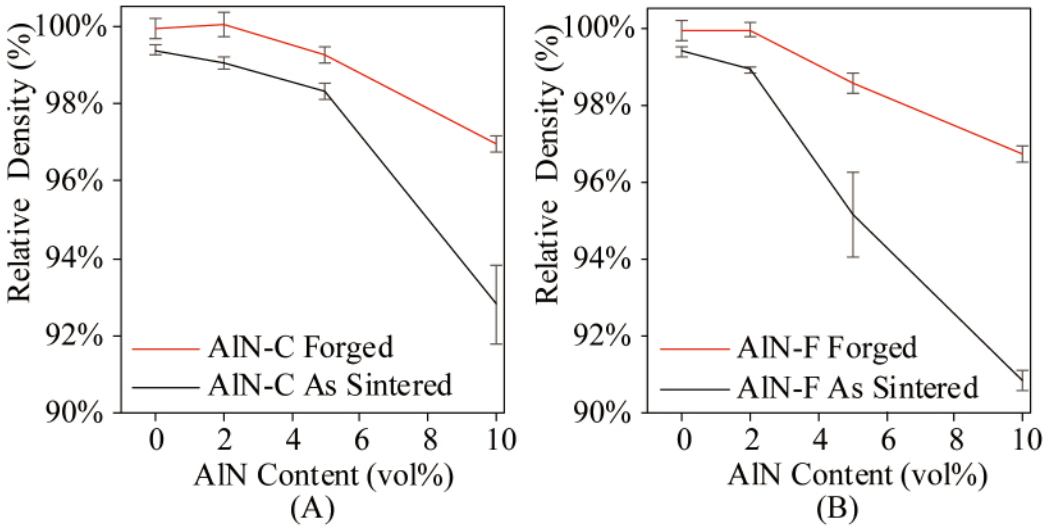

Figure 5-2 Densities of APM MMCs as measured before and after TMP. Materials prepared with (A) coarse and (B) fine AlN additions.

5.5.2 Microstructural Transitions

Optical microstructures of all alloy systems in both the as-sintered and hot worked conditions are shown in Figure 5-3. The sequences a-d illustrate the nature of pores and how the porosity increases in the as-sintered base alloy (a) and coarse AlN alloys (b-d). Residual pores in the base system were rounded with a nominal size of 10 µm to 25 µm. Pores were solely located along prior particle boundaries. With additions of AlN, porosity persisted among AlN particles in addition to prior particle boundaries. Specifically, pores

preferentially resided amongst clusters of relatively small ceramic particulate. With increased ceramic content the number and diameter of AlN-adjacent pores increased. In the extreme case of 10C, pores exceeding 50 μm as well as many finer ones persisted throughout the microstructure.

Akin to the pore development in the coarse AlN systems, the sintered microstructure of AlN-F alloys (Figure 5-3, i-k) exhibited residual porosity associated with ceramic particulate. Moreover, the exclusively fine nature of the ceramic in these alloys drives additional residual porosity. In formulations 5F (Figure 5-3j) and 10F (Figure 5-3k) the ceramic phase decorates the aluminum interparticle boundaries semi-continuously. Much of the fine ceramic material in these regions appeared well incorporated with the matrix. During sintering, the liquid phase clearly wets the ceramic particles. However, the persistent large pores amongst AlN clusters indicated that sintering mechanisms were impeded. It may be that the interparticle ceramic interferes with mass transport in the crucial solution-reprecipitation phase of sintering. Another explanation may be that the volume of liquid phase was insufficient to both wet the additional ceramic surfaces while also effectively promoting conventional liquid phase sintering mechanisms. With increased AlN content, especially for finer AlN particles, the surface area which the liquid phase must wet increases dramatically, which would essentially tie-up the liquid phase.

Hot worked microstructures are also shown in Figure 5-3; the base alloy (e) is contrasted by increasing concentration of coarse (f-h) or fine AlN additions (l-n). In all cases the

micrograph orientation is such that the loading direction was vertical. The Base alloy (Figure 5-3e) exhibited pore closure consistent with the direction of applied force. Similarly, prior particles were elongated in the direction transverse to this; prior particle boundaries were now considerably less distinguishable than the as-sintered base material. Unidentified secondary phases appear as dark gray features in these micrographs.

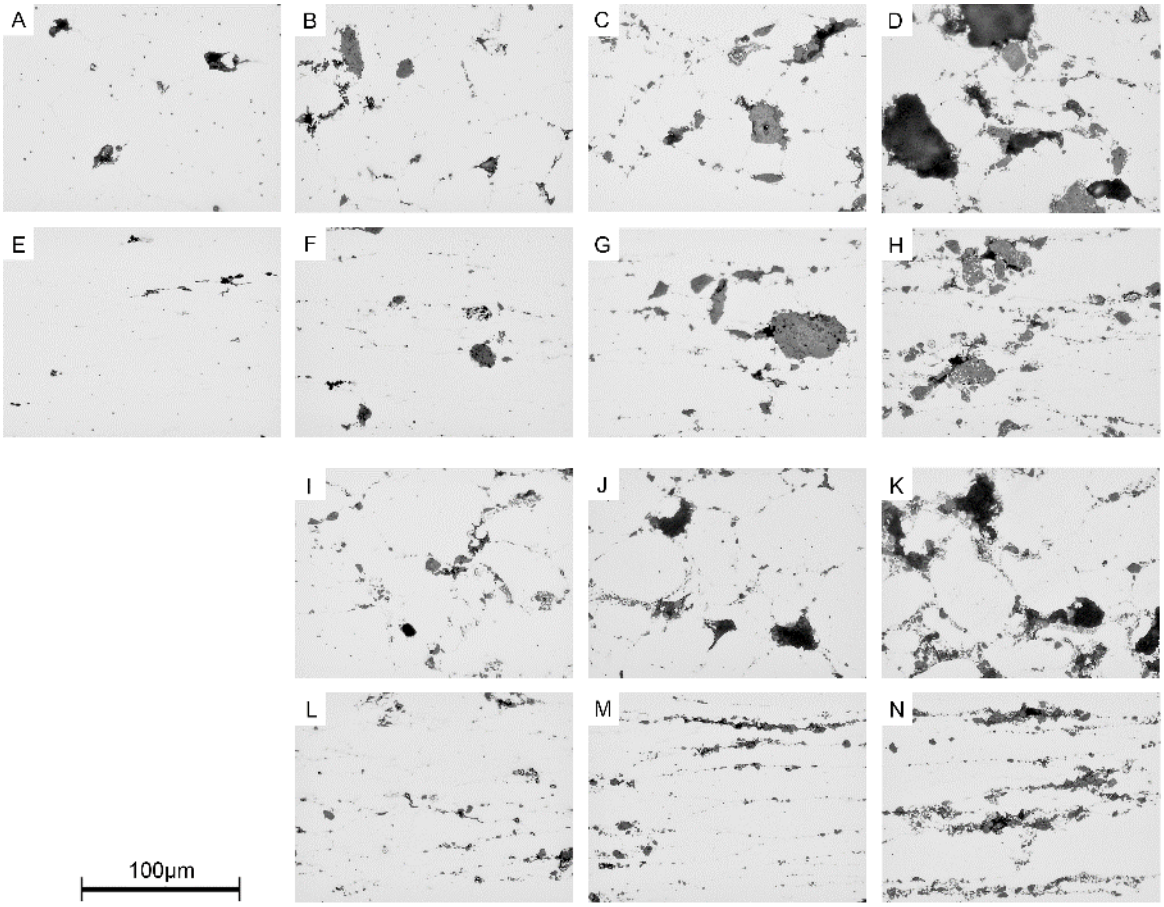

Figure 5-3 Sequence of unetched microstructures of as-sintered alloys (a) Base, (b) 2C, (c) 5C and (d) 10C contrasted by their hot worked counterpart in (e) base, (f) 2C, (g) 5C and (h) 10C. Additionally, a similar contrasting sequence of as sintered microstructures for (i) 2F, (j) 5F (k) 10F are shown with their forged counterparts in (l) 2F, (m) 5F and (n) 10F. All hot worked samples were processed at 400°C and 0.05 s^{-1} to a strain of 0.70 mm/mm.

Hot worked alloy 2C (Figure 5-3(f)) exhibits pore closure like that of the Base alloy in that pores within the metallic matrix were heavily flattened while grains were flattened and elongated consistent with the deformation direction. In addition, pores were no longer observed in direct contact with AlN particles. The higher ceramic concentrations of 5C and 10C both exhibited microstructures (Figure 5-3, g and h, respectively) where considerable residual porosity persisted adjacent to AlN particles after TMP; typically, in dense AlN cluster formations where matrix penetration would be difficult in the solid state. However, pores were considerably smaller and less numerous than their as-sintered counterparts. In the forged 5C and especially the 10C microstructures, the shear forces on the matrix phase proved enough to separate AlN particulate that was not associated with dense clusters. These particles were essentially drawn out along what would have been the prior particle boundary. The benefit here is an increased homogeneity of the ceramic, which no longer strictly existed as features decorated along these prior particle boundaries. The result was less AlN-AlN particle contact. Evidence of AlN particle fracture was not observed in the microstructure of any deformed microstructures; the apparent breakup of fine AlN, particularly in AlN-F microstructures, can be wholly attributed to the redistribution of loosely bonded clusters of ceramic.

Microstructures of fine AlN 2F, 5F and 10F after TMP are shown in Figure 5-3 l, m and n, respectively. Like their coarse counterparts, the microstructures exhibit pore flattening and ceramic redistribution from plastic deformation. Residual pores persisted alongside more complex clusters of ceramic particulates whereas cluster free regions exhibited minimal porosity. 5F and 10F showed obvious evidence of incomplete pore collapse.

The deformation-induced flow of the metallic matrix within the ceramic network was also rather heterogeneous. In this sense, the AlN-F particulates were completely enveloped by the matrix in some areas but prevailed as porous clusters in others.

Despite the redistribution of ceramic particulate through TMP, ceramic-free regions persisted throughout the microstructure of all MMC compositions. These regions represent the interior of relatively large prior aluminum particles where conventional solid-state blending cannot invoke homogenization. Based on the density and microstructural data presented above, the alloys Base, 2C, 5C, 2F and 5F were selected for constituent analysis. 10C and 10F were investigated less thoroughly due to their inferior performance.

Backscatter electron micrographs that illustrate grain evolution through TMP of Base, 2C and 5C are shown in Figure 5-4. Immediately after sintering (Figure 5-4a-c), the grain size was largely consistent with the particle size of the starting aluminum powder while grain interiors showed no evidence of subgrains or misorientation gradients. It was postulated that the residual oxide phase between adjacent powder particles had likely provided a grain boundary pinning effect, thereby limiting the average grain size to one that was comparable to the D_{50} of the starting aluminum powder. Residual porosity and AlN particulate existed exclusively along these prior particle boundaries as is expected from a conventional PM process. The porosity was rounded and typically situated at triple junctions. The nature of the microstructures in Figure 5-4a-c remained remarkably similar despite the use of three different ceramic concentrations. The most notable

difference was a lower indexing rate in the ceramic-bearing samples, as the AlN phase and porosity was not indexable. Following TMP, all materials, Figure 5-4d-f, showed extensive evidence of grain elongation and flattening consistent with the manner of applied strain. The nature of deformed grains remained reminiscent of the as-sintered microstructure, indicating that no recrystallization had occurred.

A summary of the grain boundary misorientation angles is provided in Table 5-2, expressed as the fraction of low angle grain boundaries (fLAGB). For convention, high angle grain boundaries (HAGB) are defined as adjacent grain misorientation of 15° or greater. These are shown as black boundaries in Figure 5-4. Correspondingly, LAGBs have misorientation angles less than 15° but were not highlighted in Figure 5-4 for clarity. Local misorientation angles up to 7 ° were negated from this analysis due to issues arising from pseudo-symmetric misindexing. As-sintered samples exhibited a microstructure largely devoid of LAGBs. Hence, HAGBs comprised much of the grain boundary area and it was likely that many of these were prior particle boundaries. Hot deformed samples on the other hand exhibited microstructures containing ~20-25% LAGBs. Furthermore, HAGBs appeared to remain along the prior particle boundaries of elongated grains while fine, equiaxed subgrains persisted within them. It is notable that subgrain boundaries are uniquely LAGBs.

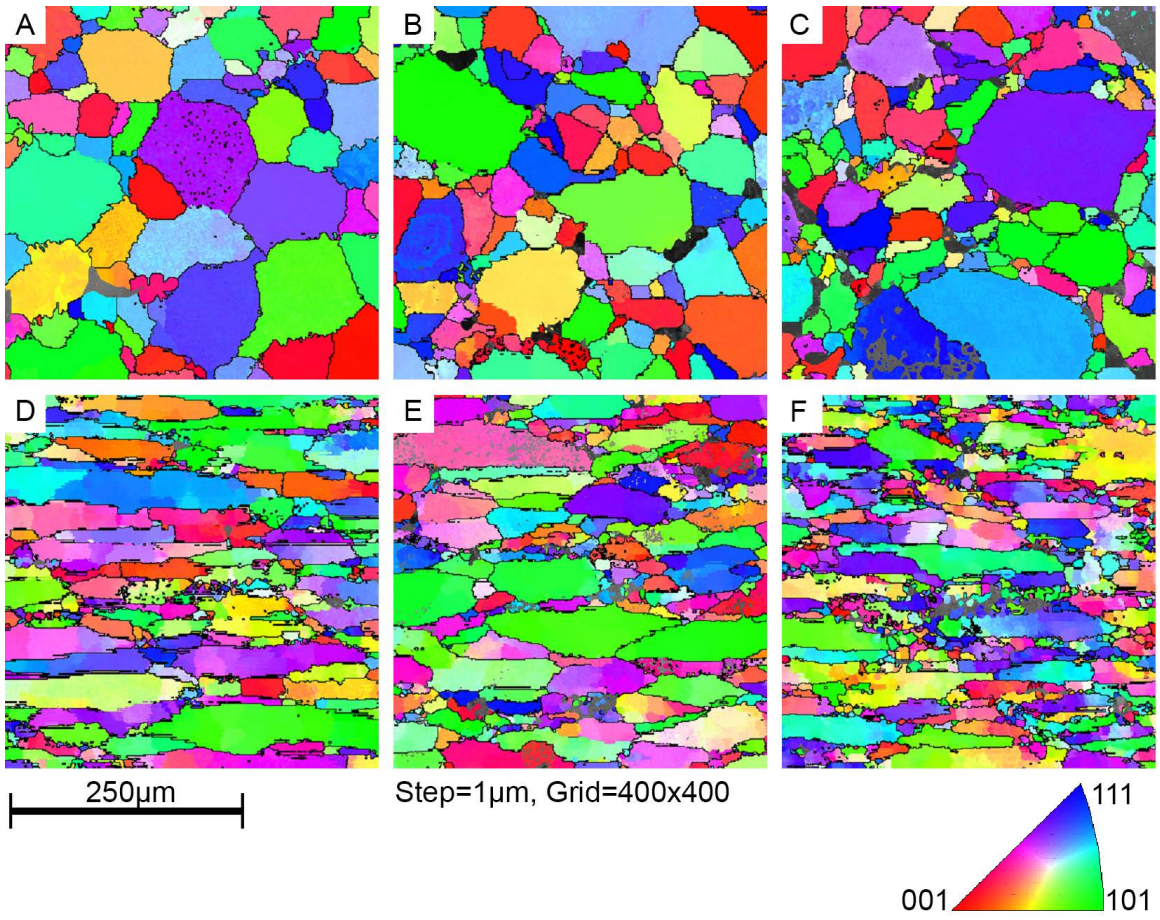

Figure 5-4 EBSD map of (a) Base, (b) 2C and (c) 5C in the as sintered condition as well as variants deformed at 500°C and 0.005 s^{-1} for (d) Base, (e) 2C and (f) 5C. TMP direction vertical with respect to page orientation.

Qualitative hot ductility assessments were made for all alloys. Most alloys under various TMP conditions proved to be sufficiently ductile to endure a true strain of 0.70 mm/mm. Samples that exhibited cracking are shown in Table 5-3. These cracks manifested at the outside circumference of the sample and grew in the axial and radial directions. Cracking was only observed at the highest TMP temperature considered. At 5 s^{-1}, all tested samples experienced some degree of cracking. Note, 10C and 10F were not processed at such strain rates, and no such ductility assessment could be made. At 0.5 s^{-1}, the relatively

porous 5F material similarly exhibited fine radial cracks. A micrograph of a crack initiation site at the surface of sample 2C can be seen in Figure 5-5, wherein the TMP direction was normal to the image. This intergranular crack path followed prior particle boundaries. This sample reached a peak temperature 8.7°C above the isothermal set point of 500°C. A comparable over-temperature was measured for all samples deformed using the same TMP conditions.

Table 5-2 Fraction of low angle grain boundaries (misorientation ≤ 15 °) in the microstructures presented in Figure 5-4.

Condition	Material	fLAGB
As-Sintered	Base	0.02
	2C	0.06
	5C	0.04
Sintered + TMP	Base	0.18
	2C	0.18
	5C	0.24

Table 5-3 Summary of the material chemistries and TMP conditions found to induce circumferential cracking within the forged product.

TMP Condition (Temperature, Strain Rate)	Fractured Samples	Over-temperature (°C)
500°C, 5 s^{-1}	Base, 2C, 5C, 2F, 5F	+10.3, 8.7, 10.2, 8.7, 9.2
500°C, 0.5 s^{-1}	5F	+1.8

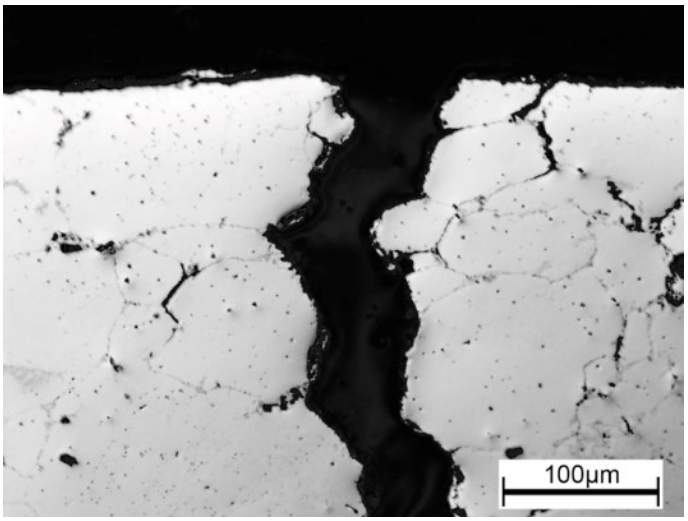

Figure 5-5 Typical appearance of cracks present at the circumference of select products after TMP. Sample 2C processed at 500˚C and 5 s^{-1}. TMP direction was normal to the plane of the image.

5.5.3 Flow Curves

Representative flow stress curves for MMC 2C are shown in Figure 5-6. Flow curves for all other material compositions are not included as the trends were largely comparable with these exemplary plots. Generally, the material exhibited a peak flow stress at low strain followed by a monotonic decay commensurate with 'flow softening'. At low temperatures and high strain rates this phenomenon was more apparent. When TMP was executed at 350°C and 0.005 s^{-1} the flow stress exhibited a monotonic decrease from a peak of 94.4 MPa to 68.5 MPa at a strain of 0.65 mm/mm. Conversely, samples deformed at 5 s^{-1} and temperatures ≥450°C exhibited a short period of strain where peak flow stress and softening were observed. Afterwards, the flow stress values remained effectively static. An exemplary case is the sample deformed at the same strain rate as the aforementioned sample, 0.005 s^{-1}, but now at 500°C. A peak in flow stress (23.6 MPa)

followed by a rapid flow softening of 24.7 % (to 17.7 MPa) was observed at a strain of only 0.054 mm/mm, followed by an additional, albeit marginal, softening of 6.4 % (to 16.6 MPa) from strain values of 0.054 mm/mm to 0.65 mm/mm. Overall, moderate levels of softening were exhibited at all temperatures, for all samples but the rate of softening varied closely with TMP temperature and strain rate.

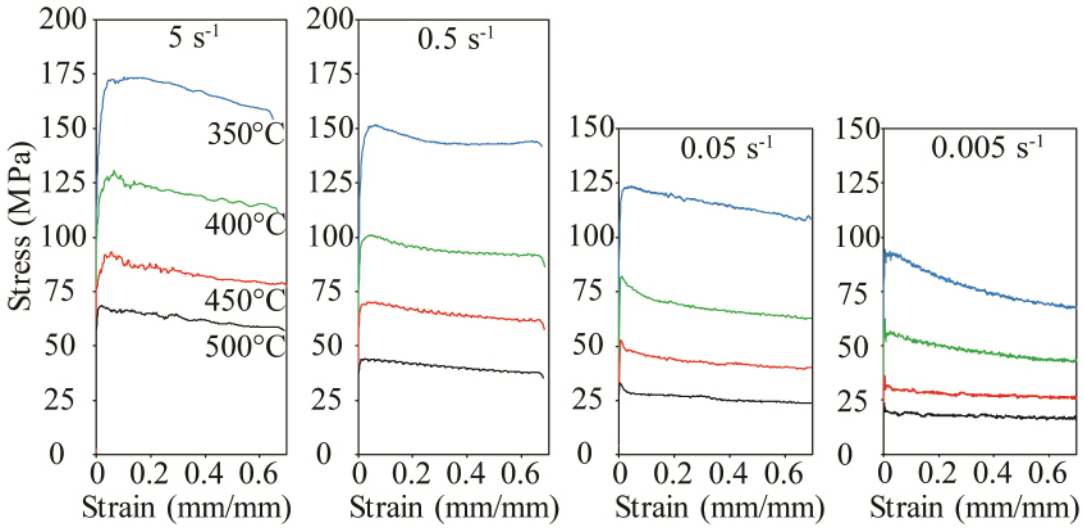

Figure 5-6 Flow stress (true stress – true strain) curves for alloy 2C developed during TMP at temperatures of 350°C to 500°C and strain rates of 5 s^{-1}, 0.5 s^{-1}, 0.05 s^{-1} and 0.005 s^{-1}.

The peak flow stress behaviour of the alloy as a function of ceramic content, TMP temperature and strain rate are shown in Table 5-4. For a given temperature and strain rate, the peak flow stress values remained largely equivalent for all alloy compositions considered. Differences between compositions Base, 2C 5C and 2F were especially small. For example, at 400°C and 0.500 s^{-1} the peak stress values only ranged from 100.7 MPa to 100.9 MPa while the average range for any set of TMP conditions was just 4.5 MPa. Interestingly, the 5F composition exhibited peak flow stresses distinct from the

other compositions. Again at 400°C and 0.500 s^{-1}, this specific composition exhibited a peak flow stress of 96.3 MPa. The change in peak flow stress value for a given composition was influenced by both temperature and strain rate. A decrease in strain rate or an increase in temperature both corresponded to a decrease in flow stress. For the range of TMP conditions considered, the flow stress appears to be influenced more strongly by temperature.

In the next stage of work, the effects of extended furnace soaking prior to TMP were briefly assessed. Work was constrained to MMC 5F deformed at 350°C or 450°C and a strain rate of 0.05 s^{-1} with an extended isothermal hold of 150 s. Flow curves for these samples are shown with their 15 s isothermal hold counterparts in Figure 5-7. The difference in flow stress at any given strain (above 0.01 mm/mm) at 350°C was approximately 15 MPa to 20 MPa. Accordingly, an extended isothermal hold substantially decreased the load require to deform the sample. To contrast this, the difference at a 450°C was much less notable. Up to a true compressive strain of 0.5 mm/mm the difference in flow stress for any given strain value was only 1 MPa to 3 MPa.

Table 5-4 Effects of TMP conditions and material composition on the peak flow stress.

Composition	True Strain Rate, Nominal (s^{-1})	Peak Flow Stress (MPa) at TMP Temperature, Nominal (°C)			
		350	400	450	500
Base	5.000	175.8	131.4	100.2	69.6
2C		173.5	130.7	93.2	68.7
5C		176.6	131.0	101.1	71.0
2F		169.3	129.8	100.3	70.5
5F		158.0	113.2	83.9	58.5
Base	0.500	147.2	100.8	72.8	45.1
2C		151.8	100.9	70.3	44.1
5C		148.3	100.7	66.6	45.1
2F		153.6	100.7	69.2	45.5
5F		130.5	96.3	60.8	40.5
Base	0.050	125.3	78.7	48.7	30.6
2C		123.4	81.9	52.8	33.3
5C		121.7	81.3	54.3	31.5
2F		124.9	76.3	50.5	32.1
5F		111.6	70.2	45.1	27.0
Base	0.005	98.4	63.5	42.3	21.9
2C		94.4	62.3	36.2	23.6
5C		99.4	65.2	38.7	22.6
2F		102.4	63.7	32.9	21.7
5F		89.1	57.9	31.9	21.0

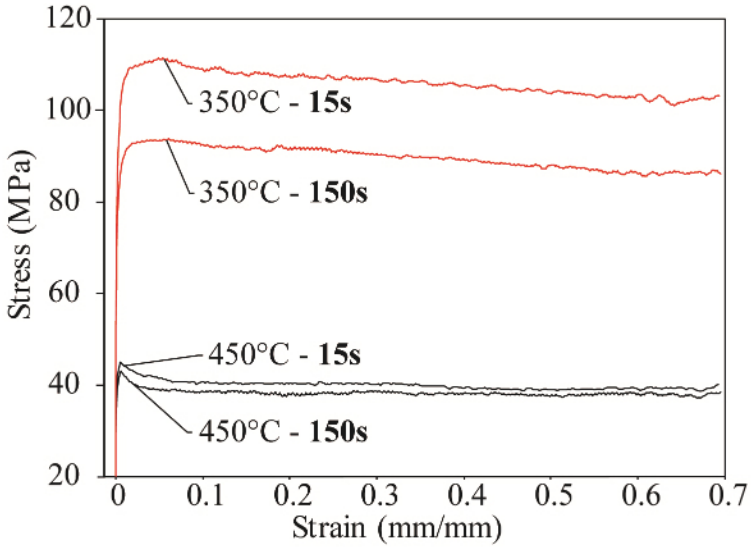

Figure 5-7 Data illustrating the effects of isothermal hold time on the flow curves for MMC 5F when deformed at 350°C and 450°C. A strain rate of 0.05 s^{-1} was employed in all instances.

5.6 Discussion

5.6.1 Porosity

In general, additions of either ceramic type began to inhibit sintering once a critical volume fraction threshold was surpassed. At a concentration of 2 vol%, the sintered density was effectively identical to that of the ceramic-free Base alloy. Since ceramic particles lie along prior particle boundaries, this concentration appeared to be sufficiently low to minimize AlN-AlN interaction allowing for adequate separation amongst discrete ceramic particles. This lack of AlN interaction was exhibited in Figure 5-3(b and i) wherein ceramic clustering was minimized and near full density was achieved directly after sintering. Increased ceramic additions saturated prior particle boundary regions with

AlN particles. Once saturated, AlN-AlN interaction became progressively more pronounced with rising ceramic contents. This increase in AlN-AlN interaction was exemplified in the string of micrographs of AlN-C in Figure 5-3 (b-d). Pores were a direct result of the inability of the matrix to penetrate these complex ceramic clusters. This phenomena has been explained in a previous study with comparable powders and blending conditions [84] as large concentrations of a fine particle size AlN were susceptible to clustering, introducing localized pore networks. Alloys containing AlN-F invariably contained a larger number of discrete AlN particles for a given volume fraction. Saturation of the grain boundaries with these finer particles must thereby occur at a lower concentration than that observed with AlN-C. This was first noted as a difference in density at 5% ceramic content. Here, 5C sintered to 98.4% and exhibited some ceramic-free prior particle boundaries (Figure 5-3c). 5F on the other hand was only 95.2% dense and exhibited prior particle boundaries (Figure 5-3j) that appeared more crowded with clustered ceramic.

Forged densities significantly exceed their precursory as-sintered values by way of pore collapse. Shear strain elongated and flattened the pores in the transverse direction. The compositions of Base, 2C, 5C and 2F all densified by approximately the same amount, from 0.6 % to 1.0 % above their as-sintered values. Incidentally, these are the samples that did not exhibit excessive AlN-AlN interaction along prior particle boundaries. In the absence of a significant amount of porosity from this effect, TMP-induced densification was largely attributable to the collapse of residual porosity inherent to the matrix. Considering compositions where ceramic clustering was evident (10C, 5F and 10F),

densification because of thermal-mechanical processing was more substantial considering their lower sintered densities, and in turn, the availability of collapsible pores. However, residual, partially-collapsed, pores prevailed in the hot forged samples, routinely appearing within dense, complex AlN clusters, as shown in Figure 5-3 (h, m and n). Evidently, the amount of strain imparted on samples was insufficient to redistribute AlN particles such that the matrix phase could penetrate the pores adequately.

5.6.2 Hot Ductility

In an MMC system with a heat treatable matrix, ductility may be adversely impacted through decohesion of the particle/matrix interface [21] and/or preferential precipitate formation/growth along grain boundaries [28]. However, these explanations were deemed insufficient in this study as cracking only occurred at relatively high strain rates and hot working temperatures. It was thereby postulated that deformation-induced heating was the principal factor of influence. In this sense, under rapid strain rates the self-heating of the material instilled through deformation could not be accommodated quickly enough within the closed-loop temperature control system of the Gleeble. This led to moderate over-heating (Table 5-3) such that the peak temperatures were now in close proximity to the incipient melting point of the Base alloy (520°C [96]). The authors thereby inferred that this had caused hot shortness that was manifested as cracking of the forged product. This problem did not occur at lower strain rates of 0.05 s^{-1} and 0.005 s^{-1}. Here, superior temperature control was maintained as thermal overshoot was <1°C during deformation. This avoided onset of hot shortness and yielded crack-free products.

5.6.3 Flow Behaviour

Evidence in this paper insinuated that the flow behaviour of the materials was consistent with DRV. The forged microstructures exhibited grains elongated transverse to the TMP direction. No equiaxed grains with HAGBs were observed. LAGBs were rampant; many finer, equiaxed, subgrains were observed within deformed prior particles. Dynamic recrystallization is therefore ruled out, and DRV is concluded to be operative. However, the flow softening behaviour exhibited under most deformation conditions in Figure 5-6 deviates from normal DRV curves. This discrepancy is attributable to dynamic precipitation (DPN). Simultaneous DRV and DPN mechanisms have been previously observed in other heat treatable APM materials [20] as well as the 2xxx series wrought aluminum alloy system [28]. In DPN, thermally motivated precipitates can form and strengthen the material in-situ leading to a rise in flow stress under certain conditions. However, if thermal exposure is adequately prolonged, over aging and a concomitant decrease in the strengthening effect transpires (manifested as a decreased flow stress). This thermal exposure can be in-situ or prior to deformation. Deformation at relatively low temperatures prompts the nucleation and growth of more and finer strengthening precipitates. However, as solid solubility rises with increasing deformation temperature, the driving force for precipitate formation decreases. This can invoke the dissolution of early-stage precipitates as well as rapid coarsening of those that are larger, and more mature. Those that remain are now less effective at strengthening such that reduced flow stresses are now needed to instill plastic deformation.

DPN effects are directly influenced by the microstructure of the material prior to deformation. This fact was particularly important in the current study as all thermal-mechanical testing was applied to specimens in the 'as-sintered' condition. In this state, Al-Cu-Mg APM alloys are known to contain a rather unique compilation of strengthening precipitates that includes phases from the complete precipitation sequence. This is driven by the temperature employed in sintering and the ensuing rate at which the specimens were cooled from this temperature. In this sense, all specimens were sintered at 600°C. This was above the alloy solidus and thereby ensured that a small amount of liquid phase enriched in alloying additions existed in the material at this temperature. Sintered parts were then cooled in a semi-accelerated manner as they were conveyed into a water jacketed segment of the furnace under high rates of flowing nitrogen. The associated cooling rate is reasonably fast (i.e. 1°C/s) at temperatures >200°C, but is reduced to a tenth of this value for the remainder of the cooling profile [97]. The resultant microstructure thereby includes solidified remnants of the liquid phase and α-Al grains that contain phases from the entire precipitation sequence; including incoherent equilibrium precipitates and even a solid solution component that dissociates during natural aging of the finished product [98]. Now considering the flow softening behaviour exhibited in Figure 5-6, it's apparent this was driven by the combination of deformation temperature and strain rate. First, consider the contrasting behaviour of curves corresponding to 350°C and 500°C for the strain rate of 0.005 s^{-1}, Figure 5-6. At 350°C the supersaturation is relatively high, so the driving force for new strengthening precipitates was accordingly high. Flow softening here was largely attributable to the loss in strength due to these in-situ forming precipitates. At 500°C no appreciable

supersaturation exists. No precipitation occurs in situ and minimal flow softening occurs. The explanation for the flow softening exhibited for samples deformed at 500°C and deformed at higher strain rates is attributable to pre-existing precipitates. These precipitates are inherent to the sintered microstructure and provide marginal strengthening effects. Again, over aging of these pre-existing precipitates during deformation reduces their strength contribution

Further proof of the influence of DPN was devised through the elongated isothermal hold tests of Figure 5-7. The corresponding DSC trace of 2C in the T1 condition has been previously studied by the authors [96]. Upon heating to 350°C and prior to deformation, the material has gone through several microstructural events, most notably static precipitation of the Type-I and/or Type –II S phase (DSC event peak at approximately 320°C) [99]. Extended thermal exposure at 350°C thereby fosters the growth and coarsening of all pre-existing precipitates present. These fewer but coarser precipitates provide less resistance towards dislocation motion. Both 15 s and 150 s holds at this temperature exhibit ongoing work softening at approximately the same rate, indicating that in both instances, precipitate growth (DPN) remains operative. At ~375°C, dissolution of the S phase precipitates commences. This reaction then continues until a temperature of approximately 505°C. Throughout this event, strengthening precipitates are dissolved into the matrix to a progressively greater extent. In the relative absence of precipitates, the flow stress behaviour of both samples processed at 450°C naturally converged, although the sample with extended hold time did show a marginally lower flow stress. As strain increased, the flow stresses remained different by approximately 1

MPa to 2 MPa. It is notable that the effects of solute drag as a result of this dissolution event are anticipated to be minimal as demonstrated in a study on a chemically comparable 2xxx series alloy [28].

Aside from DPN, ceramic content also influenced the peak flow stress. This was particularly acute at low strain values, as a definitive trend with the MMC composition emerged. For instance, as shown below in Figure 5-8, peak flow stresses were consistently higher in MMCs that were relatively lean in ceramic content but declined proportionately as the ceramic content increased. Such transitions were somewhat counter-intuitive to what may be expected through the addition of a rigid phase, as reported for other aluminum MMC systems [95]. However, it was consistent irrespective of the use of AlN-C or AlN-F. For instance, the base alloy yielded at 126 MPa, while 2C and 2F were marginally softer, with peak flow stresses 3 MPa and 1 MPa lower, respectively. 5C again exhibited only a marginal reduction in flow stress, 4 MPa weaker than Base. Considerable differences in flow stresses were then observed for 10C, 10F, which are 18 MPa and 21 MPa softer. 5F exhibited an intermediate softening of 14 MPa. The root cause for this behaviour lied in differences amongst the sintered densities of the preforms. The sintered density and ceramic content are highly correlated (i.e. correlation factor -0.942, p-value 0.000). Increased ceramic additions inherently limited the sintered density and these changes were manifested in the flow curves as slightly weaker materials. For the Gleeble samples deformed at 0.05 s^{-1} these trends can be observed in Figure 5-9. In all cases, the positive, nonzero linear relationship was highly significant and sintered density explained most of the variance in peak flow stress (R-sq and p-

values for the linear trends at 500°C, 450°C, 400°C and 350°C: 82.2 and 0.005, 78.6 and 0.008, 80.1 and 0.006, 93.7 and 0.000). These findings are consistent with the precedent that sintered preforms with a high relative density will yield at relatively high stress while those that are more porous yield at lower stresses [35]. When accounting for the sintered density of the materials, the influence of the ceramic type and concentration was not statistically significant. Following suit, the convergent behaviour of flow stress curves following the peak may be attributed to dynamic densification effects.

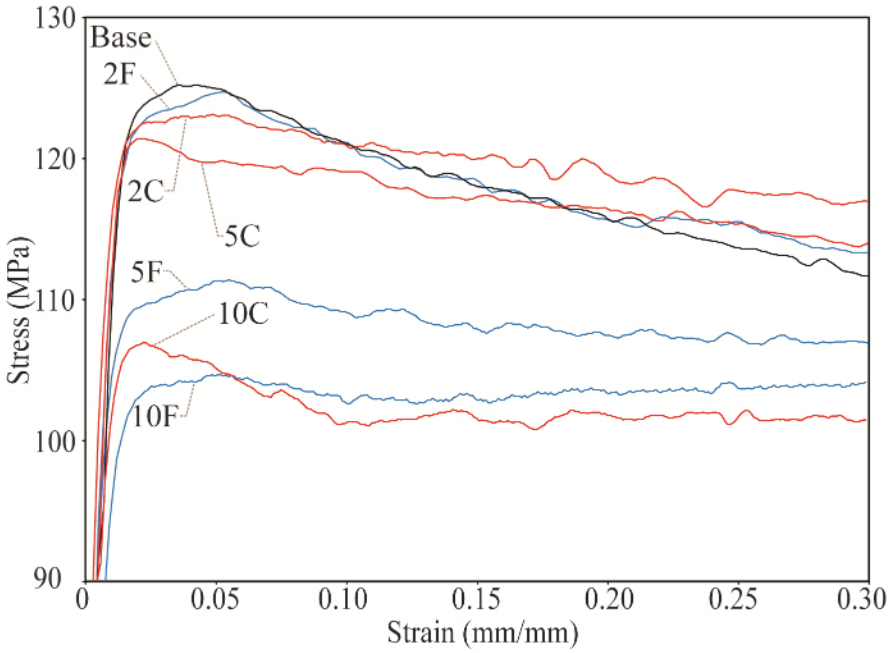

Figure 5-8 Flow curves for each material composition deformed at 350°C and 0.05 s^{-1} exhibiting the variation in peak flow stress.

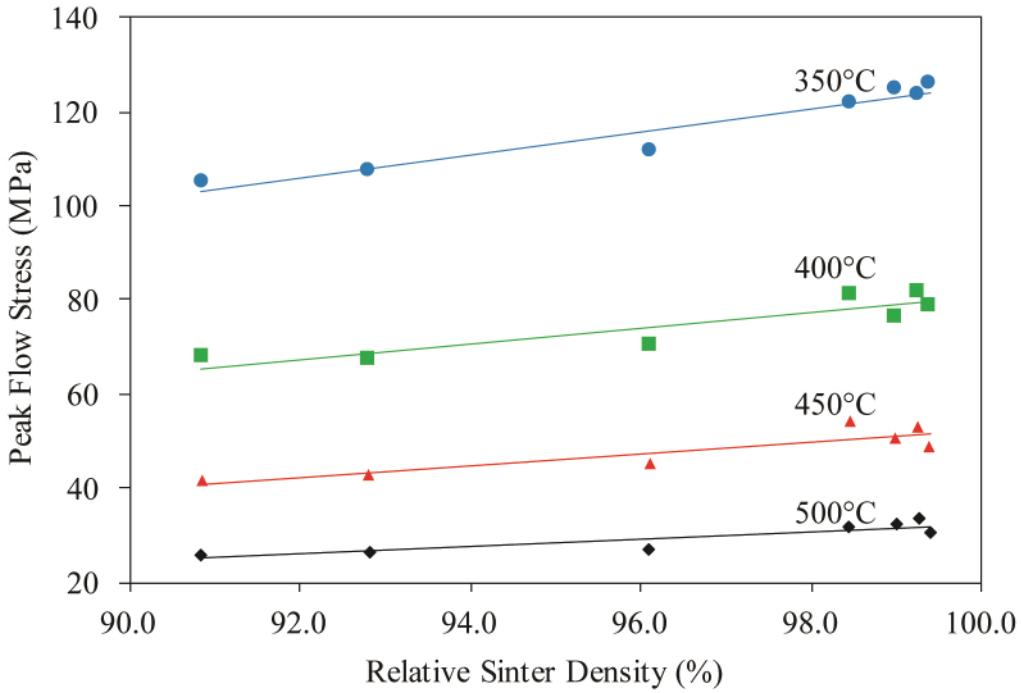

Figure 5-9 Effect of preform sintered density on the peak flow stress, samples deformed at a strain rate of 0.05 s^{-1} and temperatures 350°C to 500°C.

5.6.4 Constituent Behaviour Analysis

The Sinh Zener Hollomon constituent analysis approach was successfully applied to the materials used in this study, except for 10C and 10F compositions, which were excluded from this phase due to their limited number of test conditions. Resultant constituent values are summarized in Table 5-5. It should be noted that the calculated value of α was found to vary slightly depending on the material composition. A common value of α (0.016 MPa^{-1}) was selected from the list of calculated values which best-suited the family of materials. In literature, a larger α (0.052 MPa^{-1}) is commonly chosen [94], however in this case it proved to poorly represent data at extreme Z values.

Table 5-5 Constituent values for the APM materials modeled in accordance with equation (19) .

	α (mpa^{-1})	**n**	**s**	**Q_{HW} (kJ/mol)**	**ln(A) (s^{-1})**
Base	0.016	5.4	2619	272	42.5
2C	0.016	5.6	2622	279	43.7
5C	0.016	5.5	2649	277	43.5
2F	0.016	5.4	2626	271	42.6
5F	0.016	6.0	2543	292	46.8

The activation energy of hot working, Q_{HW}, provides valuable insight into the forging behaviour of these materials. In terms of absolute performance, the base material shows the same elevated level of temperature sensitivity characteristic of comparable age-hardenable aluminum alloys in the solutionized state [28]. This was no doubt attributed to the T1 state of the starting material, as the presence of alloying elements in solid solution and/or highly underaged precipitates allows for DPN. Here, low temperature strength of the materials is elevated through in-situ precipitation, while elevated temperature deformation more easily circumvents these strengthening effects. As alluded to earlier, a precursory isothermal hold reduced DPN effects, minimizing the temperature sensitivity of the material and reducing Q_{HW} [18]. Comparatively, differences in Q_{HW} may be attributed to the strengthening effects provided through varying ceramic content. Ceramic-bearing alloys typically show a temperature sensitivity from the inefficient recovery mechanisms of the matrix phase being able to cope with the increased dislocation densities at low temperatures. Whereas at more elevated temperatures, recovery becomes sufficiently efficient and flow behaviour rivals that of the matrix

phase. Here, differences in activation energy between materials were subtle. Base, 2C, 5C and 2F all exhibited comparable Q_{HW} values Notably, 5F possessed the highest Q_{HW} and n. Peak flow stresses were routinely less than those of Base, 2C, 5C or 2F because of the porosity negatively impacting mechanical strength. The magnitude of change in flow stress arising from this was most notable at lower temperatures and higher strain rates.

Figure 5-10 plots the calculated peak flow stress values versus strain rate for the range of temperatures observed in this study. In addition, the experimental values for the corresponding TMP parameters are superimposed to show their adherence to the Zener-Hollomon analyses. In general terms, the alloys Base, 2C, 5C and 2F performed similar enough to justify characterizing them as a single material type. Consequently, a single curve represents these four sets of data points. 5F was represented by its own set of unique curves per its regression. This plot serves as a useful tool in predicting the forging behaviour of these materials for any combination of temperature and strain rate within the boundaries considered. The deformation response of these ceramic materials can be largely attributed to the density to which they're processed prior to sintering. Given comparable degrees of densification, the effects of the type and amount of ceramic content were negligible.

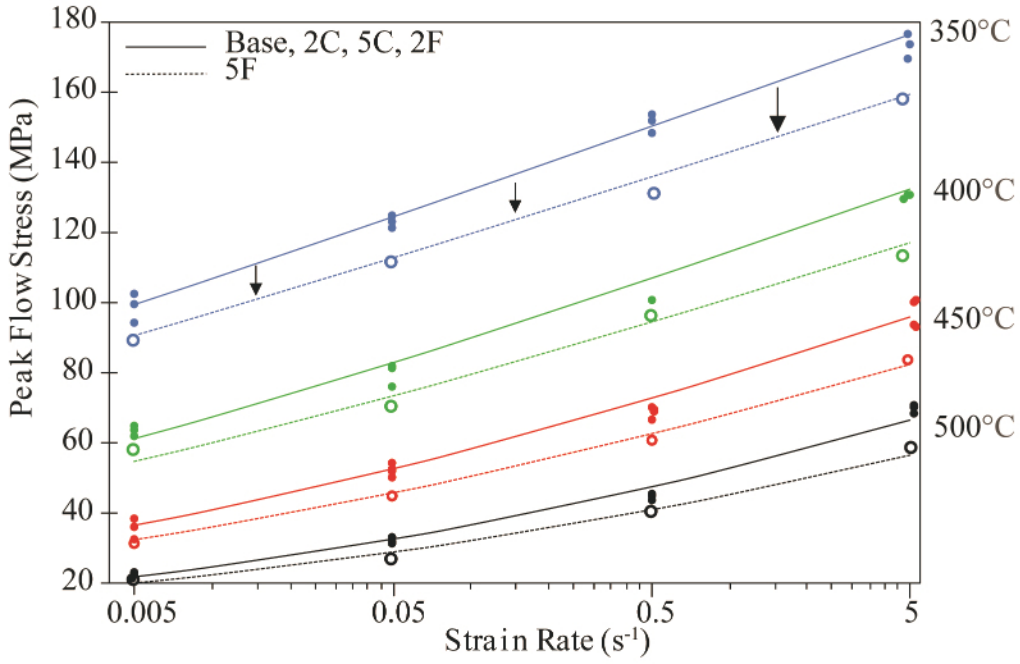

Figure 5-10 Peak flow stress data for MMC materials plotted versus strain rate. Experimental data points superimposed on Zener-Hollomon calculated curves (solid and dashed lines).

5.7 Conclusions

TMP studies were successfully performed on a variety of sintered APM materials containing varied amounts of AlN additions. Press-and-sinter samples were hot worked in the as-sintered (T1) condition at temperatures ranging from 350°C to 500°C, and strain rates of 0.005 s^{-1} to 5 s^{-1}. All samples were deformed to a strain of 0.70 mm/mm. The hot formability of these materials could be quantified through density measurements, metallography and Zener-Hollomon analyses. In general, the stress strain flow curves showed work-hardening followed by either a steady-state flow stress or work softening. More specifically, it can be concluded that:

- The density of all materials invariably increased through TMP. However, temperature and strain rate did not influence final density values significantly. Samples that were sintered to near-theoretical density (>99.0 %), including Base, 2C and 2F alloys, were forged to essentially full density (>99.9 %). Samples with an inferior sintered density did not reach their respective full density values.
- Samples deformed at 500°C were susceptible to cracking. Deformation facilitated *in-situ* heating beyond the targeted temperature under select circumstances that led to crack growth along prior particle boundaries. The lower sintered density of MMC 5F also appeared to be influential.
- Static and dynamic precipitation were exhibited throughout the deformation conditions considered. The effects of DPN were evident below the solvus, especially at the lowest deformation temperature. Temperatures of 450°C and higher exhibited evidence of precipitate dissolution, encouraging lower flow stresses.
- The implementation of isothermal holds confirmed the occurrence of precipitation events. Increased isothermal hold time allowed for precipitate coarsening and an associate reduction in flow stress. At 450°C, near-equilibrium flow stresses were approached within 15 s. At 350°C, slower kinetics were apparent, and softening occurred with 150 s isothermal hold prior to deformation.
- Additions of AlN that negatively impacted sintered density also decreased flow stress. This effect was most acute when AlN-F additions were employed.

- Zener-Hollomon analyses using a Sinh approach enabled the peak flow stress characteristics of Base, 2C, 5C, 2F and 5F systems to be mapped. The results were effectively identical for all systems except the 5F formulation wherein a clear difference emerged.

5.8 Acknowledgments

The authors would like to acknowledge Bernhard Mais (Ecka Granules) and Jessu Joys (U.S. Metal Powders) are acknowledged for the provision of the powdered metals employed. This research was funded by the Natural Sciences and Engineering Research Council of Canada (NSERC) via the Collaborative Research & Development grant CRDPJ, number [486528-15].

CHAPTER 6. SUPPLEMENTAL ANALYSIS OF THE THERMAL MECHANICAL PROCESSING OF METAL MATRIX COMPOSITES: PROCESS MAPS

The following section is an expansion of the preceding refereed journal paper, titled "*Thermal Mechanical Processing of Press and Sinter Al-Cu-Mg-Sn-(AlN) Metal Matrix Composite Materials*". Herein, process maps are constructed from the Gleeble data of select materials. Per the abundant work done by Prasad [24,26], process maps are the superimposition of power dissipation and instability maps, represented as isoefficiency contour maps. Power dissipation maps are the dimensionless efficiency of power dissipation factor, η, plotted versus temperature and strain rate. Similarly, an instability map plots the dimensionless stability parameter, ζ. Practically, these maps help determine unfavorable, unstable, deformation conditions. Such unstable conditions include, but are not limited to: void formation, particle decohesion, wedge cracking or dynamic precipitation. Furthermore, domains of stable flow can be interpreted from these maps. These 'safe' microstructural energy dissipative mechanisms may include dynamic recrystallization, dynamic recovery and superplastic forming. Process maps are used to determine the range of these mechanisms, while metallography techniques are used to determine those that are principally operative.

Derived from the Dynamic Materials Model, the power dissipation factor is a calculated representation of the total power dissipation of the system, P, or the sum of the power dissipation through plastic deformation converted to viscoplastic heat generation, G, and the dissipation through microstructural transition, J. Examples of such microstructural

transitions include DRV, DRX, superplastic flow, phase transformation and damage. The total instantaneous power dissipation during deformation is defined by [24]:

$$P = \int_0^{\dot{\bar{\varepsilon}}} \bar{\sigma} \cdot d\dot{\bar{\varepsilon}} + \int_0^{\bar{\sigma}} \dot{\bar{\varepsilon}} \cdot d\bar{\varepsilon} \tag{22}$$

Or

$$P = G + J \tag{23}$$

Where $\bar{\sigma}$ is the true stress, $\dot{\bar{\varepsilon}}$ is the true strain rate, G is the first integral in (22) and J is the second. The fraction of power towards useful microstructural change is the focus, hence, for fixed values of T and $\bar{\varepsilon}$ (true strain), the efficiency of power dissipation is defined as [24]:

$$\eta \equiv \frac{\mathrm{J}}{J_{max}} \tag{24}$$

or

$$\eta \equiv \frac{2m}{m+1} \tag{25}$$

Where:

$$m = \Delta J / \Delta G \tag{26}$$

Where m is the dissipating factor, a key parameter in defining the relative partitioning of heat generation and microstructural change; $J_{max} = 0.5\sigma\dot{\varepsilon}$ In this report, the value of m is calculated empirically using equations (14) - (16) as outlined by [25]. Practically, m values between 0 and 1 represent stable flow, whereas negative values represent a region of negative strain rate sensitivity. Determination of a condition of flow instability is

defined as a negative value of the instability parameter ξ, given by the following equation [24] (and empirically in (17)):

$$\xi(\dot{\varepsilon}) = \frac{\partial \ln[\frac{m}{m+1}]}{\partial ln\dot{\varepsilon}} + m \tag{27}$$

Base, 2C and 2F Gleeble data were revisited. Appropriate flow curves were corrected for decreases in flow stress due to adiabatic heating during forging. Tests performed at 0.5 s^{-1} and 5 s^{-1} saw substantial temperature increases over the desired setpoint, as illustrated in Table 5-3. Flow stress corrections were performed according to the methodology outlined in Dieter [100]. Temperature-corrected instantaneous flow stress values for the three selected materials are summarized in Table 6-1 (Base), Table 6-2 (2C) and Table 6-3 (2F). Four arbitrarily selected strain values were selected for comparison.

Table 6-1 Temperature-corrected instantaneous flow stress values for the material 'Base'

Strain (mm/mm)	Strain Rate (s^{-1})	Flow Stress (MPa) at TMP Temperature (°C)			
		350	**400**	**450**	**500**
0.1	5	179.6	128.8	97.8	69.7
	0.5	149.1	103.5	74.0	43.8
	0.05	120.5	72.7	41.5	26.4
	0.005	87.3	50.1	30.3	17.4
0.3	5	183.6	128.4	97.2	70.1
	0.5	146.7	100.0	73.3	42.0
	0.05	111.9	68.9	39.7	25.0
	0.005	76.3	46.4	28.6	16.4
0.5	5	182.6	128.6	97.2	69.7
	0.5	147.9	97.8	72.1	40.2
	0.05	106.0	66.7	38.3	23.5
	0.005	70.7	43.8	28.1	15.9
0.65	5	180.2	129.0	97.7	68.3
	0.5	147.5	95.3	73.2	39.0
	0.05	103.2	65.9	38.5	22.4
	0.005	67.3	42.7	27.8	15.9

Table 6-2 Temperature-corrected instantaneous flow stress values for the material '2C'

Strain (mm/mm)	Strain Rate (s^{-1})	Flow Stress (MPa) at TMP Temperature (°C)			
		350	**400**	**450**	**500**
0.1	5	176.2	127.9	89.2	67.7
	0.5	155.9	105.5	69.2	43.2
	0.05	121.0	72.3	45.8	27.7
	0.005	87.5	52.7	29.1	18.6
0.3	5	179.5	127.1	87.5	69.9
	0.5	155.0	103.6	65.1	40.8
	0.05	116.5	67.5	42.5	26.5
	0.005	77.5	48.0	27.5	17.8
0.5	5	177.4	126.8	87.5	66.9
	0.5	151.8	99.0	63.0	38.8
	0.05	112.1	64.8	41.1	24.7
	0.005	71.0	44.7	26.7	17.1
0.65	5	175.0	126.3	87.6	68.1
	0.5	149.1	95.1	61.2	37.5
	0.05	108.9	63.1	39.9	24.0
	0.005	68.4	43.2	26.2	16.6

Table 6-3 Temperature-corrected instantaneous flow stress values for the material '2F'

Strain (mm/mm)	Strain Rate (s^{-1})	Flow Stress (MPa) at TMP Temperature (°C)			
		350	**400**	**450**	**500**
0.1	5	170.9	125.0	95.8	71.8
	0.5	150.9	100.6	75.2	48.5
	0.05	120.3	70.4	43.6	27.5
	0.005	84.4	49.4	26.9	17.7
0.3	5	176.7	126.1	96.4	71.2
	0.5	151.1	96.8	74.9	47.7
	0.05	112.9	67.2	42.0	26.5
	0.005	75.2	44.9	26.7	17.4
0.5	5	176.5	125.9	94.7	70.3
	0.5	151.4	94.8	70.3	44.5
	0.05	107.4	65.3	40.8	24.9
	0.005	69.2	41.6	26.2	16.5
0.65	5	173.3	124.9	97.1	70.8
	0.5	149.6	94.3	66.9	41.6
	0.05	104.4	64.7	40.2	24.4
	0.005	66.6	39.8	25.7	16.5

Process maps were constructed for the three selected compositions, shown in Figure 6-1, Figure 6-2 and Figure 6-3 for Base, 2C and 2F, respectively. For comparison purposes the plots were constructed for flow data solely at 0.65 mm/mm. The colored scale represents the efficiency of power dissipation, η, in percent. The regions shaded with black diagonal lines are regions of instability, $\zeta < 0$.

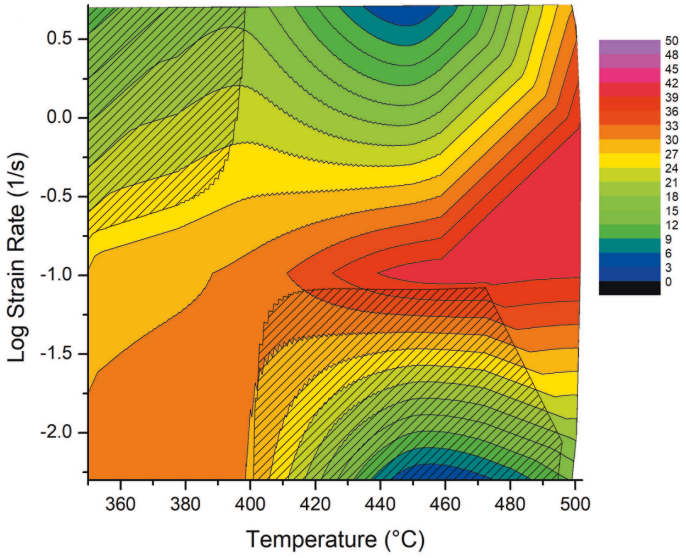

Figure 6-1 Process map of the material 'Base' deformed to a true strain of 0.65 mm/mm. Colored contours represent the efficiency value whereas the shaded portions represent regions of flow instabilities.

The ‘Base’ composition shows several distinct regions of efficiency. Two domains of low efficiency at 450°C and 5 s^{-1} or 0.005 s^{-1}, while intermediate strain rates at this temperature lie within a third domain, that of highest efficiency. Generally, the efficiency was at least 24%, while a peak efficiency of 41% was calculated at 450°C and 0.05 s^{-1}. This third domain spans from 400°C to 500°C for these intermediate strain rates. Another domain appears around 350°C and 0.005 s^{-1}. The final domain, which exhibits relatively low efficiency, appears in the window of conditions from 350°C to 400°C and 0.5 to 5 s^{-1}; incidentally, this region was also determined to produce unstable flow. A second region of unstable flow was observed between 400 and 500°C around 0.005 s^{-1}.

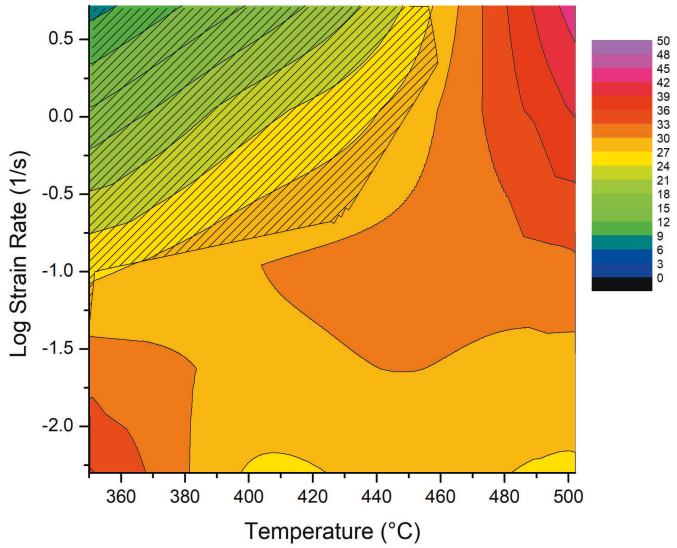

Figure 6-2 Process map of the material '2C' deformed to a true strain of 0.65 mm/mm. Colored contours represent the efficiency value whereas the shaded portions represent regions of flow instabilities.

The map corresponding to the composition 2C deformed to 0.65 mm/mm exhibited several similarities and differences to the Base one. First, the two aforementioned regions of very-low efficiency have been replaced by substantially higher efficiencies. These increased efficiencies are reflective of the changes in flow stresses encountered at all strain rates for this temperature. At 450°C and a strain rate of 0.5 s^{-1} or 5 s^{-1}, the Base material exhibited an instantaneous true flow stress of 73.2 MPa and 97.7 MPa, respectively. For the composition 2C, the respective flow stresses were 61.2 MPa and 87.5 MPa. Accordingly, no domain of instability was calculated near 450°C and 0.005 s^{-1}. However, the unstable flow regime located on the top left of this plot expanded, as did the superimposed gradient of decreasing efficiency with increasing strain rate and

decreasing temperature. Again, the highest efficiencies remain in the region of temperatures ranging from approximately 400°C to 500°C, becoming considerably more efficient at the extreme strain rates. Peak efficiency is slightly lower (38%) and occurs at the highest temperature and strain rate. The domain at low temperature and low strain rate appears largely unchanged.

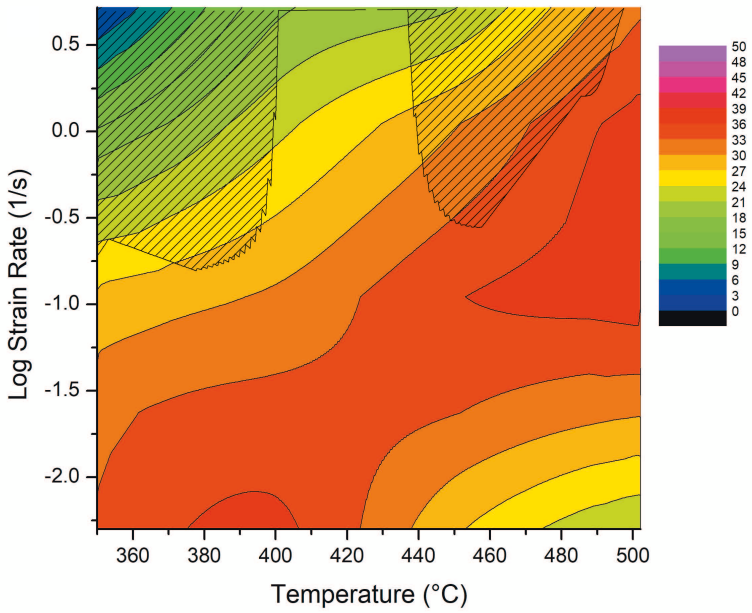

Figure 6-3 Process map of the material '2F' deformed to a true strain of 0.65 mm/mm. Colored contours represent the efficiency value whereas the shaded portions represent regions of flow instabilities.

2F exhibited a process map largely comparable to that of 2C. The domains appear to cover approximately the same temperature and strain rate conditions. The domain on the lower left of the plot is now more prominent, with a peak efficiency of 39% at 400°C and 0.005 s^{-1}. An equivalent peak of 39% is observed at 500°C and 0.5 s^{-1}, an order of magnitude lower strain rate than observed in 2C. on the other hand, 2F is less efficient at

the extremes of Z values (350°C – 5 s^{-1} and 500°C – 0.005 s^{-1}). The region of flow instability at 350°C and 5 s^{-1} decreased in area, while an adjacent second region appeared around 450°C and 5 s^{-1}. While this exists as two distinct regions, the instability parameter for the intermediate temperature value (400 C and 5 s^{-1}), was near-zero ($\zeta = 0.02$). An inaccuracy in recorded flow stress of less than 0.5 MPa (124.9 MPa actual value, 124.5 MPa threshold) at this condition would result in a negative stability parameter. Therefore, the two instability regions, as well as the area in-between, may be practically considered a single region of instability.

Optical micrographs of 2C at the extreme forging parameters of temperature and strain rate (Figure 6-4) compliment those of Base, 2C and 2F at 400°C and 0.05 s^{-1}, reported in the prior manuscript (Figure 5-3). Remarkably, under no deformation condition was there any observation of particle fracture or decohesion. The metallurgical bond between the matrix and either AlN particulate was sufficiently strong to ensure cohesion throughout strains up to at least 0.70 mm/mm. This contrasts the work of Cavaliere and Evangelista [101] on 2618 aluminum reinforced with Al_2O_3, where widespread particle fracture and decohesion occurred at any forging strain rate at or below an isothermal temperature of 400°C. The reason for the persistent domain of instability exhibited in the process maps for Base, 2C and 2F at high strain rates and favoring low temperatures is therefor a different mechanism. Deformation bands and wedge cracking, which are common instability mechanism, were similarly absent in the microstructure. It is assumed the instability is therefor related to the strong dynamic precipitation behaviour of these materials with their given thermal history, as was determined in 5.6.3.

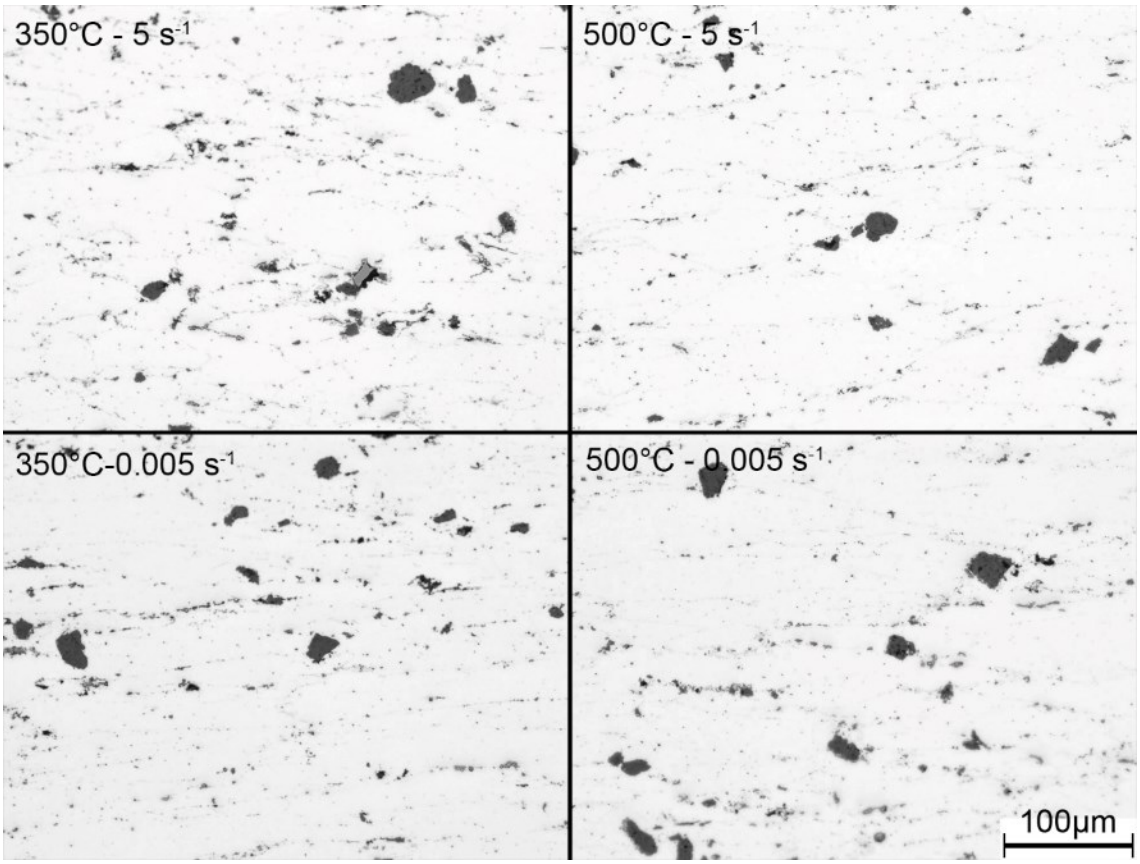

Figure 6-4 Optical micrographs of MMC composition 2C under the hot forging conditions corresponding to the four corners of its corresponding process map. All samples in the T1 condition, strained to 0.70 mm/mm true.

Recovery appears to be the dominant microstructural dissipative mechanism. Again, this mechanism was proposed in 5.6.3., substantiated by EBSD in Figure 5-4. Evidence of recrystallization was not observed. EBSD figures representing the composition 2C under additional deformation parameters (varied temperature and strain rate, otherwise equivalent) (Figure 6-5) agree with these findings. Grains are sized consistent with their sintered counterpart, albeit with an increased aspect ratio due to deformation. Within the grains are many subgrains, with substantial misorientation gradients. Again, this contrasts

the conclusion by Cavalier et al. [101] that the primary microstructural mechanism in hot deformation of a 2618 aluminum MMC was dynamic recrystallization.

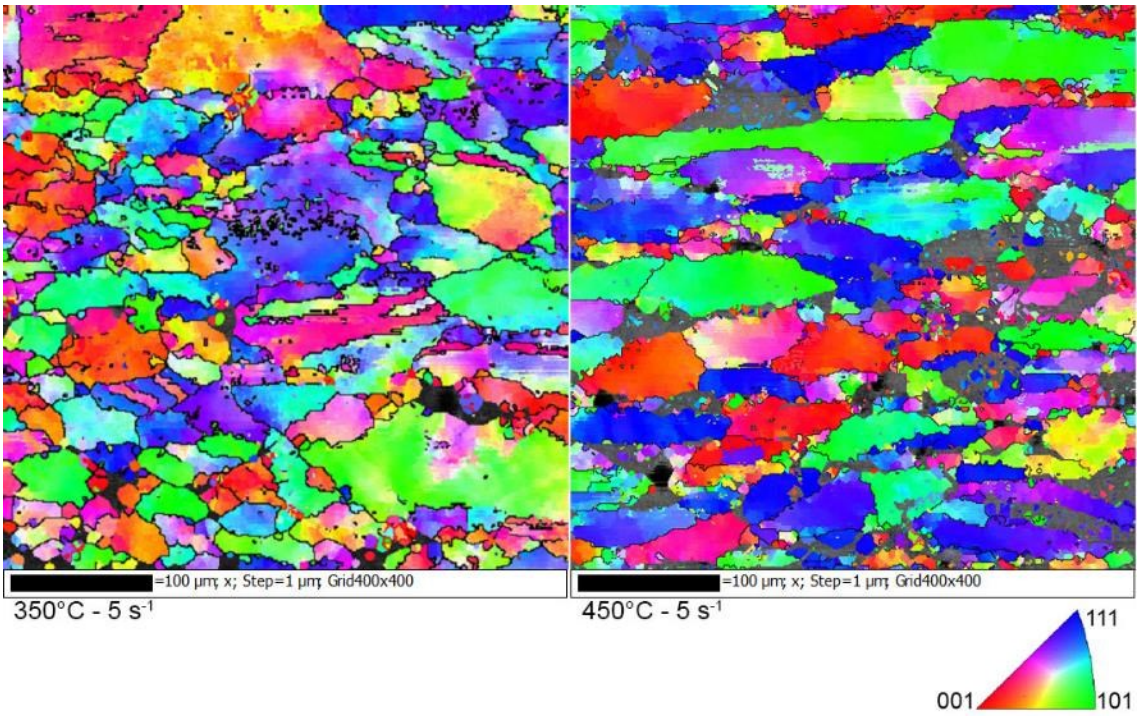

Figure 6-5 EBSD figures of 2C forged to 0.70 mm/mm at 5 s^{-1} and either 350°C or 450°C, exhibiting a microstructure consistent with dynamic recovery

Process maps proved to be another useful tool in understanding the forging response of these MMC materials. Their primary use industrially may be in developing a set of forging parameters than ensure defect free and repeatable mechanical properties in a final product. Clearly, avoiding domains of flow instability have immediate application to the selection of a desirable industrial process. The industrial applications of the efficiency contours have many but less intuitive uses [26]. They can establish processing limits (i.e. a maximum or minimum strain rate for a given temperature) to avoid undesirable

domains on the map. One can design a single step process (i.e. extrusion) such that it occurs at peak microstructural efficiency. Alternatively, a multi step process (i.e. forging, rolling) may be completed in such a way that workability is optimized for the bulk of deformation and followed by a finishing operation in a different domain that promotes a desirable final microstructure (i.e. a domain that invokes DRX). For this study, the findings suggest that dynamic recovery occur uniformly across the map. The usefulness of these maps here is therefor to avoid the calculated flow instability about 350°C and 5 s^{-1} while optimizing the efficiency.

CHAPTER 7. DEVELOPMENT OF A PROCESS TO INVESTIGATE THE MECHANICAL PROPERTIES OF A POWDER FORGED ALUMINUM ALLOY

Gregory A. W. Sweet [1], Bruce W. Williams[3], Alan Taylor [4], Richard L. Hexemer, Jr. [5], Ian W. Donaldson [6] and Donald Paul Bishop [2]

1 – Graduate Student, Dalhousie University, Halifax, Nova Scotia, Canada
2 – Professor, Materials Engineering, Dalhousie University, Halifax, Nova Scotia, Canada
3 – Research Scientist, CanmetMATERIALS, Natural Resources Canada, Hamilton, Ontario, Canada
4 - Vice President – Lightweight Technology, GKN Sinter Metals LLC, Auburn Hills, Michigan, USA
5 – Research Engineer, GKN Sinter Metals LLC, Conover, North Carolina, USA
6 – Director of R&D North America, GKN Sinter Metals LLC, Auburn Hills, Michigan, USA

Status: Published Conference Proceedings. Presented at MPIF Powdermet 2017 in Las Vegas, NV, USA. Presented June 13-16, 2017.

Author Contribution: The following experimental procedures, results and discussions were completed by G.A. Sweet, with technical guidance, reviewer and editorial roles played by the subsequent authors.

7.1 Forward to Chapter 7

At this point the authors had proven the suitability of many material systems to hot deformation on a lab scale. Furthermore, substantial increases in mechanical properties were anticipated based on analogous hot deformation lab work done within the group. Standard tensile and fatigue specimens were unobtainable from Gleeble-forged products, necessitating larger preforms and a procedure to hot deform them. This project investigated processing larger, high sinter quality preforms and developing a procedure to emulate the Gleeble test apparatus using a higher capacity load frame.

7.2 ABSTRACT

The objective of this work was to develop a forging process in which aluminum powder metallurgy components can be characterized to assess a wide variety of mechanical properties. Conventional lab-scale upset forging equipment involves the processing of limited amounts of material, typically on the order of tens of grams. Investigation of fundamental mechanical properties such as tensile or fatigue using standardized test specimen is therefore prohibitive. Given the persistent nature of the internal oxide network within aluminum PM compacts and the ability to disrupt it through elevated temperature plastic deformation, the observation of such mechanical properties is of considerable interest. This study follows the development of the process in which samples on the order of hundreds of grams are forged and characterized. The flow behaviour of a commercial aluminum PM alloy was modeled using a Gleeble 3500 thermal-mechanical system. Larger preforms were designed and tested using an Interlaken 1100 kN hydraulic press with heated tooling. Considerations included lubrication and frictional behaviour, specimen geometry and surface conditions. Significant gains in mechanical properties of an aluminum PM alloy were observed because of isothermal forging. Modulus, ductility and fatigue strength all saw remarkable gains over the sinter T6 condition. It is believed that these were largely underpinned by the elimination of residual porosity and a considerable disruption of the residual oxide networks that would have persevered in the sintered product.

7.3 Introduction

Aluminum powder metallurgy has generally been limited to typical compact, sinter, size and optional heat treats. It has generally been used for the manufacture of components where mass is of critical importance. Also due to the PM process they tend to be high volume automotive parts that benefit from PM's cost competitiveness. However, most of the currently available powder metallurgy aluminum alloys have similar mechanical properties to their die cast counterparts which has restricted their use. Recent developments in powder metal Aluminum alloys and the auto industries need to reduce mass as a way to satisfy lower government CO_2 mandates [102] and reductions in overall fleet fuel mileage has resulted in increased interest in high performance PM Aluminum materials. One way to improve properties is to use powder forging (PF) technology like that used for PM steel. The use of PF with high deformation has shown the ability to completely close open porosity [20] and significantly improve mechanical properties [92]. This work seeks to explore basic powder forging process parameters and how they relate to mechanical properties.

7.4 Materials

The material used in this study was an aluminum powder metallurgy (APM) alloy made of constituent powders blended to a nominal composition of 3.0 wt% Cu, 1.5 wt% Mg and 0.5 wt% Sn. The nature of these powders is explained in Table 7-1. A powdered

lubricant, Licowax C, was added at a concentration of 1.5 wt% to facilitate die compaction.

Table 7-1 Chemical nature and particle size of constituent metal powders utilized.

Element	Powder Supplier	Powder Type	Particle Size (D_{50}, mm)
Aluminum	Ampal	Elemental	99
Copper	Ecka Granules	50:50 Al: Cu Master Alloy	16
Magnesium	Tangshan Weihao	Elemental	16
Tin	Ecka Granules	Elemental	12

7.5 Experimental Techniques

Samples of the APM alloy blend were uniaxially compacted in series of cylindrical floating dies measuring 15 mm, 30 mm, or 50 mm in diameter using a Satec systems model 5594-200HVL 1000 kN load frame. Compacts were then sintered at 600°C in an industrial mesh belt furnace used in commercial APM manufacturing under flowing, high purity nitrogen. Sintered specimens were then open die upset forged in accordance with a true stress and true strain convention. Tests were carried out isothermally at 350°C, 400°C, 450°C and 500°C under a controlled array of strain rates that ranged from 0.001 s^{-1} to 5 s^{-1}. Forging trials were completed using two load frames. The first was a Gleeble 3500 thermal-mechanical system. Tests with this system were limited to 15mm diameter specimens machined to final dimensions of 10 mm diameter and 15 mm height to ensure

compatibility with the test frame and its load capacity. Testing was conducted in closed-loop strain rate control using a diametrical strain "C" gauge. Specimen temperature was controlled through the application of direct resistant heating coupled with a type-K thermocouple welded to the circumference. All samples were isothermally held at the test temperature for 15 seconds prior to testing and water quenched immediately after reaching the strain set point. Sintered pucks with nominal diameters of 30 and 50 mm (the later hereafter referred to as "upscaled specimens") were upset forged under isothermal conditions in an Interlaken Technology press with a 1100 kN force capacity and a maximum stroke rate of 5000 mm/min, a speed which was obtainable by a hydraulic accumulator system. This frame was instrumented to acquire load and displacement data for the complete duration of a test and was equipped with heated P20 tool steel platens allow for open die isothermal forging. Samples were heated in a box furnace for 3 hours at the desired test temperature prior to being transferred to the press for forging. Each specimen was water quenched immediately after forging was completed. The lubrication strategy for Gleeble samples was a nickel-graphite anti-seize compound applied at the sample-platen interface. For tests in the Interlaken frame, samples were coated in either an aerosol boron nitride suspension or a graphite spray immediately prior to heating. Ring compression tests were also carried out on the Interlaken press to assess frictional conditions. The ring geometry was 27 mm OD x 13.5 mm ID x 9 mm tall.

Density measurements were taken using water immersion coupled with vacuum assisted oil impregnation in accordance with MPIF standard 42. Values are reported as a

percentage of the maximum theoretical value attainable. Metallography was completed by mounting specimens in epoxy and then polishing on a Struers Tegramin semi-automatic polishing system using standard oil-based diamond suspensions. Samples were etched using Keller's reagent before imaging with an Olympus BX51 optical microscope. A Tecnai OSIRIS Transmission Electron Microscope (TEM) was used on a forged and T6 heat treated sample to study the microstructure and chemical nature of prior particle boundaries (PPB) in the deformed material. Tensile tests were carried out on the same load frame as used in compaction, with a 50 kN load cell set up in tension and an Epsilon model 3542 extensometer that remained attached to the sample through the point of fracture. Tests were carried out per MPIF standard 10. All specimens were heat treated to the T6 state (solutionized at 510°C in air for 2 h, water quenched, aged at 190°C for 10 h). Calorimetry measurements were performed using an SDT Q600 Differential Scanning Calorimeter (DSC) using the material in the T1 condition. DSC samples were heated to 600°C at a rate of 10°C/min under flowing nitrogen. Error in tensile and density tests represents one standard deviation about the mean of no less than three samples. Fatigue tests were carried out on an Instron model 1332 servo hydraulic load frame equipped with a fixture for three-point bending. Tests were based on the staircase statistical method outlined in MPIF standard 56 using an R-ratio of 0.1 and a runout criterion of 10^6 cycles. Error in fatigue tests represent the 10% and 90% confidence interval in accordance with the calculations recommended in MPIF standard 56.

7.6 Results and Discussion

In the context of fundamental studies, an advantageous forging sequence is one designed such that meaningful mechanical property data can be extracted from the deformed products. The following section outlines an example of a process whereby lab-scale Gleeble experiments eventually led to the design and successful processing of upscaled forging tests amenable to mechanical property assessments. In this instance, an APM alloy is used as an exemplary material to validate the feasibility of the forging process and quantitatively ascertain the performance gains achievable through it. In all instances, the magnitude of gains instilled through forging were taken relative to counterpart slugs of the same material that were not plastically deformed (i.e. sintered condition) but also heat treated to the T6 state.

7.6.1 Lab Scale Forging

In the first stage of process development, research was restricted to the smallest (i.e. 10 mm diameter) samples considered and the response of these specimens to lab scale forging using a Gleeble 3500 thermomechanical testing device. An image of the sample chamber of this instrument is shown in Figure 7-1. In operation, a cylindrical specimen is placed between the electrically conductive platens such that a specified current can then be passed through the sample and thereby heat it in a highly controlled manner. Stress is then applied via a closed loop controlled hydraulic ram, capable of strain rates on the order of 5 s^{-1}. Using this instrument, as-sintered samples were successfully

deformed to a maximum true strain of 0.70 mm/mm at isothermal temperatures of 350, 400, 450 and 500°C. Under these conditions, all samples were free from any surface defects. However, it was apparent that friction prevailed at the specimen/platen interfaces as all specimens showed evidence of barrelling, despite the use of a high temperature lubricant at the specimen-platen interfaces.

The principal reason for completing Gleeble-type tests was that they enabled the acquisition of compressive true stress versus true strain data (so called "flow stress curves") for the material under a wide range of forging conditions in a reasonably short period of time. Such data can be fed directly into finite element simulations to facilitate process modelling and aid in the design of upscaled forging processes through the provision of critical data on attributes such as peak flow stress and how this varies under different forging conditions.

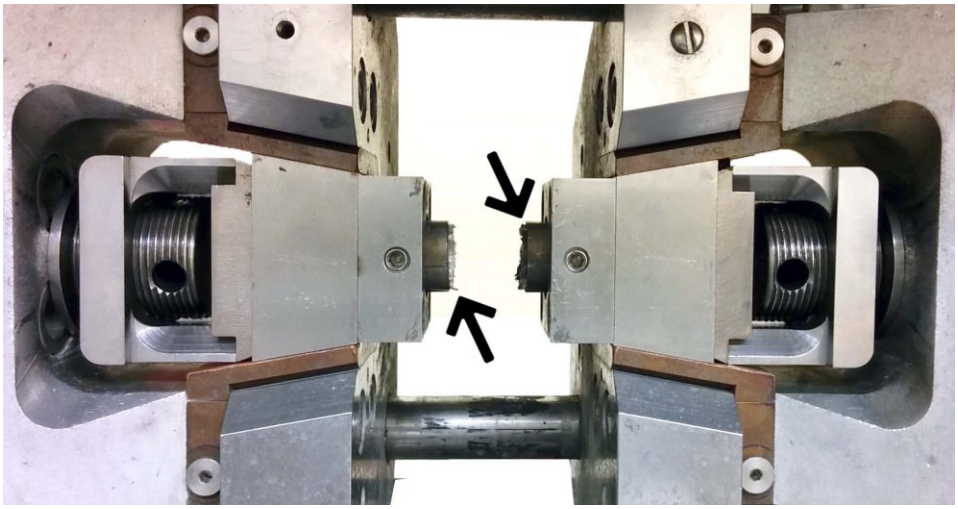

Figure 7-1 Specimen chamber of a Gleeble 3500 thermomechanical tester. Arrows indicate the location of the lubricated forging platens, between which the sample was placed, heated, and subsequently upset forged.

A suite of flow stress curves for the exemplary material studied are shown in Figure 7-2. In all cases, the maximum compressive strain was fixed at 0.70 mm/mm to ensure that the diameter of forged product did not exceed that of the platens. Hence, final strain values were all identical and could not to be used to infer the relative extent of hot ductility inherent to the material. Nonetheless, such flow curves are critical in characterizing a material prior to upscaling, as they accurately dictate the minimum force capacity requirements needed when forging larger specimens. Critically, the peak or maximum flow stress represents the point at which the material resists deformation the most. Regardless of temperature, this stress was consistently achieved at relatively low strains, followed by a monotonic decay. However, the nature of this decay as a function of deformation strain varied considerably with both temperature and strain rate. In certain instances, the peak flow stress preceded a domain wherein no appreciable change in flow stress occurred. This behaviour accompanied samples deformed in the combinations of high test temperatures and slow strain rates, such as those deformed at temperatures of at least 450°C and strain rates of, at most, 0.05 s^{-1}. For example, a specimen deformed at 500°C and 0.005 s^{-1} changed from 18.0 MPa at a strain of 0.01 mm/mm to 16.9 at the maximum strain of 0.70 mm/mm. On the contrary, when deformed at 350°C and 0.005 s^{-1}, a reduction in flow stress from 87.1 to 66.4 MPa was observed over the same range of strain. All tests conducted at 350°C and 400°C or strain rates of 0.5 s^{-1} or 5 s^{-1} exhibited a decrease in flow stress of at least 5 MPa.

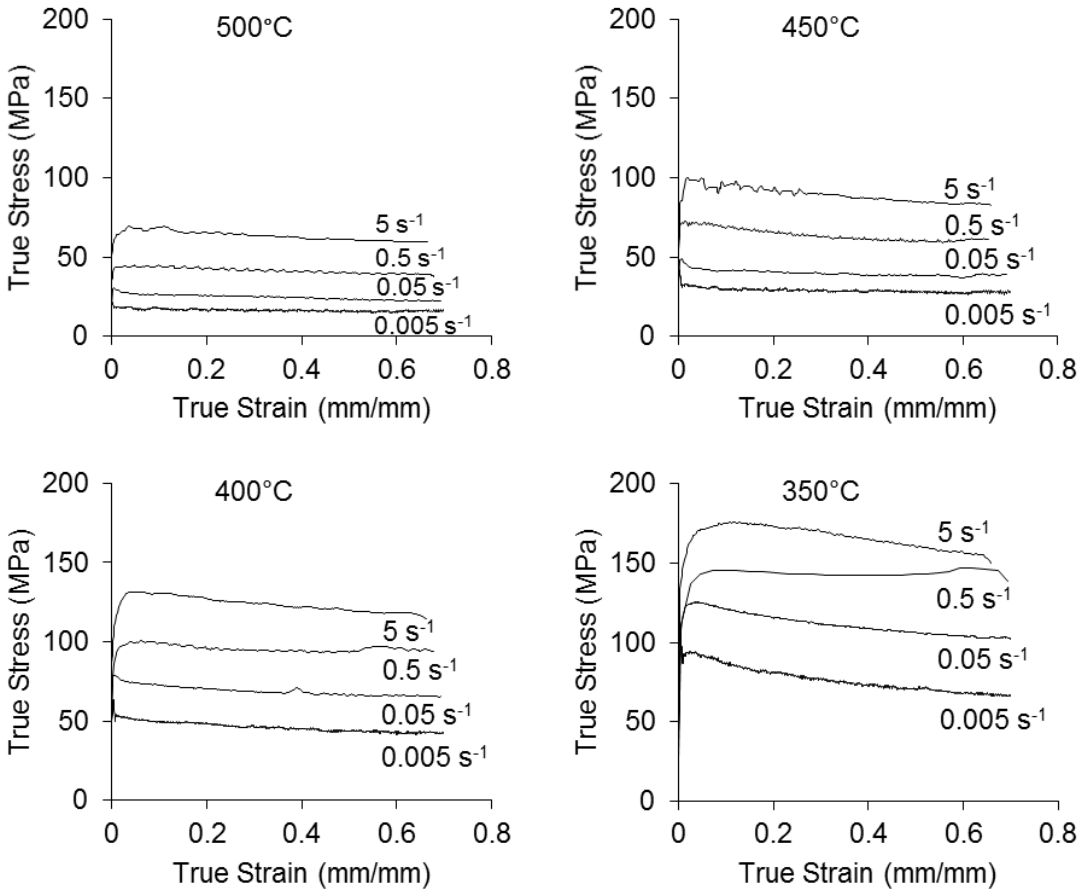

Figure 7-2 Flow stress curves generated from samples of the sintered APM alloy when isothermally forged under various temperatures and strain rates.

The exemplary APM alloy of study had a nominal chemistry of Al-3Cu-1.5Mg-0.5Sn. As such, this was a precipitation hardenable system would be principally strengthened through the formation of S-type (Al_2CuMg) precipitates via the following sequence:

$$Super\ Saturated\ Solid\ Solution \rightarrow GPZ \rightarrow S' \rightarrow S$$

Although such precipitation events are deliberately instilled in the material via the application of post-forge heat treatment procedures, they can also transpire at kinetically

influential rates during thermo-mechanical working itself given the utilization of relatively high temperatures and extensive levels of plastic strain. Accordingly, in scenarios wherein the starting material contains underaged precipitates, heating at moderate temperatures can evolve these into a more effective strengthening phase thereby increasing flow stress. However, when peak or overaged precipitates exist and/or when forging temperatures exceed the alloy solvus, the precipitates will either evolve into a less effective strengthener or dissolve into solid solution. Both concepts thereby invoke appreciable softening of the material. Collectively, these transitions complicate the forging process as they impart appreciable changes to the microstructure *in-situ* and in turn, the mechanical properties of the alloy during the deformation cycle itself.

To study these concepts in more detail, a sample of the APM alloy was extracted from the as-sintered preform and assessed using DSC. The resultant thermograph is shown in Figure 7-3. Here, it was obvious that an array of thermal events occurred upon heating as evident by the presence of endo and exothermic peaks. Aluminum alloys with similar compositions to the APM system of interest have been studied extensively through DSC. It is known that dissolution events and melting are synonymous with endothermic peaks while precipitation events give rise to exothermic transitions. Hence, the most plausible reactions can be assigned to each peak as annotated in Figure 7-3. As described previously, the work softening phenomenon was most evident at low temperatures. At 350°C the DSC trace suggests that the material was being deformed at a temperature wherein the precipitation/coarsening of S phase should have proceeded rapidly thereby giving rise to a microstructure largely commensurate with annealing (i.e. relatively large

and widely spaced precipitates of S-phase). Accordingly, the shape of the resultant flow curve was an inflated peak flow stress followed by work softening as precipitates coarsened, lost coherency and otherwise became less effective at impeding dislocation motion *in-situ*.

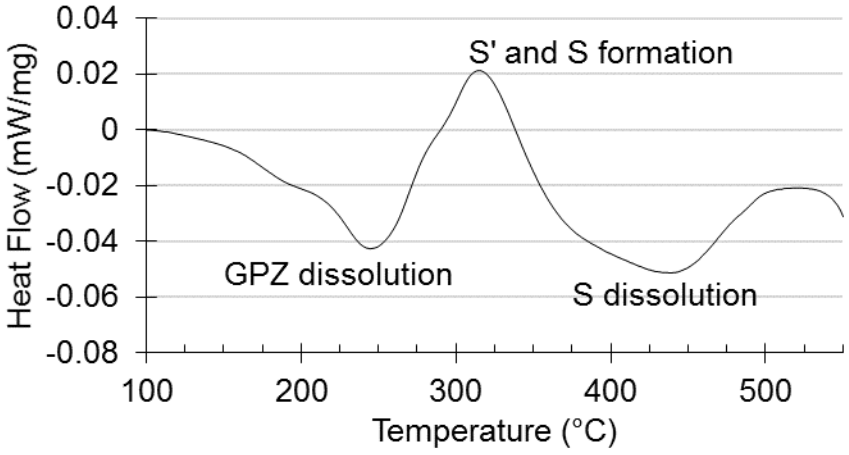

Figure 7-3 DSC thermogram of the APM material in the as sintered (T1) condition.

All the higher temperatures considered lie within the confines of the S phase dissolution trough. This implied that any pre-existing precipitates should eventually be dissolved into solid solution during the forging process. However, this would not necessarily ensure that a common microstructure would prevail given that the kinetics of dissolution and solid solubilities of copper and magnesium would both increase with the progressive rise in forging temperatures from 400 to 500°C. As such, correspondingly lower and lower concentrations of precipitates would be expected to exist within the alloy as forging temperature increased. This then led to progressive reductions in peak flow stresses (i.e. σ_{max} ~ 130 MPa at 400°C/5 s^{-1} versus σ_{max} ~ 65 MPa at 500°C/5 s^{-1}) and a

reduced propensity for work softening; especially at 500°C wherein the post-peak change in flow stress was effectively nil.

Figure 7-4 shows the change in geometry of a typical sample due to deformation in the Gleeble apparatus. The size of deformed samples is exceedingly small for the execution of standardized physical and mechanical testing per MPIF and ASTM standard protocols. For this reason, deformed samples of this nature are very limited in terms of the material characterization techniques that can be applied. Hence, it was only the density and microstructural attributes that could be investigated as discussed below.

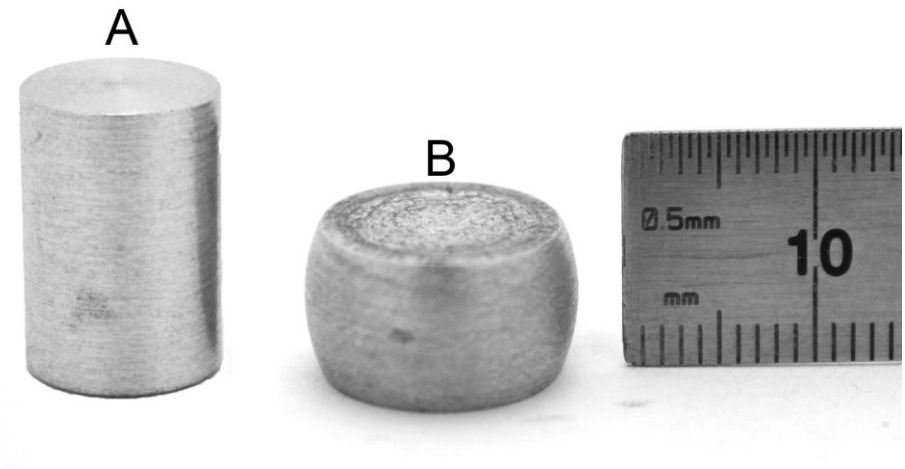

Figure 7-4 Pressed, sintered, and machined Gleeble specimens (a) before and (b) after deformation at 450°C ($\dot{\varepsilon} = 0.5$ s^{-1}; $\varepsilon = 0.70$ mm/mm).

An investigation into the effects of forging on the density of the APM alloy showed promising results. In all cases the density of forged samples exceeded the mean value of the as-sintered counterpart specimens. The relative sintered density of the material was determined to be near theoretical at 99.53%. However, forging increased this to a final value of 99.94% which impinged on the full theoretical limit. This value represented an

average calculated from all the lab-scale forged specimens as there were no obvious trends suggestive that final density was directly influenced by temperature or strain rate.

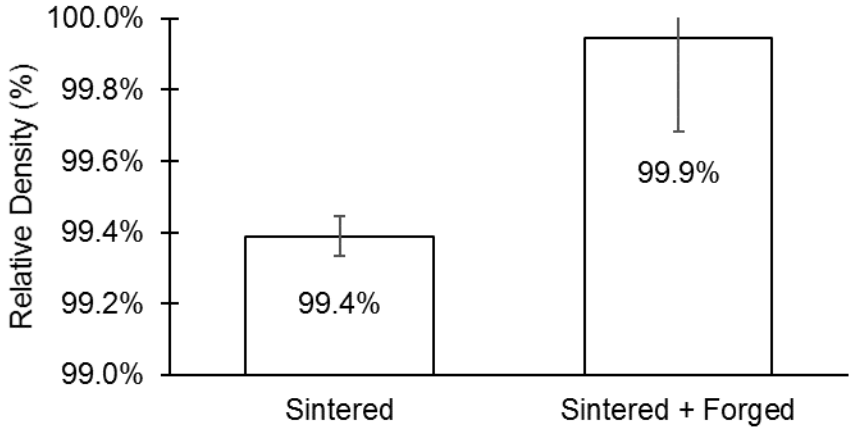

Figure 7-5 Comparison of the relative densities measured for sintered and sintered + forged samples.

Examination of the microstructure in transverse and axial orientations confirmed that samples were devoid of any obvious cracking. As alluded to earlier, friction between the sample and forging platens produced the barreled shape seen in Figure 7-4. Accordingly, a region of material deformed to a lesser extent than the bulk (often referred to as the 'dead zone') was observed adjacent to the platens. This was a direct result of the friction conditions. Furthermore, the outer circumference of the sample, the barreled surface, would have experienced tensile forces during deformation. Hence, although no fracture was observed in either of these areas, reductions in the efficiency of pore collapse would be expected. Based on this knowledge, the microstructures of upset forged cylinders are commonly discretized into the three zones as shown schematically in Figure 7-6a. Microstructurally, the sintered compact shown in Figure 7-6b exhibited a structure

consistent with an APM alloy of a high sinter quality. In this sense, pores (black phase) were isolated, heavily rounded, and remained located along grain boundaries. Figure 7-6c shows the microstructure of the same material after forging within Zone II. Here, forging-induced plastic deformation was clear as the grains were now elongated in directions orthogonal to the loading axis. Pores were collapsed and elongated as well consistent with the heightened density of the sintered + forged compact. Furthermore, prior particle boundaries in the sintered + forged sample were much less distinguishable than in the sintered compact. Hence, it was inferred that some level of disruption of the semi-continuous network of oxide/nitride phases that would have invariably existed at these locations had transpired. This concept is discussed in more detail in the section dedicated to upscaled forging trials.

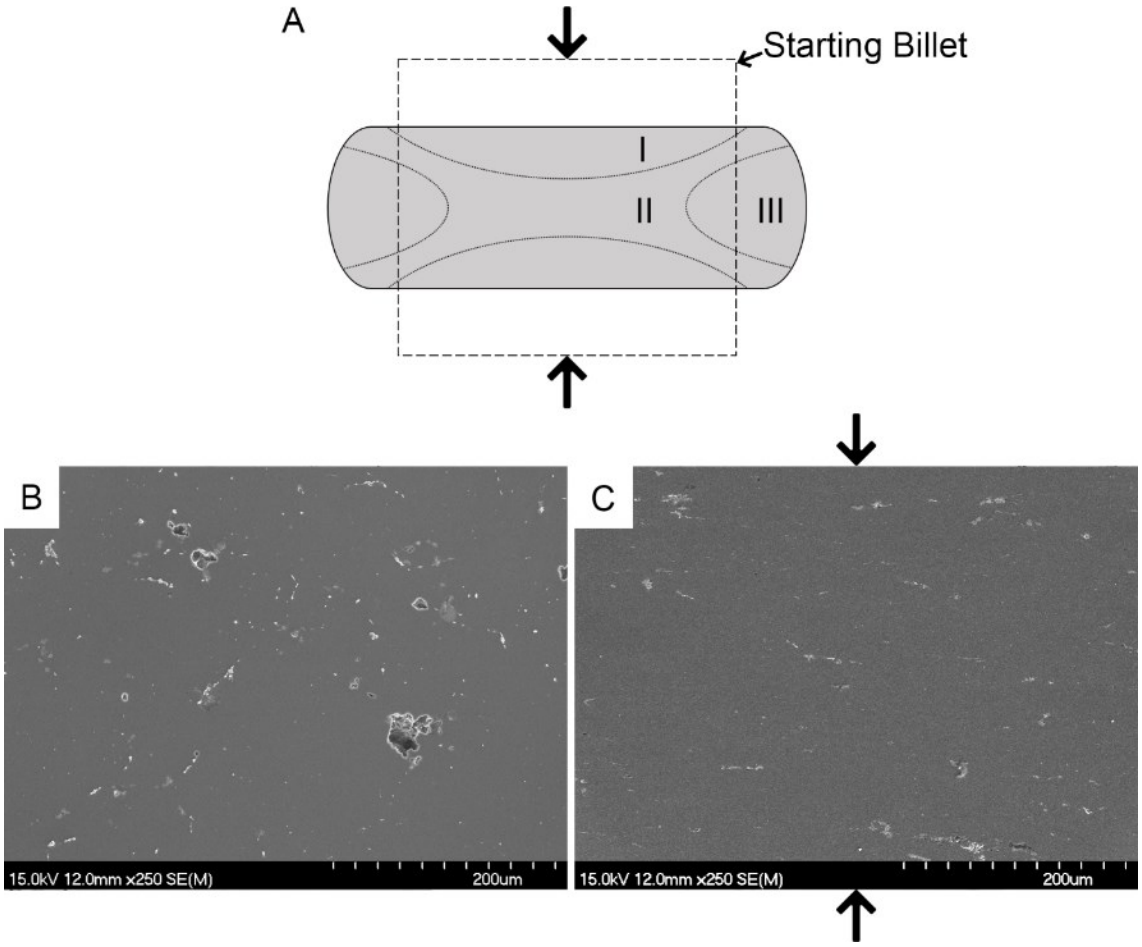

Figure 7-6 (a) Schematic of the three distinctive zones that form during inhomogeneous deformation due to friction during compression tests (adapted from [100]), accompanied by the microstructures of the alloy in the (b) as-sintered and (c) sintered + forged condition. The latter micrograph was taken from the bulk of the material (zone II). Arrows indicate forging direction.

7.6.2 Upscaled Forging Design

Objectively, quantification of the mechanical properties of APM materials in a sintered + forged condition was critical. Hence, the ability to machine standard sized mechanical property specimens such as TRS bars, tensile, and hourglass rotating bending fatigue bars

from the forged product was likewise necessary. This necessitated the processing of sintered preforms substantially larger than those amenable to Gleeble-type instruments. Through an iterative design process, two appropriately sized preforms were selected as they could be forged under meaningful conditions within the capabilities of the Interlaken press (Figure 7-7) while affording a sintered + forged product geometry suitable for extraction of the desired test specimens. These two geometries, shown in Figure 7-8, are outlined in Table 7-2 along with the geometries of the test specimens that can be machined from the sintered + forged part when deformed within a prescribed range of applied true strain. In many cases, multiple specimens could be cut from a single forging. However, in others, the full range of specimen geometries desired could not be accommodated (those denoted by "**N/A**").

(a)

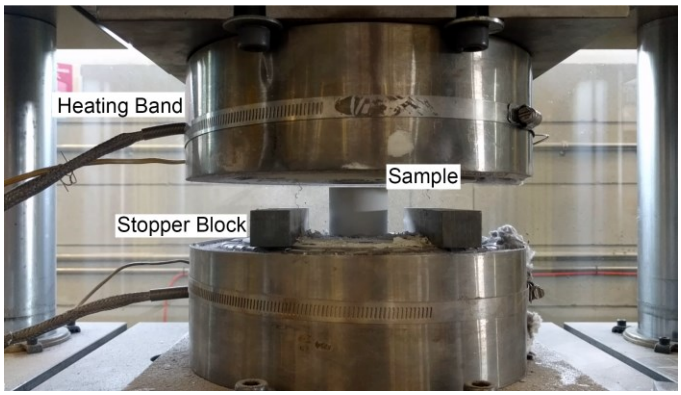

(b)

Figure 7-7 (a) Interlaken hydraulic load frame utilized for upscaled isothermal forging trials. (b) Close up of the heated tooling, sample and stopper block arrangement.

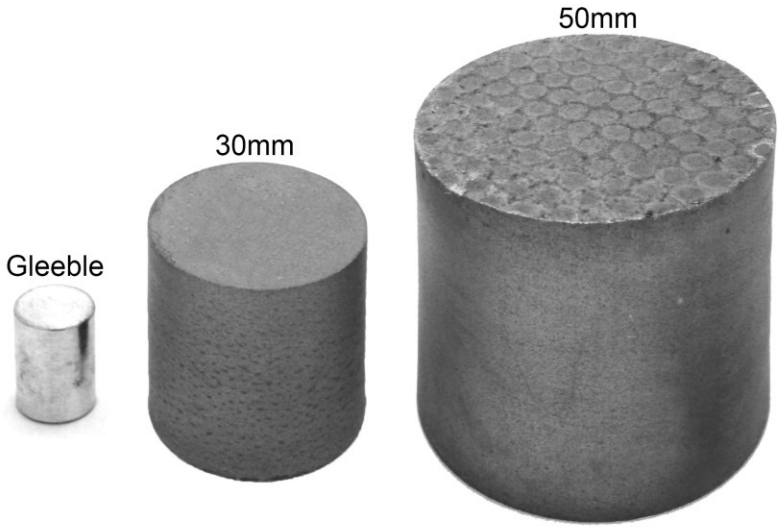

Figure 7-8 Comparison of a machined Gleeble sample alongside the sintered 30 mm and 50 mm preforms utilized in upscaled forging trials.

The 30 mm diameter preforms required a fraction of the powder of 50 mm diameter samples, while only affording a useful strain range whereby TRS bars and sub-sized tensile specimens (i.e. those with a 12.5 mm gauge length) were extractable. Full sized tensile bars (25.4 mm gauge length) and those required for rotating bending fatigue could not be extracted from these smaller preforms under any level of strain. The larger preforms afforded a greater breadth of attainable specimen geometries. The range of strains in which TRS and substandard tensile specimens were extractable now extended from 0.00 mm/mm, a non-deformed sample, up to 1.85 mm/mm and 1.65 mm/mm respectively. This allows for a thorough, uninterrupted investigation into properties from the as-sintered to a heavily deformed condition. Furthermore, standard sized tensile specimens could be produced at strains greater than 0.90 mm/mm. Similarly, hourglass fatigue samples can be extracted above this strain as well.

Table 7-2 List of preform geometry details and the types of mechanical property specimens that could be extracted under specific levels of applied forging strain.

Preform (OD x H, mm)	Mass (g)	Extractable Sample			Required Forging Strain (mm/mm)
		Type	Nominal Size (mm)	MPIF Std. #	
30 x 30	55	TRS	6.4 x 12.7 x 31.7	41	0.30 – 1.50
		Sub-Sized Tensile	8 x 8 x 40	10 mod.	0.65 - 1.25
		Tensile	8 x 8 x 75	10	N/A
		RBF	10 x 10 x 75	56	N/A
50 x 44	215	TRS	6.4 x 12.7 x 31.7	41	0.00 – 1.85
		Sub-Sized Tensile	8 x 8 x 40	10 mod.	0.00 – 1.65
		Tensile	8 x 8 x 75	10	0.90 – 1.65
		RBF	10 x 10 x 75	56	0.90 – 1.40

N/A – Specimen could not be extracted from the sintered + forged product regardless of the amount of forging strain applied.

Geometrically, the 50 mm preform was the most appropriate, as it afforded research over the greatest breadth of strain while providing a means to engage all manners of mechanical testing sought. However, the force required to forge these larger specimens also required consideration in the context of the forging press capabilities. Accordingly, Table 7-3 qualitatively represents the range in forging parameters in which a preform can be processed within the Interlaken system employed. This go/no go chart specifically indicates under a given true strain rate and isothermal forging temperature whether the preform can be deformed to a critical thickness. This thickness, 8mm, was chosen as the upper limit of deformation that would still produce full sized tensile specimens. The

critical thickness is based on the maximum achievable strain whereby a tensile specimen can be extracted using the Interlaken 1100 kN instrumented hydraulic press. Both 30 mm and 50 mm preforms are considered. Calculations are performed assuming the peak flow stress values extracted from Figure 7-2. The combinations of true strain rate and temperature labelled 'N' indicate a situation where the required load exceeds that of the forging system. By their smaller size, 30 mm preforms were not restricted by temperature or true strain rate. Conversely, 50 mm preforms required greater loads and thus face several restrictions. At 350°C and strain rates greater than 0.05 s^{-1}, as well as 400°C and 5 s^{-1}, the peak flow stresses would be sufficiently high to limit deformation. While deformation is entirely possible under these conditions, achieving 8 mm final thickness was prohibitive. Although not represented in Table 7-3 the ram displacement rate required to deform both preform geometries at 5 s^{-1} exceeded the capacity of the frame. However, 1 s^{-1} was attainable and therefore implemented as the upper limit.

Table 7-3 Go/No Go table for the ability to forge the 30 mm and 50 mm preforms to a critical thickness of 8 mm at various strain rates and temperatures.

30 mm / 50 mm		Strain Rate (s^{-1})			
		0.005	0.05	0.5	5
Temperature (°C)	500	Y	Y	Y	Y
		Y	Y	Y	Y
	450	Y	Y	Y	Y
		Y	Y	Y	Y
	400	Y	Y	Y	Y
		Y	Y	Y	N
	350	Y	Y	Y	Y
		Y	N	N	N

Proper lubrication during hot work is critical as it can enhance the homogeneity of deformation and simultaneously reduce the load demands of the press. Interfacial friction between a material and a forging platen inhibits sliding, and thereby constrains adjacent material from deforming. Minimizing the coefficient of friction is therefore critical to homogenous deformation. Ring compression tests using machined rings of OD:ID:Height = 6:3:2 ratio (Figure 7-9) were used to determine the coefficient of friction (COF) for tests using several lubrication strategies and test temperatures (Table 7-4). Lubricants were limited to boron nitride and graphite sprays, applied to cold samples. Rings were deformed to an approximate reduction in height of 50%. The reduction in height and the percent decrease of the mean inner ring diameter were recorded. Approximate COF values were then extrapolated from curves published by Schey [103] (Figure 7-9). Conditions that produce a COF much greater than 0.30 result in "sticking" friction. Graphite lubricant applied in a single coat proved relatively ineffective at preventing sticking friction during deformation. At 450°C and 500°C the COF was more than the measurement scale. A marginal improvement was observed when deformed at 400°C. Graphite spray applied in several coats gave a more desirable result. However, a single application of BN spray proved to be the best option. Hence, this lubricant strategy was then adopted for all upscaled forging trials.

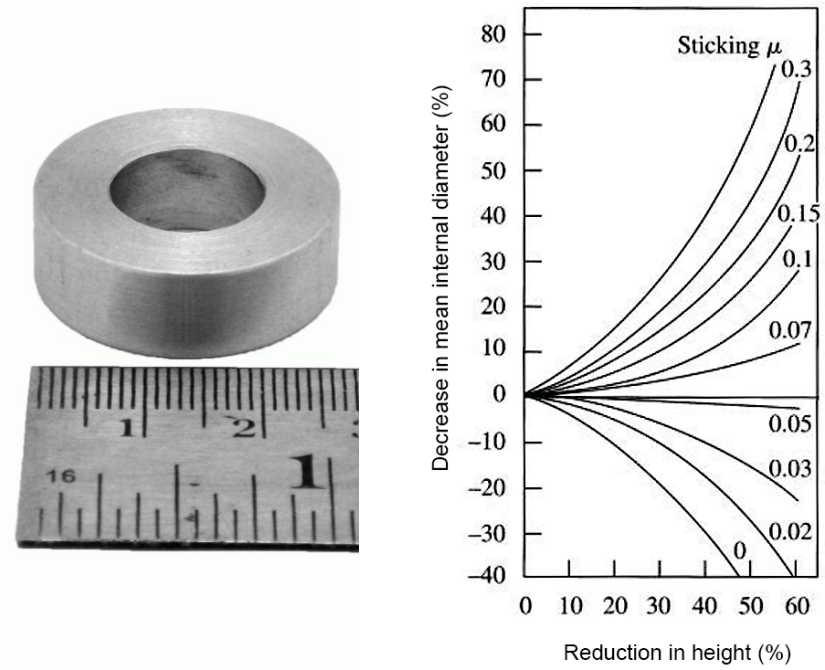

(a) (b)

Figure 7-9 (a) Nondeformed ring compression test specimen and (b) the corresponding Coefficient of Friction calibration plot. Calibration plot adapted from [103].

Table 7-4 Coefficient of friction values measured at the different temperatures and lubrication strategies considered.

Lubricant Strategy	**Temperature (°C)**	**Coefficient of Friction**
Graphite	400	0.29
Graphite	450	>0.30
Graphite	500	>0.30
Layered Graphite	400	0.24
Boron Nitride	400	0.22

Throughout this study, the convention was chosen as true stress and true strain. Testing on the Gleeble was straightforward due to an inherent closed loop feedback system coupled with the direct measurement of strain via the attached C-gauge extensometer. This fostered the attenuation of largely static true strain rates throughout the complete deformation cycle. However, the operational nature of the Interlaken press coupled with the use of larger samples required open-loop ram displacement. Here, the ram control on the Interlaken was manipulated to achieve a static true strain rate having a consistency aligned with that achieved in the more precise Gleeble system. Forging tests were simulated with the preform dimensions as well as the desired forged dimensions. For a given sample and set of forging parameters, a required data set describing ram position versus time was then extracted. A regression of this ram behaviour was then fed into the controlling software.

Having applied the procedure, Figure 7-10 directly compares data on the true flow stress and true strain rate as functions of applied true strain for Gleeble and Interlaken tests. All samples were deformed at a test temperature of 450°C. The flow curves for the samples deformed using the Interlaken frame compared well to those acquired with the Gleeble. In all cases, the peak flow stress values interpolated well with this prior data. Following the peak flow stress value, the materials exhibited a work softening behaviour. Whereas the Gleeble-sourced flow curves exhibited monotonous decays, the larger samples exhibited work softening prior to a secondary rise in flow stress synonymous with work hardening. This discrepancy may be attributable to an increased coefficient of friction in the upscaled forging experiments. Gleeble samples and ring compression test were

inherently machined whereas upscaled preforms were deformed with their as-sintered surface conditions left intact. This difference in surface finish likely increased the friction coefficient above that presented in Table 7-4. Furthermore, the interfacial coefficient of friction has been shown to increase with increasing strain [104], effectively accelerating friction effects with strain. Tests performed on the Interlaken frame exhibited a decrease in flow stress as the strain approached the target value. This is attributable to the decrease in true strain rate at such high strains, as discussed below.

The plots of instantaneous strain rate (Figure 7-10b) show comparatively consistent values for both test systems. Regardless of strain rate, either frame could rapidly achieve the target strain rate and maintain it for most of the test cycle. As the strain values exceeded approximately 0.8 mm/mm the instantaneous strain rate using the Interlaken frame began to decay. This deviation can be attributed to the difference in the theoretically required displacement rate and that of the regression fed into the controlling software. Furthermore, hydraulic ram deceleration effects may be occurring. To curtail this issue, further optimization of the strain rate for this frame was executed using stopper blocks coupled with regressions exceeding the target strain values. Stopper blocks were machined from cold rolled plain carbon steel to a thickness corresponding to the desired final true strain of a given test. The regression was modified such that the target strain exceeded that which could be achieved with the stopper block in place. During testing, a sample was deformed uninhibited until it reached the target strain, where the stopper blocks would contact both dies and physically stop the test in an abrupt manner. An

exemplary instantaneous strain rate plot is exhibited in Figure 7-10b with 'SB'. Here, the true strain rate is held exceptionally close to the target strain rate up until the target strain.

The corresponding flow stress plot in Figure 7-10a, 'Interlaken – 0.1 s^{-1} w/SB' showed no evidence of strain rate deceleration throughout deformation. The peak flow stress values for lab scale and upscaled forging experiments are compared in Figure 7-11 as a qualitative means of determining the comparability between the two different processing routes. Peak flow stress values for true strain values up to -0.50 mm/mm were taken to circumvent the apparent strain hardening effects due to the deterioration of friction conditions at higher strains. Evidently, the upscaled forging experiments produced peak flow stress values that largely agreed with those found in lab scale work. Upscale experiments at 400°C had flow stresses consistently below what would be expected from lab scale work. Extended thermal exposure of the upscaled specimen had likely contributed to this behaviour. In this sense, deformation in the Gleeble system was engaged immediately after a rapid heating and a 15 s isothermal hold. Conversely, upscaled specimens were heated in a box furnace and held for 3 h at temperature to ensure temperature homogeneity. As such, any strengthening phase in the upscaled specimen is likely to have overaged to the point where it no longer strengthened the material to the same degree as the equivalent Gleeble test.

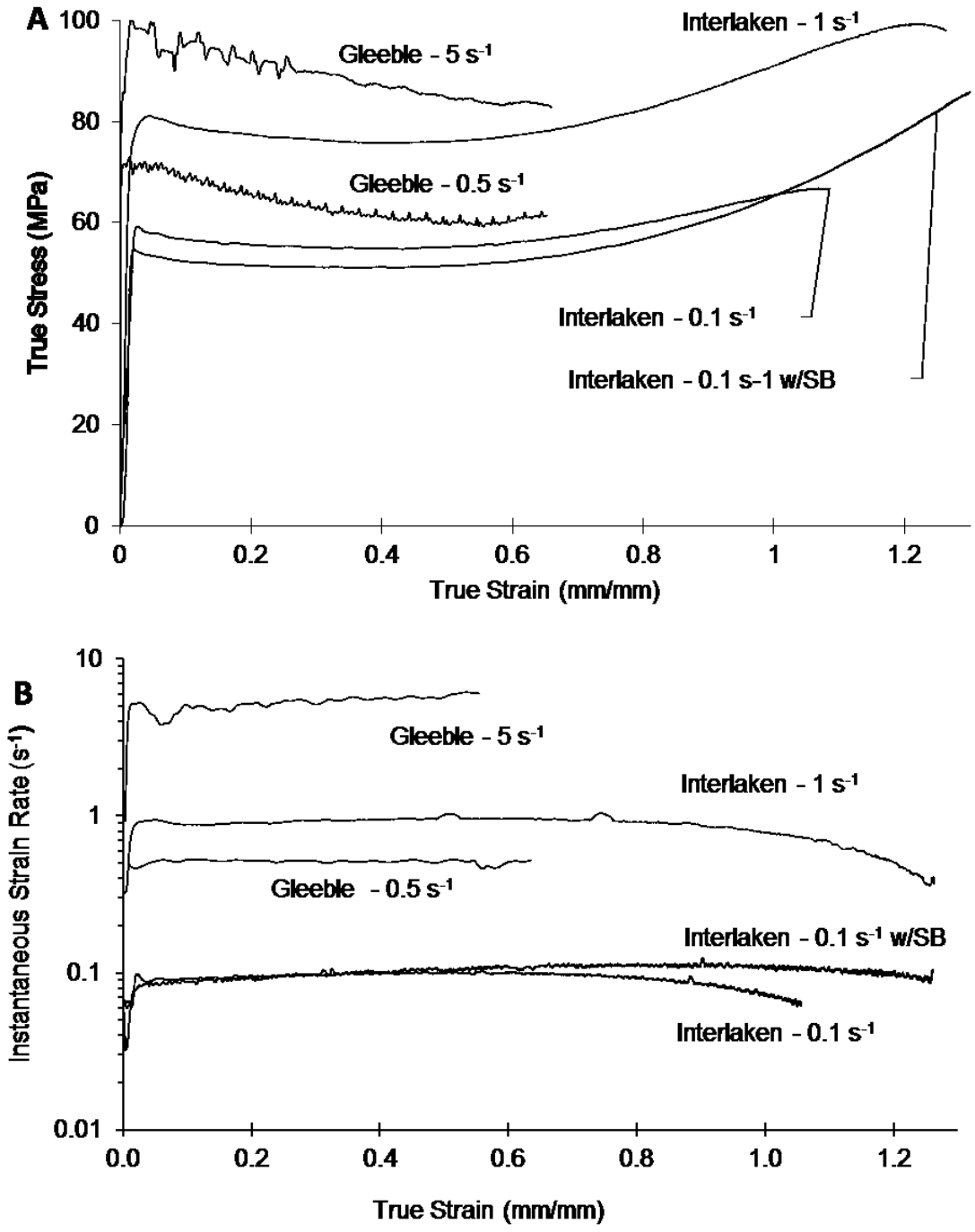

Figure 7-10 Data on the (a) true flow stress and (b) true strain rate as functions of applied true strain for samples deformed using the Gleeble and Interlaken systems.

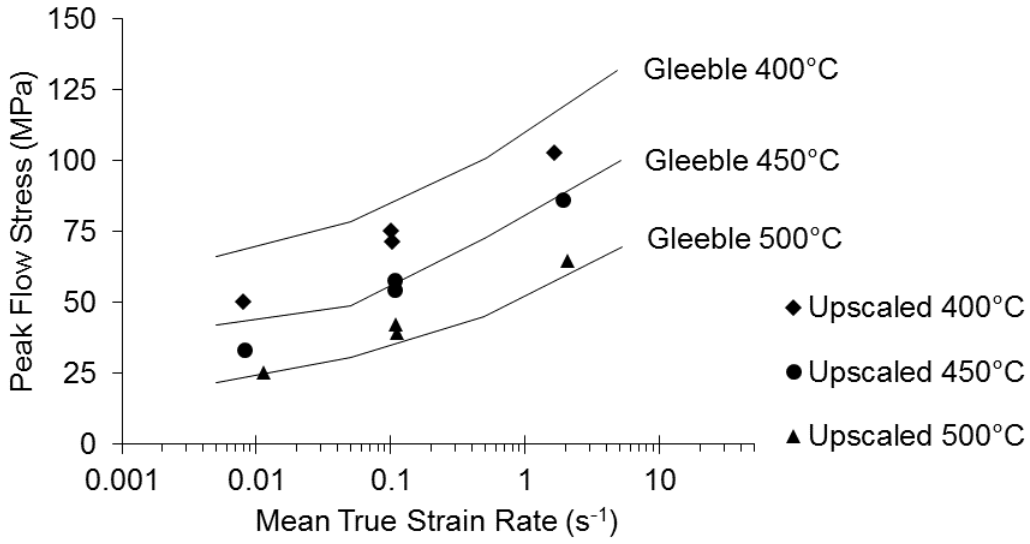

Figure 7-11 Comparison of the peak flow stress values measured in lab scale and upscaled forging tests.

The difference in flow stress between Gleeble and upscale experiments at 500°C was less significant and became insignificant at the slowest strain rate considered. Hence, differences due to precipitate strengthening effects for tests at this temperatures and these slow strain rates were anticipated to be limited given the minimal flow softening exhibited in Figure 7-2 at 500°C and due to precipitate dissolution. The similarity in peak flow behaviour at 450°C is likely due to the net effect of microstructural coarsening and frictional differences between the two procedures.

7.6.3 Properties of Sintered + Forged Cylinders

Successful upscaled forging of both 30 and 50 mm preforms was completed. All samples were deformed at 450°C, under an applied strain rate of 1 s^{-1}, and a net true strain 1.20

mm/mm using BN lubricant. A microstructural investigation of Zone I (Figure 7-12a) indicated grains within this region had undergone minimal strain. Here pores remained, and prior particles were relatively nondeformed. However, the microstructure within the Zone II regions (Figure 7-12b, several mm below the surface) showed a microstructure similar to the Gleeble-deformed sample in Figure 7-6b in that prior particles were elongated in the direction orthogonal to the pressing direction and pores were collapsed.

Transmission Electron Microscopy (TEM) analyses coupled with EDS mapping was strategically performed on a 50 mm sample deformed at 450°C ($\dot{\varepsilon} = 1.0$ s^{-1}; $\varepsilon = 1.0$ mm/mm) and heat treated to the T6 condition. The area of interest was the heavily deformed Zone II. Prior particle boundaries (PPB) were evident throughout the microstructure, decorated by a discontinuous oxide phase. Figure 7-13 shows an exemplary region of a PPB that contained oxides now disrupted into discrete particles. A section rich in oxide phase is noted by a white arrow, while the remainder of the boundary having shown no appreciable oxygen content. The discretized dark phases present in a semi-continuous chain along the PPB were Cu and Mg-rich precipitates (i.e. S-phase precipitates). EDS analysis of the oxide-rich phase indicated it was substantially enriched with magnesium as, indicating the phase was likely MgO or $MgAl_2O_4$ [105]. The discontinuous nature of the oxide phase suggested that shear strain during deformation effectively elongated the PPBs so as disrupt the pre-existing oxide film and thereby intensify the extent of metallic bonding along regions that were once prior particle boundaries of reduced mechanical integrity.

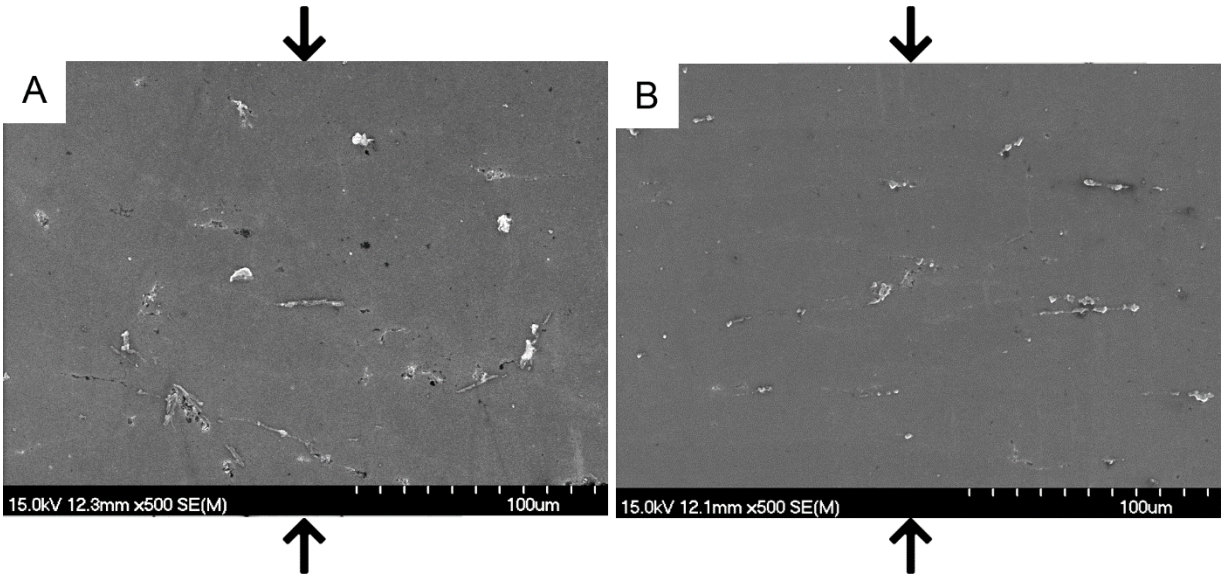

Figure 7-12 SEM micrographs recorded from a 30 mm sample deformed at 450°C ($\dot{\varepsilon} = 1.0\ s^{-1}$; ε = -1.0 mm/mm) showing an area representative of the (a) Zone I, and (b) Zone II microstructures. Forging direction indicated by arrows.

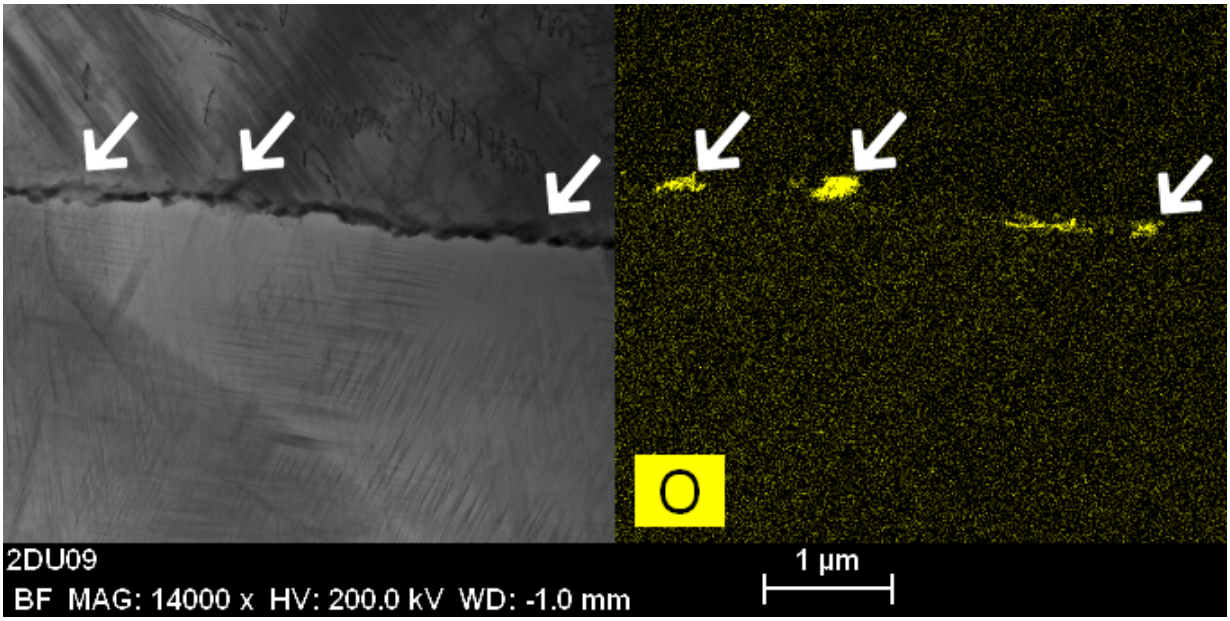

Figure 7-13 Bright field TEM image of a PPB within a forged 50 mm sample and the corresponding EDS map for oxygen. White arrows indicate regions enriched in oxygen. Sample was deformed at 450°C ($\dot{\varepsilon} = 1.0\ s^{-1}$; ε = -1.2 mm/mm), forging direction was vertical.

For both 30 mm and 50 mm preforms, mechanical property specimens were successfully extracted. TRS specimens used in three-point bend fatigue tests were extracted from sinter + forged 30 mm preforms, while standard tensile specimens were extracted from sintered + forged 50 mm preforms. In both cases, counterpart samples of the material in the sintered T6 condition were produced for comparison purposes. Tensile properties of the material (Table 7-5) showed several benefits due to forging. First was the notable improvement of ~10% in Young's modulus such that the sintered + forged product was well aligned with conventional wrought aluminum alloys (i.e. 68 to 74 GPa). This appears to be at least partially driven by the densification that occurred during deformation. However, this may also be a direct reflection of enhanced dispersion strengthening of the residual oxide and its subsequent incorporation with the alloy matrix. It is known that particle de-cohesion during low temperature loading leads to void formation, which significantly inhibits the elastic modulus [21]. The residual oxide phase observed by TEM in Figure 7-13 exhibits no evidence of porosity or de-cohesion with the matrix. This incorporation with the matrix suggests this dispersoid phase may allow for load transfer from the matrix phase, effectively increasing the modulus.

The ductility gains achieved through forging were similarly remarkable in that this attribute had doubled within the sinter + forged sample. Again, mechanical property gains through densification are applicable. However, the resilient oxide layer that persists in sintered APM parts and inhibits the ductility of samples appears to be considerably disrupted. The prior particle boundary shown in Figure 7-13 exhibits a discretized oxide phase and considerable metal-metal bonding between adjacent prior particles. It is

anticipated that the increased fraction of metal-metal bonding afforded through forging was the root cause for the observed ductility gains. Both the 0.2% yield strength and tensile strength saw significant gains due to of forging, again attributable to densification and residual oxide disruption.

Table 7-5 Comparison of tensile properties measured for the Al-3Cu-1.5Mg-0.5Sn APM alloy before and after isothermal forging. All specimens heat treated to the T6 temper prior to testing.

Condition	**E (GPa)**	**Yield Strength (MPa)**	**Tensile Strength (MPa)**	**Ductility (%)**
Sintered + T6	65.6 ± 1.0	304 ± 9	375 ± 9	5.0 ± 1.7
Sintered + Forged + T6	72.4 ± 1.7	323 ± 1	401 ± 3	10.3 ± 1.7

The fatigue properties of the APM alloy similarly also exhibited considerable gains following forging. Here, the sintered compact showed a fatigue strength ($\sigma_{a,50}$) of 215 MPa prior to forging, and more than a 50 MPa (24%) increase following forging. Such a substantial increase in a dynamic property is significant for an APM material. This performance increase is again largely attributable to the densification and microstructural refinement provided through forging. Again, the improved incorporation of residual oxide phases through forging seems like a logical explanation. Here, the added resistance towards oxide particle de-cohesion would thereby translate into a lessened number of sites for fatigue cracks to grow and coalesce, thereby enhancing fatigue strength. It was also plausible that the improvement in the elastic modulus also contributed to the heightened fatigue performance.

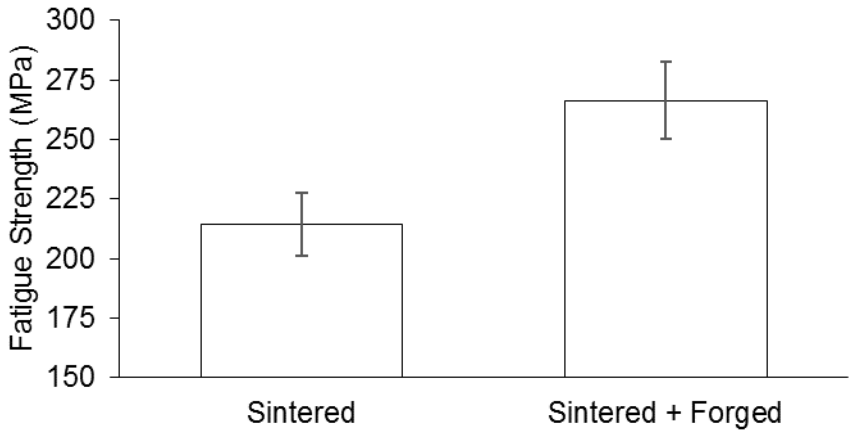

Figure 7-14 Three-point bend fatigue strength of the exemplary APM alloy before and after forging. All specimens processed into the T6 temper prior to testing.

7.7 CONCLUSIONS

A successful design of a forging process in which APM alloys could be processed was established. Using lab-scale Gleeble data the authors first determined whether an APM alloy could endure forging. Subsequently, Gleeble data was used to scale experiments such that samples capable of producing standardized test specimen were possible. Using an instrumented 1100 kN Interlaken hydraulic press with heated tooling, isothermal forging of upscaled samples was successful. From this study, the following conclusions regarding the experimental design can be drawn:

- Gleeble data proved critical in preform design and load calculations.
- Two preform geometry designs were enough to successfully extract standardized TRS, tensile and rotating bending fatigue hourglass specimen.

- Upscaled sintered + forged samples could be produced in a manner largely consistent with Gleeble data. Higher strains were achievable in the upscaled forging samples.
- The preform designs were such that mechanical property specimen could be extracted from samples deformed from 350 – 500°C and 0.005 s^{-1} and 1 s^{-1}.
- A constant true strain rate was achieved through modelling of the required ram displacement rate.

Furthermore, the following conclusions regarding the material system response can be drawn:

- APM alloys were successfully forged. In all cases, densification occurred.
- Layered spray graphite and spray BN provided marginal reduction in coefficient of friction over a single layer graphite application.
- Significant gains in mechanical properties of an APM alloy were observed. Modulus, ductility and fatigue strength all saw remarkable gains over the sinter T6 condition. It is believed that these were largely underpinned by the elimination of residual porosity and a considerable disruption of the residual oxide networks that would have persevered in the sintered product.

7.8 Acknowledgements

The authors would like to acknowledge the Natural Sciences and Engineering Research Council of Canada (NSERC) for financial support via the Collaborative Research & Development grant CRDPJ 486528 - 15. Dr. Bernhard Mais (Kymera International) and Mr. Jessu Joys (Ampal Inc.) are acknowledged for the provision of the powdered metals employed. Laboratory assistance provided by colleagues at Dalhousie University (Randy Cooke, Dean Grijm) and CanmetMATERIALS (Jonathan McKinley, Lucian Blaga, and Dr. Babak Shalchi Amirkhiz) is gratefully appreciated as well.

CHAPTER 8. MICROSTRUCTURAL EVOLUTION OF A FORGED 2XXX SERIES ALUMINUM POWDER METALLURGY ALLOY

Gregory A. W. Sweet [1], Babak Shalchi Amirkhiz[3], Bruce W. Williams[3], Alan Taylor[4], Richard L. Hexemer, Jr. [5], Ian W. Donaldson [6] and Donald Paul Bishop [2]

1 – Graduate Student, Dalhousie University, Halifax, Nova Scotia, Canada
2 – Professor, Materials Engineering, Dalhousie University, Halifax, Nova Scotia, Canada
3 – Research Scientist, CanmetMATERIALS, Natural Resources Canada, Hamilton, Ontario, Canada
4 - Vice President – Lightweight Technology, GKN Sinter Metals LLC, Auburn Hills, Michigan, USA
5 – Research Engineer, GKN Sinter Metals LLC, Conover, North Carolina, USA
6 – Director of R&D North America, GKN Sinter Metals LLC, Auburn Hills, Michigan, USA

Status: Submitted to Materials Characterization January 16, 2019.

Author Contributions: The following experimental procedures, results and discussions were completed by G.A. Sweet. TEM work was performed by B.S. Amirkhiz. Reviewer and editorial roles were played by all coauthors.

8.1 Forward to Chapter 8

Motivated by the promising mechanical properties reported in the previous manuscript, this project further expanded on the evolution of mechanical properties through hot deformation operations. A refined set of forging parameters were selected in this study to focus resources elsewhere. The isothermal forging temperature was fixed at 450°C and strain rates ranged from 0.1 s^{-1} to 1.0 s^{-1}. These parameters fell within the deformation domain of greatest efficiency found in Chapter 6, and avoided regions of flow instability. Furthermore, the fastest available deformation rates were selected for industrial productivity reasons. This manuscript specifically focussed on the microstructural

influence of residual oxides and their role. Ceramic-bearing materials were studied in parallel, but findings were separated into a subsequent manuscript.

8.2 Abstract

The microstructural response to hot upset forging was studied for a commercially relevant 2000-series aluminum powder metallurgy alloy. Sufficiently large specimens were produced such that the tensile property development was recorded for true compressive forging strains 0 mm/mm to 1.55 mm/mm. Full theoretical density values were obtained and up to a four-fold improvement in tensile ductility was observed. The tensile strength of a sintered-T6 component was measured at 357 MPa, while forging to 1.40 mm/mm increased that to 418 MPa. Microstructural reinforcement was found to be predominantly S-phase precipitates. Prior particle boundaries (PPB) of an unforged specimen were found to be continuously decorated with MgO and Mg_2Sn crystallites. Such boundaries in hot forged specimen were discretized into clusters, producing regions of PPB devoid of oxides or other secondary phases. Improvements to mechanical properties were largely attributed to this effect.

8.3 Introduction

Aluminum powder metallurgy (APM) is a part production technology especially relevant to lightweighting in the automotive industry. Industrially, compaction of aluminum alloy powder blends and subsequent sintering/sizing into near-net shape components has been

used in the production of internal combustion engines and automatic transmissions, to name a few. Due to the ongoing development in this field, APM alloys have recently been adopted in rotating transmission components, such as planetary gear carriers used in 9 speed General Motors transmissions [106]. To meet these demanding conditions, APM materials that sintered to near full theoretical density were developed. To encourage further proliferation, means to improve the physical and mechanical properties of these advantageous material systems are an area of significant research interest. One of these is powder forging; a technology now exploited extensively in the ferrous powder metallurgy market as a means to improve mechanical properties through residual pore collapse [107]. Select investigations of powder forged APM materials have been published over the past several decades [37,51,108]. MacAskill et al. demonstrated that hot rotary forging of a 7xxx series APM alloy fully densified the material and increased fatigue life by 110% relative to the nondeformed equivalent [109]. Mann et al. similarly investigated rotary hot swaging of a 99.5% dense 2xxx series APM alloy, whereby a 25% increase in tensile strength and over 300% increase in tensile ductility was concluded [19]. In these works, pore collapse and the disruption of the continuous oxide layer were attributed to the performance gains. Despite this, an in-depth study of the nature of oxide boundary disruption through elevated temperature forging of commercial APM systems has been lacking.

Unlike ferrous powder metallurgy where detrimental oxide phases can be eliminated by sintering in a reducing atmosphere, APM technology is challenged by a resilient oxide film on the surface of aluminum particulate that cannot be reduced by any practical

atmospheric conditions [1]. Instead, additions of elemental magnesium promote chemical reduction of this continuous film into discrete MgO or $MgAl_2O_4$ nano-particulate. This provides localized sites that are devoid of oxygen and fosters the requisite metallic bonding between adjacent Al particles [105]. Although this approach improves sinterability, oxide(s) persist in sintered compacts as a semi-continuous network situated along prior particle boundaries [36] that limits mechanical properties of commercial AMP alloys. It has been suggested that hot deformation of a sintered APM compact disperses this oxide phase [6,90]. However, the composition and distribution of these residual phases, as well as their redistribution through hot deformation, have yet to be studied. Hence, the purpose of the present study is to investigate the microstructure of a commercial powder forged APM alloy and then correlate these observations to transitions in mechanical properties.

8.4 Materials and Methodology

An APM alloy prepared by conventional press and sinter powder metallurgy techniques was the focus material in this study. Its nominal composition was 3.0% Cu, 1.5% Mg and 0.5% Sn, in wt%; the measured composition of the sintered compacts is reported in Table 8-1. The composition was attained by solid state blending of elemental and master alloy powders as outlined in a previous study [110]. The powder mixture was then compacted into cylindrical specimens (50 mm diameter x 44 mm tall) with a green density of 2.48 g/cc using an Instron model 5594-200HVL 1 MN load frame coupled with a floating die tool set. Compacts were subsequently sintered in an industrial mesh belt furnace used in

the production of commercial APM automotive components. The heating profile consisted of a 10-minute isothermal hold at 400°C followed by a 15-minute isothermal hold at 600°C under flowing high purity nitrogen.

Table 8-1 Chemical analysis of the starting, sintered specimen, acquired by ICP-OES. All values reported in wt%.

Al	Cu	Mg	Sn	Ca	Fe	Si	Mn	Ti
Balance	3.09	1.63	0.59	0.13	0.14	0.05	0.002	0.045

Samples were then isothermally upset forged in an Interlaken Technology 1100 kN press with a 5000 mm/min maximum stroke rate, which allowed for a deformation rate at least 1 s^{-1} for the 50 mm cylinder geometry. This frame was outfitted with displacement and load data acquisition as well as heated (450°C) H13 tool steel platens. Prior to forging, sintered preforms were heated to 450°C for 90 minutes. Both the dies and samples were coated with an aerosol boron nitride dry lubricant prior to heating. Deformation was performed using open loop, nonlinear position control as outlined in [96]. The displacement versus time response was varied to ensure the true strain rate was consistently 0.1 s^{-1} up to a true compressive strain of 1.55 mm/mm. This slower rate was chosen due to preliminary unpublished results showing the microstructural and mechanical similarities when deformed at a rate of 0.1 s^{-1} or 1 s^{-1}. A series of forging strains from 0 mm/mm to 1.55 mm/mm were employed. Samples were water quenched following deformation. Before analysis, all samples were heat treated to the T6 state by solutionizing for 2 h at 510°C, water quenching, and artificial aging for 10 h at 190°C.

Density measurements were performed according to MPIF (Metal Powder Industries Federation) Standard 42 on 10 mm wide rectangular sections extracted from the forged pucks. Tensile samples were subsequently machined from these sections and tested in accordance with MPIF Standard 10. Error bars in reported density and tensile tests represent one standard deviation about the mean of no less than three unique samples. For microstructural assessment, samples were hot mounted in Bakelite and polished on a Struers Tegramin semi-automatic polishing system using standard oil-based diamond suspensions and colloidal oxide solutions. Images were acquired using an Olympus BX51 optical microscope and a Hitachi S-4700 cold field SEM. TEM samples were prepared from an as-sintered and a forged material, both in the T6 temper, by first diamond saw sectioning to approximately 2 mm in thickness, ground using SiC to <500 μm and punched to 3 mm discs. Discs were mechanically thinned further using alumina suspensions and dimpled. The dimpled disc was ion milled until perforation using a Gatan 691 PIPS. The precipitates and prior particle phases were observed using a Tecnai Osiris Transmission Electron Microscope (TEM) equipped with a 200 keV X-FEG gun coupled with a Super-X windowless EDX detector system. A spatial resolution down to 1 nm was achieved during EDS mapping using a sub-nanometer electron probe. Metallography samples were extracted from a 2 mm wafer cut along the forging axis and through the center of deformed samples to obtain a transverse section of the full diameter. Micrographs were captured such that the forging direction was vertically aligned with the image, except when noted otherwise in the text.

Supporting thermodynamic calculations were performed using the 'Equilib' equilibrium phase calculation and 'Phase Diagram' modules of the thermodynamic database computing system FactSage, version 6.4. The FTlite light metal alloys database and FToxid oxides database were used simultaneously, with all relevant liquid or solid solutions included in calculations. The composition outlined in Table 8-1 (excluding Ca, Ti and Mn) was used for all such calculations to predict the primary phases that should theoretically exist within the materials of interest and correlate these findings to experimental results. A pressure of 1 atm and temperature range of 100°C to 600°C were selected for calculations.

8.5 Results and Discussion

8.5.1 Physical and Mechanical Property Effects

The density of both sintered and sinter forged compacts were obtained following T6 heat treatment. Figure 8-1 indicates that in the sintered T6 condition, the density of the powder metallurgy compact was 98.7%, with a standard deviation of 0.27%. Following hot upset forging at 450°C, the density of compacts invariably increased with a concurrent decrease in error. An initial period of rapid densification occurs up to a true forging strain of 0.3 mm/mm, where a mean density of 99.7% and standard deviation of 0.11% was achieved. Subsequently, an intermediate period of reduced densification persisted to 1.40 mm/mm at which a peak density of 100.0% was achieved. Finally, an apparent de-densification occurred when deformed to 1.55 mm/mm. At the peak density, the error values were

diminished by an order of magnitude over the sintered counterpart. Research on powder forged titanium connecting rods [32] exhibited comparable densification trends with forging strain. However, de-densification in the current research is unique. During forging, the laterally unconstrained cylinders experience frictional forces at the die-sample interface, and consequently develop a tensile hoop strain around the outside diameter. Figure 8-2 is oriented such that the viewing axis and forging axis were parallel, and the imaged area was the along the circumference midway through thickness; obvious intergranular fracture of near-surface prior-particle boundaries was evident. These cracks were on the order of 100's of μm. Accordingly, it was postulated that this resultant tensile strain had locally de-densified the material.

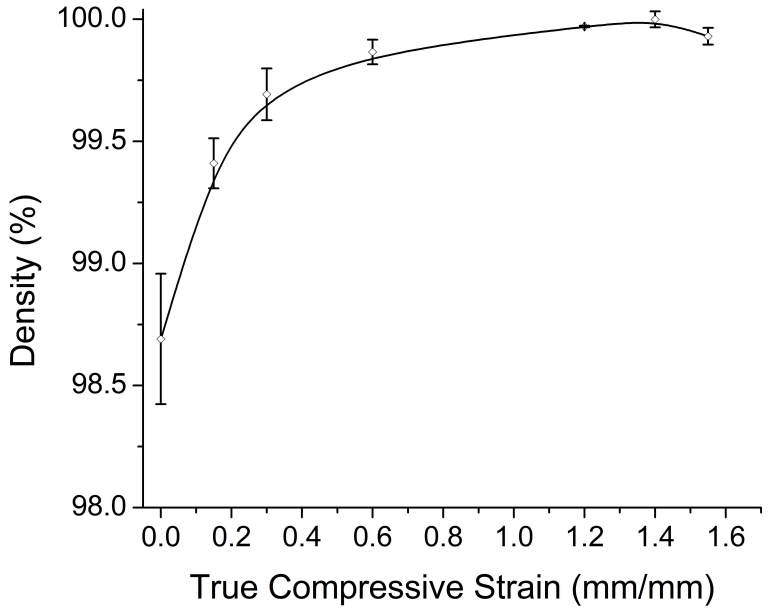

Figure 8-1 Density of sintered and sintered-forged samples displayed as a function of true compressive forging strain

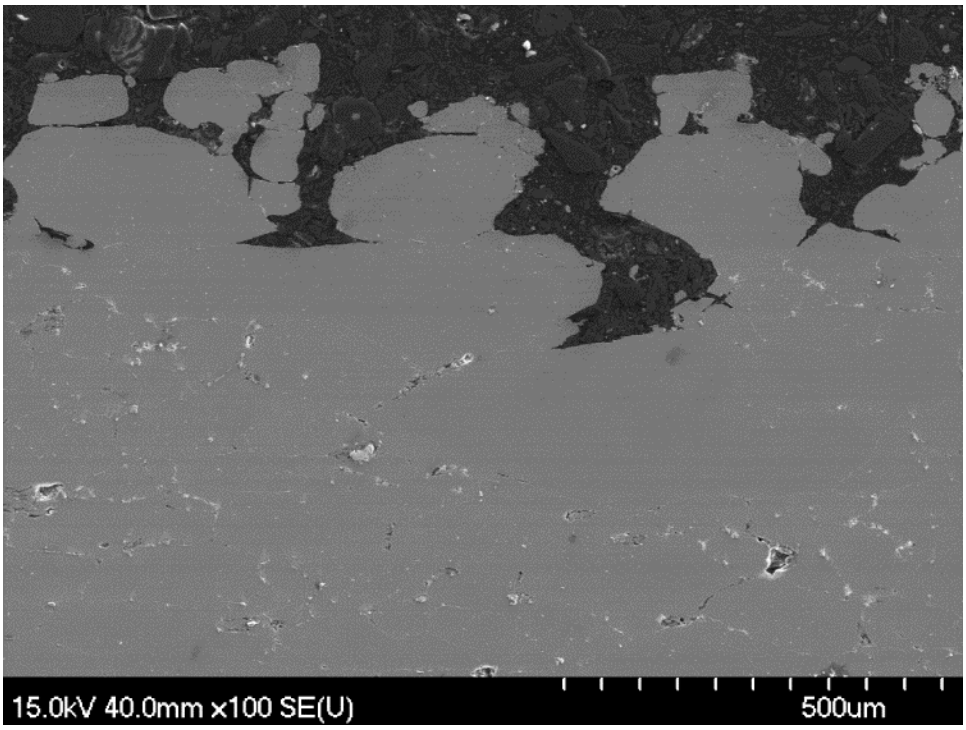

Figure 8-2 Electron micrograph of surface cracks present on the outside circumference of samples hot upset forged at 1.55 mm/mm. The forging axis is aligned with the beam.

Tensile behaviour also trended positively with the net amount of forging strain (Figure 8-3). For the ultimate tensile strength (UTS), this property had invariably increased over the sintered compact. For example, whereas the sintered compact exhibited a mean UTS of 357 MPa, a much higher value of 418 MPa was obtained once forged to 1.40 mm/mm. Akin to the density trends, a marginal decrease in UTS was then observed for strains greater than 1.40 mm/mm. The gains in UTS correlated with a marginal increase in strain hardening exponent from 0.121 at 0 mm/mm strain to 0.132 at 1.55 mm/mm strain. Interestingly, the trend of UTS vs strain did not match the nonlinear trend of density, as would be expected from a powder forged part [30]. An explanation may be that the sintered density of the compacts was sufficiently close to their theoretical value that the

bulk of potential density-related tensile strength has been established already. The trend in yield strength versus forging strain appeared to correlate positively akin to the UTS data, given the maximum 0.2% offset value of 325 MPa at 1.40 mm/mm and subsequent drop in yield at a higher forging strain. However, the trend was not statistically significant. Neither forging strain nor ensuing densification appeared to improve yield strength appreciably. The authors have previously found that hot forging this material at 450°C and 0.1 s^{-1} does not instill any grain refinement via recrystallization [110]. Grains remained approximately equivalent in size before and after forging, although they had become progressively more lenticular with strain. Accordingly, the forging conditions were selected to isolate the influence of precipitates and secondary phases on the mechanical properties due to grain size.

Tensile ductility (Figure 8-4) unequivocally increased with upset forging strain. The sintered-T6 compact exhibited a respectable mean tensile ductility of 4.2% yet deforming to a strain of only 0.3 mm/mm nearly doubled this figure. A significant linear trend continued up to a forging strain of 1.40 mm/mm, peaking at 17.0%. The mean ductility marginally decreased above this strain, although the difference was marginal. De-densification at large forging strains may have negatively influenced tensile ductility.

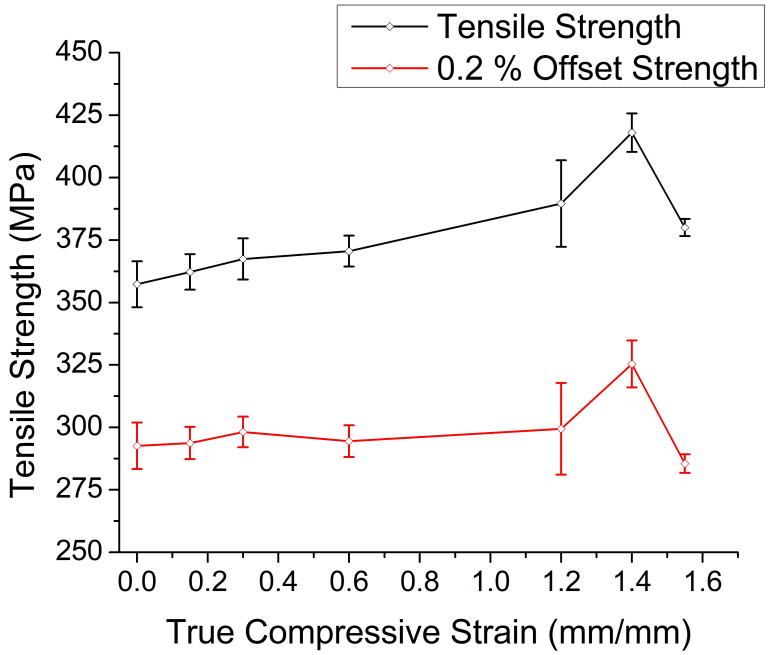

Figure 8-3 0.2% offset strength and tensile strength as a function of true compressive upset forging strain

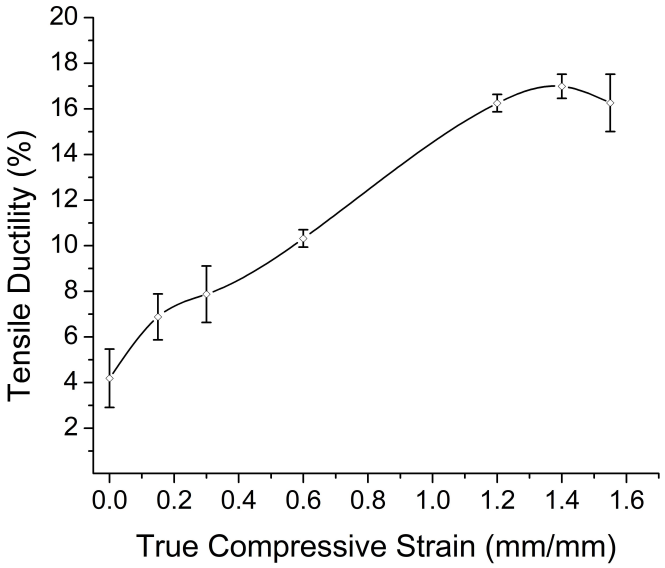

Figure 8-4 Tensile ductility as a function of true compressive upset forging strain

8.5.2 General Microstructure Assessment

Initially, FactSAGE thermodynamic calculations were performed to determine the composition of plausible stable phases under relevant processing temperatures. Additions of Mg and Sn are strong sintering aids in APM processing, allowing for the disruption of Al_2O_3 and inhibiting the in-situ formation of non-wetting of AlN during sintering, respectively. Quantifying the nature of the resultant secondary phases and how they are manipulated through hot deformation are of practical importance. Specimens of this alloy were measured to have 0.099 to 0.159 wt% oxygen and 0.013 to 0.024 wt% nitrogen; the higher values of each were chosen for calculation purposes. Two stable phases were identified throughout the temperature range studied. Namely, 0.4 wt% MgO and 0.07 wt% AlN were predicted to be the sole O and N-bearing phases present.

A pseudo-binary phase diagram for the composition listed in Table 8-1 (excluding Ca, Mn and Ti) is shown in Figure 8-5. Starting at the sintering temperature, 600°C, the approximate liquid fraction was calculated to be 16.3 wt%. Upon cooling from sintering to approximately 560°C, liquid constituents solidify solely into α-Al. Solidification of α from the liquid occurs until the solidus at approximately 541°C. A solid solution of Mg_2Si and Mg_2Sn (i.e. $Mg_2(Si,Sn)$), and Al_7Cu_2Fe are among the last phases to solidify from the liquid, at 559°C and 554°C respectively. Both phases were determined to be stable below the solidus. Room temperature solid solubility of Si and Sn are minimal in α (Si max of 0.032 wt%, Sn insoluble), the bulk of their mass was associated with $Mg_2(Si,Sn)$. A maximum of 0.83 wt% Mg_2Sn and 0.14 wt% Mg_2Si were calculated.

Two phase fields were identified below the solvus, α + θ above approximately 304°C, and α + θ + S below that. TEM and thermodynamics work by Hutchinson and Ringer on alloys of comparable chemistry have exhibited an exclusive S-phase precipitate sequence [111]. Following this precedent, the composite Al-Cu-Mg phase diagram of Figure 8-6 was constructed. For a given Cu and Mg composition, the diagram outlines the stable precipitate type when aged at 190°C, the artificial aging temperature of this alloy. The noted coarse black boundary represents the solubility limit of Cu and Mg in α at the solutionizing temperature, 510°C. Increasing Cu or Mg beyond the limit of this boundary would produce undesirable primary S phase. The nominal Cu and Mg composition of the alloy in this study, noted by a red square, indicated a propensity towards the sole precipitation of S. However, the Mg-harvesting effect of MgO and $Mg_2(Si,Sn)$ manipulate this. The soluble Mg at 510°C was decreased from the nominal value to 1.08 wt%. Whereas, Cu harvesting from Al_7Cu_2Fe marginally decreased the solid solution concentration to 3.07 wt%. Hence, the effective composition of the alloy shifts left into the α + θ + S phase field, as noted by the red circle. At 190°C the amounts of S and θ were calculated at 3.86 wt% and 2.33 wt%, respectively.

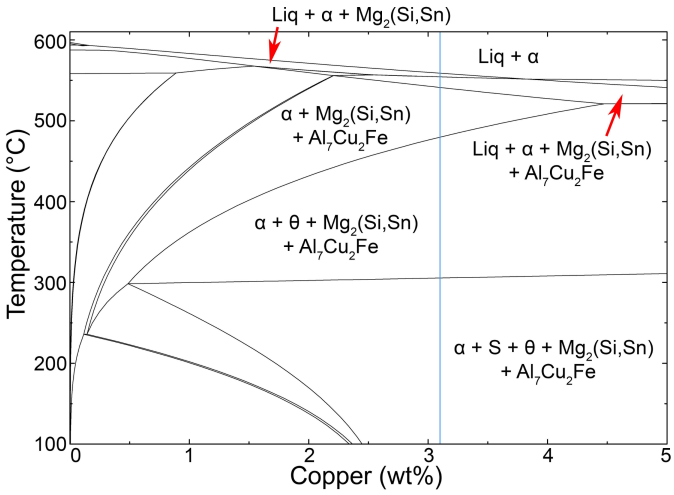

Figure 8-5 Pseudo-binary phase diagram of the alloy system with composition outlined in Table 8-1, the blue line represents the copper concentration used in this study.

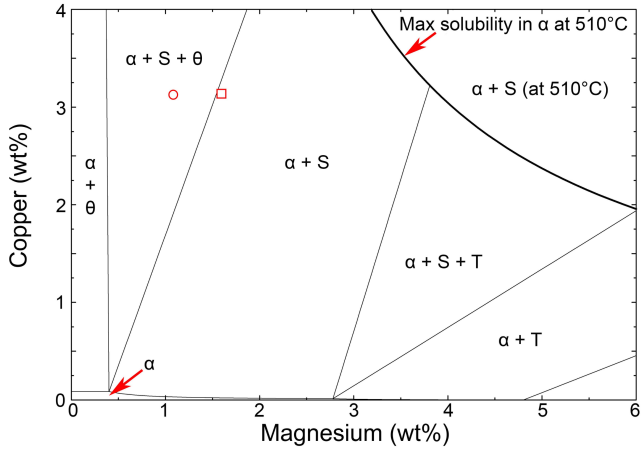

Figure 8-6 Aluminum-rich corner of the Al-Cu-Mg phase diagram at the artificial aging temperature of 190°C. The annotated curved boundary represents the a - a + S phase boundary at the solutionizing temperature of 510°C. The square data label represents 3.1% Cu and 1.6% Mg, while the circle data label represents the reduction in soluble Mg due to secondary phase formation.

Electron micrographs of the bulk microstructure in the APM alloy when sintered-T6 and sintered-forged-T6 (Figure 8-7) show the impact of hot forging. Exemplary residual porosity in the material prior to forging (as noted in the image with yellow arrows) was rounded and relatively coarse generally ranging in size from 5 to 50μm in diameter. Following upset forging, such porosity was effectively eliminated. In addition, secondary phases appeared heterogeneously distributed in light contrast to the α-Al grains. EDS analysis of these phases, magnified in Figure 8-7c and summarized in Table 8-2, indicated a broad degree of chemical variability among two visually unique morphologies. The composition of the phases proved their complex nature, as neither Al_7Cu_2Mg nor $Mg_2(Si,Sn)$ was found exclusively. Rather, the brighter phase contrast of areas 1 and 2 were predominantly Al-Cu-Fe and enriched with oxygen. Areas 3 and 4 were lean in Cu and Fe and enriched in Al-Mg-O with an appreciable amount of Sn. Since these phases were located along prior particle boundaries, and they were enriched with liquid-phase soluble metallic elements, it is reasonable to identify them as the solidified final liquid. However, the enrichment with oxygen contradicts thermodynamic calculations. There was insufficient Mg present in the identified points to determine whether MgO was in fact the sole oxide phase.

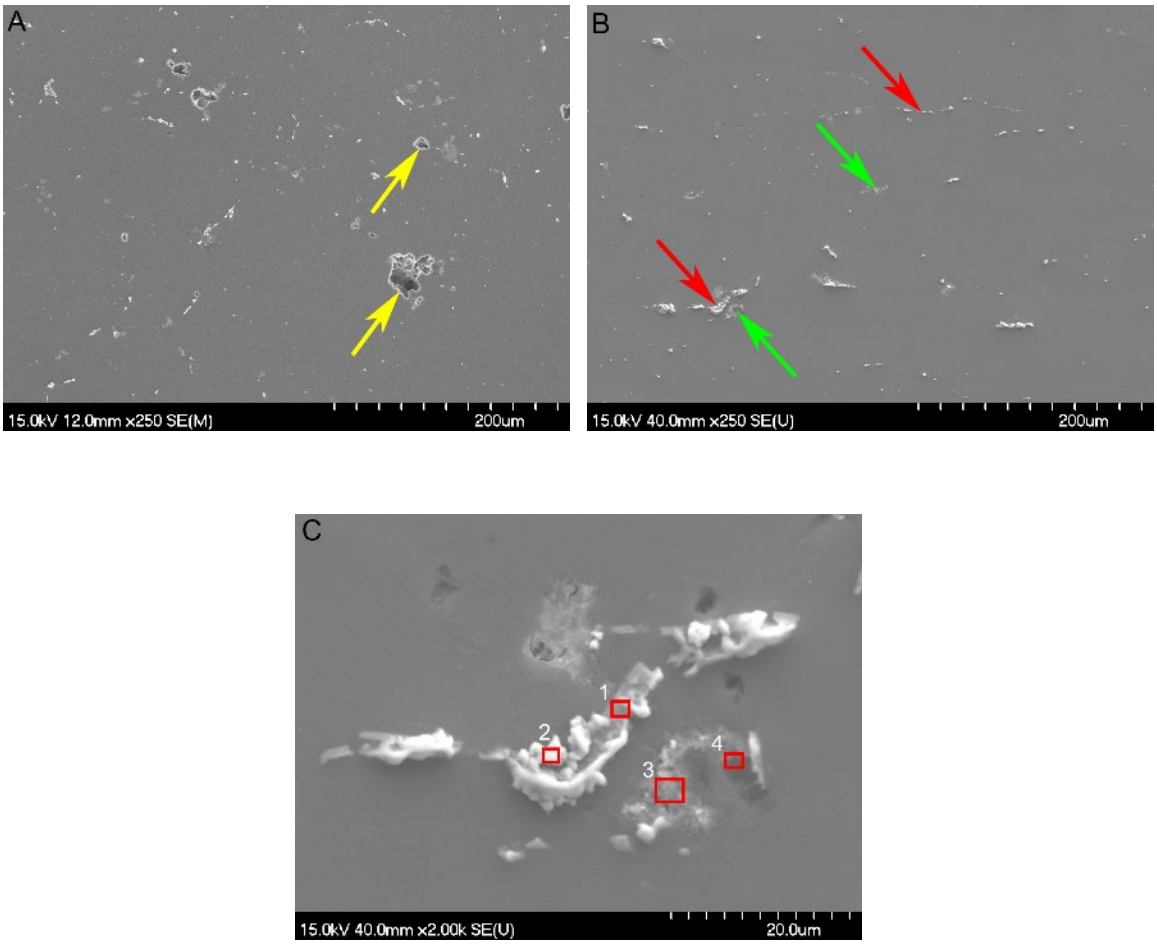

Figure 8-7 SEM micrographs showing the bulk T6 microstructure of the APM alloy (a) as-sintered and (b) after hot forging to 1.40 mm/mm true strain. The micrograph (c) identifies the four secondary phase area of interest presented in Table 8-2. The area of this micrograph corresponds to the annotated cluster of secondary phases in the bottom-left corner in b).

Table 8-2 EDS composition of secondary phases noted in Figure 8-7c.

	Composition (at%)						
Area	**Al**	**Mg**	**Cu**	**Sn**	**Fe**	**Si**	**O**
1	58.1	1.6	20.8	0.4	12.6	0.0	6.5
2	35.5	1.7	51.4	1.0	2.3	0.7	7.4
3	28.7	5.5	0.6	7.5	0.1	2.5	55.2
4	41.8	7.5	0.8	1.2	0.0	0.3	48.4

TEM bright field images and corresponding diffraction patterns (Figure 8-8) illustrate the nature of the dominant precipitate phase within the α-aluminum grains before and after forging. Such data were acquired such that the $[001]_{Al}$ zone axis was oriented closely parallel to the electron beam. In both cases, orthogonal lath-type precipitates were dominant. Wang et al. have published in-depth precipitate mechanism for the Al-Cu-Mg system [99,112–114]. The proposed precipitation sequence from a homogenous state was described as [114]:

$$SSSS \rightarrow Cu - Mg\ Co\ Clusters \rightarrow S''/GPB2 \rightarrow S(Type\ I) \rightarrow S(Type\ II)$$

Where the formation of the Type II variant is strongly dependant of solution treatment and cold working prior to aging. Type II are non-coherent with the matrix and have an orientation relationship rotated by ~4° [114]. An inference to whether Type I or Type II was dominant within the APM alloy was not made in the current work. However, the superlattice patterns in the current research matched well with the S phase variants $\langle 100 \rangle_S$, $\langle 021 \rangle_S$ and $\langle 013 \rangle_S$ in an Al matrix as reported by Wang and Starink [112]. Following forging, it did not appear that the nature of these precipitates changed

significantly. This behaviour was not unexpected, as the chemical makeup and heat treatment procedures were identical.

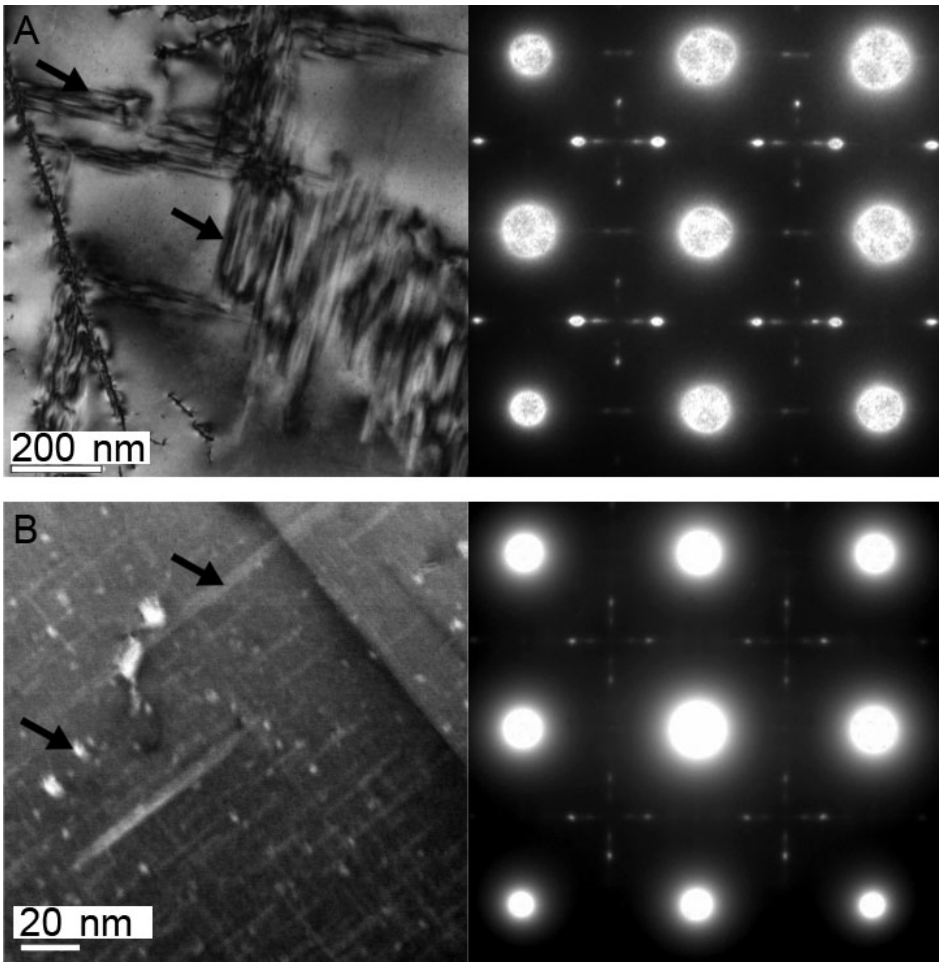

Figure 8-8 TEM micrographs showing the bulk T6 microstructure of the APM alloy (a) as-sintered and (b) after hot forging to 1.40 mm/mm true strain. Diffraction patterns reveal S phase (Al_2CuMg, annotated with black arrows) with Al viewed along its [001] zone axis, where superlattice spots correlating with the S-phase precipitates are visible. Forged sample deformed to a total strain of 1.40 mm/mm.

Additional TEM bright field imaging revealed a secondary precipitate morphology within the α-aluminum grains. Namely, spiral-shaped, incoherent precipitates in addition to the

dominant lath-shape S-phase as annotated with green and red arrows respectively in Figure 8-9a. Imaged areas of thinner cross section (Figure 8-9b) revealed a comparable snapshot of this phase, with apparent strain-induced contrast effects around its circumference. EDS mapping of this region (Figure 8-9c to e) confirmed the enrichment of predominantly Cu and Mg in this phase with a lesser amount of Si, to infer that this feature was a heterogeneously nucleated variant of S-phase. This is substantiated by the work of Hutchinson and Ringer [111] where the authors observed quenched-in dislocation loops and helices on which S phase heterogeneously nucleated. Furthermore, the authors noted that trace levels of Si manipulate GPB-zone formation within the S-phase precipitation sequence. In this study as well as the work by Hutchinson et al., precipitate-free zones adjacent to heterogeneous S phase were observed. In the current work, these were approximately 100 nm in width. From this, it was determined that the material had a preferred solute-dislocation interaction.

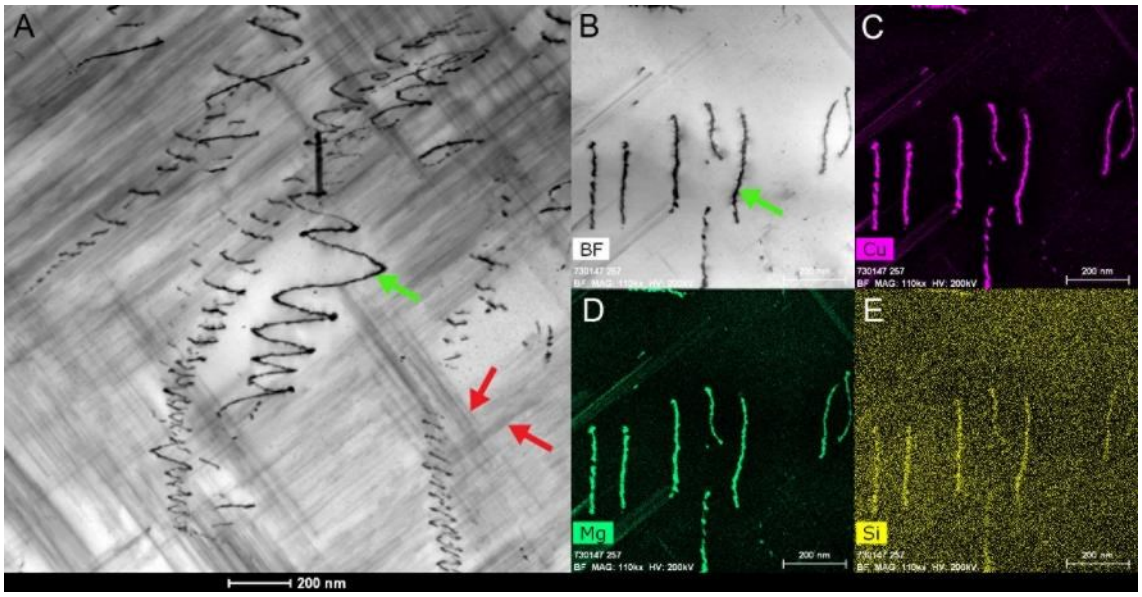

Figure 8-9 TEM micrographs of the sintered-forged (1.40mm/mm)-T6 specimen showing; (a) a bright field image of sprial heterogeneous precipitates on helical dislocations, (b) a second bright field image of another morphology of the heterogeneous precipitates along with accompanying EDS elemental maps of (c) Cu, (d) Mg and (e) Si.

8.5.3 Prior Particle Boundary Assessment

Prior particle boundaries (PPBs) in APM materials represent the oxygen-rich surface of aluminum powder particles utilized in the raw powder mixture. Elimination of this surface layer is practically impossible. Hence, in-situ chemical disruption of it through intentional Mg additions so as to form MgO and/or $MgAl_2O_4$ is the default approach [105,115] despite the fact that a semi-continuous brittle oxide layer prevails after sintering; a feature known to diminish the dynamic mechanical properties of APM alloys. Therefore, investigating the microstructural changes in PPBs is of critical importance. Characterization of several PPBs was performed on sintered T6 and sinter-forge-T6 specimens. Optical metallography was particularly valuable in this, as PPBs were not

easily resolvable in scanning electron metallography images (Figure 8-7). Optically, PPB artifacts show (in dark contrast) as a continuous film decorating prior particles. Figure 8-10 demonstrates the typical PPB morphology for a sintered compact and one forged to 1.40 mm/mm. In the former, the PPB remains distinctly continuous, while exhibiting domains that were both uniform and highly irregular (the latter annotated by red arrows). With the localized shear strain of upset forging, the PPBs (Figure 8-10b) become elongated orthogonal to the forging direction (vertical with the page). Instead of an apparent continuous line, the forged PPBs now appeared discretized.

A section of a PPB comparable to that annotated in Figure 8-10a was investigated at higher resolution using TEM (Figure 8-11). Accompanying elemental maps highlight the complex nature of these boundaries in a sintered-T6 compact. Two distinct prior particles with unique S phase precipitate orientations are evident in the bright field image, split vertically and roughly equally. The boundary phase appeared irregular and was decorated with phases in dark contrast. Elemental maps indicated that these boundary phases were effectively continuous with phases enriched in O, Mg, Sn, N and semi-continuously with Cu. The occurrence of O appears exclusively with Mg, and solely in thin bands. Discrete Cu also appears associated with Mg, presumably as heterogeneously precipitated incoherent S phase. Several intermediate regions seemingly devoid of secondary phases (red arrows) but isolated from either parent prior particle were also evident. Remarkably, the oxide film exists along the circumference of theses regions and the core PPB itself.

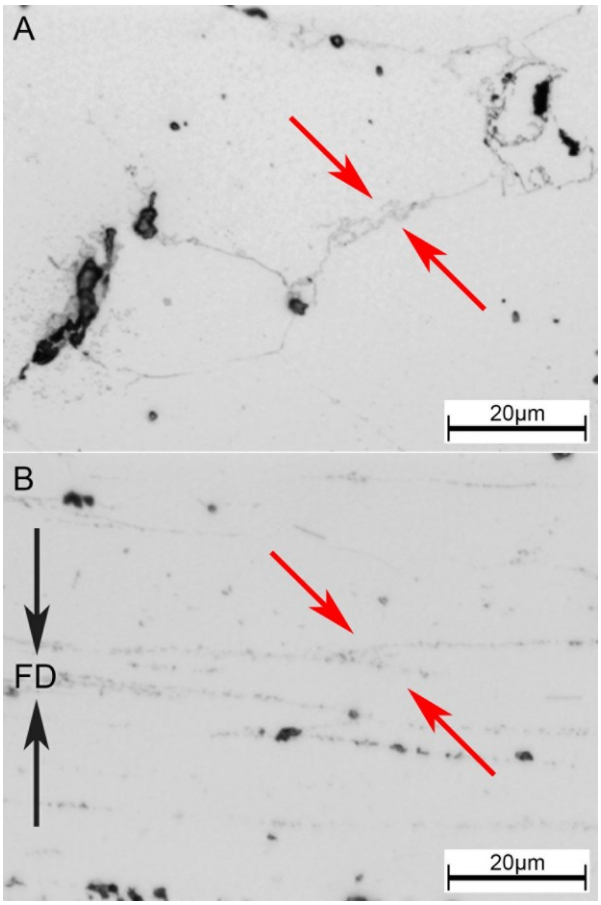

Figure 8-10 Optical micrographs contrasting the prior particle boundary nature of the APM alloy (a) as-sintered and (b) after hot forging to 1.40 mm/mm true strain. Red arrows indicate a comparable region of PPB investigated in TEM. Both specimens in the T6 state.

The occurrence of oxygen is characteristic of aluminum powders, including the air atomized one in the current research. Invariably, an atomized powder will react with even trace amounts of oxygen in the atmosphere to produce an amorphous layer of Al_2O_3 [116]. Mg additions to aluminum PM compacts have proven to be a critical sintering aid, whereby the continuous alumina film is discretized into $MgAl_2O_4$ or MgO [117] and provides a form of metallic bonding for two prior particles [118]. FactSage calculations suggested stable, solid MgO would be the exclusive oxygen-bearing phase at any

temperature within the scope of this research. MgO was solid at these temperatures and insoluble in the solid or liquid phases. An enhanced section of PPB and an accompanying diffraction pattern (Figure 8-12) confirm this. Blue arrows annotate secondary phases in dark contrast between two prior particles. With the aperture over the dark phases, diffraction rings were observed, confirming the presence of nano-sized crystallites in this region. Neither Al_2O_3 nor $MgAl_2O_4$ were detected, while MgO d-spacing values (ICDD reference pattern 00-004-0829) matched the rings annotated as #2 (200), #4 (220), #6 (222), #7 (420) and #8 (422).

Tin is another common sintering aid, known to dampen the in-situ formation of AlN during compact sintering [11]. Thermodynamic calculations suggest that, upon cooling from the sintering temperature, Sn is among the last of the liquid constituents to solidify. Sn and Mg from the liquid phase produce Mg_2Sn at approximately 560°C. Mg_2Sn d-spacing values (ICDD reference pattern 00-031-0812) were confirmed to match with diffraction rings #1 (420), #2 (530), #3 (640), #4 (644) and #5 (162). Coupled with the Sn map in Figure 8-11, the PPB appeared to be decorated with a continuous network of Mg_2Sn crystallites.

Nitrogen concentrations along the PPB are attributable to AlN that formed during sintering in a nitrogen atmosphere. Although impeded by Sn additions, AlN has been shown to grow in-situ during the sintering of APM alloys [10]. Although the occurrence of this phase was not identified using the TEM, thermodynamic calculations implied its presence.

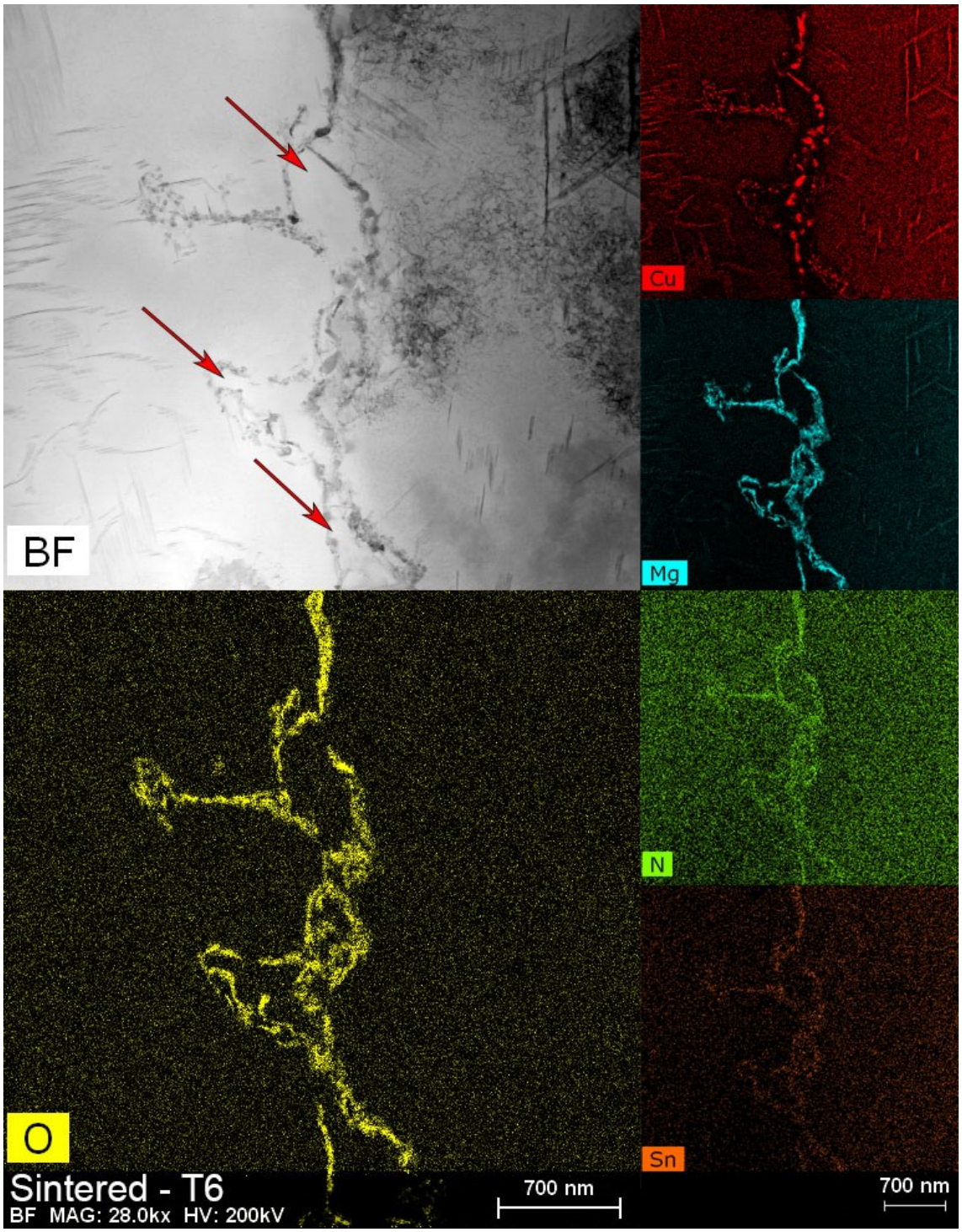

Figure 8-11 TEM micrographs highlighting the nature of the prior particle boundary of a sintered T6 specimen: including the bright field image and the EDS-acquired elemental maps of oxygen, copper, magnesium, nitrogen and tin.

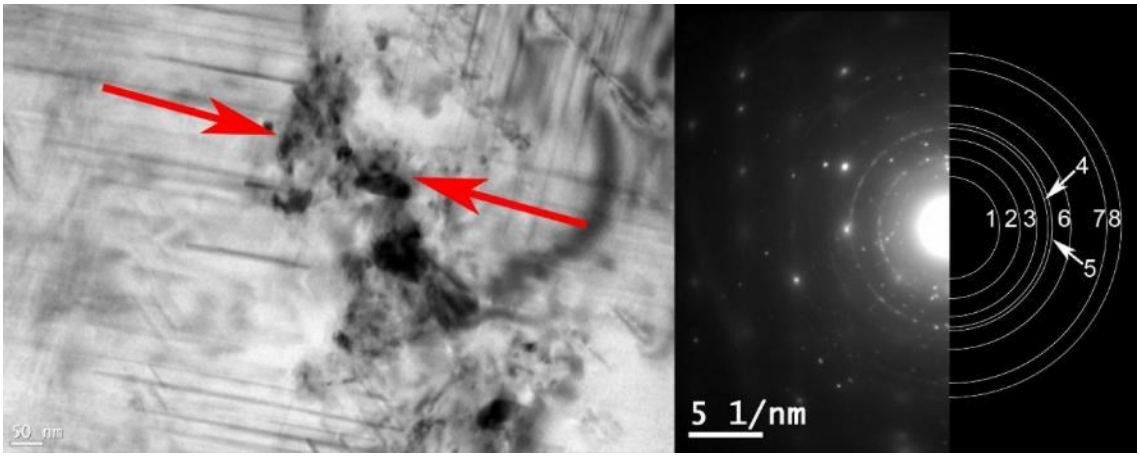

Figure 8-12 TEM micrograph of the phases along a prior particle boundary and the corresponding, annotated, diffraction pattern. Identified ring patterns correspond to (HKL): 1-Mg_2Sn (420), 2-MgO (200) and Mg_2Sn (530), 3-Mg_2Sn (640), 4-MgO (220) and Mg_2Sn (644), 5-Mg_2Sn (162), 6-MgO (222), 7-MgO (420) and 8-MgO (422).

Once forged, the nature of the PPB changed considerably from the sintered condition as exemplified in Figure 8-13. Here, three distinct prior particles were observed, isolated by a PPB triple point. The bright field image is oriented such that the forging direction is approximately from top left to mid-right. The PPB was again decorated with multiple phases in dark contrast, yet it now exhibited reduced irregularity relative to that observed in the sintered-T6 condition. Furthermore, the left prior particle was comprised of four subgrains, the boundaries of which were devoid of any O/Sn/N-bearing phases characteristic of a PPB.

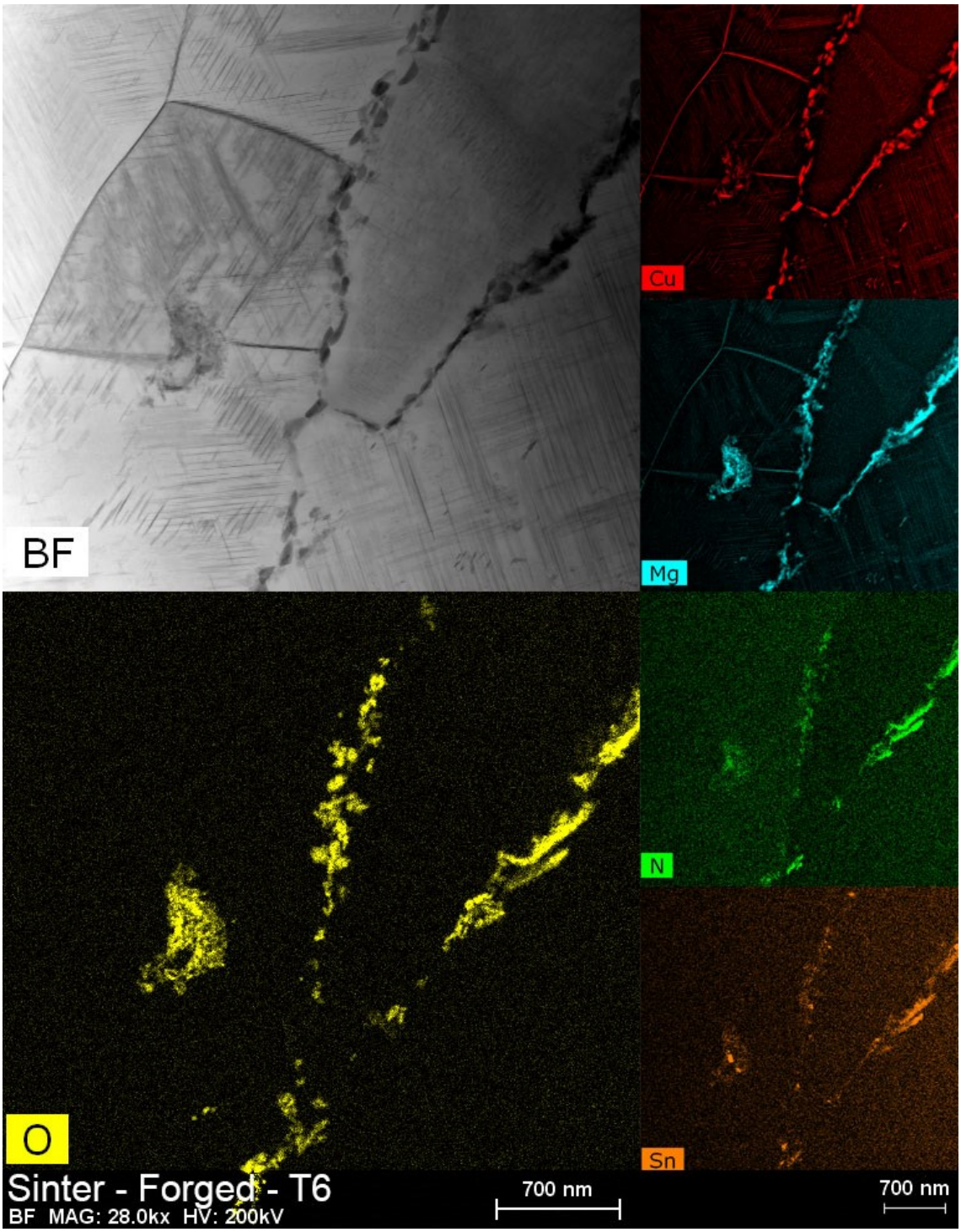

Figure 8-13 TEM micrographs highlighting the nature of the prior particle boundary of a sintered – forged (1.40mm/mm) - T6 specimen. Included are the bright field image and the EDS-acquired elemental maps of oxygen, copper, magnesium, nitrogen and tin.

Oxygen distribution along the forged PPB was indicative of significant localized shear strain. In this sense, MgO was discretized further into clusters of fine crystallites and separated by oxide-free segments of PPB. While it was previously known that a continuous nano-scale metallic phase existed in the PPB [118], this breakup phenomena produces significantly finer segments of MgO on the order of a few 100's of nm in length. Such a significant disruption in the oxide phase is anticipated to be the primary mechanism for the improvement in ductility measurements observed with forging strain in Figure 8-4.

Sn and N concentrations followed a distribution pattern comparable with O. Mg_2Sn and AlN phases were similarly discretized into clusters and separated by metallic regions. Hence, improvements in mechanical properties must be considered to have been influenced by the redistribution of these phases along the PPB as well.

8.6 Conclusions

The complex microstructure of a sintered aluminum powder metallurgy (APM) alloy before and after hot upset forging was investigated. Hot deformation parameters were fixed at 450°C and 0.1 s^{-1} to isloate the microstructural and mechanical effects of precipitates and secondary phases. The response to hot upset forging brought about considerable improvements in physical and mechanical properties. Given the unique processing of APM compoenents, the microstructure exhibited Sn and O-bearing phases

uncommon to wrought metallurgy products. The following conclusions were drawn about the microstructural highlights observed in this manuscript.

- Densification from 98.7% to 100.0% through hot upset forging was observed. Forging to 1.40 mm/mm was effective at eliminating most of residual porosity.
- The precipitate phases in the sintered-T6 and sinter-forged-T6 conditions were comparable and were dominated by those produced through the S (Al_2CuMg) phase precipitation sequences.
- Oxygen-rich regions originating at prior particle boundaries, were apparent in the sintered compact as a continuous film of oxide phase. These were identified to contain a fine dispersion of MgO and Mg_2Sn phases.
- Upset forging the sintered compact effectively disrupted the residual oxide phase into a semi-continuous network that fostered the occurrence of metallic bonding between adjacent prior particles. Critically, the tensile ductility responded positively as a linear increase was observed up to a maximum value of 17.0% at a forging strain of 1.40 mm/mm, representing a 4-fold improvement.

8.7 Acknowledgments

The authors would like to acknowledge Bernhard Mais (Ecka Granules) and Jessu Joys (U.S. Metal Powders) for the provision of the powdered metals employed. This research was funded by the Natural Sciences and Engineering Research Council of Canada (NSERC) via the Collaborative Research & Development grant CRDPJ, number [486528-15].

CHAPTER 9. A MICROSTRUCTURAL AND MECHANICAL PROPERTY INVESTIGATION OF A HOT UPSET FORGED 2XXX SERIES ALUMINUM POWDER METALLURGY ALLOY REINFORCED WITH ALN.

Gregory A. W. Sweet [1], Bruce W. Williams[3], Alan Taylor [4], Richard L. Hexemer, Jr. [5], Ian W. Donaldson [6] and Donald Paul Bishop [2]

1 – Graduate Student, Dalhousie University, Halifax, Nova Scotia, Canada
2 – Professor, Materials Engineering, Dalhousie University, Halifax, Nova Scotia, Canada
3 – Research Scientist, CanmetMATERIALS, Natural Resources Canada, Hamilton, Ontario, Canada
4 - Vice President – Lightweight Technology, GKN Sinter Metals LLC, Auburn Hills, Michigan, USA
5 – Research Engineer, GKN Sinter Metals LLC, Conover, North Carolina, USA
6 – Director of R&D North America, GKN Sinter Metals LLC, Auburn Hills, Michigan, USA

Status: Submitted to Materials Science and Engineering: A on March 3, 2019

Author Contribution: The following experimental procedures, results and discussions were completed by G.A. Sweet, with technical guidance, reviewer and editorial roles played by the subsequent authors.

9.1 Forward to Chapter 9

This manuscript parallels the content outlined in Chapter 8 but with a specific focus on the evolution of ceramic-bearing materials in response to hot forging. A more thorough investigation of mechanical properties was performed, including tensile and fatigue testing. Anisotropic effects were probed via fatigue tests and a qualitative analysis of the Al-AlN interface was inferred through TEM observations.

9.2 ABSTRACT

Metal-matrix composites (MMC) of a 2000-series aluminum alloy coupled AlN were fabricated through a commercially-relevant aluminum powder metallurgy (APM) approach. Cylindrical preforms containing 0 to 5 volume % AlN were produced to investigate the mechanical properties and microstructure evolution through hot upset forging. Specimen were deformed to a maximum strain of 0.15 to 1.55 mm/mm at rates of 0.1 s^{-1} to 1.0 s^{-1}. TEM observations of forged products indicated the Al-AlN interfaces were free of defects and of high quality. Near-full (>99.5 % theoretical) densities were observed at 1.40 mm/mm. At this strain a substantial increase in all tensile properties was observed. With an elastic modulus of 77 GPa was realized in a forged product with 5% AlN, accompanied by a 0.2% offset strength of 325 MPa and a UTS of at least 400 MPa. Versus an undeformed sample, forged MMC's exhibited up to a five-fold increase in tensile ductility. Likewise, improvements of up to 98 MPa (57%) in fatigue strength were recorded. Mechanical gains were a result of densification and residual oxide disruption, as well as the enhanced dispersion of the AlN phase.

9.3 INTRODUCTION

Aluminum alloys reinforced with ceramic particulate have been an area of research interest with commercial success in the automotive marketplace [119]. Engineered additions of discontinuous particulates are incorporated in an aluminum matrix to leverage the desirable mechanical properties (I.e. modulus, strength, lower coefficient of

thermal expansion) of ceramic powders. With effective ceramic additions, aluminum metal matrix composites (MMCs) can exhibit superior mechanical properties such as strength-to-weight ratios, fatigue performance, wear resistance and modulus. Traditionally, commercial automotive applications of these materials have been dominated by additions of either SiC or Al_2O_3 [120]. Other particulates such as ZrO_2, B_4C, TiC, BN, TiN and graphite additions have also been incorporated into 1000, 2000, 6000 and 7000 series aluminum alloys [21]. In other works, aluminum MMCs that contain AlN additions have been considered. AlN is attractive in that it is not excessively reactive with aluminum while possessing a high hardness, modulus, and high thermal conductivity coupled with low coefficients of thermal expansion and friction [86]. Furthermore, studies have shown that the interfacial strength between Al and AlN is sufficiently strong to allow for load transfer to the ceramic phase [121] [53,122].

Aluminum MMCs containing AlN are now exploited on a commercial, high volume scale when processed through press-sinter-size aluminum powder metallurgy (APM) technology [106]. This process commences with solid state blending of the metallic matrix constituent powders with AlN particulate. The powder mix is then consolidated into the prescribed shape via uniaxial die compaction. Compacts are then pressureless sintered and, finally, sized into near-net shape components. MMCs processed in this manner are now utilized in demanding automotive applications, such as planetary carriers in General Motors 9T50 9-speed automatic transmissions [106]. Fundamental studies on these MMCs with various types and concentrations of AlN demonstrated promising benefits. For instance, green strength was improved by 4x, sintered densities that

impinged on full theoretical values were achieved, and elastic modulus values increased [123].

While highly successful in its own right, increased market proliferation for Al-AlN APM MMCs is envisioned for powder forged variants wherein residual porosity may be eliminated and the residual oxide networks disrupted. In and of itself, powder forging is a commercially mature technology within the ferrous powder metallurgy market [124]. Here, a carefully-designed sintered preform is hot deformed into a final geometry in a single stoke, simultaneously collapsing's residual porosity and refining the microstructure [29]. Wrought components undergo significant plastic strain during forging, creating acute texture and in some instances, planes of weakness along stringers of impurities. Such features can impart anisotropy in mechanical properties, whereas powder forged ferrous components have shown isotropic properties in light of the relatively limited level of plastic strain required [29]. Chawla et al. set the precedent for a powder forged APM MMC, whereby a 20 vol% SiC-reinforced 2000 series alloy was successfully forged to produce properties on par with extrusion practices [37]. Despite this, investigations on the mechanical properties of powder forged APM MMC materials are lacking, particularly those reinforced with AlN. Sensibly, the purpose of this study is to fill this void by investigating the physical and mechanical properties of hot upset forged commercially relevant AlN-reinforced APM MMC systems.

9.4 MATERIALS AND METHODOLOGY

A description of the starting powders utilized to prepare the APM MMCs studied is shown in Table 9-1. In all instances the matrix component was an admixed blend of the metallic powders prepared with a nominal composition of 95 Al, 3 Cu, 1.5 Mg and 0.5 Sn (weight %). One of two AlN additions were then admixed to this matrix pre-mix at concentrations of 0, 2 or 5 volume %. The AlN additions were either AlN-C (Coarse) or AlN-F (Fine), which were named to reflect their relative average particle size. The system devoid of AlN additions is referred to as 'Base' and individual MMC compositions are referred to by the concentration and type of AlN employed (i.e. 5C for an MMC that contained 5 volume % coarse AlN). Once each material of interest was produced as a homogenized mixture, 1.5% by weight of a lubricant powder (namely, Licowax C, Clariant Corporation), was incorporated to aid die compaction.

Table 9-1 Type, size and composition of the constituent powders employed in raw blend production.

Powder	Powder Type	Size	Composition (wt%)							
		(D_{50}, μm)	Al	Mg	Si	Cu	Fe	Sn	O	N
Al	Elemental	99	Bal.	T	0.02	T	0.10	0.03	-	-
Cu	50:50 Al: Cu Master	16	Bal.	0.01	0.02	46.5	0.05	0.05	-	-
Mg	Elemental	32	0.01	Bal.	0.01	T	0.01	T	-	-
Sn	Elemental	12	T	T	T	T	0.01	Bal.	-	-
AlN-C	Ceramic	12	Bal.	-	-	-	0.05	-	1.3	32.0
AlN-F	Ceramic	3	Bal.	-	-	-	0.05	-	1.5	32.0

T – trace amount, below detectable threshold.

Details on blending, compaction and sintering of the feed material are documented in a prior study by the authors [110]. Under these parameters, cylindrical specimens were produced measuring 50 mm diameter x 44 mm tall in the green state and then sintered. Forging simulations were carried out on the sintered billets using an Interlaken Technology 1100 kN press (Figure 9-1) with a maximum stroke rate of 5000 mm/mm obtained by employing a hydraulic accumulator system. The load frame was instrumented to acquire load and displacement data throughout the duration of each forging experiment. A pseudo-true strain rate control strategy was employed to emulate conventional lab-scale hot upset deformation simulation equipment. This was accomplished by following an open-loop sinusoidal position versus time stroke profile regression that was calibrated for a cylindrical sample geometry, as outlined in [96]. Forging tests were carried out isothermally; as-sintered samples were preheated to 450°C in a box furnace for 3 hours while H13 tool steel platens were simultaneously heated to the same temperature. Forging platens and samples were both coated with an aerosol boron nitride lubricant prior to heating. Deformation was carried out at a true strain rate of 0.1 s^{-1} for the bulk of work, except for select experiments wherein a faster rate of 1.0 s^{-1} was implemented. In addition to select samples being tested in the as-sintered state, forgings were carried out to true strains of 0.15 mm/mm up to 1.55 mm/mm. Once forged, each sample was water quenched to room temperature and then heat treated to the T6 state (isothermal hold at 510°C for two hours, water quench to room temperature, 10-hour isothermal hold at 190°C) prior to sectioning/machining into mechanical property specimens.

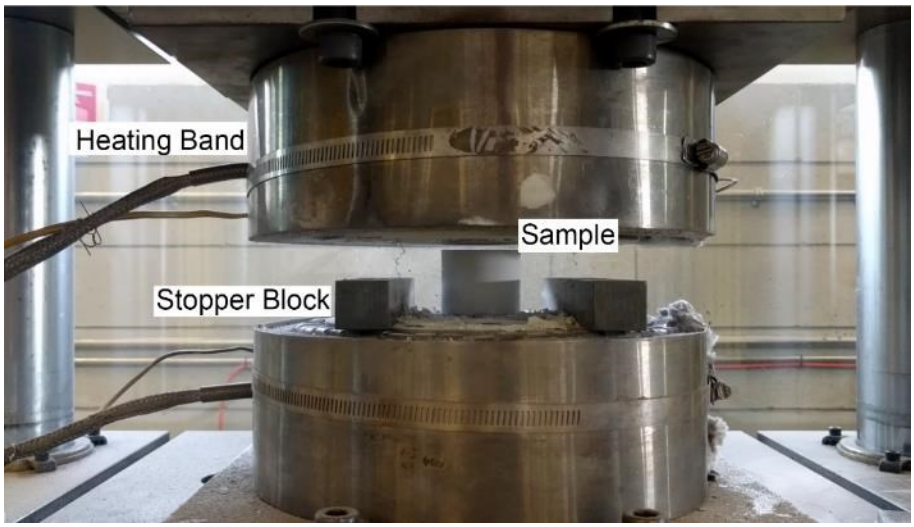

Figure 9-1 Photograph of the sample and die assembly in the Interlaken 110 load frame prior to deformation.

Density measurements were performed on T6 treated samples using the Archimedes approach outlined in the MPIF standard 42, using the oil-free 'dry' method. Measurements were reported as a percent of the theoretically attainable maximum value. Metallography samples were sectioned using a diamond abrasive saw and hot mounted in Bakelite. Each was ground and polished using a standard progression of SiC abrasive papers, diamond oils and colloidal silica media using a Struers Tegramin semi-automatic polishing system. The microstructures of unetched samples were imaged using an Olympus BX51 optical microscope, while scanning electron microscopy (SEM) micrographs were captured using a Hitachi S-4700 cold field SEM. For high magnification microscopy studies, 2mm thick wafers were cut from bulk T6 samples, thinned to ~500 μm using SiC paper, and then punched into 3 mm discs. Discs were further thinned using alumina suspensions and dimpled. The dimpled disc was milled until perforation using a Gatan 691 PIPS ion mill. These samples were investigated using

a Technai Osiris (Scanning) transmission electron microscope (TEM) equipped with a 200 kV X-FEG gun and an EDX detector system. Element mapping was carried out under 1 nm spatial resolution by obtaining a sub-nanometric electron probe. All metallography samples were sectioned such that the viewing axis was oriented parallel to the forging axis and with the chord axis horizontal to the page, unless noted otherwise. In all instances where mechanical properties were assessed, specimens were machined from forged pucks heat treated to the T6 state. MPIF standard 10 was followed for machining and testing of tensile specimens, except the gauge length was halved to 12.5 mm. This was necessary to extract tensile data from forgings that were strained to less than 0.90 mm/mm, which were too small (diametrically) to produce standard length specimen. Dynamic elastic modulus measurements were performed on 70.0 x 12.0 x 3.00 mm rectangular plates using the impulse excitation method according to the NPL Measurement Good Practice Guide No 98 [87]. Fatigue strength was evaluated using a staircase statistical approach employed per MPIF standard 56. Here, 31.7 mm x 11.5 mm x 9.0 mm rectangular 'TRS' specimens were machined from forged pucks in three different geometries as shown in Figure 9-2. With respect to the forging axis, three axes were identified: The Longitudinal axis, Radial axis and the Chord axis (any straight, offset line parallel to the radial axis). Extracted samples geometries were C-L (i.e. the chord axis was parallel to the loading direction and the longitudinal (forging) axis oriented with the crack growth direction), C-R (radial axis parallel to the crack growth direction) and L-C. In most instances, specimens of the C-L type were machined and tested. However, all three were extracted from 0.35 mm/mm forgings to investigate anisotropy in fatigue performance. All fatigue specimens were loaded in an Instron

model 1332 servo-hydraulic load frame set up for three-point bend testing. Tests were carried out at room temperature in a non-humidity-controlled atmosphere. The runout criterion was chosen at 10^6 cycles using a step size of 5 MPa and an R-ratio of 0.1. The reported values of fatigue strength are 50% survival stress, while error bars represent the 10% and 90% survival stress (i.e. 50% confidence that either 10% or 90% of samples will endure 10^6 cycles). These error bars were adopted to conform with standard practices, while measurements elsewhere in the manuscript are reported as a single standard deviation about a mean value. Statistically significant inferences were made using a threshold value of $\alpha = 5\%$ throughout.

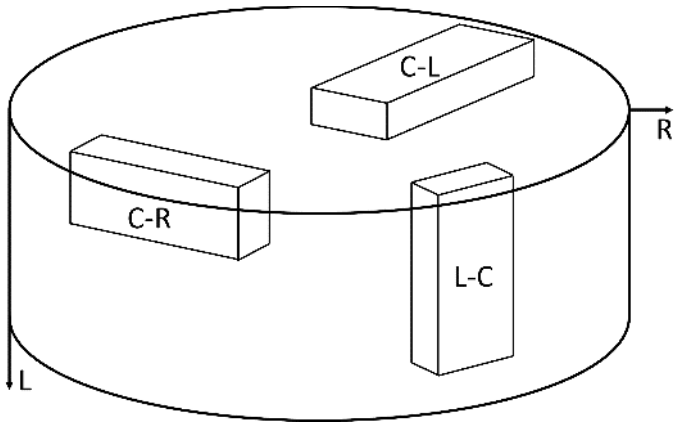

Figure 9-2 Schematic of TRS specimen orientations sectioned from cylindrical, forged pucks. Specimen were sectioned in three orientations relative to the Chord, Radial and Longitudinal (forging) axes.

9.5 Results and Discussion

50 mm cylinders of all compositions were successfully forged up to a maximum true strain of 1.55 mm/mm. Higher strains were prohibitive due to the exponential increases in load rapidly approaching the safety limits of the frame. Preliminary thermal-mechanical data for these MMC's were obtained using a Gleeble 3500 at temperatures ranging from 350°C to 500°C and 0.005 s^{-1} to 5 s^{-1} [110]. Deforming at the highest temperature and above 0.5 s^{-1} lead to adiabatic heating-induced hot cracking. In this study, deforming at a true strain rate of 0.1 s^{-1} and 1.0 s^{-1} were equally successful, the latter being the highest nominal value obtainable for the prescribed preforms on the Interlaken frame. Preliminary unpublished results inferred the difference in mechanical properties between the two rates to be minimal. Accordingly, the former rate was selected as the convention for the bulk of tests while 450°C was chosen as the sole forging temperature for this study, as it afforded the lowest flow stress values while mitigating the risk of hot cracking.

9.5.1 Physical Attributes

Densification of the material 2C was investigated as a function of hot upset forging strain, as shown in Figure 9-3. In the sintered-T6 condition, this material was 98.7% of the theoretical maximum. Densification was rapid up to 99.2% at a true compressive strain of 0.30 mm/mm, followed by an intermediate rate of densification up to 1.20 mm/mm. Further deformation up to 1.55 did not produce any significant changes.

However, the maximum observed densities were very near the maximum value coming in at 99.8% of full theoretical for 2C. The densification response of this system compared well with the conclusions of a prior study on the forging of the ceramic-free version of this material [125]. Therein, preforms densified from 98.7% to a peak of 100.0% at a strain of 1.40 mm/mm. In the current study, the discrepancy in peak density values suggests entrained porosity associated with the ceramic phase.

The suite of micrographs in Figure 9-4 coincide with these density observations. Here, the forging direction is oriented vertically within each micrograph. Several unique phases in both light and dark contrast within the matrix were apparent. Remnants of the prior liquid phase were observed in light contrast with the matrix [19]. Admixed AlN particulate were dark gray in contrast. AlN appeared intact, with no evidence of particle fracture having occurred during hot deformation. Porosity was observed in black contrast in three unique morphologies. First, as the sole phase adjacent to two or more aluminum grains. Second adjacent to two or more prior particles along and entrained in the complex morphological features of AlN particulate (dark gray contrast). Third, as internal porosity within certain AlN particles. The latter was a permanent feature, given the lack of evidence of AlN fracture and pore filling during deformation at any strain. A magnified AlN-C particle shown in Figure 9-5 highlights this entrained permanent porosity within an otherwise pore-free matrix hot upset forged to 1.40 mm/mm. At a compressive strain of 0.15 mm/mm (Figure 9-4(a)), both the first and second pore morphologies were on the order of 1's to 10's of micrometers in size, with a shape typically irregular or lenticular.

Pores did not appear within grains, but rather as the vacant regions at the rounded corners of prior particles.

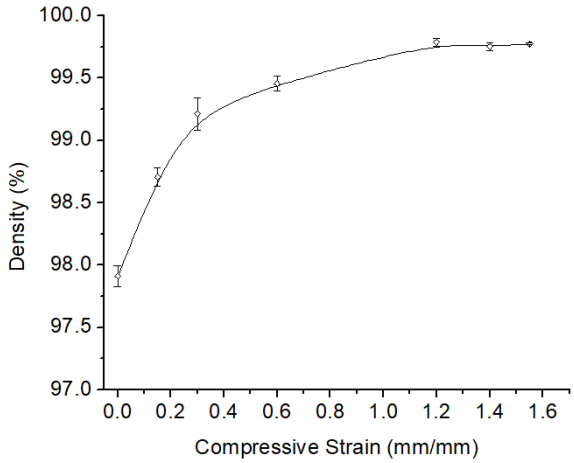

Figure 9-3 Densification trend of MMC 2C as a function of hot upset forging strain.

Porosity in the microstructure at a compressive strain of 0.30 mm/mm (Figure 9-4(b)) was less prevalent in general. The largest observed pores had a more flattened and elongated shape, with the major geometrical axis typically normal to the forging axis as would be expected from an open-die forging operation. Finer porosity remained more equiaxed in nature. Coarser pores were effectively eliminated at a strain of 0.60 mm/mm (Figure 9-4(c)); evidence of few flattened and elongated coarse pores persisted (red arrow) as did the sporadic occurrence of fine equiaxed pores. These fine pores prevailed even after deformation to 1.40 mm/mm, albeit in decreased numbers. The 0.2% density discrepancy of 2C and its theoretical maximum appeared to be the sum of fine equiaxed porosity within the matrix and the inherent internal porosity of AlN particulate.

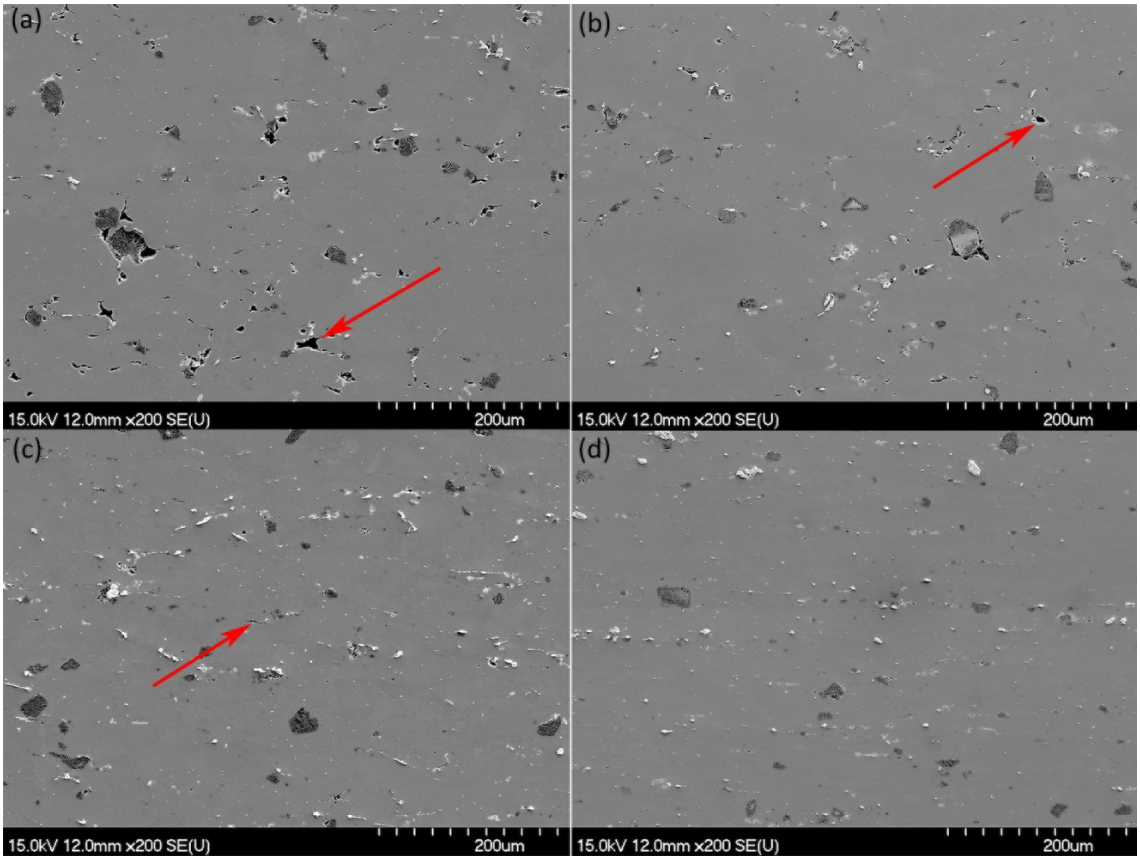

Figure 9-4 Electron micrographs of the hot upset material 2C at strains of (a) 0.15 mm/mm, (b) 0.30 mm/mm, (c) 0.6 mm/mm and (d) 1.4mm/mm. Irregular particles in gray contrast are AlN, regions of black contrast and selectively annotated with red arrows are residual porosity.

In prior studies with relatively small specimens (1.2 cm^3), AlN additions were found to negatively affect as-sintered density yet this was reversible through hot deformation up to 0.70 mm/mm [110]. The larger specimen (77.0 cm^3) used in this study showed comparable trends. In this sense, additions of AlN-C or AlN-F rapidly decreased the sintered density to 97.0% for 5C and 95.7% for 5F; AlN-F being more detrimental. Hot upset forging to a uniform strain value of 1.40 mm/mm was successful in eliminating the AlN-associated porosity. 2C and 2F approached full density while 5C and 5F were near-

theoretical with values at least 99.5%. Despite the density of the sintered compacts being acutely sensitive to AlN-F additions, hot upset forging of materials with the finer ceramic proved to produce the highest densities. For a given forging condition, the density of AlN-F bearing materials exceeded AlN-C ones by 0.1 to 0.2%. likely attributable to the lesser internal porosity of the smaller particulate.

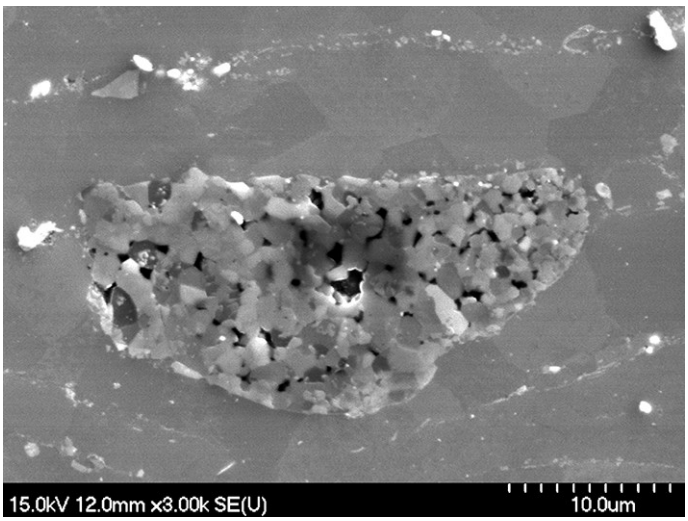

Figure 9-5 Coarse AlN-C particle within an aluminum matrix, showing porosity in black contrast within the ceramic phase.

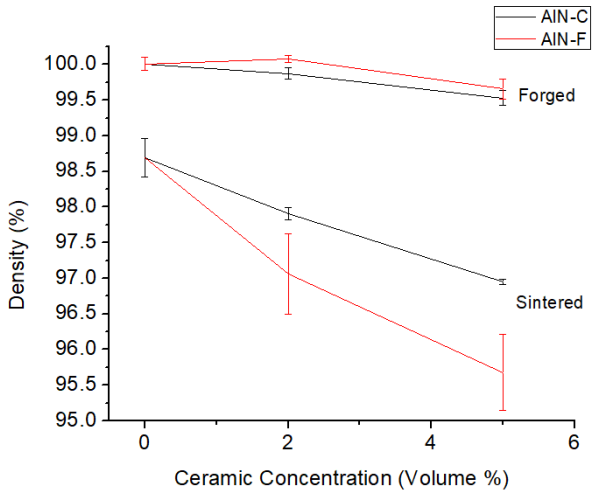

Figure 9-6 Comparison of sintered and forged densities for MMC systems that utilized different types and concentrations of AlN particulate. All samples hot upset forged to a true strain of 1.40 mm/mm.

Electron micrographs of additional MMCs at a fixed upset forging strain of 1.40 mm/mm are presented in Figure 9-7. Without AlN, the Base material (Figure 9-7(a)) exhibited limited fine equiaxed pores. Such pores measured up to approximately 5 μm in size, while many were submicron. Secondary phases in bright contrast with the matrix and were the remnants of the liquid phase that was present during sintering. At this higher resolution a fine horizontal network of phases in light contrast with the matrix was evident. This is characteristic of APM materials and represents the oxygen-rich prior surface of powder particles, deemed prior particle boundaries (PPBs). Hot upset forging strain deformed the PPBs such that they were elongated in a direction normal to the forging axis. The relatively low density of 5C was attributed to the entrained porosity from the ceramic phase. The micrograph for this MMC (Figure 9-7(b)) shows the bulk of the black pore phase was associated with coarse AlN-C particles. Fine equiaxed pores

within the matrix appeared similar in size and distribution to other MMC compositions in this study.

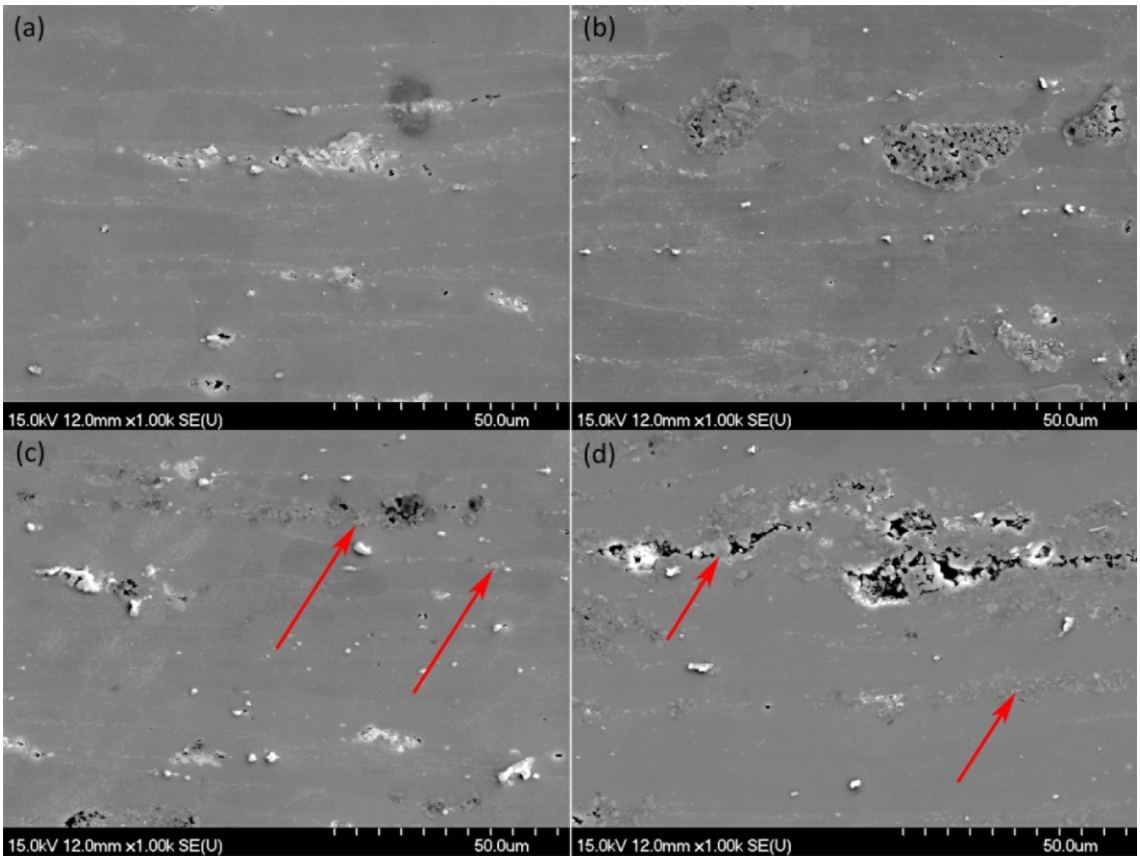

Figure 9-7 Microstructures of materials (a) Base, (b) 5C, (c)2F and (d) 5F hot upset forged to a true strain of 1.40 mm/mm. Red arrows highlight the typical contrast of AlN-F particulate.

Micrographs of MMC made with 2% and 5% of the finer AlN-F are shown in Figure 9-7(c) and Figure 9-7(d) respectively. Here, AlN particulate persists as a slightly darker gray phase in contrast with the matrix, as identified by red arrows. For the most part, AlN-F appears well incorporated with the matrix and free of pores. AlN appeared concentrated in regions along prior particle boundaries; the matrix phase penetrated these

concentrated regions. However, 2% AlN, 2F exhibited several regions of AlN with entrained porosity. The fine particle size of this powder rules out the possibility these are entrained pores within coarser particles. Rather, the authors have shown before that clusters of AlN-F have a propensity to hinder matrix infiltration [84,96]. 5% AlN-F further increased the occurrence of clusters, as shown in Figure 9-7(d) as several large pores lined with fine AlN particulate persisted. Although elongated and flattened in a manner consistent with other pores in this study, the lateral flanks of these pores had failed to bond in a metallurgically cohesive manner after forging. Again, AlN-F particles did not appear to fracture during hot deformation. Rather, loosely bound clusters were redistributed through the application of forging strain.

Successful incorporation of AlN within the material critically relies on the ceramic/matrix bond. A sufficient bond is one that allows load transfer between the constituents yet does not fracture during plastic deformation of the bulk composite when forged into shape [21]. Accordingly, studies on these interfaces were completed through TEM/EDX. When processing the MMC systems, it is to be recalled that a mixture of powders described in Table 9-1 was prepared, compacted, and then sintered. Accordingly, particles of Al (oxidized with a thin surface film of Al_2O_3 because of air atomization) and AlN were forced into direct intimate contact during mixing/compaction. The metallurgy of the Al-AlN interfaces could then be modified during sintering because of chemical reactions, liquid phase formation, atomic diffusion, etc. An exemplary Al-AlN interface for the material 2C hot upset forged to 1.40 mm/mm is shown in Figure 9-8. The α-aluminum particle on the left of the bright field (BF) image was isolated from

the AlN particulate by a thin interface running diagonally within the image. The EDS map of nitrogen highlights the monolithic AlN particle. The feathered nature of the edge this element suggests the boundary is misoriented slightly and arbitrarily from the beam axis.

EDX mapping inferred that the interface was evidently enriched in several unique phases. First, both Cu and Mg maps exhibited regions of overlap but at discrete concentrations. This suggested that the S-phase (Al_2CuMg) had precipitated within the interfacial region. Extensive overlapping in the maps for Mg, O and Sn was also observed with each element distributed along the interface as a thin film. Thermodynamically, it is known that the pre-existing surface layer of Al_2O_3 on the air atomized aluminum particles will react with elemental Mg during sintering to form $MgAl_2O_4$ or MgO [117]. Hence, the overlap between Mg and O maps imply that one or both phases were present as would be expected. In the case of Sn, it is known that minor additions of this element promote high densities in liquid phase sintered APM alloys when present in conjunction with Mg [9]. The ensuing liquid phase formed between these elements is known to readily wet PPBs and thereby throttle the growth rate of AlN on the surface of Al particles [126] and/or Al-rich liquid phase [11] so as to aid densification. Hence, the combined presence of these elements at the Al-AlN interface was also as expected. Overall, it was clear that the Al-AlN interface was complex and that it was modified through sintering-induced interactions. Furthermore, as all inspected interfaces had a high level of integrity and were free of defects (voids, micro cracks, etc.), it was inferred that Al-AlN bonding was of a high quality in the forged MMC products.

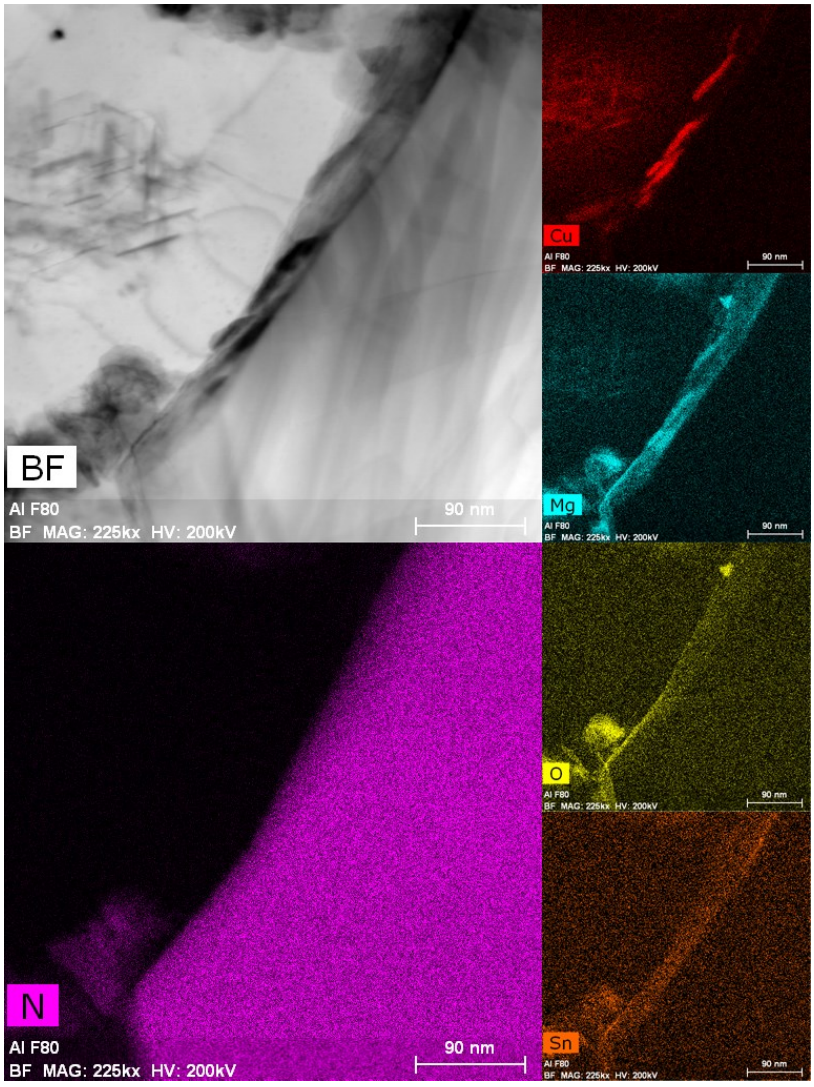

Figure 9-8 TEM analysis of an exemplary Al-AlN interface including a BF image and EDX maps for the key elements of interest. Material was 2C hot upset forged to 1.40 mm/mm at a rate of 0.1 s^{-1}.

9.5.2 Mechanical Performance

Changes in tensile behaviour as a function of hot upset forging strain were observed, as summarized for 2C in Figure 9-9. Data for the unforged material from a previous study by Sweet et al. [123] are represented on the figure as 0.00 mm/mm. The assessed strains

of 0.30 mm/mm and 1.40 mm/mm were chosen as they encompassed the breadth of values from which tensile specimen could be successfully extracted, as outlined in a previous publication [96]. The unforged and 0.30 mm/mm conditions produced insignificantly changes in tensile properties, except for the mean tensile ductility increasing from 2.7% to 4.9%. Increasing the forging strain from 0.30 mm/mm to 1.40 mm/mm similarly enhanced tensile ductility 11.6%. The additional forging strain also afforded significant increase in the load bearing capacity of the material as the 0.2% offset strength and tensile strength increased by 30 MPa and 60 MPa, respectively. The observed nonlinearity of strengths with forging strain raises questions about the underlying microstructural mechanism. A prior study showed no microstructural evidence confirming of recrystallization or grain refinement under comparable forging conditions and up to 0.70 mm/mm forging strain. Accordingly, it was inferred that the offset strength improvements were largely attributable to pore collapse. Improvements in UTS and ductility were unequivocal and are discussed in the following text.

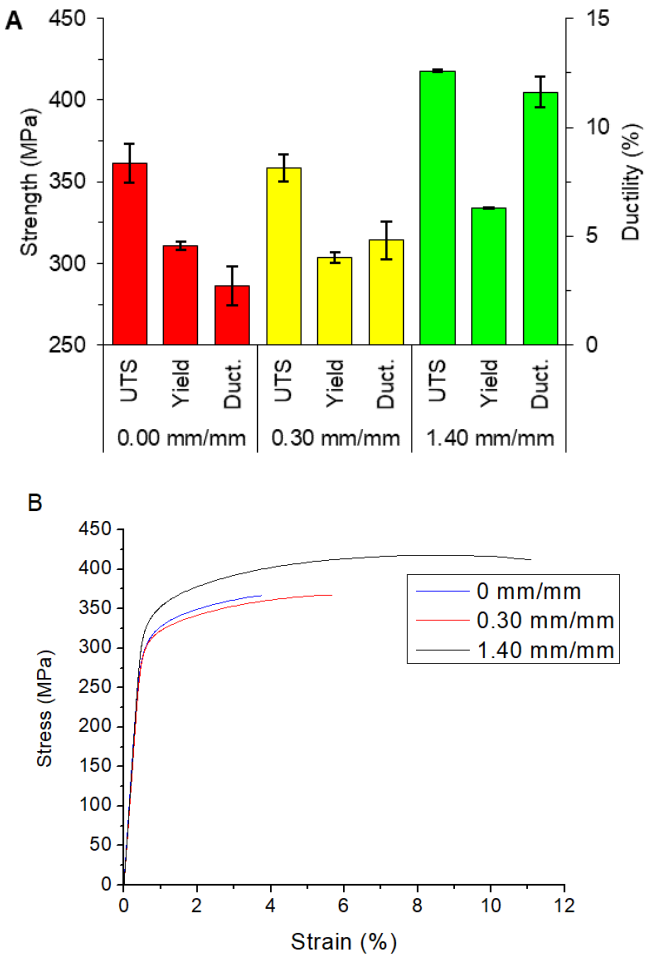

Figure 9-9 (a) Summarized tensile properties and (b) stress-strain curves of MMC 2C when forged to different levels of true strain. All samples heat treated to the T6 state. Data for 0.00 mm/mm from [123].

Modulus measurements performed by impulse excitation are summarized in Figure 9-10 for the 5 MMC compositions before and after forging to an upset strain of 1.40 mm/mm and heat treating to the T6 state. Significant trends in dynamic moduli were observed as a function of either ceramic addition. Both 2C and 2F improved to within less than a single standard deviation of each other, for a mean value of 74.0 GPa. Likewise, a mean elastic modulus of 77.0 GPa was observed with 5% AlN. These measurements significantly

exceeded the elastic modulus measurements of the unforged specimen, which are represented by dashed lines on the figure. For a given chemistry, improvements were generally in the range of 0.8 to 2.8 GPa (for 2C and 5C, respectively). 5F uniquely improved by 9.2 GPa over the sintered equivalent. The beneficial improvements in modulus correlate well with densification observed in Figure 9-6. For 5F, it was concluded that finer PSD of this ceramic introduced significant porosity within AlN clusters, whereby the sintered density and mechanical properties were uncharacteristically low. Now, hot upset forging was particularly beneficial in disrupting clusters of AlN, collapsing pores and revealing the potential of this material. Similarly, the more modest modulus gains of the remaining systems were attributed to the densification effect of hot upset forging and the proportionality thereof. Evidently, the particle size of the ceramic phase did not produce any significant effect on modulus.

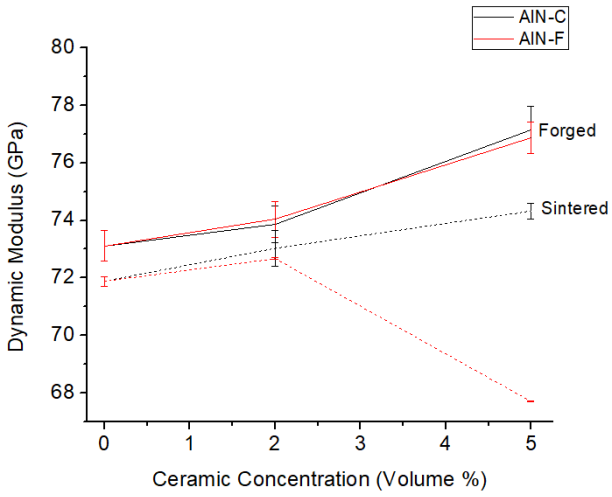

Figure 9-10 Dynamic elastic modulus of MMC materials hot upset forged to 1.40 mm/mm at a rate of 0.1 s^{-1} as measured by the impulse excitation method. All materials heat treated to the T6 state. Data for 0.00 mm/mm from [123].

0.2% offset yield strength values as a function of ceramic additions (Figure 9-11) showed marginal but statistically insignificant negative trends for AlN-C addition and AlN-F additions. While density measurements suggested AlN-F additions were the better option, yield strength observations were ambivalent to AlN particle size. The mean yield strength values for AlN-C and AlN-F-bearing MMC's were effectively identical at 331 MPa and 328 MPa, respectively. The marginal but insignificant downward trend in 0.2% offset strength correlated with the tendency for higher residual porosity with increased ceramic content. However, the concentration of ceramic used in this study were within a range that did not invoke any significant negative effect. Akin to the trends discussed in Figure 9-9, hot upset forging had a positive impact on the yield strength. Sintered T6 materials in the prior study were acutely sensitive to AlN additions [123], especially of the AlN-F variant. Difference in load bearing capacity were attributed to the inherent sinterability of the material system. Hot forging invoked densification to near-theoretical values regardless of chemical makeup, eliminating any differences observed in the sintered product. Base, 2C, 5C and 2F all improved over the unforged equivalent by 21 to 42 MPa, while 5F again exhibited the largest increase, 79 MPa, by it exhibiting the greatest density change.

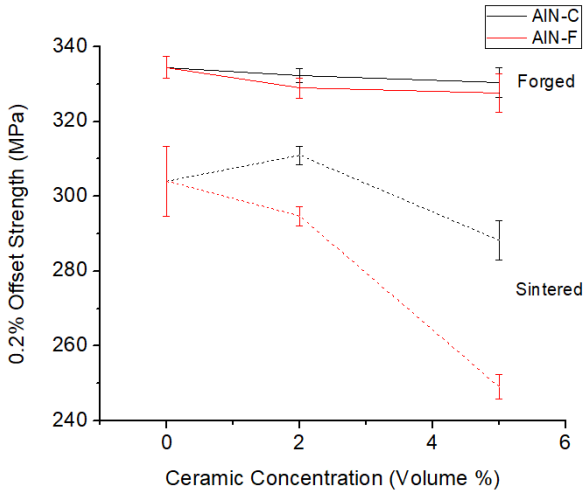

Figure 9-11 Effect of AlN type and concentration on yield strength. All materials hot upset forged to 1.40 mm/mm at a rate of 0.1 s^{-1} and heat treated to the T6 state. Data for 0.00 mm/mm from [123].

Significant negative linear trends in ultimate tensile strength (UTS) were observed through the additions of either ceramic type, as shown in Figure 9-12. Uniquely, the disparity trend associated with additions of either coarse or fine AlN appeared again. In this sense, 5F measured 12 MPa below Base, while the coarser ceramic phase of 5C was over double that. Not only did this oppose what was observed for yield strength trends in this study, it opposed the UTS behaviour for the same MMC compositions in the sintered T6 condition. There, additions of either ceramic type still produced a more severe decrease in UTS, but the unforged equivalent of 5C and 5F were 48 MPa and 91 MPa lower than the sintered Base system, respectively. Accordingly, the net effect of hot upset forging on UTS for the finer, AlN-F-bearing system was the most pronounced. Forged 5F exceeded its sintered counterpart by 130 MPa, while 5C exhibited a 74 MPa gain. Without any AlN, the Base system showed a noteworthy 51 MPa improvement through

hot upset forging. These unique observations were elucidated by ductility and strain hardening behaviours.

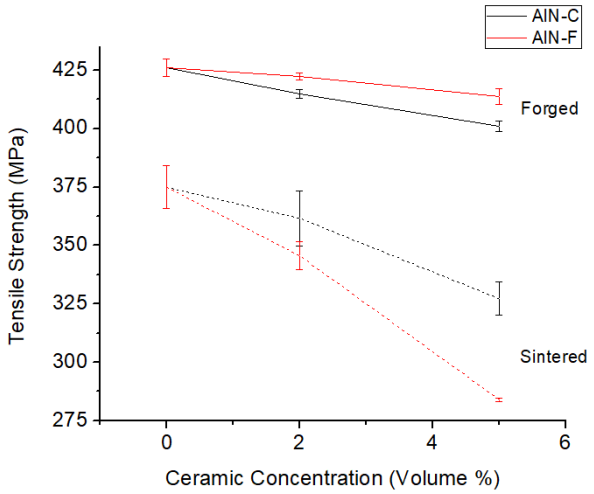

Figure 9-12 Effect of AlN type and concentration on UTS. All materials hot upset forged to 1.40 mm/mm at a rate of 0.1 s^{-1} and heat treated to the T6 state. Data for 0.00 mm/mm from [123].

The negative trend in UTS may be partially caused by the associated decrease in density with ceramic additions. Residual pores would not contribute to the load bearing capacity of the bulk material, while possibly promoting micro void formation and coalescence. However, a larger driving force would be the reduced tensile ductility for ceramic-bearing materials, shown in Figure 9-13. The strain at fracture for 2C forged to 1.40 mm/mm was 3.4% below that of Base, and 5C was an additional 3.9% lower than that. 5F was similar measuring 7.2% below Base. Such decreases in ductility were not unexpected for the ceramic-bearing systems. Rigid AlN particles are brittle and effectively unable to flow plastically with the matrix. Assuming a circumstance of plastic strain without particle decohesion or fracture, the matrix phase would undergo strain localization

adjacent to AlN particulate thereby facilitating the declines observed. The decreased UTS values for ceramic-bearing materials was attributed partially to this effect. Substantial gains in UTS through forging were similarly attributed to the evidence of tensile ductility in forged samples being substantially improved over the sintered equivalent materials. Base exhibited ductility values 10.0% greater than in the previous works, a three-fold improvement. Similarly, AlN-C bearing composited exhibited a four-fold increase, while the increase to AlN-F MMC's were five-fold. Improvements in tensile ductility through hot forging were previously attributed to the disruption of residual oxide phases. In the sintered condition, a semi-continuous network of MgO had been identified along prior particle boundaries [125]. Upon forging, localized shear strain discretized the MgO phase into clusters of fine crystallites separated by segments of prior particle boundary free of oxides. Effectively, the fraction of metallic bonding between adjacent prior-particles was enhanced, improving tensile ductility.

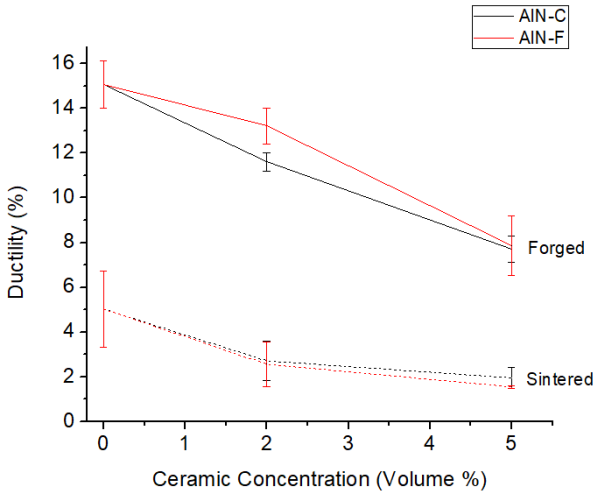

Figure 9-13 Tensile ductility values as a function of ceramic type and concentration at a fixed strain of 1.40 mm/mm and rate of 0.1 s^{-1}.

AlN-C and AlN-F-bearing composites exhibited comparable densities, yield strength and tensile ductilities, yet the UTS behaviour favored the AlN-F addition. Evidently, the strain hardening behaviour was suspect. Figure 9-14 plots the calculated strain hardening exponent for the five materials compositions hot upset forged to 1.40 mm/mm. Additions of AlN-F did not deviate from the strain hardening behaviour versus the Base material. The mean value for these materials was 0.127. On the other hand, AlN-C additions resulted in significant decreases with increased ceramic additions, to a value of 0.104 in 5C. Martin et al. observed this phenomenon in SiC-reinforced Al2124, concluding it was the onset of plastic localisation [127]. Li et al. summarized that a metal matrix composite should exhibit comparable strain hardening behaviour to the matrix phase if particle fracture is not a dominant effect [128]. The forged microstructures presented in Figure 9-4, Figure 9-5 and Figure 9-7 consistently exhibited no evidence whatsoever of particle fracture due to hot forging strain. The indifference in 0.2% yield strength substantiated these observations. Accordingly, the phenomenon was hypothesized to occur during tensile testing during the plastic deformation regime. Optical micrographs in the homogenous deformation regions of tensile samples (Figure 9-15) confirm this. 5C exhibited extensive particle fracture normal to the tensile axis. Fractured particles were qualitatively observed to favor coarser particles, while the finest AlN were less-so. The finer ceramic phase of 5F did not exhibit the same wide-spread particle fracture. Observations of fracture were made, but the prevalence was reduced, and again only favored coarser particulate.

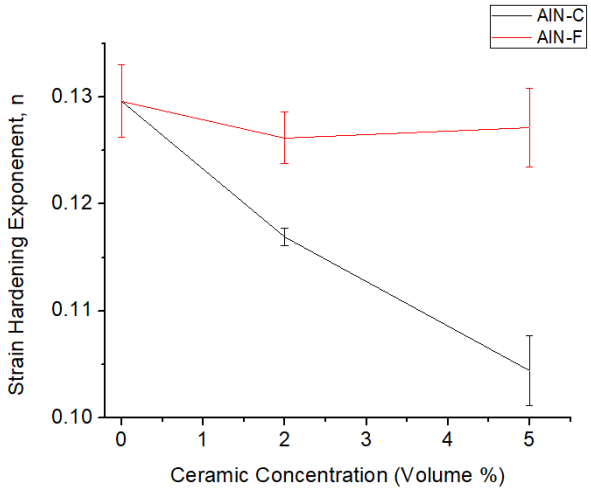

Figure 9-14 Strain hardening exponent of materials hot upset forged to 1.40 mm/mm at a rate of 0.1 s^{-1}.

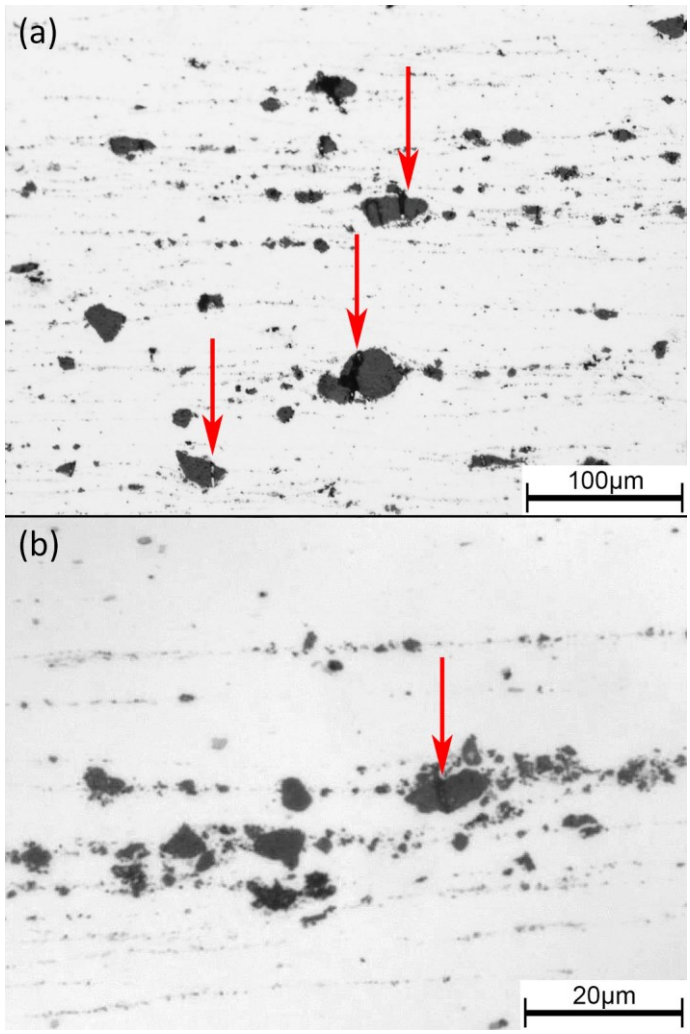

Figure 9-15 Examples of fractured AlN particles observed within the microstructures of (a) 5C and (b) 5F after tensile testing. The direction of tensile loading was horizontal while the forging axis was oriented vertically. Micrographs taken from the gauge sections of broken tensile specimens.

Fatigue characteristics were assessed in the final phase of research via three-point bending. The effects of hot upset forging strain, strain rate, ceramic type, and extent of anisotropy were considered for select MMCs to explore the breadth of fatigue behaviours. Table 9-2 summarizes the mean fatigue strength, $\sigma_{a,50}$, as well as the 10% and 90% confidence intervals deduced using a staircase approach. When forged in an

identical manner (1.40 mm/mm at a rate of 0.1 s^{-1}) and tested in the C-L orientation, both AlN-F (Data set 1) and AlN-C (Data set 2) exhibited comparable values for 50% survival stresses with that for 2F found to be only 11 MPa lower than the counterpart 2C sample. Counterintuitively, the superior UTS, ductility and *n* of the AlN-F material did not translate to superior fatigue performance in this context. However, the net effect of upset forging was a 42% increase in the survival stress for 2F over the unforged equivalent while 2C improved by 98 MPa (57%) [123]. Undoubtedly, densification from hot upset forging strain contributed largely to the improved fatigue response of these materials. The discrepancy in performance between the two AlN types is attributed to the subtle microstructural differences observed herein. In this sense, the bulk of residual porosity in forged MMCs containing AlN-C was located within the larger AlN particles themselves (Figure 9-5). While weakened by such features, these particles remained coherent and would thereby maintain appreciable load bearing capacity. On the contrary, residual porosity in the denser AlN-F forgings resided within loosely bound agglomerations of small, discrete AlN particulates (Figure 9-7(c-d)). Such clusters of ceramic would possess substantially less load bearing capacity, and as such, provide points for facilitated crack initiation and concomitantly, propagation. For the C-L orientation, the crack growth direction runs parallel to the forging axis, as shown in Figure 9-16(a) for 2F and Figure 9-16(b) for 2C. Through forging, prior particles were flattened in this direction and elongated normal to this axis. Fatigue fracture was transgranular with evidence of residual pores and AlN particulate along the crack path. Fractured AlN-C particles were observed, while evidence of fractured AlN-F was inconclusive.

Table 9-2 Fatigue strengths of select MMC forgings.

Material	Data Set	Strain Rate (s^{-1})	Strain (mm/mm)	Sample Orientation	Fatigue Strength (MPa)		
					$\sigma_{a,10}$	$\sigma_{a,50\%}$	$\sigma_{a,90\%}$
2F	1	0.1	1.40	C-L	268	258	247
	2	0.1	1.40	C-L	284	269	254
	3	1.0	1.40	C-L	281	268	256
2C	4	0.1	0.35	C-L	266	260	254
	5	0.1	0.35	C-R	269	264	258
	6	0.1	0.35	L-C	226	218	211

Higher forging strain rates were of interest for their relevance to both industrial productivity and process robustness reasons. The effect of strain rate on fatigue performance was explored by repeating the forging operation of test 2 at a rate one order of magnitude faster, 1 s^{-1} (test 3). The 10%, 50% and 90% survival stresses for the faster and slower rates were indifferent, with a 1 MPa to 3 MPa difference favoring the slower rate. Likewise, the crack paths for these materials were effectively indistinguishable; cracks progressed in a trans granular mode in a direction normal to the elongated axis of prior particles. Occasional fractured AlN particulate were observed along the crack path, but not observed in the adjacent material. Debonding of the ceramic phase was likewise not observed. Microstructurally, both forging parameter conditions fell within the dynamic recovery regime for this material, as observed in unpublished findings. Neither microstructures from data set 2 or 3 exhibited any recrystallization or significant

differences. Given dynamic recovery was the microstructural restoration mechanism, the faster strain rate used in data set 3 was anticipated to exhibit a finer subgrain structure. However, subsequent solution treatment during T6 processing proved effective at eliminating any subtle microstructural differences that may have manifested.

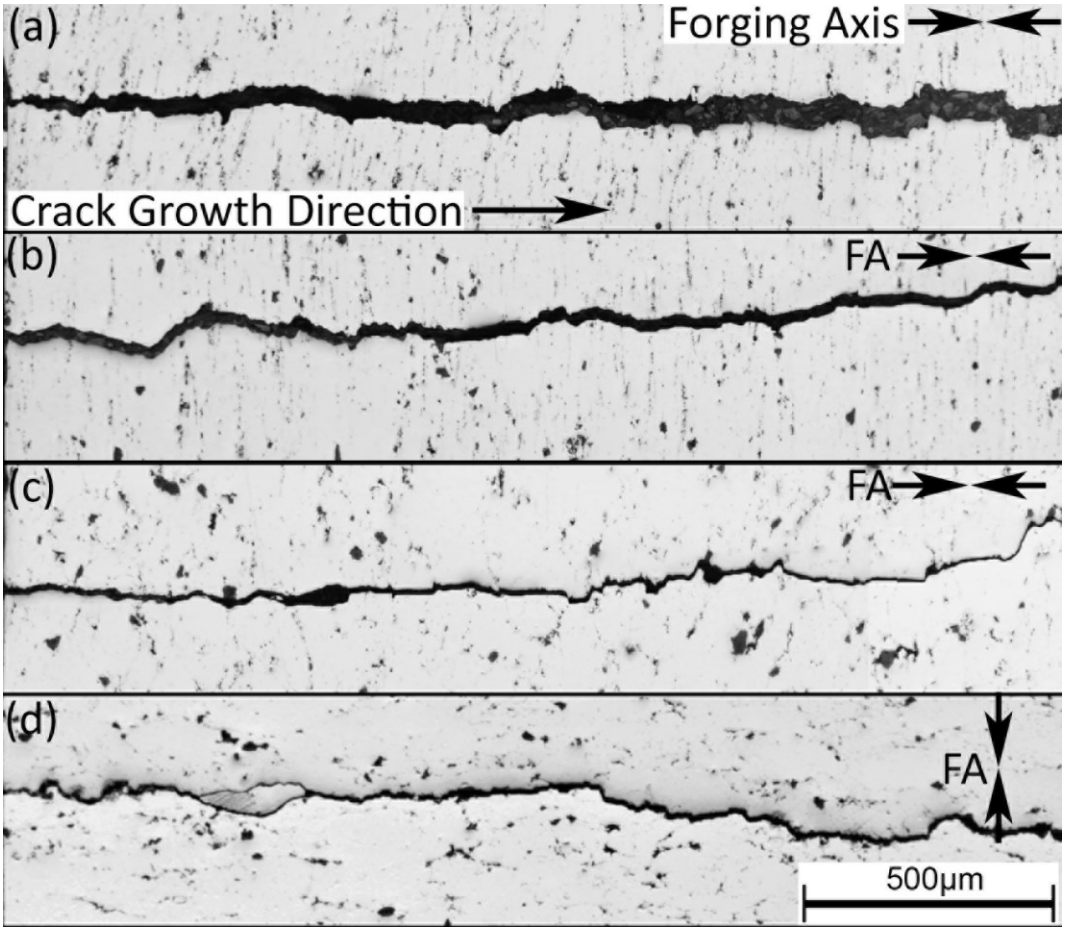

Figure 9-16 Optical micrographs revealing the fatigue crack paths within fractured fatigue bars of (a) 2F (data set 1) and (b) 2C (Data set 2) at a strain of 1.40 mm/mm in the C-L orientation, followed by 2C at a forging strain of 0,35 mm/mm in the (c) C-L (data set 4) and (d) L-C (data set 6) oritentations. Crack growth direction is from left to right. The forging axis (FA) is noted for reference.

Fatigue properties as a function of forging strain indicated an early onset of performance followed by effectively stable results. The 50% survival stress for 2C strained to 0.35 mm/mm and tested in the C-L orientation (data set 4) represented a substantial 88 MPa (52%) increase over the same material prior to hot forging. Further forging strain to 1.40 mm/mm produced specimen with a 50% survival stress 9 MPa higher but with considerable overlap in the confidence intervals. At a confidence level of 90%, the difference between the means at the two forging strains were not significant (p-value = 0.114). In general, fatigue strength trends positively with increases in static mechanical properties. Interestingly, fatigue behaviour in this study did not correlate positively with conditions that produced the highest ductility and UTS results (see Figure 9-9), as would be anticipated. Rather, this behaviour matched the densification behaviour in Figure 9-3. Hot deformation to a strain of 0.30 mm/mm represent the end of the first densification regime, whereby the bulk of porosity had been collapsed. Samples for data set 4 correspond to a density of at least 99.2%. Further forging strain accomplished densities up to 99.8% (data set 2), along with the invariably beneficial, aforementioned, disruption of the residual oxide phase [125]. From a process robustness point a view, these results emphasize that substantial and uniform improvements in fatigue behaviour can be established under a wide range of forging strains, as would be invariable in forging complex shapes. Fatigue cracks for test 2 shown in Figure 9-16(c) again show a transgranular fracture path with evidence of fractured AlN along the crack path.

Finally, three sample orientations were extracted from identically processed MMC 2C forgings to investigate whether this material exhibited anisotropic fatigue behaviour. All

samples were hot deformed to 0.35 mm/mm at a rate of 0.1 s^{-1}. The orientations C-L and C-R (Data sets 4 and 5) exhibited excellent 50% survival stress values, convincingly within their respective confidence intervals. The L-C orientation (Data set 6) was significantly lower. Still, the performance of the L-C orientation was 47 MPa (27%) over the same material prior to hot upset forging. The crack path observed for the L-C orientation shown in Figure 9-16(d) were expectedly unique within this study. Fatigue fracture exhibited evidence of both transgranular and intergranular fracture along with normal evidence of residual pores and AlN particulate along the crack path. In this unique orientation, the crack growth direction was normal to the forging axis and cracks progressed parallel to the elongated grains and prior boundaries. TEM observations in Figure 9-8 as well as more thorough investigations in [125] exhibit heterogeneously enriched and brittle $Mg_2(Sn,Si)$ and MgO phases along these boundaries. Despite this preferential crack path, results were substantially improved over the unforged counterpart.

9.6 Conclusions

APM metal-matrix composite compacts were successfully forged up to true compressive strain values of 1.55 mm/mm. Samples were processed in the as-sintered condition with the sintered surface intact to maximize industrial relevance. Two different size AlN ceramic powders were admixed up to 5% by volume. Tensile and fatigue specimen extracted from cylinders forged from 0 to 1.55 mm/mm afforded the ability to quantify

the effects of hot deformation on these commercial APM materials. Some notable conclusions are as follows:

- Significant improvements in density were obtained via forging. 2C was over 99.0% dense at a strain of 0.30 mm/mm, and all materials were at least 99.5% dense at a strain of 1.40 mm/mm.
- The Al-AlN interface was lined with heterogeneous precipitates, residual oxides and Sn. The interfacial bond strength achieved herein was enough to avoid any decohesion during hot deformation or during mechanical testing.
- AlN additions invariably and significantly improved the elastic modulus, up to 74.0 GPa at 2 vol% and 77.0% at 5 vol%. These values represent increases of 0.8 to 9.2 GPa over the sintered-T6 material counterparts.
- Tensile ductility was dramatically improved through hot upset forging. At a strain of 1.40 mm/mm, the difference versus a sintered T6 counterpart ranged from a three- fold change for the Base material to a five-fold change for MMCs containing 5 vol% AlN.
- Forging strains as low as 0.35 mm/mm were enough to invoke significant gains in bending fatigue performance. The largest improvement was 92 MPa (54%) over a sintered-T6 condition.

9.7 ACKNOWLEDGEMENTS

The authors would like to acknowledge the Natural Sciences and Engineering Research Council of Canada (NSERC) for financial support via the Collaborative Research & Development grant CRDPJ 486528 - 15. Dr. Bernhard Mais (Kymera International) and Mr. Jessu Joys (Ampal Inc.) are acknowledged for the provision of the powdered metals employed. Laboratory assistance provided by colleagues at Dalhousie University (Randy Cooke, Dean Grijm) and CanmetMATERIALS (Jonathan McKinley, Lucian Blaga) is gratefully appreciated as well.

CHAPTER 10. FINAL CONCLUSIONS AND FUTURE WORK

Preliminary investigations using spark plasma sintering (SPS) on an aluminum powder coupled with ceramic particulate were effective in enlightening the authors to the mechanical benefits of rigid secondary phases on the mechanical properties. Ceramic additions up to 10 vol% of AlN and SiC powders proved effective at enhancing the hardness and bend strength over a nonreinforced specimen. A D_{50} = 97.3 μm air atomized aluminum powder was blended with nominally fine (D_{50} = 3.7 μm and D_{50} = 3.0 μm, respectively) and nominally coarse (D_{50} = 21.3 μm and D_{50} = 11.8 μm, respectively) SiC and AlN powders. Additions of finer ceramic particulate were attractive to establish a homogenous distribution. However, due to the size ratio of aluminum and ceramic particulate, finer particulate tended to cluster between prior particles and introduce residual porosity. AlN was chosen as the sole ceramic phase over SiC due to its promising properties over the well-established SiC type. Specifically, AlN is nonreactive with aluminum, exhibits a strong interfacial bonding with aluminum, exhibits a high hardness, low coefficient of thermal expansion and high thermal conductivity.

AlN was successfully incorporated into a commercial press and sinter aluminum alloy. The nominal target chemistry of the matrix phase was 3% Cu, 1.5% Mg and 0.5% Sn in wt% and were blended from elemental and master alloys. 0 to 10 vol% of either ‘coarse’ or ‘fine’ AlN particulate were admixed (AlN-C and AlN-F, respectively). Compaction was performed exclusively at Dalhousie University and sintering was carried out using by GKN Sinter Metals (Conover, NC) in mesh belt furnaces designed for the industrial processing of powder metal aluminum parts.

Lean additions of AlN were found to be suitable in processing parts to a high sinter quality. Invariably, excessive additions proved to diminish the sintered density. AlN-C was added up to 5 vol% and AlN-F up to 2vol% without significant effects to the sinterability. Finer ceramic particulate tended to cluster and entrain pores between adjacent metallic powder particles. Coarser particles incorporated well with the matrix and generally were pore free. AlN particles were determined to be load bearing constituents of the microstructure. Dynamic elastic modulus measurements improved from 71.9 GPa with no AlN up to a peak of 74.3 GPa in the material 5C. However, other significant changes in mechanical properties were muted due to the invariable decreases in sintered density through AlN additions. 0.2% yield strength measurements for materials Base, 2C and 2F were effectively identical. Similarly, the fatigue strength (50% survival stress) for these materials was found to be indifferent. While significant gains were not observed, the success in matching the performance of the Base system using AlN additions was a promising finding. 2C exhibited a density of 99.2%, 0.3% lower than Base. 2F was an additional 0.1% lower. Given the ceramic-bearing materials exhibited comparable mechanical properties at a lower sintered density, the authors anticipated significant benefits through the elimination of residual porosity through hot forging.

Hot forging experiments were performed on APM materials containing varied amounts of AlN additions. Preliminary assessment of the forgeability were conducted using a Gleeble 3500 Thermal-mechanical system set up for compression tests. 15 mm tall by 10 mm cylinders were machined from press-and-sinter samples and tested in their as-

sintered (T1) condition. Forgings were conducted isothermally from 350°C to 500°C and true strain rates of 0.005 s^{-1} to 5 s^{-1}. All samples were deformed to a strain of 0.70 mm/mm, the maximum obtainable from the equipment. All specimen and conditions exhibited success in deformation. The sole exception was evidence of adiabatic heating induced hot cracking issues at 500°C coupled with strain rates greater than 0.5 s^{-1}. Preliminary testing using the Gleeble proved essential in enlightening the dynamic flow behaviour of material. One particularly valuable technique employed was constituent modelling using the Zener-Hollomon approach. Herein, the peak flow stress during deformation was modelled as a function of temperature, strain rate and composition.

Zener-Hollomon modelling concluded that the materials Base, 2C, 5C and 2F exhibited effectively identical flow behaviour. The matrix material was responsible for the entire flow behaviour and ceramic additions did not negatively influence this. 5F did however exhibit a deviate from the aforementioned materials. This composition was wholly softer due to the significantly higher residual porosity of the forging preform. Despite this, every material exhibited substantial increases in density through hot forging. Densification was incurred through forging strain and was effectively independent of strain rate and temperature. Compositions that were sintered to near-theoretical density (>99.0 %), including Base, 2C and 2F alloys, were forged to essentially full density (>99.9 %). Hot forging proved especially useful in promoting high densities of samples that were compromised due to the high concentration of ceramic. 5F sintered to only 95.2%, whereas the mean density of deformed specimen was 98.5%.

Microstructurally, all specimen exhibited behaviours consistent with static (SPN) and dynamic precipitation (DPN). The as-sintered microstructure of preforms included solidified remnants of the liquid phase and α-Al grains that contain phases from the entire precipitation sequence; including incoherent equilibrium precipitates and even a solid solution component. Inflated peak flow stresses under high Z-value deformation conditions (low temperature, high strain rate) were associated with the in-situ age hardening of solid solution microstructure constituents. Increasing isothermal holds at 450°C holds before deformation from 15 s to 150 s proved effective in overaging these features and decreasing flow stresses.

Superimposed Isoefficiency and flow instability contour plots were constructed for the compositions Base, 2C and 2F to quantify the microstructural events and their efficiency during hot deformation. Several domains of temperature and strain rate were noted in this analysis, the most significant of which was for temperatures 400°C to 500°C covering all strain rates. Peak power dissipation efficiency was comparable for all materials, ranging from 38% to 41% at intermediate strain rates. The extreme of strain rates used in this study proved to be less efficient, especially for the Base system. This manifested as instantaneous flow stresses at 0.65 mm/mm forging strain being approximately 10 MPa greater than either ceramic-bearing material. Electron Backscatter Diffraction was used to conclude that dynamic recovery was the active microstructural mechanism that occurred in this and other domains. The inherent chemical makeup of the studied materials coupled with the scope of forging parameters were not conducive to inciting dynamic recrystallization. A domain of flow instability was identified for all materials deformed

near 350°C and 5 s^{-1}. In literature, this domain was found to be associated with the fracture of ceramic particulate or decohesion from the matrix [101]. Uniquely, no microstructures deformed under these conditions or any other in this dissertation were found to exhibit any of these defects. Rather, the authors attributed this region of flow instability to the strong effects of DPN that occurred.

Gleeble tests were limited in the size of specimen which could be produced, and accordingly, insufficient to extract standard sized mechanical property specimen. The author developed a procedure to emulate the Gleeble process to extract such specimen. 44 mm tall by 50 mm cylinders were pressed and sintered in the same manner as the lab-scale specimen produced thus far. Forgings were conducted at CanmetMATERIALS metal forming lab (Hamilton, ON) using a 1100kN hydraulic load frame capable of up to 5000 mm/min. This setup could deform the 50 mm cylinders at a true strain rate better than 1 s^{-1} and to a maximum strain of 1.55 mm/mm. An open-loop, sinusoidal position versus time regression was fed to the control software to maintain a constant true strain rate throughout deformation. The frame was equipped with heated forging platens capable of maintaining 450°C as well as instrumentation to record load and position data. The upscaled forging setup proved to provide flow data in good agreement with Gleeble data. Standard sized fatigue, tensile and impulse excitation specimen were extractable from any samples deformed to a true strain of 1.85 mm/mm.

A microstructural assessment was performed on select materials to investigate the microstructural evolution during hot forging and correlate it to mechanical properties.

Transmission Electron Microscopy (TEM) was employed to observe the nature of precipitates and impurities. T6-treated specimen in the sintered condition and sinter-forged condition were indifferent in their precipitates. Both were dominated by precipitated produced through accepted S phase (Al_2CuMg) sequences. Oxygen-rich regions were evident throughout all microstructures as a semi-continuous network. Oxide phases are unique and inherent to aluminum powder metallurgy products and represent the oxidized prior surface of aluminum particles. Al_2O_3 was invariably reduced during sintering to produce MgO, which formed continuous but discrete crystallites in a metallic matrix along prior particle boundaries. Forged specimens exhibited disrupted oxide networks along boundaries. The continuous string of crystallites was dispersed into a semi-continuous nature that fostered regions of purely metallic bonding between prior particles. The interface between Al and AlN particles was observed to be lined with residual oxide phases, heterogeneous S phase precipitates and Sn. The Al-AlN interface was highly effective in avoiding any decohesion in during hot deformation or mechanical testing.

Mechanical properties benefitted substantially from forging operations. Changes in tensile ductility were the most dramatic, as summarized in Figure 10-1 for materials containing up to 5 vol% AlN. Sintered-T6 specimen generally ranged in ductility from 1 % to 5 % and favored compositions with no ceramic. 2 vol% of either AlN ceramic additions effectively halved the ductility. Further ceramic additions only marginally reduced ductility from these values. Ceramic additions entrained porosity that persisted in the final product, while simultaneously providing a favorable crack path along prior

particle boundaries. Hot deformation eliminated the bulk of residual porosity and disrupted the continuous and brittle MgO/Mg_2Sn crystallite structure between adjacent prior particles. This effect was enhanced with increasing forging strain. Enhanced metallic bonding between prior particles was attributed to the bulk of tensile ductility improvement.

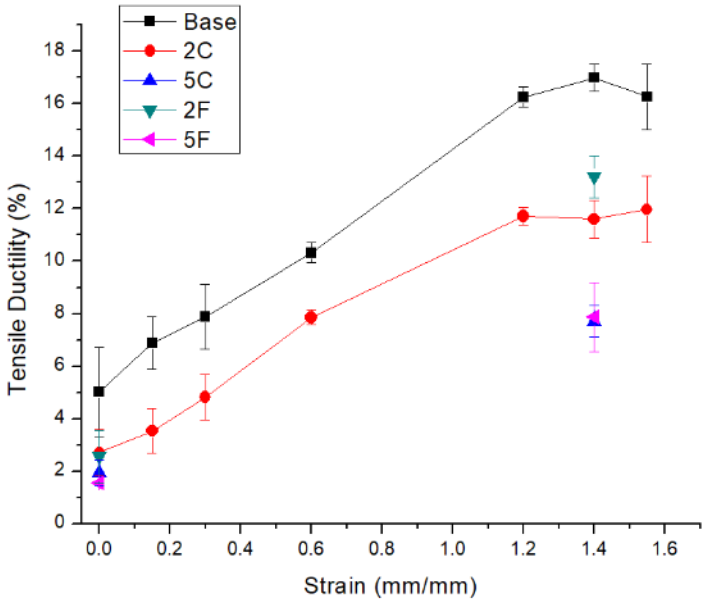

Figure 10-1 Effect of forging strain on the T6 tensile ductility of 50 mm cylinders deformed at 450°C and 0.1 s^{-1} with and without ceramic additions.

0.2% yield strength and ultimate tensile strength (UTS) values for hot forged specimen likewise improved over their sintered counterparts. The magnitude of change in 0.2% yield strength was influenced by the densification incurred through deformation. relatively dense materials (>99.0%) Base, 2C and 2F exhibited gains from 21 to 34 MPa, 5F meanwhile increased by 79 MPa while densified from 95.3% to 99.7%. The disruption

of residual oxides through hot deformation did not explain yield strength improvements. On the other hand, UTS dramatically improved through ductility improvements achieved through this oxide disruption. 51 MPa to 130 MPa increases were observed, again favoring ceramic-bearing systems. The UTS of Sinter-T6 specimen were particularity sensitive to ceramic additions due to their inferior tensile ductility. Forged specimens were considerably less sensitive to ceramic additions. 5F was only 12 MPa weaker than Base when hot deformed to 1.40 mm/mm, while the sintered counterparts exhibited a 91 MPa delta. AlN-F ceramic additions routinely exhibited greater UTS values than AlN-C ones. Coarser AlN tended to fracture during room temperature plastic deformation, lowering the strain hardening behaviour of specimen.

Fatigue testing rounded-out the mechanical properties assessed in this dissertation. Rectangular machined TRS bars were extracted from both sintered and forged specimen and subject to cyclic loading in a three-point bend fixture. A staircase statistical approach was employed to determine the 10%, 50% and 90% survival stresses for each material at a runout criterion of 10^6 cycles. The compact geometries of fatigue specimen allowed for several orientations to be extracted from forged specimen to investigate anisotropic effects. Otherwise, the authors refined the variables to forging strain, strain rate and composition. The breadth of fatigue tests in this study are summarized in Table 10-1. Base, 2C and 2F were not significantly different from each other in the sintered condition or when forged to 1.40 mm/mm at 450°C and 0.1 s^{-1}. Fatigue performance was effectively independent of elastic modulus, UTS and ductility differences associated with AlN additions. Forged did however outperform sintered specimen by up to 57%, the bulk

of which develops at a strain of only 0.35 mm/mm. this strain corresponds with the end of the first observed stage of densification whereby the bulk of porosity was eliminated. Statistically, there was no benefit to increasing forging strain to 1.40 mm/mm. Hot deformed specimen exhibited mild anisotropic effects. Grains in deformed specimen were flattened and elongated orthogonal to the forging axis. Testing specimen in the C-L or C-R orientations (forging axis orthogonal to cyclic tensile stresses) produced peak fatigue strengths, while the L-C orientation (forging axis and cyclic tensile stresses parallel) was 42 MPa short of peak performance. Micrographs of fatigue crack paths indicated crack typically followed a transgranular path, except for the L-C orientations. Here the crack path was a mixture of intergranular and transgranular, followed elongated and oxide enriched prior particle boundaries.

Table 10-1 Summary of fatigue performance for T6 specimen in the sintered and various forged conditions.

Material	Temp (°C)	Strain Rate (s^{-1})	Strain (mm/mm)	Sample Orientation	Fatigue Strength (MPa)			$\sigma_{a,50}$ change over Sintered MPa, (%)
					$\sigma_{a,10}$	$\sigma_{a,50}$	$\sigma_{a,90}$	
Base	----------Sintered----------				248	204	161	-
2C	----------Sintered----------				179	172	164	-
2F	----------Sintered----------				189	182	174	-
Base	450	0.1	1.40	C-L	282	266	250	+62 (30%)
2C	450	0.1	0.35	L-C	226	218	211	+47 (27%)
2C	450	0.1	0.35	C-R	266	260	254	+88 (52%)
2C	450	0.1	0.35	C-L	269	264	258	+92 (54%)
2C	450	0.1	1.40	C-L	284	269	254	+98 (57%)
2C	450	1.0	1.40	C-L	281	268	256	+97 (57%)
2F	450	0.1	1.40	C-L	268	258	247	+76 (42%)

10.1 Suggested Future Work

Throughout the evolution of this project the author attempted to address as many questions as possible regarding the forgeability of APM components. However, the inherent breadth of variables available to a researcher in powder metallurgy exceeded a reasonable scope for a dissertation. Accordingly, many questions arose through discovery of the capabilities and limitations of the research topic. The following test discusses several areas of suggested future work with the aim of expanding the understanding of the forgeability of APM materials as well as enhancing the mechanical properties of the pertinent material system.

One key property not discovered through this research was the strain at fracture for a given set of forging conditions. This value is inherently challenging to obtain in hot compression testing due to exponentially increasing load requirements as well as frictional effects. Tensile testing is likewise complicated through flow instabilities. Hot torsion testing is free of such limitations and are commonplace for modelling the flow behaviour of material until fracture. Obtaining these data could provide valuable information for optimizing the range of forging temperatures while avoiding hot cracking issues.

Homogeneity of the ceramic phase in an aluminum matrix was a recurring topic in this study. The distribution of ceramic particulate in sintered APM components was determined by solid state mixing of constituent powders. As such, obtaining a

microstructure whereby AlN was distributed within aluminum prior particles was unobtainable. Furthermore, 2 - 5 vol% of AlN powder was sufficient to saturate prior particle boundaries and introduce considerable porosity. The author suggests investigating the following approaches to improve the homogeneity of the sintered compacts. First, solid state mechanical alloying of the ceramic phase with the aluminum constituent powder. This approach would ensure enhanced homogeneity while potentially avoiding the inter-powder friction and porosity penalties associate with conventionally blended AlN. Mechanical alloying is understandably undesirable for low cost, high volume products. The author suggests investigating different Al:AlN particle size ratios as an alternative. The ratio of mean particle size for Al:AlN-C was 7:1, while the finer AlN-F powder was greater. Decreasing the Al particle size would help mitigate the occurrence of large-ceramic free particulate throughout the microstructure. Additionally, the increased interparticle boundary would likely tolerate greater bulk concentrations of ceramic before clustering occurred. Obviously, this would be performed at the expense of an increase in oxygen content and interparticle friction due to the increase surface area of the Al powder.

Questions pertaining to the metallic consistently routinely arose throughout this project. The author persisted throughout with a single chemistry despite perceived limitations. This is not meant to be an overhaul of the matrix system, but rather as minor changes to optimize the material. First, the author noted the occurrence of heterogeneously precipitates S phase occurring on dislocation loops/helices in Figure 8-9. Given their large and incoherent nature, contributions to the strength would be negligible, likely

diminishing them through Cu and Mg harvesting. Literature has shown that microalloying with Si additions of 0.1 to 0.5% remedy this [111]. The prevalence of these heterogeneously precipitated phase decreases while enhancing precipitation hardening through Si-modified GPB zones. The second proposed chemical alteration is the minimization of elemental Sn additions. Sn additions are essential promoting high sinter quality of APM materials. However, Sn precipitates from the liquid phase as Mg_2Sn following sintering. TEM observations showed Mg_2Sn between prior particles as either fine crystallite or relatively coarse (10's of μm) isolated phases. These particles are inherently brittle and were occasionally observed to fracture following hot deformation. Hence, their occurrence within the microstructure is most likely negative. The author suggests that a modest compromise in the sinter quality of the alloy through reduced Sn would be offset through forging operations. Elimination of Mg_2Sn would potentially improve the dynamic mechanical properties. A bonus of this change would be a reduction in Mg harvesting through Mg_2Sn formation, increasing precipitate concentration.

REFERENCES

1. German, R. M. *Powder Metallurgy & Particulate Materials Processing*; MPIF: Princeton, 2005; ISBN 0976205718.

2. Gale, W. F.; Totemeier, T. C. *Smithells Metals Reference Book*; 8th ed.; Elsevier, 2004;

3. Cooke, R. W.; Bishop, D. P.; Hexemer, R. L.; Donaldson, I. W. Effects of zirconium additions on the sintering response of an aluminum—copper—Magnesium alloy. *Int. J. powder Metall. 49*, 37–46.

4. Schaffer, G. B.; Sercombe, T. B.; Lumley, R. N. Liquid phase sintering of aluminium alloys. *Mater. Chem. Phys.* **2001**, *67*, 85–91, doi:Doi 10.1016/S0254-0584(00)00424-7.

5. Smith, W. F. *Structure and Properties of Engineering Alloys*; 2nd ed.; McGraw-Hill, 1993; ISBN 0-07-59172-5.

6. Bishop, D. P.; Caley, W. F.; Kipouros, G. J.; Hexemer, R. L.; Donaldson, I. W. Powder metallurgy processing of 2xxx and 7xxx series aluminium alloys. *Can. Metall. Q.* **2011**, *50*, 246–252, doi:Doi 10.1179/1879139511y.0000000003.

7. Cooke, R. W.; Hexemer, R. L.; Donaldson, I. W.; Bishop, D. P. PM processing of an Al-Cu-Mg alloy with a low Cu:Mg ratio. *Powder Metall.* **2012**, *55*, 29–35.

8. German, R. M.; Suri, P.; Park, S. J. Review: liquid phase sintering. *J. Mater. Sci.* **2008**, *44*, 1–39, doi:10.1007/s10853-008-3008-0.

9. MacAskill, I. A.; Hexemer, R. L.; Donaldson, I. W.; Bishop, D. P. Effects of magnesium, tin and nitrogen on the sintering response of aluminum powder. *J. Mater. Process. Technol.* **2010**, *210*, 2252–2260, doi:DOI 10.1016/j.jmatprotec.2010.08.018.

10. Kent, D.; Drennan, J.; Schaffer, G. B. A morphological study of nitride formed on Al at low temperature in the presence of Mg. *Acta Mater.* **2011**, *59*, 2469–2480, doi:DOI 10.1016/j.actamat.2010.12.050.

11. Schaffer, G. B.; Yao, J.-Y.; Bonner, S. J.; Crossin, E.; Pas, S. J.; Hill, A. J. The effect of tin and nitrogen on liquid phase sintering of Al–Cu–Mg–Si alloys. *Acta Mater.* **2008**, *56*, 2615–2624, doi:10.1016/j.actamat.2008.01.047.

12. Xie, G.; Ohashi, O.; Yamaguchi, N.; Song, M.; Mitsuishi, K.; Furuya, K.; Noda, T. Behavior of oxide film at interface between particles of Al-Mg alloy powder compacts prepared by pulsed electric-current sintering. *Japan J. Appl. Phys.* **2003**, *42*, 4725–4728.

13. McQueen, H. J.; Spigerelli, S.; Kassner, M. E.; Evangelista, E. Chapter 14. Extrusion. In *Hot Deformation and Processing of Aluminum Alloys*; CRC Press, 2011.

14. Altan, T.; Ngaile, G.; Shen, G. *Cold and Hot Forging: Fundamentals and Applications, Volume 1*; ASM International: Materials Park, OH, 2005; ISBN 0871708051.

15. Zener, C.; Hollomon, J. H. Effect of Strain Rate Upon Plastic Flow of Steel. *J. Appl. Phys.* **1944**, *15*, 22, doi:10.1063/1.1707363.

16. Humphreys, F. J.; Hatherly, M. *Recrystallization and Related Annealing Phenomena*; Elsevier, 2004; ISBN 9780080441641.

17. McQueen, H. J.; Spigerelli, S.; Kassner, M. E.; Evangelista, E. Front Matter. In *Hot Deformation and Processing of Aluminum Alloys*; CRC Press: Boca Raton, 2011; p. 59.

18. McQueen, H. J.; Spigerelli, S.; Kassner, M. E.; Evangelista, E. Chapter 4. Hot Working of Aluminum. In *Hot Deformation and Processing of Aluminum Alloys*; CRC Press, 2011; pp. 36–42.

19. Mann, R. E. D.; Hexemer, R. L.; Donaldson, I. W.; Bishop, D. P. Hot deformation of an Al–Cu–Mg powder metallurgy alloy. *Mater. Sci. Eng. A* **2011**, *528*, 5476–5483, doi:10.1016/j.msea.2011.03.081.

20. Mosher, W. G. E.; Kipouros, G. J.; Caley, W. F.; Donaldson, I. W.; Bishop, D. P. On hot deformation of aluminium–silicon powder metallurgy alloys. *Powder Metall.* **2011**, *54*, 366–375, doi:10.1179/003258910X12678035166773.

21. McQueen, H. J.; Spigerelli, S.; Kassner, M. E.; Evangelista, E. Chapter 7. Aluminum Matrix Composites. In *Hot Deformation and Processing of Aluminum Alloys*; CRC Press, 2011.

22. Cepeda-Jiménez, C. M.; Ruano, O. A.; Carsí, M.; Carreño, F. Study of hot deformation of an Al–Cu–Mg alloy using processing maps and microstructural characterization. *Mater. Sci. Eng. A* **2012**, *552*, 530–539, doi:10.1016/j.msea.2012.05.082.

23. Ravichandran, N.; Prasad, Y. V. R. K. Dynamic recrystallization during hot deformation of aluminum: A study using processing maps. *Metall. Trans. A* **1991**, *22*, 2339–2348, doi:10.1007/BF02665000.

24. Prasad, Y. V. R. K. Processing Maps: A Status Report. *J. Mater. Eng. Perform.* **2013**, *22*, 2867–2874, doi:10.1007/s11665-013-0732-7.

25. Li, H. Z.; Wang, H. J.; Liang, X. P.; Liu, H. T.; Liu, Y.; Zhang, X. M. Hot deformation and processing map of 2519A aluminum alloy. *Mater. Sci. Eng. A* **2011**, *528*, 1548–1552, doi:10.1016/j.msea.2010.10.080.

26. Prasad, Y. V. R. K.; Sasidhara, S. *Hot Working Guide: A Compendium of Processing Maps*; 1st ed.; ASM International, 1997; ISBN 1615032029.

27. McQueen, H. J.; Spigerelli, S.; Kassner, M. E.; Evangelista, E. Chapter 5. Hot Working of Dispersoid and Solute Alloys. In *Hot Deformation and Processing of Aluminum Alloys*; CRC Press, 2011; pp. 143–190 ISBN 978-1-57444-678-4.

28. McQueen, H. J.; Spigerelli, S.; Kassner, M. E.; Evangelista, E. Chapter 6. Precipitation Hardening Alloys. In *Hot Deformation and Processing of Aluminum Alloys*; CRC Press, 2011.

29. James, W. B. Powder Forging. *Rev. Part. Mater.* **1994**, *2*, 173–214.

30. Bose, A.; Eisen, W. B. *Hot consolidation of powders & particulates*; Metal Powder Industries Federation, 2003; ISBN 1878954490.

31. Committee, A. I. H. *ASM Handbook, Volume 07 - Powder Metal Technologies and Applications*; ASM International, 1998; ISBN 978-0-87170-387-3.

32. Qiu, J. W.; Liu, Y.; Liu, Y. B.; Liu, B.; Wang, B.; Ryba, E.; Tang, H. P. Microstructures and mechanical properties of titanium alloy connecting rod made by powder forging process. *Mater. Des.* **2012**, *33*, 213–219, doi:10.1016/j.matdes.2011.07.034.

33. Dashwood, R. .; Schaffer, G. . Powder forging of a sintered Al–3.8Cu–1Mg–0.8Si–0.1Sn alloy. *Mater. Sci. Eng. A* **2002**, *323*, 206–212, doi:10.1016/S0921-5093(01)01354-5.

34. El-Domiaty, A.; Shaker, M. A note on the workability of porous-steel preforms. *J. Mater. Process. Technol.* **1991**, *25*, 229–233, doi:10.1016/0924-0136(91)90091-R.

35. Abdel-Rahman, M.; El-Sheikh, M. N. Workability in forging of powder metallurgy compacts. *J. Mater. Process. Technol.* **1995**, *54*, 97–102, doi:10.1016/0924-0136(95)01926-X.

36. Xie, G.; Ohashi, O.; Song, M.; Mitsuishi, K.; Yasuda, H.; Furuya, K.; Noda, T. Electron microscopic observation of interfaces of aluminium powder compacts prepared by spark plasma sintering. *J. Electron Microsc. (Tokyo).* **2002**, *51*, S149–S153, doi:DOI 10.1093/jmicro/51.Supplement.S149.

37. Chawla, N.; Williams, J. .; Saha, R. Mechanical behavior and microstructure characterization of sinter-forged SiC particle reinforced aluminum matrix composites. *J. Light Met.* **2002**, *2*, 215–227, doi:10.1016/S1471-5317(03)00005-1.

38. Zhang, J.-T.; Liu, L.-S.; Zhai, P.-C.; Fu, Z.-Y.; Zhang, Q.-J. Effect of fabrication process on the microstructure and dynamic compressive properties of SiCp/Al composites fabricated by spark plasma sintering. *Mater. Lett.* **2008**, *62*, 443–446, doi:10.1016/j.matlet.2007.04.118.

39. Chu, K.; Jia, C.; Tian, W.; Liang, X.; Chen, H.; Guo, H. Thermal conductivity of spark plasma sintering consolidated SiCp/Al composites containing pores: Numerical study and experimental validation. *Compos. Part A Appl. Sci. Manuf.* **2010**, *41*, 161–167, doi:10.1016/j.compositesa.2009.10.001.

40. Yang, M.; Zhang, D.; Gu, X.; Zhang, L. Fabrication and properties of SiCp/Al composites by pulsed electric current sintering. *J. Mater. Sci.* **2005**, *40*, 5029–5031, doi:DOI 10.1007/s10853-005-1814-1.

41. Mizuuchi, K.; Inoue, K.; Agari, Y.; Nagaoka, T.; Sugioka, M.; Tanaka, M.; Takeuchi, T.; Tani, J.; Kawahara, M.; Makino, Y.; Ito, M. Processing of Al/SiC composites in continuous solid–liquid co-existent state by SPS and their thermal properties. *Compos. Part B Eng.* **2012**, *43*, 2012–2019, doi:10.1016/j.compositesb.2012.02.004.

42. Parvin, N.; Assadifard, R.; Safarzadeh, P.; Sheibani, S.; Marashi, P. Preparation and mechanical properties of SiC-reinforced Al6061 composite by mechanical alloying. *Mater. Sci. Eng. A* **2008**, *492*, 134–140, doi:10.1016/j.msea.2008.05.004.

43. Grácio, J. J.; Picu, C. R.; Vincze, G.; Mathew, N.; Schubert, T.; Lopes, A.; Buchheim, C. Mechanical Behavior of Al-SiC Nanocomposites Produced by Ball Milling and Spark Plasma Sintering. *Metall. Mater. Trans. A* **2013**, *44*, 5259–5269, doi:10.1007/s11661-013-1874-9.

44. Yang, M.; Zhang, D.; Gu, X.; Zhang, L. Effects of SiC particle size on CTEs of SiCp/Al composites by pulsed electric current sintering. *Mater. Chem. Phys.* **2006**, *99*, 170–173, doi:10.1016/j.matchemphys.2005.10.019.

45. Saberi, Y.; Zebarjad, S. M.; Akbari, G. H. On the role of nano-size SiC on lattice strain and grain size of Al/SiC nanocomposite. *J. Alloys Compd.* **2009**, *484*, 637–640, doi:10.1016/j.jallcom.2009.05.009.

46. Zhang, J.; Shi, H.; Cai, M.; Liu, L.; Zhai, P. The dynamic properties of SiCp/Al composites fabricated by spark plasma sintering with powders prepared by mechanical alloying process. *Mater. Sci. Eng. A* **2009**, *527*, 218–224, doi:10.1016/j.msea.2009.08.067.

47. Tan, M.; Xin, Q.; Li, Z.; Zong, B. Y. Influence of SiC and Al 2 O 3 particulate reinforcements and heat treatments on mechanical properties and damage evolution of Al-2618 metal matrix composites. **2001**, *6*, 2045–2053.

48. Song, M. Effects of volume fraction of SiC particles on mechanical properties of SiC/Al composites. *Trans. Nonferrous Met. Soc. China* **2009**, *19*, 1400–1404, doi:10.1016/S1003-6326(09)60040-6.

49. Narayanasamy, R.; Ramesh, T.; Prabhakar, M. Effect of particle size of SiC in aluminium matrix on workability and strain hardening behaviour of P/M composite. *Mater. Sci. Eng. A* **2009**, *504*, 13–23, doi:10.1016/j.msea.2008.11.037.

50. Qu, X.; Zhang, L.; Wu, M.; Ren, S. Review of metal matrix composites with high thermal conductivity for thermal management applications. *Prog. Nat. Sci. Mater. Int.* **2011**, *21*, 189–197, doi:10.1016/S1002-0071(12)60029-X.

51. Lee, H. S.; Yeo, J. S.; Hong, S. H.; Yoon, D. J.; Na, K. H. The fabrication process and mechanical properties of SiCp/Al–Si metal matrix composites for automobile air-conditioner compressor pistons. *J. Mater. Process. Technol.* **2001**, *113*, 202–208, doi:10.1016/s0924-0136(01)00680-x.

52. de Araujo, E. R.; de Souza, M. M. S.; Filho, F. A.; Gonzalez, C. H.; de Araújo Filho, O. O. Preparation of Metal Matrix Aluminum Alloys Composites Reinforced by Silicon Nitride and Aluminum Nitride through Powder Metallurgy Techniques. *Mater. Sci. Forum* **2012**, *727–728*, 259–262, doi:10.4028/www.scientific.net/MSF.727-728.259.

53. Wang, J.; Yi, D.; Su, X.; Yin, F.; Li, H. Properties of submicron AlN particulate reinforced aluminum matrix composite. *Mater. Des.* **2009**, *30*, 78–81, doi:10.1016/j.matdes.2008.04.039.

54. Abdoli, H.; Saebnouri, E.; Sadrnezhaad, S. K.; Ghanbari, M.; Shahrabi, T. Processing and surface properties of Al–AlN composites produced from nanostructured milled powders. *J. Alloys Compd.* **2010**, *490*, 624–630, doi:10.1016/j.jallcom.2009.10.121.

55. Dun, B.; Jia, X. A.; Jia, C. C.; Chu, K. Thermal conductivity behavior of SPS consolidated AlN/Al composites for thermal management applications. *Rare Met.* **2011**, *30*, 189–194, doi:DOI 10.1007/s12598-011-0222-8.

56. Suganuma, K. Whisker/matrix interface microstructure in 6061 aluminum composite reinforced with α-silicon nitride whisker. *Compos. Interfaces* **1994**, *2*, 15–27, doi:10.1163/156855494X00030.

57. Benko, E.; Morgiel, J.; Czeppe, T. BN sintered with Al: Microstructure and hardness. *Ceram. Int.* **1997**, *23*, 89–91, doi:10.1016/0272-8842(95)00137-9.

58. Du, Y.; Li, S.; Zhang, K.; Lu, K. BN/Al composite formation by high-energy ball milling. *Scr. Mater.* **1997**, *36*, 7–14, doi:10.1016/S1359-6462(96)00335-1.

59. Tang, F.; Anderson, I. .; Biner, S. . Solid state sintering and consolidation of Al powders and Al matrix composites. *J. Light Met.* **2002**, *2*, 201–214, doi:10.1016/S1471-5317(03)00004-X.

60. El Kabir, T.; Joulain, A.; Gauthier-Brunet, V.; Dubois, S.; Bonneville, J.; Bertheau, D. Hot isostatic pressing synthesis and mechanical properties of Al/Al–Cu–Fe composite materials. *J. Mater. Res.* **2011**, *23*, 904–910, doi:10.1557/jmr.2008.0111.

61. Laplanche, G.; Joulain, A.; Bonneville, J.; Gauthier-Brunet, V.; Dubois, S.; Kabir, T. El Microstructural and mechanical study of an Al matrix composite reinforced by Al-Cu-Fe icosahedral particles. *J. Mater. Res.* **2011**, *25*, 957–965, doi:10.1557/JMR.2010.0118.

62. Ebisawa, M.; Hara, T.; Hayashi, T.; Ushio, H. *Production Process of Metal Matrix Composite (MMC) Engine Block*; 1991;

63. Hunt, Jr., W. H. Aluminum Metal Matrix Composites Today. *Mater. Sci. Forum* **2000**, *331–337*, 71–84, doi:10.4028/www.scientific.net/MSF.331-337.71.

64. Hayashi, T.; Ushio, H.; Ebisawa, M. *The Properties of Hybrid Fiber Reinforced Metal and It's Application for Engine Block*; 1989;

65. Kawai, C.; Park, J.-J. Mechanical and thermal properties of Al-Si3N4 composites fabricated by the infiltration of molten Al into a porous Si3N4 ceramic with network. *J. Mater. Sci. Lett.* **2001**, *20*, 385–388, doi:10.1023/A:1006735130117.

66. Blucher, J. .; Narusawa, U.; Katsumata, M.; Nemeth, A. Continuous manufacturing of fiber-reinforced metal matrix composite wires — technology and product characteristics. *Compos. Part A Appl. Sci. Manuf.* **2001**, *32*, 1759–1766, doi:10.1016/S1359-835X(01)00024-0.

67. Tang, F.; Meeks, H.; Spowart, J. E.; Gnaeupel-Herold, T.; Prask, H.; Anderson, I. E. Consolidation effects on tensile properties of an elemental Al matrix composite. *Mater. Sci. Eng. A* **2004**, *386*, 194–204, doi:10.1016/j.msea.2004.07.040.

68. Scudino, S.; Liu, G.; Sakaliyska, M.; Surreddi, K. B.; Eckert, J. Powder metallurgy of Al-based metal matrix composites reinforced with β-Al3Mg2 intermetallic particles: Analysis and modeling of mechanical properties. *Acta Mater.* **2009**, *57*, 4529–4538, doi:10.1016/j.actamat.2009.06.017.

69. Imai, T.; L'Esperance, G.; Hong, B. D.; Mabuchi, M.; Tozawa, Y. Effect of fabrication processing on superplasticity of silicon nitride whisker reinforced aluminum alloy composite 1992, *9*, 181–193.

70. Ali, F.; Scudino, S.; Liu, G.; Srivastava, V. C.; Mukhopadhyay, N. K.; Samadi Khoshkhoo, M.; Prashanth, K. G.; Uhlenwinkel, V.; Calin, M.; Eckert, J. Modeling the strengthening effect of Al–Cu–Fe quasicrystalline particles in Al-based metal matrix composites. *J. Alloys Compd.* **2012**, *536*, S130–S133, doi:10.1016/j.jallcom.2011.12.022.

71. Xie, G.; Ohashi, O.; Song, M.; Furuya, K.; Noda, T. Behavior of oxide film at the interface between particles in sintered al powders by pulsed electric-current sintering. *Metall. Mater. Trans. A* **2003**, *34A*, 699–703.

72. Sweet, G. A.; Brochu, M.; Hexemer, R. L.; Donaldson, I. W.; Bishop, D. P. Microstructure and mechanical properties of air atomized aluminum powder consolidated via spark plasma sintering. *Mater. Sci. Eng. A* **2014**, *608*, 273–282, doi:10.1016/j.msea.2014.04.078.

73. Orrù, R.; Licheri, R.; Locci, A. M.; Cincotti, A.; Cao, G. Consolidation/synthesis of materials by electric current activated/assisted sintering. *Mater. Sci. Eng. R Reports* **2009**, *63*, 127–287, doi:10.1016/j.mser.2008.09.003.

74. MPIF Method for determination of density of compacted or sintered powder metallurgy (PM) products MPIF Standard 42 2008, 4.

75. MPIF Method for determination of transverse rupture strength of powder metallurgy (PM) materials MPIF Standard 41 2008, 3.

76. ASTM Standard test method for flexural properties of unreinforced plastics and electrical insulating materials ASTM D790-10 2010, 11.

77. Materials Properties Charts Available online: https://www.ceramicindustry.com/ext/resources/pdfs/2013-CCD-Material-Charts.pdf (accessed on Apr 16, 2015).

78. Kuriyagawa, T.; Saeki, M.; Syoji, K. Electrorheological fluid-assisted ultra-precision polishing for small three-dimensional parts. *Precis. Eng.* **2002**, *26*, 370–380, doi:10.1016/S0141-6359(02)00112-5.

79. Voisin, T.; Durand, L.; Karnatak, N.; Le Gallet, S.; Thomas, M.; Le Berre, Y.; Castagne, J. F.; Couret, A. Temperature control during Spark Plasma Sintering and application to up-scaling and complex shaping. *J. Mater. Process. Technol.* **2013**, *213*, 269–278, doi:DOI 10.1016/j.jmatprotec.2012.09.023.

80. Macke, A.; Schultz, B. F.; Rohatgi, P. Metal Matrix Composites Offer the Automotive Industry and Opportunity to Reduce Vehicle Weight, Improve Performance.

81. Allison, J. E.; Cole, G. S. Metal-matrix composites in the automotive industry: Opportunities and challenges. *JOM* **1993**, *45*, 19–24, doi:10.1007/BF03223361.

82. Mavhungu, S. T.; Akinlabi, E. T.; Onitiri, M. A.; Varachia, F. M. Aluminum Matrix Composites for Industrial Use: Advances and Trends. *Procedia Manuf.* **2017**, *7*, doi:10.1016/j.promfg.2016.12.045.

83. Koli, D. K.; Agnihotri, G.; Purohit, R.; Scholar, R. Advanced Aluminium Matrix Composites: The Critical Need of Automotive and Aerospace Engineering Fields. *Mater. Today Proc.* **2015**, *2*, 3032–3041, doi:10.1016/j.matpr.2015.07.290.

84. Sweet, G. A.; Brochu, M.; Hexemer, R. L.; Donaldson, I. W.; Bishop, D. P. Consolidation Of Aluminum-Based Metal Matrix Composites Via Spark Plasma Sintering. *Mater. Sci. Eng. A* **2015**, doi:10.1016/j.msea.2015.09.027.

85. Chawla, N.; Jones, J. W.; Andres, C.; Allison, J. E. Effect of SiC volume fraction and particle size on the fatigue resistance of a 2080 Al/SiC p composite. *Metall. Mater. Trans. A* **1998**, *29*, 2843–2854, doi:10.1007/s11661-998-0325-5.

86. Couturier, R.; Ducret, D.; Merle, P.; Disson, J. P.; Joubert, P. Elaboration and characterization of a metal matrix composite: Al/AlN. *J. Eur. Ceram. Soc.* **1997**, *17*, 1861–1866, doi:10.1016/S0955-2219(97)87873-9.

87. Lord, J. D.; Morrell, R. *Elastic Modulus Measurement*; 2007;

88. Dieter, G. E. *Mechanical Metallurgy*; 3rd ed.; McGraw-Hill: New York, 1986;

89. Grayson, G. N.; Schaffer, G. B.; Griffiths, J. R. Fatigue crack propagation in a sintered 2xxx series aluminium alloy. *Mater. Sci. Eng. A* **2006**, *434*, 1–6, doi:10.1016/j.msea.2006.07.017.

90. Kim, Y. W.; Griffith, W. M.; Froes, F. H. Surface Oxides in P/M Aluminum-Alloys. *J. Met.* **1985**, *37*, 27–33.

91. Yi, J. Z.; Gao, Y. X.; Lee, P. D.; Flower, H. M.; Lindley, T. C. Scatter in fatigue life due to effects of porosity in cast A356-T6 aluminum-silicon alloys. *Metall. Mater. Trans. A* **2003**, *34*, 1879–1890, doi:10.1007/s11661-003-0153-6.

92. Park, J.-O.; Kim, K.-J.; Kang, D.-Y.; Lee, Y.; Kim, Y.-H. An experimental study on the optimization of powder forging process parameters for an aluminum-alloy piston. *J. Mater. Process. Technol.* **2001**, *113*, 486–492, doi:10.1016/S0924-0136(01)00663-X.

93. Asgharzadeh, H.; Simchi, A.; Kim, H. S. Dynamic restoration and microstructural evolution during hot deformation of a P/M Al6063 alloy. *Mater. Sci. Eng. A* **2012**, *542*, 56–63, doi:10.1016/j.msea.2012.02.031.

94. McQueen, H. J.; Ryan, N. . Constitutive analysis in hot working. *Mater. Sci. Eng. A* **2002**, *322*, 43–63, doi:10.1016/S0921-5093(01)01117-0.

95. Mcqueen, H. J.; Zhao, J.; Sauerborn, M. Constitutive Analysis, Extrusion Modeling of 2618 Particulate Composites. In *Processing and Fabrication of Advanced Materials X,*; Indianapolis, 2001; pp. 467–472.

96. Sweet, G. A.; Bishop, D. P.; Williams, B. W.; Taylor, A.; Hexemer, R. L.; Donaldson, I. W. Development of a process to investigate the mechanical properties of a powder forged aluminum alloy. In *Powdermet 2017*; MPIF: Las Vegas, 2017.

97. Hennessey, C. W.; Caley, W. F.; Kipouros, G. J.; Bishop, D. P. *Development of a PM aluminum alloy : Effect of post-sinter cooling conditions*; American Powder Metallurgy Institute, 2006; Vol. 42;.

98. Bishop, D. P.; McNally, R. L.; Geiman, T. E. Metallurgical considerations in the manufacture and development of aluminum P/M camshaft bearing caps. In *Proceedings of the Second Powder Metallurgy Aluminum & Light Alloys for Automotive Applications Conference*; Metal Powder Industries Federation: Troy, Michigan, 2000; pp. 177–185.

99. Parel, T. S.; Wang, S. C.; Starink, M. J. Hardening of an Al-Cu-Mg alloy containing Types I and II S phase precipitates. *Mater. Des.* **2010**, *31*, S2–S5, doi:10.1016/j.matdes.2009.12.048.

100. Dieter, G. E.; Kuhn, H. A.; S.L. Semiatin *Handbook of Workability and Process Design*; ASM International: Materials Park, OH, 2003; ISBN 0871707780.

101. Cavaliere, P.; Evangelista, E. Isothermal forging of metal matrix composites: Recrystallization behaviour by means of deformation efficiency. **2005**, doi:10.1016/j.compscitech.2005.04.047.

102. Hirsch, J. Recent development in aluminium for automotive applications. *Trans. Nonferrous Met. Soc. China* **2014**, *24*, 1995–2002, doi:10.1016/S1003-6326(14)63305-7.

103. Schey, J. A. *Introduction to manufacturing processes*; McGraw-Hill series in mechanical engineering and materials science; McGraw-Hill, 2000; ISBN 9780070311367.

104. Li, Y.; Onodera, E.; Chiba, A. Friction Coefficient in Hot Compression of Cylindrical Sample. **2010**, *51*, 1210–1215, doi:10.2320/matertrans.M2010056.

105. Xie, G.; Ohashi, O.; Yamaguchi, N.; Song, M.; Mitsuishi, K.; Furuya, K.; Noda, T. Reduction of Surface Oxide Films in Al–Mg Alloy Powders by Pulse Electric Current Sintering. *J. Mater. Res.* **2004**, *19*, 815–819, doi:10.1557/jmr.2004.19.3.815.

106. 2018 Award-Winning Powder Metal Parts Available online: https://www.mpif.org/News/Press-Releases/2018-Design-Excellence-Awards.asp (accessed on Aug 16, 2018).

107. Whittaker, D. The competition for automotive connecting rod markets. *Met. Powder Rep.* **2001**, *56*, 2–6, doi:10.1016/S0026-0657(01)80216-2.

108. Falsafi, J.; Rosochowska, M.; Jadhav, P.; Tricker, D. Lower Cost Automotive Piston from 2124/SiC/25p Metal-Matrix Composite. *SAE Int. J. Engines* **2017**, *10*, 2017-01–1048, doi:10.4271/2017-01-1048.

109. MacAskill, I. a.; LaDepha, a. D. P.; Milligan, J. H.; Fulton, J. J.; Bishop, D. P. Effects of cold and hot densification on the mechanical properties of a 7XXX series powder metallurgy alloy. *Powder Metall.* **2009**, *52*, 304–310, doi:10.1179/174329009X409723.

110. Sweet, G.; Wells, M.; Taylor, A.; Hexemer, R.; Donaldson, I.; Bishop, D. Thermal Mechanical Processing of Press and Sinter Al-Cu-Mg-Sn-(AlN) Metal Matrix Composite Materials. *Metals (Basel).* **2018**, *8*, 480, doi:10.3390/met8070480.

111. Hutchinson, C. R.; Ringer, S. P. Precipitation processes in Al-Cu-Mg alloys microalloyed with Si. *Metall. Mater. Trans. A* **2000**, *31*, 2721–2733, doi:10.1007/BF02830331.

112. Wang, S. C.; Starink, M. J. Precipitates and intermetallic phases in precipitation hardening Al-Cu-Mg-(Li) based alloys. *Int. Mater. Rev.* **2005**, *50*, 193–215, doi:10.1179/174328005X14357org/10.1179/174328005X14357.

113. Wang, S. C.; Starink, M. J.; Gao, N. Precipitation hardening in Al-Cu-Mg alloys revisited. *Scr. Mater.* **2006**, *54*, 287–291, doi:10.1016/j.scriptamat.2005.09.010.

114. Wang, S. C.; Starink, M. J. Two types of S phase precipitates in Al-Cu-Mg alloys. *Acta Mater.* **2007**, *55*, 933–941, doi:10.1016/j.actamat.2006.09.015.

115. Boland, C. D.; Hexemer, R. L.; Donaldson, I. W.; Bishop, D. P. Industrial processing of a novel Al–Cu–Mg powder metallurgy alloy. *Mater. Sci. Eng. A* **2013**, *559*, 902–908, doi:10.1016/j.msea.2012.09.049.

116. Trunov, M. a.; Schoenitz, M.; Zhu, X. Y.; Dreizin, E. L. Effect of polymorphic phase transformations in Al2O3 film on oxidation kinetics of aluminum powders. *Combust. Flame* **2005**, *140*, 310–318, doi:DOI 10.1016/j.combustflame.2004.10.010.

117. Xie, G.; Ohashi, O.; Song, M.; Mitsuishi, K.; Furuya, K. Reduction mechanism of surface oxide films and characterization of formations on pulse electric-current sintered Al-Mg alloy powders. *Appl. Surf. Sci.* **2005**, *241*, 102–106, doi:DOI 10.1016/j.apsusc.2004.09.025.

118. Xie, G.; Ohashi, O.; Sato, T.; Yamaguchi, N.; Song, M.; Mitsuishi, K.; Furuya, K. Effect of Mg on the Sintering of Al-Mg Alloy Powders by Pulse Electric-Current Sintering Process. *Mater. Trans.* **2004**, *45*, 904–909, doi:10.2320/matertrans.45.904.

119. Cole, G. S.; Sherman, A. M. Light weight materials for automotive applications. *Mater. Charact.* **1995**, *35*, 3–9, doi:10.1016/1044-5803(95)00063-1.

120. Chawla, N.; Chawla, K. K. Metal-matrix composites in ground transportation. *JOM* **2006**, *58*, 67–70, doi:10.1007/s11837-006-0231-5.

121. Zhang, Q.; Chen, G.; Wu, G.; Xiu, Z.; Luan, B. Property characteristics of a AlNp/Al composite fabricated by squeeze casting technology. *Mater. Lett.* **2003**, *57*, 1453–1458, doi:10.1016/S0167-577X(02)01006-6.

122. Farnoush, H.; Haghshenas Fatmehsari, D.; Aghazadeh Mohandesi, J.; Abdoli, H. Evaluation of strengthening behavior of Al–AlN nanostructured composite by the use of modified Heckel model and response surface methodology. *J. Alloys Compd.* **2012**, *517*, 45–53, doi:10.1016/J.JALLCOM.2011.11.138.

123. Sweet, G. A.; Hexemer, R. L.; Donaldson, I. W.; Taylor, A.; Bishop, D. P. *Powder metallurgical processing of a 2XXX series powder aluminum metallurgy metal alloy reinforced with AlN particulate additions*; Submitted to Materials Science and Engineering: A, 2019;

124. Whittaker, D. PowderMet 2013: Powder forging demonstrates superiority in the connecting rod competition Available online: http://www.ipmd.net/articles/002342.html (accessed on Apr 12, 2016).

125. Sweet, G. A.; Amirkhis, B. A.; Williams, B. W.; Taylor, A.; Hexemer Junior, R.; Donaldson, I. W.; Bishop, D. P. *Microstructural evolution of a forged 2xxx series aluminum powder metallurgy alloy*; Submitted to Materials Characterization, 2019;

126. Sercombe, T. B.; Schaffer, G. B. On the role of tin in the nitridation of aluminium powder. *Scr. Mater.* **2006**, *55*, 323–326, doi:10.1016/j.scriptamat.2006.04.045.

127. Martin, E.; Forn, A.; Nogué, R. Strain hardening behaviour and temperature effect on Al-2124/SiCp. *J. Mater. Process. Technol.* **2003**, *143–144*, 1–4, doi:10.1016/S0924-0136(03)00292-9.

128. Li, Y.; Ramesh, K. T.; Chin, E. S. C. The mechanical response of an A359/SiCp MMC and the A359 aluminum matrix to dynamic shearing deformations. *Mater. Sci. Eng. A* **2004**, *382*, 162–170, doi:10.1016/J.MSEA.2004.04.062.

APPENDIX A: COPYRIGHT RELEASE

MPIF Release (Chapter 7)

January 17, 2019

POWDERMET 2017
Metal Powder Industries federation
105 College Road East
Princeton, NJ 08540-6692

I am preparing my PhD thesis for submission to the Faculty of Graduate Studies at Dalhousie University, Halifax, Nova Scotia, Canada. I am seeking your permission to include a manuscript version of the following paper(s) as a chapter in the thesis:

DEVELOPMENT OF A PROCESS TO INVESTIGATE THE MECHANICAL PROPERTIES OF A POWDER FORGED ALUMINUM ALLOY; G.A. Sweet, D.P Bishop, B.W. Williams, A. Taylor, R.L. Hexemer and I.W. Donaldson

Canadian graduate theses are reproduced by the Library and Archives of Canada (formerly National Library of Canada) through a non-exclusive, world-wide license to reproduce, loan, distribute, or sell theses. I am also seeking your permission for the material described above to be reproduced and distributed by the LAC(NLC). Further details about the LAC(NLC) thesis program are available on the LAC(NLC) website (www.nlc-bnc.ca).

Full publication details and a copy of this permission letter will be included in the thesis.

Yours sincerely,

Greg Sweet

Permission is granted for:

a) the inclusion of the material described above in your thesis.

b) for the material described above to be included in the copy of your thesis that is sent to the Library and Archives of Canada (formerly National Library of Canada) for reproduction and distribution.

Name: James P. Adams Title: Executive Director/CEO

Signature: Date: January 17, 2019